Semiconductor laser for modelling and controlling spiking cells and networks

Axel Dolcemascolo

UNIVERSITÉ CÔTE D'AZUR

ÉCOLE DOCTORALE
SCIENCES FONDAMENTALES ET APPLIQUÉES

Laser à semi-conducteur pour modéliser et contrôler des cellules et des réseaux excitables

Axel DOLCEMASCOLO

Institut de Physique de Nice

Présentée en vue de l'obtention du grade de docteur en Physique
de l'Université Côte d'Azur
Dirigée par: Stéphane Barland
Soutenue le : 14 Décembre, 2018

Devant le jury composé de :
Daniel Brunner, Rapporteur, Institut FEMTO-ST
Cristina Masoller, Rapporteur, Universitat Politècnica de Catalunya
Franco Prati, Examinateur, Università dell'Insubria
Giovanna Tissoni, Examinateur, Institut de Physique de Nice
Romain Veltz, Examinateur, Inria Sophia Antipolis
Stéphane Barland, Directeur, Institut de Physique de Nice

Région Provence-Alpes-Côte d'Azur

cnrs dépasser les frontières

Titre et composition du jury

Laser à semi-conducteur pour modéliser et contrôler des cellules et des réseaux excitables

Rapporteurs:

- ◇ **Daniel Brunner**, CNRS researcher, Département d'Optique, Institut FEMTO-ST, UMR CNRS 6174 15B Avenue des Montboucons, 25030 Besançon, France
- ◇ **Cristina Masoller**, Associate Professor, Departament de Física Universitat Politècnica de Catalunya, Colom 11, Terrassa 08222, Barcelona, Spain

Examinateurs:

- ◇ **Franco Prati**, Associate Professor, Università dell'Insubria Dipartimento di Scienza e Alta Tecnologia, via Valleggio 11, 22100 Como, Italy
- ◇ **Giovanna Tissoni**, Maître de conférences UNS, Université Côte d'Azur, CNRS UMR 7335, Institut de Physique de Nice, 1361 Route des Lucioles, F-06560 Valbonne, France
- ◇ **Romain Veltz**, Inria Sophia Antipolis, MathNeuro Team, 2004 route des Lucioles - BP93, 06902 Sophia Antipolis, France

Directeur de thèse:

- ◇ **Stéphane Barland**, CNRS researcher, Université Côte d'Azur, CNRS UMR 7335, Institut de Physique de Nice, 1361 Route des Lucioles, F-06560 Valbonne, France

Résumé et mots clés

Laser à semi-conducteur pour modéliser et contrôler des cellules et des réseaux excitables

Résumé

Les systèmes “excitables” sont omniprésents dans la nature, le plus paradigmatique d'entre eux étant le neurone, qui répond de façon “tout ou rien” aux perturbations externes. Cette particularité étant clairement établie comme l'un des points clé pour le fonctionnement des systèmes nerveux, son analyse dans des systèmes modèles (mathématiques ou physiques) peut d'une part aider à la compréhension de la dynamique d'ensembles de neurones couplés et d'autre part ouvrir des voies pour un traitement neuromimétique de l'information. C'est dans cette logique que s'inscrit la préparation de cette thèse de doctorat.

Dans ce mémoire, nous utilisons des systèmes basés sur des lasers à semiconducteur pour d'une part modéliser des systèmes excitables ou des ensembles de systèmes neuromimétiques couplés et d'autre part pour contrôler (grâce à l'optogénétique) des canaux ioniques impliqués dans l'émission de potentiels d'action par des neurones de mammifères.

Le long du premier chapitre, nous présentons de manière synthétique les concepts dynamiques sur lesquels nous nous appuierons dans la suite du manuscrit. Par la suite, nous décrivons brièvement le contexte de ce travail du point de vue de la synchronisation, notamment de cellules excitables. Enfin, nous discutons le contexte applicatif potentiel de ces travaux, c'est à dire l'utilisation de systèmes photoniques dits “neuromimétiques” dans le but de traiter de l'information.

Dans le chapitre 2, nous analysons tout d'abord du point de vue théorique et bibliographique le caractère excitable d'un laser à semiconducteur sous l'influence d'un forçage optique cohérent. Par la suite, nous détaillons nos

travaux expérimentaux d'abord, puis numériques et théoriques, sur la réponse de ce système "neuromimétique" à des perturbations répétées dans le temps. Tandis que le modèle mathématique simplifié prévoit un comportement de type intégrateur en réponse à des perturbations répétées, nous montrons que le comportement est en fait souvent résonateur, ce qui confère à ce système la propriété étonnante d'émettre une impulsion seulement s'il reçoit deux perturbations séparées d'un intervalle de temps bien précis. Nous montrons également que ce système peut convertir des perturbations de différente intensité en une série d'impulsions toutes identiques mais dont le nombre dépend de l'intensité de la perturbation incidente.

Dans le chapitre 3, nous analysons (de nouveau expérimentalement, puis numériquement et théoriquement) le comportement dynamique d'un réseau de lasers à semiconducteur couplés dans un régime de chaos lent-rapide. Nous nous basons sur une étude antérieure montrant qu'un seul de ces éléments peut présenter une dynamique neuromimétique (en particulier l'émission chaotique d'impulsions originant du phénomène de canard). De façon surprenante pour un système ayant un si grand nombre de degrés de liberté, nous observons une dynamique qui semble chaotique de basse dimension. Nous examinons l'impact des propriétés statistiques de la population considérée sur la dynamique et relions nos observations expérimentales et numériques à l'existence d'une variété critique calculable analytiquement pour le champ moyen et près duquel converge la dynamique grâce au caractère lent-rapide du système.

Dans le chapitre 4 enfin, nous présentons une brève étude expérimentale de la réponse de cellules biologiques à des perturbations lumineuses. En effet, les techniques optogénétiques permettent de rendre des cellules (en particulier des neurones) sensibles à la lumière grâce au contrôle optique de l'ouverture et de la fermeture de canaux ioniques. Ainsi, après avoir étudié dans les chapitres précédents des systèmes optiques sur la base de considérations provenant de systèmes biologiques, nous amenons matériellement un système laser vers un système biologique. Nous posons ici les bases d'un système photonique simple permettant avec une complexité très modérée de réaliser des mesures de la réponse de cellules à des perturbations optiques spatialement localisées.

Mots clés

Excitabilité, laser a semiconducteur, laser avec injection, période réfractaire, excitabilité multiple, comportement résonateur, réseau neuromorphique, oscillateurs couples par impulsions, synchronisation, impulsions chaotiques, synchronisation du chaos, mixed mode oscillations, photo switch, canaux TREK1, optogénétique.

Abstract and keywords

Semiconductor laser for modelling and controlling spiking cells and networks

Abstract

Excitable systems are everywhere in Nature, and among them the neuron, which responds to an external stimulus with an all-or-none type of response, is often regarded as the most typical example. This excitability behaviour is clearly established as to be one of the underlying operating mechanisms of the nervous system and its analysis in model systems (being them mathematical of physical) can, from one hand, shed some light on the dynamics of neural networks, and from the other, open novel ways for a neuro-mimetic treatment of information. The work presented in this PhD thesis was realized in this perspective.

In this dissertation we will consider systems based on semiconductor lasers both for modelling excitable systems or coupled neuromorphic networks and for controlling (in an optogenetic outlook) ionic channels that are involved in the emission of action potentials of neurons in mammals.

During the first chapter, we will briefly present the dynamical concepts on which we will build our understanding for the rest of the manuscript. Thereafter, we will describe the context of this work from the point of view of synchronized systems, in particular excitable cells. Finally, we will discuss in this context the applications potential of this work, namely the possibility of using "neuromimetic" photonic systems as a was to treat information.

In chapter 2 we will firstly analyse from a theoretical and bibliographical standpoint the excitable character of a laser with coherent injection. Later, we will firstly detail our results, firstly experimental and subsequently numerical and theoretical, on the response of this "neuromimetic" system to perturbations

repeated in time. Whereas the simplified mathematical model envisions an integrator behaviour in response to repeated perturbations, we will show that the system often acts as a resonator, thus imparting the remarkable property of being able to emit a single pulse only if it receives two perturbations that are separated by a specific time interval. We will also illustrate how this system can convert perturbations of different intensity in a series of all identical pulses whose number depends on the intensity of the incoming perturbation.

In the third chapter we will analyse, first experimentally and later numerically and theoretically, the dynamical behaviour of a network of coupled semiconductor lasers in a slow-fast chaotic regime. We will rely on a previous study documenting that a single such element can present a neuromimetic dynamics (in particular, the emission of chaotic pulses originating from a canard phenomenon). Surprisingly for a system having such a large number of degrees of freedom, we observe a dynamics which seems low dimensional chaotic. We will examine the impact of statistical properties of the selected population on the dynamics, and we will link our experimental and numerical observations to the existence of a slow manifold for the mean field, computable analytically, and towards whom the dynamics converges thanks to the slow-fact nature of the system.

Finally in chapter 4 we will present a short experimental study on the response of biological cells to light perturbations. Indeed, optogenetic techniques enables to render the cells (in particular neurons) sensitive to light due to the optical control of the opening and closing of ionic channels. Hence, after having studied in the previous chapters optical systems on the basis of observations derived from biological systems, we will physically transfer an optical system towards a biological one. Here we lay the groundwork of a photonic system which allows, with a moderate complexity, to realize cell measurements in response to spatially localized optical perturbations.

Keywords

Excitability, semiconductor laser, laser with injection, refractory period, multipulse excitability, resonator behavior, neuromorphic network, pulse-coupled oscillators, synchronization, chaotic spiking, chaos synchronization, mixed mode oscillations, photoswitch, TREK1 channels, optogenetics.

Remerciements - Acknowledgements - Ringraziamenti

Douce France
Cher pays de ma souffrance
Bercée de tendre insouciance
Je t'ai gardée dans mon cœur!
Ma recherche, à Sophia Antipolis
Où, avec les autres doctorants
J'ai partagé tant de malice
Oui je t'aime
Et je te donne ce poème
Oui je t'aime
Dans la joie ou la douleur

Douce France - Charles Trenet, rivisited[1]

Usually the acknowledgements of a thesis defense either contains lots of peoples and names and facts and "thank you" and citations; or just a few selected people along with some general comments about the lab life, family, the universe and whatnot. This acknowledgments section belongs to the former type (lots of names and stuff). In the following, given the multi-language nature of my Phd studies, I will express my special appreciation and thanks either in English or in Italian, with just a few touches of French.

To begin, I would like to thank the people that were instrumental to my PhD studies during these years: *tout d'abord* my supervisor Dr. Stéphane Barland, for the many discussions, explanation, remarks in the workplace, and for its patience in teaching me a lot of soft and hard skills, useful both inside and outside the lab. I started my career as a "student", and I am now transitioning

[1] With the help of Dr. Patrice Camelin.

towards being a "worker". So thank you for pushing me to become a better version of myself, *je vais tirer la leçon* of my experiences here at the lab. I wish that I wrote down all of the different "francesismi"[2] that you said during these years, like: "non importa cosa", "farne tutto un formaggio" o "dare la marmellata ai maiali", because they are hilarious.

Next, I would like to thank Dr. Romain Veltz, our "matematico di fiducia"[3], that has welcomed me to INRIA for some time, where the food is (arguably) better and the pc screens are larger. I learned from him everything I know about slow-fast systems and more, and I have enjoyed our discussions together (the ones that I managed to understand at least). I would also like to mention Dr. Elif Koksal Ersoz, with whom I have shared the office while I was at INRIA, who has been a gracious host and friend. Special thanks to Prof. Franco Prati that has introduced me to the optics world and its community, and has helped me find my current PhD program.

Other collaborators on my project include Dr. Bruno Garbin and Dr. Pierre Walczak, with whom I shared the lab; Dr. Francesco Marino, with whom I shared the matrix setup; the people from Philips: Ralph Gudde, Dr. Roland Jaeger and Dr. Michael Miller and from CERSA-MCI: Jean François Fardeau and José Roméro. Thanks also to the collaborators at the biology institute iBV in Nice: Dr. Guillaume Sandoz and Dr. Olena Butenko.

I would now like to thank the residents of the INPHYNI lab: starting from the *service administrafit, et notamment* Nathalie, Isabelle and François-Regis, *ainsi que* the IT department (i.e. Christian), for their constant help to navigate the administrative and the web world respectively. Many thanks also to the electronic department: Jean-Claude et Arnaud. And a general thank you to all of the other members of the lab, with whom I have shared sometimes a meal and sometimes a joke.

And now to my peers: a PhD program would not be the same if there were not the PhD students. I have enjoyed the discussions, the jokes, the football sessions, the game nights, the hangouts and more with you, and you've made it fun. I have never felt more as a PhD student than during the JDPN days, or the various meetings together, while sharing a common history, a common goal and common fears. I would like to thank the "old ones": Thibaut, Samir, Tao, Simona, Bruno and François; the "ones of my year": Jean, Aurélien, Guido and Florent and "the younger ones": Sylvain, Marius, Ana, Vittorio, Antonin, Julián, Alexis and Pierre. And finally, a special thanks to three PhD students (or ex-students) in particular for special merits: thanks to Patrice, for always being available and helpful, both for me and for other students, you are the grand-mother of all of the PhD students of the lab; thanks to Cristina, whose steps I have followed to get here, who introduced me to the lab, to the people

[2]French expressions translated literally in italian.
[3]Trusted mathematician of choice.

and to France and has been an Italian ally and friend through all; and thanks to Michelle, with whom I have shared many good times, for being a good friend.

One of the best things about a PhD program is that you get to meet many different people, at conferences or from other institutes, that come from many parts of the world, and who you could never meet otherwise. I don't remember all of the names, so I will just thank Wouter as a representative of them all.

E adesso passiamo *aux Italiens*. Vorrei ringraziare innanzitutto la mia famiglia: Carmela, Pasquale, Denis ed Erika per il loro supporto, durante ed oltre il dottorato. Un bacione in particolare a mia mamma ed ai suoi messaggi inoltrati su Whatsapp, che ancora devo capire dove li trovi. Ringrazio anche il resto degli zii, cugini e parenti per far parte della nostra bella famiglia: Fernanda, Marino, Manuel, Noemi, Mattia, Letizia, Nem, Jacopo, Salvatore, Fiorella, Davide, Gabriele, Jonathan, Tonino, Miriam, Andrea e Sofia. Un saluto speciale a Nonna Vincenzina, la capostipite della famiglia.

Ringrazio i miei amici di lunga data: Salvatore, Ilaria, Giulia e Alice, che mi hanno s(u/o)pportato e sono stati vicini nonostante la lontananza; ed i miei ex-colleghi universitari: Cecilia, Davide, Manrico, Michele, Riccardo, Samuele e quel pazzo di Manuele; spero di rivedervi presto.

Infine, dulcis in fundo, vorrei ringraziare il mio fidanzato Luca, per essermi stato vicino, fisicamente e figurativamente, durante questi anni di trasferta. Nonostante la distanza, mi hai tenuto compagnia nelle notti buie e tristi e solitarie, e mi hai motivato per arrivare fino alla fine. E senza dubbio grazie a te credo di aver triplicato la mia cerchia sociale di Como e dintorni. A te dedico questa tesi. Un abbraccio ed un bacio.

Thanks to all that I should have mentioned but I forgot.

Axel

Figure 1: xkcd comic

Preface

In this dissertation we will explore the behaviour of dynamical systems which can be made to be excitable, that is, that will respond to a stimulus by an all-or-none type of response. Excitable systems can be found in many shapes and forms in Nature, from biological to chemical to physical settings. The most famous example of an excitable system is that of a neuron, where an action potential is generated if the stimulus overcomes a certain threshold, which then travels across the axon.

In our case we will consider excitable optical systems, where the excitable response will be in the form of light pulses. However the neuron model will often be taken as a reference with whom we have to confront. The connection between the optical systems and its biological counterparts will in fact be a source of insight into the type of properties that we can expect to observe. Furthermore the two different worlds, the biological one and the optical one, are also strongly connected by a wealth of mathematical models and techniques which underlay the behaviour of both.

Starting from the case of a single excitable optical element, we will describe in detail its properties and dynamical behaviour, both experimentally and numerically. Later, we will expand our study to encompass a network of coupled elements, in order to get an understanding on the behaviour of many chaotically spiking units as a crude optical model of a network of spiking neurons. Finally, we will probe the excitable behaviour of actual biological cells in an experiment which employs a novel technique based on the optical control of ion channel activity.

Contents

Chapter 1

General introduction

The aim of this manuscript is to report the results obtained when studying the dynamical behaviour of semiconductor laser systems in the regime where they act in ways that are similar to that of excitable cells, as in the case of neurons. In particular, we will explore the controllable excitable nature of a single semiconductor laser with injection, and the synchronization and dynamical properties of a network of coupled semiconductor lasers. We will also probe the excitable properties of actual photo-active biological cells in an experiment in collaboration with a biology research group.

Before going into the details of the work, we will briefly introduce the concepts of oscillator systems, excitability and network of coupled oscillators which will constitute a valuable background for the following description of the experiments and their results. Later in section 1.3 we will introduce the content of the various chapters of this thesis in a nutshell.

1.1 Oscillator and excitable systems in Nature

Let us now begin with an introduction on oscillator systems, with a particular interest on excitable systems. It is worth mentioning that not every oscillator system is excitable and not every excitable system can oscillate with a limit cycle. However in many cases a system can switch from an excitable behaviour to an oscillatory behaviour by increasing the parameter which represents the strength of the external perturbation. This switch is usually related to a bifurcation in the model, as in the case of Class 1 and Class 2 of neural excitability [Izhikevich 1999], which we will describe later. In the former case the oscillations appear due to a saddle-nose bifurcation on a limit cycle, while in the latter due to an Andronov-Hopf bifurcation.

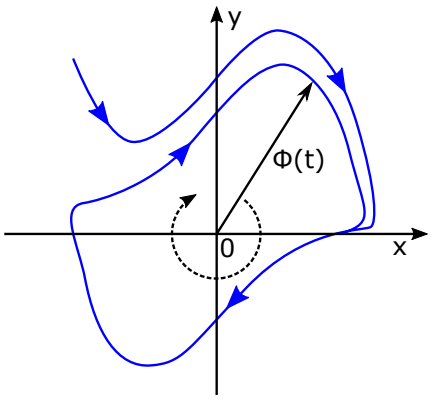

Figure 1.1: Schematic example of a 2D self-sustained oscillator with a stable limit cycle. $\phi(t)$ is called the *phase* of the oscillator.

1.1.1 Self-sustained oscillator systems

Periodic phenomena are abundant in Nature in an impressive variety, and as humans we are sensitive to these various rhythms probably because our own perception of time depends on the periodic oscillations of our biological clocks [Groos 1985]. While in some cases these oscillatory processes may come from the mutual synchronization of myriads of individual processes, in other cases these oscillations are the result of the intrinsic dynamics of isolated and simple oscillatory elements that can oscillate at their natural frequency without interacting with the outside world. Examples of these self-sustained oscillator systems can be found in biology (like in the case of the Circadian rhythms that govern the behavior and methabolic processes of many different living organisms), in chemistry (as in the Malonic acid reaction), in physics (as in the case of a laser with optoelectronic feedback [Al-Naimee 2009], a case which will be studied in detail later in this thesis), in electronic circuits (as in the famous Van der Pol circuit with non-linear resistance [van der Pol 1927]) and in many other contexts [Winfree 1967, Winfree 2001].

When observing the dynamics of these processes in the space of their dynamical variables (phase space), one can usually observe that their periodic oscillations describe a closed curve, called a *limit cycle*. Figure 1.1 shows a schematic representation of such a limit cycle in the case of a 2D system. This limit cycle attracts phase trajectories that starts close to it, and is therefore called an attractor of the dynamical system. Given that this cycle repeats itself after each loop, we can define an angle variable $\phi(t)$ (called *phase*), such that, starting at $t = t_0$ from an arbitrary point on the cycle, it will increase monotonically along the trajectory, and each rotation of the point around the cycle will correspond to a 2π gain in phase. In many models it is possible to reduce the motion of the system along the limit cycle to a dynamical equation regarding the phase (a *phase model*). Here we will not dwell on the study of such oscillator systems, so for a further description of their properties we refer the reader to

[Pikovsky 2003].

1.1.2 Excitability phenomenon and classes of neural excitability

Excitability is a typical feature of neural and muscle cells, and is defined by an all-or-none type of response to a stimulus. The main properties of excitable systems are the following:

- given a perturbation whose strength is under a certain threshold, the system only relaxes following a response which is linearly dependent to the strength of the perturbation,
- given a perturbation whose amplitude is higher than the threshold, the system reacts with a large-amplitude nonlinear response, whose shape and amplitude are almost independent from the input perturbation.

The system is then either mostly unaffected (for under-threshold perturbations) or it generates a large response always similar to itself (when the perturbation overcomes the threshold).

Historically one of the first documented examples of this phenomenon appeared in 1952 in [Hodgkin 1952a, Hodgkin 1952b], where the authors, Hodgkin and Huxley, were able to measure the current-voltage relations in the of a giant axon of *loligo*, a type of squid. They remarked that the membrane potential of the axon behaved in an excitable manner with respect to voltage perturbations, and they were able to reproduce their results by introducing an equivalent electrical circuit that could model the membrane potential dynamics. They received the 1963 Nobel prize in Physiology or Medicine for their work.

From this point onwards, neurons have always been regarded as the epitome of an excitable system. Figure 1.2(a) shows a schematic depiction of a typical neuron, consisting of a cell body (*soma*), thin structure that arises from the body (*dendrites*), and a long slender extension of the cell body called *axon*. Panel (b) shows instead the response of the membrane potential to a stimulus perturbation as it would be measured at a point on the axon. At rest, the membrane potential (the voltage difference between the interior and the exterior of the cell) is around -70 mV. Then, given a stimulus, the potential either relaxes back to the resting state (for stimuli lower than the threshold), or it quickly rises to a peak of around 40 mV (for stimuli higher than the threshold). After the rise, the potential quickly drops and overshoots at around -90 mV, before relaxing back again to the resting state. These types of spikes, also called *action potentials* can quickly travel along the axon until the end, where the neuron connect with other neurons at synapses, or to motor cells or glands. This type of spike communication is widely accepted as the mechanism underlying the

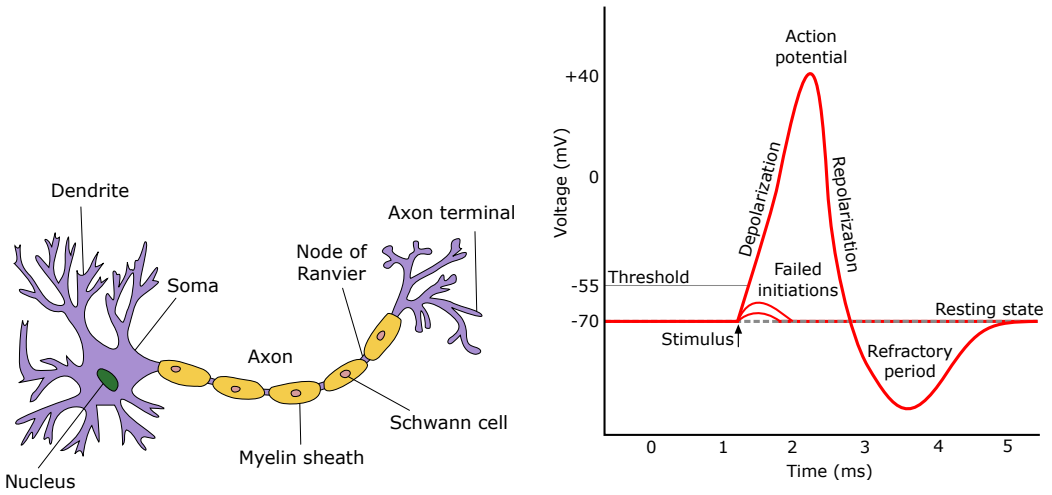

(a) Depiction of a typical neuron[1].

(b) Approximate plot of the excitable response of a neuron to external stimuli. If the stimulus is over-threshold, a typical action potential is observed; otherwise, the voltage only relaxes to the resting state[2].

Figure 1.2: Representation of the shape of a typical neuron (a), and of its action potential response to a stimulus (b). Reprinted from [Alpha3031 2018].

exchange of information between the various neurons in the brain.

Beyond the original biological setting, excitable systems have been studied for many years and in many different contexts such as chemistry [Belousov 1958][3] and [Neumann 1977, Kuhnert 1989], specialized plant movements [Trebacz 2006, Noblin 2012, Brownlee 2013], human "mexican waves" (when rows of spectators rise up in a stadium) [Farkas 2002] and in optics and optoelectronics in the case of lasers with saturable absorber [Dubbeldam 1999, Larotonda 2002], laser with optical feedback [Giudici 1997], laser with injection [Coullet 1998, Barland 2003, Goulding 2007, Kelleher 2011] and resonant tunnelling diodes [Romeira 2013]. For an extended overview of excitable optoelectronic devices we refer to the review paper [Prucnal 2016].

Classes of Neural excitability Neural excitability is a very broad subject in mathematical neuroscience, and many different models have been proposed to describe the generation and propagation of action potentials in excitable membranes. The most prominent and ubiquitous in this field are Hodgkin-Huxley [Hodgkin 1952a], FitzHugh-Nagumo [FitzHugh 1955], Con-

[1]Original in the public domain, redrawn in SVG by User:Dhp1080, CC BY-SA 3.0, https://commons.wikimedia.org/wiki/File:Neuron.svg

[2]Original by en:User:Chris 73, updated by en:User:Diberri, converted to SVG by tiZom - Own work, CC BY-SA 3.0, https://commons.wikimedia.org/w/index.php?curid=2241513

[3]For an historical perspective on this reaction, see [Winfree 1984, Pechenkin 2009]

nor [Connor 1977], Morris-Lecar [Morris 1981] and the more recent Izhikevich model [Izhikevich 2007]. These models have been widely studied with bifurcation theory tools and other mathematical techniques. Two relevant references on the subject are [Hoppensteadt 1997, Izhikevich 2000b].

The fact that these models are excitable suggests that their activity is close to a bifurcation point where the perturbation strength plays the role of the bifurcation parameter: if the perturbation is lower than a certain threshold, the system just returns to the equilibrium, while if the threshold is overcome, there is a sudden change in dynamics and a spike can be generated. A classification of the type of excitability depending on the transition between equilibrium state and spiking state has been proposed by Hodgkin [Hodgkin 1948] and goes as follow:

- **Class 1 Neural excitability:** When action potentials can be generated with arbitrarily low frequency as the strength of the applied current increases;
- **Class 2 Neural excitability:** When action potentials can be generated in a certain frequency band that is relatively insensitive to changes in the applied current. In particular, at the transition between resting state and periodic spiking, the spike trains appear with a finite frequency.

Class 1 neurons fire with a frequency that varies smoothly over a range of about 5-150 Hz, while the frequency band of Class 2 neurons is usually 75-150 Hz, but it can vary from neuron to neuron [Hoppensteadt 1997]. Figure 1.3(ii) shows a schematic depiction of the spiking frequency dependence from the applied current near the bifurcation point for the two excitability classes.

This type of behaviour can be explained by many types of bifurcations, however two typical examples are usually introduced as the most representative case for the two classes, which are displayed in Figure 1.3(i). They are:

- *Saddle-node on invariant circle (SNIC) bifurcation* - Class 1: This bifurcation is characterized by the collision and disappearance of two equilibria, a saddle and a node, that lie on a limit circle. In the case of the plotted figure, an unstable focus is also present in the center of the invariant circle. As the applied current increases, the saddle and node points come closer to each other, and when they merge only a limit cycle remain with a frequency that can be arbitrarily low the closer is the current to the bifurcation point.
- *Subcritical Andronov-Hopf bifurcation* - Class 2: This bifurcation is characterized by the birth of an unstable limit cycle around an equilibrium point. Even though the limit cycle is unstable, the system can oscillate one or more times around the limit cycle attractor before going back to the stable point. Note that the cycle is born with a finite frequency, which explains the fact that the frequency of oscillations cannot be arbitrarily

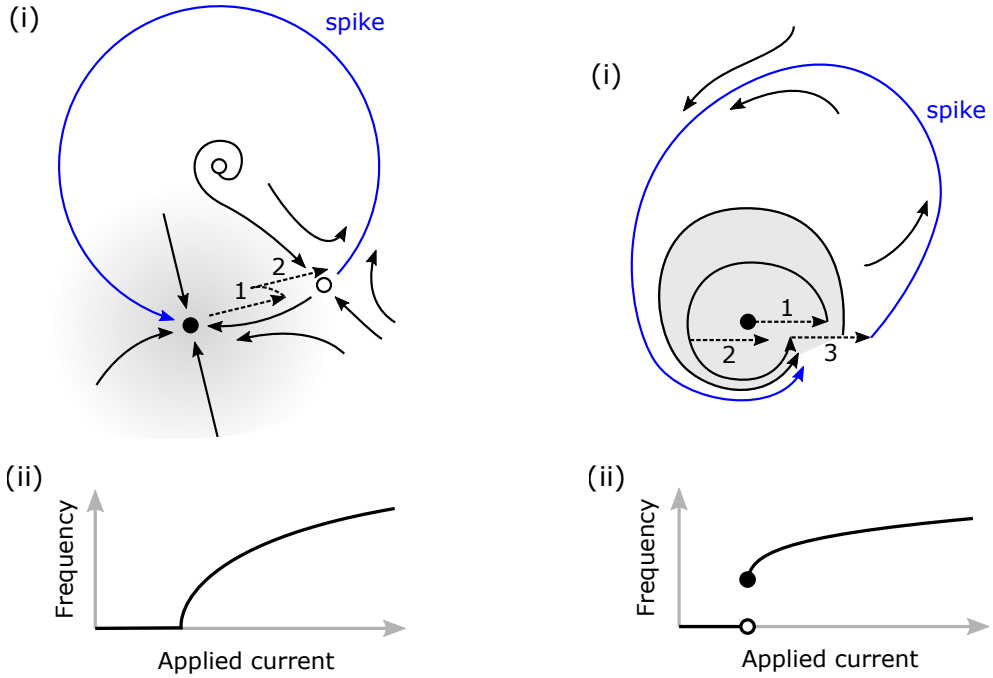

(a) Saddle-node on invariant circle (SNIC) bifurcation (Class 1 neural excitability, integrator behaviour)

(b) Subcritical Andronov-Hopf bifurcation (Class 2 neural excitability, resonator behaviour)

Figure 1.3: Class 1 and Class 2 neural excitability: most typical bifurcation example and empirical definition. *(i)* Depiction of the two bifurcation examples (SNIC bifurcation and subcritical Andronov-Hopf bifurcation), which are also characterized by an integrator and resonator behaviour respectively when perturbed with a double consecutive subthreshold perturbation. *(ii)* Empirical definition of the excitability Class (Class 1 can display arbitrarily low spiking frequency, while Class 2 transitions from the resting state to a finite spiking frequency as the applied current increases).

low.

These two bifurcations can then describe very well the empirical behaviour of Class 1 and Class 2 type of neurons. Class 1 excitability can be observed with the Morris-Lecar and Connor models, while Class 2 can be observed with the Morrix-Lecar, FitzHugh-Nagumo, Hodgking-Huxley models. Other differences between the two classes of excitability are summarized in the table of Figure 2.50 of [Hoppensteadt 1997]. Other references include [Izhikevich 1999, Izhikevich 2000b, Izhikevich 2007].

Integrator and resonator behaviour A particularly important difference between the two classes of neurons for the purpose of this thesis is their behaviour as either *integrators* or *resonators*. Neuronal models are defined as resonators if they display subthreshold oscillations (small oscillations around

the resting state that do not trigger an excitable response), while they are integrators otherwise [Izhikevich 2007]. An important consequence of this distinction, which is where the two categories get their name, is the following:

- **Integrators:** These are type of neurons that, given two or more successive subthreshold perturbation, will integrate (possible with some leak) all of the incoming perturbation, and if the sum of the perturbations is greater than the threshold, a spike will be generated. The basic model that can reproduce this dynamics is that of a circuit where a resistor and a capacitance are arranged in parallel, which is called *leaky integrate-and-fire (LIF)* model.
- **Resonators:** These neurons are characterized by subthreshold oscillations, and they will respond with a higher efficiency to an input perturbation with a definite frequency, which is the one where the period of the perturbation matches the period of their subthreshold oscillations.

Again, we can introduce two bifurcations as typical examples that can explain these two different types of behaviours. They are again the SNIC bifurcation and the subcritical Andronov-Hopf bifurcation, and their integrator/resonator behaviour can be explained as follows:

- *Saddle-node on invariant circle (SNIC) bifurcation* - Integrator: Figure 1.3(a)(i) shows the case where two perturbations with equal strength are applied to the resting system. Here the first perturbation will displace the system towards the unstable saddle, which plays the role of the threshold, but not enough to overcome it. Then after some time the second perturbation will be applied. In this case the sum the consecutive underthreshold perturbations will be enough to overcome the threshold and therefore generate a spike, which in this case is the attracting trajectory that goes from the saddle to the node. Note that the timing of the two perturbations is not relevant: they just need to be close enough in time so that the sum of the two can overcome the threshold (the closer they are, the higher the efficiency of generating a spike).
- *Subcritical Andronov-Hopf bifurcation* - Resonator: Figure 1.3(b)(i) shows again the case where we apply two perturbations with equal strength to the resting system. After the first perturbation (1), the system starts to oscillate around the stable focus. What happens next depends on the timings of the second perturbation. If the second perturbation is applied at (2), the system is displaced inside the attracting region of the focus (the gray shaded region), so it will just relax back to the stable node. However, if instead the perturbation is applied at (3), the system will escape from this attracting region and follow the limit cycle attractor around the focus, which will constitute a spike. Note that in this case the timing is important: one needs to wait exactly one subthreshold oscillation period in order to have a higher efficiency to generate a spike.

As we have seen, the bifurcation example that belonged to the Class 1 neural excitability (SNIC bifurcation) was also an integrator-type of system, while the bifurcation example that belonged to the Class 2 neural excitability (subcritical Andronov-Hopf bifurcation) was also a resonator-type of system. This equivalence (Class 1 as integrators and Class 2 as resonators) is generally valid even for other types of bifurcations, so one can usually consider the resonator and integrator behaviour as a property of the respective excitability Class. However, this is not strictly the case 100% of the times. As an example, the saddle-node bifurcation can also display an integrator behaviour, while its type of excitability is mostly of Class 2. A summary of neurocomputational properties for integrators and resonators system are displayed in Figure 7.15 of [Izhikevich 2007].

1.2 Complex networks and synchronization

In the previous section we have introduced the concepts of *oscillator* and of *excitable system*. Even though they are somewhat separate concepts, the study of networks of oscillators and of networks of excitable elements (as in the case of pulse-coupled theta neurons) are linked together by a wealth of multidisciplinary studies and papers that could go under the broad umbrella topic of *complex networks and synchronization*. In what follows we will introduce the case of networks of coupled phase oscillators, which can be thought of as the first step necessary in understanding more complex types of coupled elements. However one should not be fooled by the apparent simplicity of the topic which, by itself, could (and is) the subject of many research papers and books. Here we will just introduce the main issues along with some photonic applications and refer to the bibliography for a deeper exploration of the subject.

1.2.1 Synchronization in networks of coupled phase oscillators

Historically the scientific interest in the synchronization of coupled oscillators can be traced back to the famous "clock experiment" by Christiaan Huygens (1629-1695), the famous Dutch mathematician, astronomer and physicist. In a letter to his father in 1665, he writes[4]

> While I was forced to stay in bed for a few days and made observations on my two clocks of the new workshop, I noticed a wonderful effect that nobody could have thought of before. The two clocks, while hanging [on the wall] side by side with a distance of one or two feet between, kept in pace relative to each other with a precision so high that the two pendulums always swung together, and

[4]English translation from French by Carsten Henkel, reprinted in Appendix A1 of [Pikovsky 2003].

> never varied. [...] here we have found two clocks that never come to disagree, which seems unbelievable and yet is very true.

This "odd kind of sympathy" between the two clocks was explained by Huygens by the interaction between the two clocks through the vibrations of the wall or the beam where they were hanged. The same type of mutual influence resulting in synchronization was later observed for organ pipes [Rayleigh 1894], locking phenomena in circuits and radio technology [Appleton 1922, van der Pol 1927, Adler 1946], pacemaker cells in the heart [Michaels 1987], animal behaviour like flashing fireflies [Buck 1988, Ermentrout 1991] or chirping crickets [Walker 1969], coupled cortical neurons [Crook 1997] and brain networks [Varela 2001], to name a few. We refer to [Pikovsky 2003] for a detailed historical account of these studies.

The most notorious phase-coupled model: the Kuramoto model
Phase-coupled models have been studied intensively in recent years. However, one model in particular is stands out as a reference model in the literature: the Kuramoto model [Kuramoto 1975, Kuramoto 1984]. Inspired by an earlier work by Winfree [Winfree 1967], Kuramoto proposed the phase-coupled oscillator model:

$$\dot{\theta}_i = \omega_i - \sum_{j=1}^{n} K_{ij} \sin(\theta_i - \theta_j), \qquad i \in \{1, \dots, n\} \tag{1.1}$$

He also showed that, in the case of mean field coupling ($K_{ij} = K/n$), synchronization in this model can occur if the coupling K exceeds a certain threshold value, which is a function of the distribution of the natural frequencies ω_i. If instead the coupling is too week, the oscillators will be desynchronized.

For intermediate couplings, part of the oscillators are phase locked ($\dot{\theta}_i = 0$) and part are rotating out of synchrony with the locked oscillators. This partial synchronization case that emerges directly from the Kuramoto model can also be found in other coupled oscillators models, as in the Ginzburg-Landau equation [Kuramoto 2002], a ring of phase oscillators [Abrams 2004], identical oscillators with group coupling [Abrams 2008] or the case of coupled Kuramoto oscillators with inertia [Olmi 2015]. Given their incongruous nature, these states have been called *chimera states* and have been later observed experimentally in liquid crystals [Hagerstrom 2012], chemical oscillators [Tinsley 2012, Nkomo 2013], optoelectronic systems [Larger 2015] and many other systems (see the introduction of [Rakshit 2017] for other examples).

Other important properties of this model include the possibility of deriving a mean-field model in the large n limit (a Fokker-Planck equation), including the case of white-noise forces (a nonlinear Fokker-Planck equation) and the existence of stable standing waves and stable travelling waves solutions transitions organized around a codimension-two Takens-Bogdanov bifurcation point [Acebrón 2005].

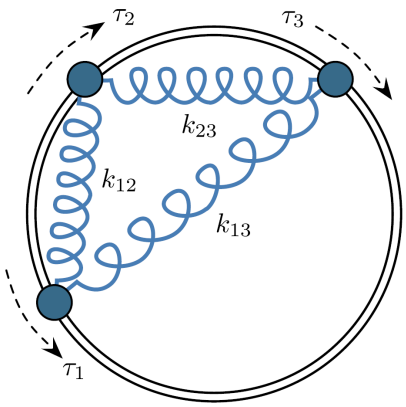

Figure 1.4: Mechanical analogue of a coupled oscillator network. Reprinted from [Dörfler 2014], with permission from Elsevier.

Mathematically, the Kuramoto model is one of the simplest way that one can employ to describe a system of n oscillators, each characterized by a phase angle θ_i and a natural rotation frequency ω_i that interact in an addictive, anti-symmetric, diffusive interaction [Dörfler 2014]. Recently published surveys on this topic, with an emphasis on the history and applications of this type of models throughout science and engineering are [Acebrón 2005, Arenas 2008, Dorogovtsev 2008, Dörfler 2014].

A mechanical analogue of a coupled oscillator network A particularly useful mechanical analogue of this coupled oscillator model is that of a spring network, as shown in Figure 1.4 (as described in [Dörfler 2014]). The system consists on a group of particles that are constrained to move on a unit circle without colliding, each with its inertial and damping coefficients $M_i > 0$ and $D_i > 0$ respectively and driven by an external driving torque τ_i. The system of spring-interconnected particles obeys the model [Dörfler 2013]:

$$M_i\ddot{\theta}_i + D_i\dot{\theta}_i = \tau_i - \sum_{j=1}^{n} k_{ij}\sin(\theta_i - \theta_j), \qquad i \in \{1,\dots,n\} \tag{1.2}$$

where the coupling strengths between two particles are given by the positive stiffness coefficients of the various springs, such that $k_{ij} = k_{ji}$. Note how in the limit of small masses M_i and uniformly-high viscous damping we recover the Kuramoto model. Intuitively, one can then imagine that, if the neighbouring coupling is weak and the network strongly heterogeneous (i.e. with strongly dissimilar natural frequencies), each particle will travel at their natural frequency $\omega_i = \tau_i/D$ and the system will not display any coherent behaviour. On the other hand, if the enforced coupling is strong and the network is sufficiently homogeneous, the network could synchronize such that the frequencies, or even all the phases, can become aligned.

1.2.2 Neural oscillations and complex network dynamics in neuroscience

As already mentioned, neural excitability and neural oscillations are very broad subjects in mathematical neuroscience. We already introduced the principal oscillator models for single neurons (e.g. Hodgkin-Huxley, FitzHugh-Nagumo) and in order to understand what are the mechanisms that underlay various forms of rhythmic behaviour (e.g. spiking and bursting) in the case of complex networks, a wealth of dynamical systems techniques have been employed. Among them, we can cite *reduction techniques*, such as the separation of time scales reviewed in [Rinzel 2013, Kuehn 2015], various applications of *synchrony of neural models* [Arenas 2008, Pikovsky 2003], or of group networks [Sorrentino 2007], the *clustering* of different groups of oscillators [Boccaletti 2006, Nekorkin 1999], *symmetric dynamics* [Golubitsky 1988, Golubitsky 2002], and continuous spatially-extended models like *neural mass models* [Wilson 1972, Touboul 2011, Spiegler 2011], used to describe mesoscopic brain oscillations and epileptic patterns, and *neural field equations* [Wilson 1972, Wilson 1973, Amari 1977, Veltz 2011, Faye 2018] which support travelling waves, spatially periodic patterns, oscillatory dynamics and localized activity [Bressloff 2012].

In the case of weakly coupled phase oscillators (as in the case of the Kuramoto model), a mathematical tool in particular has had a profound impact on the study of oscillator networks: the *theory of weakly coupled oscillators* [Kuramoto 1984, Ermentrout 1984], already introduced in the previous subsection. It is now a standard tool in the study of oscillatory networks [Ermentrout 1984, Van Vreeswijk 1994, Chow 1998, Lewis 2003, Corinto 2007] and in networks of relaxation oscillators [Coombes 2001, Izhikevich 2000a]. For a comprehensive review of this framework, we refer to [Hoppensteadt 1997], and for a review of oscillatory network dynamics and weakly coupled oscillator theory we refer to [Strogatz 2000, Ashwin 2016], along with the surveys mentioned in the previous subsection 1.2.1.

1.2.3 Neuro-inspired photonic networks and applications

So far we have explored many types of mathematical models and physical applications that claim to model the behaviour of a single neuron or that of a neural network. However, there is another approach towards neuromorphic networks that aims to exploit their properties to code and compute information. This is more or less the same difference between trying to understand the mechanics and aerodynamics of a flying bird, and actually constructing a functioning airplane. The underlying assumption is that the most complex and powerful computation machine in the universe, i.e. the human brain, operates thanks to a decentralised interconnected neu-

ral architecture that exploits spike communication in order to analyse sensory information and transform them into a sensible interpretation of reality [Diesmann 1999, Borst 1999, Kumar 2010, Ostojic 2014]. This architecture has then become an inspiration to build technological applications that could surpass the good old von Neumann processors, without forgetting that each system has its own properties and limitations. To paraphrase Yann LeCun, "if we modelled airplanes to imitate Nature, they would have feathers instead of metal wings"[5].

One of the favourable properties that are credited for the performance advantages of neural network is the ability of each neuron to operate on information encoded as *spikes*. This type of *spiking signal processing*, which is neither analog nor digital and process information using both space and time [Thorpe 2001, Maass 2002], has been found to be both expressive and resistent to noise [Sarpeshkar 1998, Tait 2013], and such that it could solve unconventional computing problems and outperform current technology in both power efficiency and complexity [Tononi 2008, Ananthanarayanan 2009, Modha 2011]. As an order of magnitude estimation, the enormous computational performance of modern supercomputers comes at a cost of around ~ 10 MW in power consumption, while the human brain suffice with a mere ~ 20 W [Van der Sande 2017].

In the case of photonic devices, neuromorphic properties have been exploited to achieve: a synchronization state between many coupled oscillator laser arrays in Kuramoto-like networks [York 1991, Kozyreff 2000, Oliva 2001]; excitable devices realized with semiconductor lasers with optical or electrical feedback (see [Prucnal 2016], section 3 for a complete list) that can display typical features of excitable system such as a refractory period [Selmi 2014, Garbin 2017a] and computational properties such as temporal pattern recognition [Shastri 2016] and stable recurrent memory [Garbin 2014, Garbin 2015b, Shastri 2016]. For an overview on excitable lasers and spike processing, we refer to [Prucnal 2016].

A special mention has to be given to one of the more promising applications of neuro-inspired optical networks: *reservoir computing*. This novel computational paradigm currently employed in the field of machine learning consists in a collection of connected units that are trained in order to generate a desired output. Typically, an input sequence drives the complex dynamics of a reservoir that non-linearly encodes the input. The output is then obtained by a linear combination of the reservoir state. The system is trained in order to find the best set of output coefficients usually through a linear regression. The characteristic of the reservoir computing is that the training is only performed on the readout layer, that is, the last layer of units before the output is calculated. Realizations of photonic reservoir computing have been realized on a passive silicon chip [Vandoorne 2014], in diffractively coupled VCSELs [Brunner 2015] and delay-

[5] https://www.youtube.com/watch?v=RgUcQceqC_Y

based optical or optoelectronic systems [Duport 2016, Brunner 2013]. A review on the recent advances in this field can be found in [Van der Sande 2017].

1.3 Content of this thesis

Chapter 2 will be devoted to the study of a single semiconductor laser device with injection. We will demonstrate its excitable nature by using dynamical models of increasing complexity, from the simple Adler model to a Class B laser-with-injection formulation. Probing the system with different types of perturbation, we will describe how a refractory period can be detected; how a shift from an integrator to a resonator behaviour can been observed when changing the model parameters and the possibility of controllable multipulse excitability.

In Chapter 3 we will introduce a setup consisting of a network of coupled laser devices in an all-to-all configuration. Groups of coupled lasers of different sizes can be studied in this way, and we will record their behaviour as the bifurcation parameter driving the mean field dynamics is varied. The dynamics that we can expect from the mean field of the population will be related to a property of the selected population (the average output-power threshold). A reduction in the complexity of the mean field dynamics will be reported and explained through an analytical study and numerical simulations.

Finally Chapter 4 will contain a short investigation into the property of biological cells in collaboration with a biology group in Nice. In particular, we will observe how the laser light coming from an optical fiber can be used to optically control the activation of potassium channels in the membrane of single cells, which lead to a flow of current across the membrane that can be measured in a voltage-clamped experiment.

Chapter 2

Single semiconductor laser device with injection as an excitable spiking element

2.1 Introduction to the chapter

In this chapter we will describe an experiment which consists in a semiconductor laser with injected signal. The basic elements of this setup are two separate lasers: a master laser, in this case an edge-emitting tunable laser, and a slave laser, in this case a VCSEL. The signal coming from the master laser is injected into the slave laser, and this allows for an interaction between the two signals.

Given that with this configuration we are coupling two periodic systems together, it can be expected that the two laser frequencies can synchronize, in much the same way as the famous 17th century observation of the synchronization of two heavy pendulum clocks hanging from a wall by Huygens, recently reproduced in [Oliveira 2015]. This synchronization phenomenon is very common in many other oscillator systems in Nature, from biology to chemistry to neuroscience. In the case of electrical oscillators, a modelling equation for the evolution of the phase difference ϕ of two oscillators was introduced by Adler [Adler 1946], and reads:

$$\dot{\phi} = \omega - \sin\phi \tag{2.1}$$

where ω is a parameter that represents the detuning in frequency between the two oscillators. Even though it is seemingly very simple, this model can be considered as the first order approximation of our experiment for low levels of injected signal and small detuning. Furthermore, it can describe to first order two of the most important features that characterize our system: the locking region and the excitability behaviour. In fact, it turns out that, at lower injection, the frequency of the slave laser is locked to the frequency of the master laser when the bifurcation parameter ω is in the range $-1 < \omega < 1$.

At the boundary values of ± 1 a Saddle-Node on a limit circle bifurcation is present, so that inside the locking region the dynamics is governed by a Saddle-Node pair of fixed points. The existence of these two points allows for the system to be excitable when displaced from its stable state by a phase perturbation.

Our experiment is designed so that we are capable, when inside the locking region, to perturb the system with phase perturbations of different shapes and sizes, and to record the response of the system on a fraction of nanosecond time-scale. By carefully probing the system with these different perturbations, we have been able to observe different properties of the system, such as:

- A *single excitable response* following a single perturbation of different amplitudes, where each response is associated with a 2π phase rotation and a spike in intensity;
- The *refractory period* that follows from a first perturbation;
- A *resonator property* for couples of perturbations at different delays;
- *Controllable multipulse excitability.*

Many of these properties, like the excitability and refractory period, can be qualitatively explained using the Adler model, while others, like the resonator property and the multipulse excitability, cannot. In both cases, the study of a theoretical model of a Class B laser with injection will allow us to make analytical and numerical observations which will be able to bridge our experimental observations with the theory.

The rest of the chapter is then organized as follows: we will firstly introduce the system of a laser with injected signal in Section 2.2, while later we will describe in detail the experimental setup and results of the experiment in Section 2.3. These results will be divided into subsections, each of which will explain a different property of the system between the ones that we listed earlier. Then Section 2.4 will take care of the theory starting from a physical model of the system, and describing all of the aforementioned properties from a theoretical and numerical side. Finally, we will summarize our results in the Conclusions and perspectives 2.5.

The experimental and numerical results reported in this chapter have been published or are being published in:

- Bruno Garbin[1], Axel Dolcemascolo[2], Franco Prati[3], Julien Javaloyes[4], Giovanna Tissoni[2], and Stéphane Barland[2]. *"Refractory Period of an Excitable Semiconductor Laser with Optical Injection."*, Physical Review E **95**, no. 1 (2017) - [Garbin 2017a];
- Axel Dolcemascolo[2], Bruno Garbin[1], Betrand Peyce[2], Romain Veltz[5], and Stéphane Barland[2]. *"Resonator neuron and triggering multipulse excitability in laser with injected signal."*, Physical Review E **98**, no. 6 (2018) - [Dolcemascolo 2018].

and are the outcome of the collaboration of all the people mentioned above.

[1]The Dodd-Walls Centre for Photonic and Quantum Technologies, Department of Physics, The University of Auckland, Auckland, New Zealand.
[2]Université Côte d'Azur, CNRS UMR 7335, Institut de Physique de Nice, 1361 Route des Lucioles, F-06560 Valbonne, France
[3]Department of Science and High Technology, University of Insubria, Via Valleggio 11, 22100 Como, Italy
[4]Departament de Física, Universitat de les Illes Balears, C/ Valldemossa km 7.5, 07122 Palma de Mallorca, Spain
[5]Inria Sophia Antipolis, MathNeuro Team, 2004 route des Lucioles - BP93, 06902 Sophia Antipolis, France

2.2 Introduction on the laser with injected signal (LIS)

2.2.1 Laser with injected signal (LIS)

Laser systems in general can be very complex since the phenomena that accounts for the dynamics in these systems can span from electromagnetic theory to quantum theory to atomic physics. Furthermore, there are many different active media that can be used for a laser that can be implemented in a variety of designs of optical cavities, which increases the difficulty of an uniform model to describe their dynamics.

A limited (but very broad) topic in the study of the dynamics of laser systems is that of lasers with optical injection (LIS for short). These are systems where the light coming from another light source is injected into the laser cavity, and the result is usually a substantial modification of the dynamical properties of the system. One of the first (and most famous) attempts to influence the laser properties of a semiconductor laser using an external optical feedback dates back to [Lang 1980], where they observed how the injection assured a single-mode operation under high-speed modulation and the appearance of multi-stable and hysteresis phenomena. Later other theoretical and experimental studies followed, which outlined the injection locking properties of the laser system [Lang 1982, Mogensen 1985], with the inclusion of the linewidth enhancement factor α in the theory [Lang 1982, Henry 1982], and the locking bandwidth and relaxation oscillations [Petitbon 1986]. For a more complete history on the subject, we refer the interested reader to [Tartwijk 1995].

One could argue that the fundamental effect that underlies much of the dynamics of lasers with injection is the locking of the frequency of the injected laser to the frequency of the injected light. This means that the laser emits light with a frequency which is dictated by the external source. In order to observe this effect, two conditions must be satisfied:

1. The detuning between the frequency of the injected laser and the natural frequency of the laser oscillator must be small;
2. The injection power should not be too small.

This synchronization phenomenon between two coupled oscillators (such as two lasers) is very common in many other oscillator systems in Nature. It happens in biology [Winfree 2001, Glass 1988] as in the case of fireflies that have been observed to flash in unison in some south Asia forests, chemistry [Kuramoto 1984], electrical circuits [Lee 2003] and even in neurons [Timofeev 2012]. Theoretically, the first treatment of the locking of electrical oscillators was presented by van der Pol in 1927 [van der Pol 1927] and then further developed by Adler

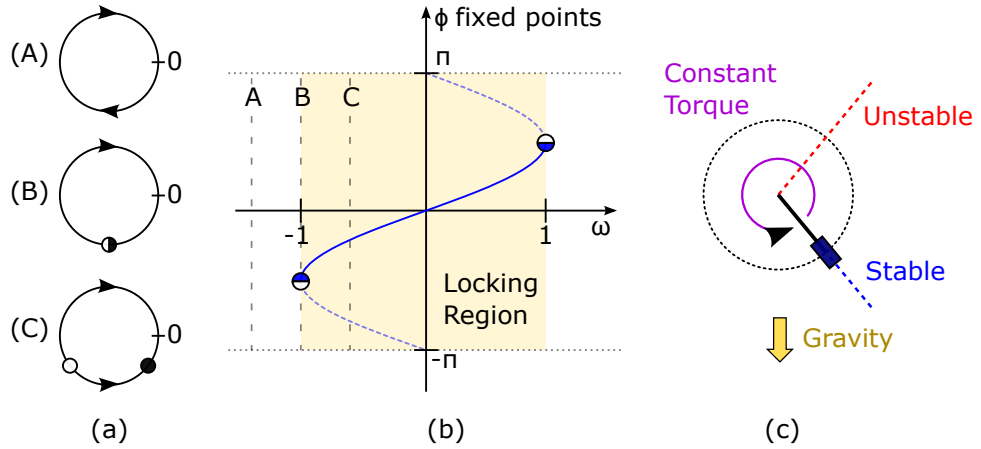

Figure 2.1: Adler model as in Equation 2.2. (a) Representation of the dynamics of the system on the circle for three different values of ω, corresponding to the positions A, B and C marked on the right. (b) Plot of the two fixed points (the dashed one corresponds to the unstable point) as a function of the detuning parameter ω. The locked region exists for small detuning ($-1 < \omega < 1$). At values of $\omega = \pm 1$ the birth of a saddle-node bifurcation is clearly visible. (c) Mechanical example of an overdamped pendulum with constant torque, that in the limit of high viscosity follows the Adler equation.

[Adler 1946], who also introduced the Adler equation:

$$\frac{d\phi}{dt} = \omega - \sin\phi \tag{2.2}$$

which is a one-dimensional phase equation that describes the evolution of the phase difference ϕ between the two oscillators, while the parameter ω represents the detuning (difference in frequency) between them. Figure 2.1(b) shows a representation of the fixed points of the equation when changing the detuning parameter. For small detuning ($-1 < \omega < 1$) the dynamics of the system is determined by a stable fixed point and an unstable fixed point that are born from a saddle-node bifurcation on a limit cycle in phase space. The system will then be attracted towards the stable point which means that there will be a stable phase difference between the two oscillators (this is the locked region of the model). For bigger values of the detuning ($\omega < -1$ and $\omega > 1$) there is no fixed point, and the phase difference will either always increase or always decrease, depending on the sign of ω (this is the unlocked region of the model).

This simple model is the basis of the locking mechanism for two coupled oscillators, and many complex models for coupled oscillators in different fields can be ultimately reduced to this equation. An example of such a reduction emerges from the LIS model: in the paper from [Coullet 1998] it is demonstrated how the dynamical model for the LIS can be reduced to the phase equation:

$$\frac{\partial\Theta}{\partial t} = \Delta - \sin(\Theta) + \frac{\partial^2\Theta}{\partial x^2} - \Upsilon\left(\frac{\partial\Theta}{\partial x}\right)^2 \tag{2.3}$$

where Θ represents the relative phase of the laser and the external field, Δ is the external detuning normalised to the strength of the injected laser and the coefficient Υ measures the dispersive-diffusive character of the medium. If we ignore the evolution along the transverse spatial direction x, we then obtain an Adler-like equation for the evolution of the phase difference.

Given its importance in understanding the behaviour of many systems and in order to build an empirical intuition on the dynamics, it is also interesting to consider a mechanical example of the Adler model, namely an overdamped pendulum with constant torque, as is depicted in Figure 2.1(c). Starting from an equation for the angular momentum, in [Coullet 2005] it is shown that the equation of motion of the pendulum reads:

$$\theta'' + \beta\theta' + \sin\theta = \gamma \tag{2.4}$$

where β is a normalised parameter proportional to the viscous torque and inversely proportional to the square root of the inertia, γ is proportional to the strength of the forcing, and the time has been normalised to the free oscillating period of the pendulum. In the limit of high viscosity (β large), we can drop the inertial term θ'' so that the equation of motion reduces to:

$$\theta' = \frac{1}{\beta}(\gamma - \sin\theta) \tag{2.5}$$

which is just the Adler equation after we apply another normalization of the time to get rid of the β parameter. For a small forcing, there will then be two fixed points on the circle, a stable posisition (the blue line in Figure 2.1(c)) and an unstable position (the red line), and after a monotonic motion the pendulum will alight on the stable position. If the forcing is instead too small or too large, there will be periodic oscillations of the pendulum, either clockwise or anti-clockwise.

Even though the Adler model is a simple explanation of the dynamic of the LIS under some parameter range, that does not mean that it is able to describe the whole range of dynamical behaviours that can be observed fron the LIS model, among which we can cite *stationary states* (steady states and limit cycles), *bifurcations of stationary points* (saddle-node and Hopf bifurcations), *dynamics of limit cycles* (period-doubling bifurcations, saddle-node of limit cycle, torus bifurcation), *chaos dynamics* (series of period-doublings leading into chaos, sudden chaotic transitions), *multistability* of different solutions giving rise to hysteresis cycles and even *pulse excitability* or *multipulse excitability*. A detailed description of these dynamical effects and more can be found in [Wieczorek 2005a].

The model that is used in order to study the broad LIS dynamics is usually a system of nonlinear differential equations that comes from a rearrangement of the so called Maxwell-Bloch equations [Arecchi 1965], a system of equations for

the system of two-level atoms that are combined with the Maxwell equations for the electric field inside a cavity. An example of such a model is [Hachair 2006, Prati 2010]

$$\begin{cases} \dfrac{\partial E}{\partial t} = \epsilon \left[E_I + P - (1 + i\theta)E + i\nabla_\perp^2 E \right] \\ \dfrac{\partial P}{\partial t} = \Gamma_D (1 + i\Delta_D) \left[(1 - i\alpha)DE - P \right] \\ \dfrac{\partial D}{\partial t} = b \left[\mu - D - \dfrac{1}{2}(EP^* + E^* P) + d\nabla_\perp^2 D \right] \end{cases} \tag{2.6}$$

where E is the slowly varying envelope of the electric field, P is the effective macroscopic polarization and D is a population variable proportional to the excess of carriers with respect to transparency. E_I is the amplitude of the injected field while μ is a parameter related to the pump current normalized so that the threshold for the solitary laser is $\mu_{th} = 1$ when it emits on axis. Three important parameters are θ, Γ and Δ where:

$$\theta = \frac{\omega_C - \omega}{\kappa} = \begin{array}{l} \text{detuning between the cavity longitudinal mode} \\ \text{frequency and the frequency of the injected field} \end{array} \tag{2.7}$$

and $\Gamma_D = \Gamma(D)$ and $\Delta_D = \Delta(D)$ are two real functions of D that determine the shape of the susceptibility curve. In the cited papers [Hachair 2006, Prati 2010] they set $\Gamma(D) = 0.276 + 1.016D$ and $\Delta(D) = -\alpha + 2\delta(D)/\Gamma(D)$, where $\delta(D) = -0.169 + 0.216D$, as the best fit of gain curves calculated with a microscopic model. There are three different time scales in the system, namely:

$$\begin{aligned} \tau_p &= \text{photon lifetime inside the cavity} \\ \tau_d &= \text{dephasing time of the microscopic dipoles (typically 100 fs)} \\ \tau_c &= \text{carrier nonradiative recombination time} \end{aligned} \tag{2.8}$$

that are taken into accounts in the parameters $\epsilon = \tau_d/\tau_p$ and $b = \tau_d/\tau_c$, while the time is already scaled to the dephasing rate τ_d. Finally, α is the linewidth enhancement factor of the laser and d is the diffusion coefficient for the carriers.

We should also mention that the formulation of this model is not unique and there are examples of different models that are mentioned in the literature. A non-exhaustive overview of such models can be found in Figure 2.2. They can differ between one another based on the inclusion or exclusion of diffraction terms in the E and D variables, time scale re-normalizations, changes in the reference frequency and redefinition of physical parameters (sometimes redefining existing parameters in other models) depending on the context and on the needs of the model. What is common between the various formulations is the classifications of the dynamical properties of the different models in three different classes: A, B and C. They were proposed by [Tredicce 1985] in order to

make sense of the possible different assumptions that one can make to simplify the system. Indeed the fact that there are three different time scales allows for the possibility of an adiabatic elimination of the rate equations of the fast variables if the time scales are widely different. In particular, if we introduce the relaxation rates:

$$\begin{aligned} \kappa &= 1/\tau_p &&= \text{cavity dumping constant} \\ \gamma_\perp &= 1/\tau_d &&= \text{relaxation rate of the atomic polarization } P \\ \gamma_\parallel &= 1/\tau_c &&= \text{relaxation rate of the population difference } D \end{aligned} \tag{2.9}$$

we can distinguish the three classes as:

Class A characterized by the condition:

$$\kappa << \gamma_\perp, \gamma_\parallel \tag{2.10}$$

The lasers in this class are the ones where the loss rate for the field (σ) is much less than the other two timescales, namely the polarization loss rate (τ_p) and the population inversion loss (b). Because of this difference, it is possible to perform an adiabatic elimination of the atomic variables so that we are left with one equation for the field. Starting from a LIS model which includes diffraction in the transverse plane for the electric field, one can obtain the equation [Coullet 1989]:

$$\frac{\partial A}{\partial T} = A - (1 + i\alpha)|A|^2 A + (1 + i\beta)\nabla^2 A \tag{2.11}$$

where A is the first order expansion term of the electric field close to threshold, α is the linewidth enhancement factor and β is a parameter related to the cavity detuning. This equation is also known as the complex Ginzburg-Landau equation, which was first postulated as a model for the theory of superconductivity, but also describes a vast variety of phenomena, from superfluidity and Bose-Einstein condensation to liquid crystals and strings in field theory [Aranson 2002]. There can also be slightly different formulations of this Class A equation for the field, as the one which is thoroughly studied in [Mayol 2002].

Class B characterized by the condition:

$$\gamma_\parallel << \kappa << \gamma_\perp \tag{2.12}$$

In this case the atomic polarization can be adiabatically eliminated so that the dynamic behaviour of this class of laser can be described by the coupled equations for the electric field and for the population inversion.

While in absence of injection the Class B model is fully equivalent to the motion in a Toda potential with intensity dependent losses [Oppo 1985]

and therefore does not show chaotic behaviour, when adding the injected field the number of degrees of freedom is enlarged and the dynamics can become very complicated, as shown in [Wieczorek 2005a].

Class C where the relaxations rates κ, $\gamma_\perp$ and $\gamma_\parallel$ have the same order of magnitude and therefore no adiabatic elimination is possible. We then have to rely on the full Maxwell-Bloch equations in order to describe their dynamics.

In our case, we will mostly deal with a Class B model since our injected laser is a semiconductor laser. We will then use a model with two coupled equations: one for the electric field and one for the carriers.

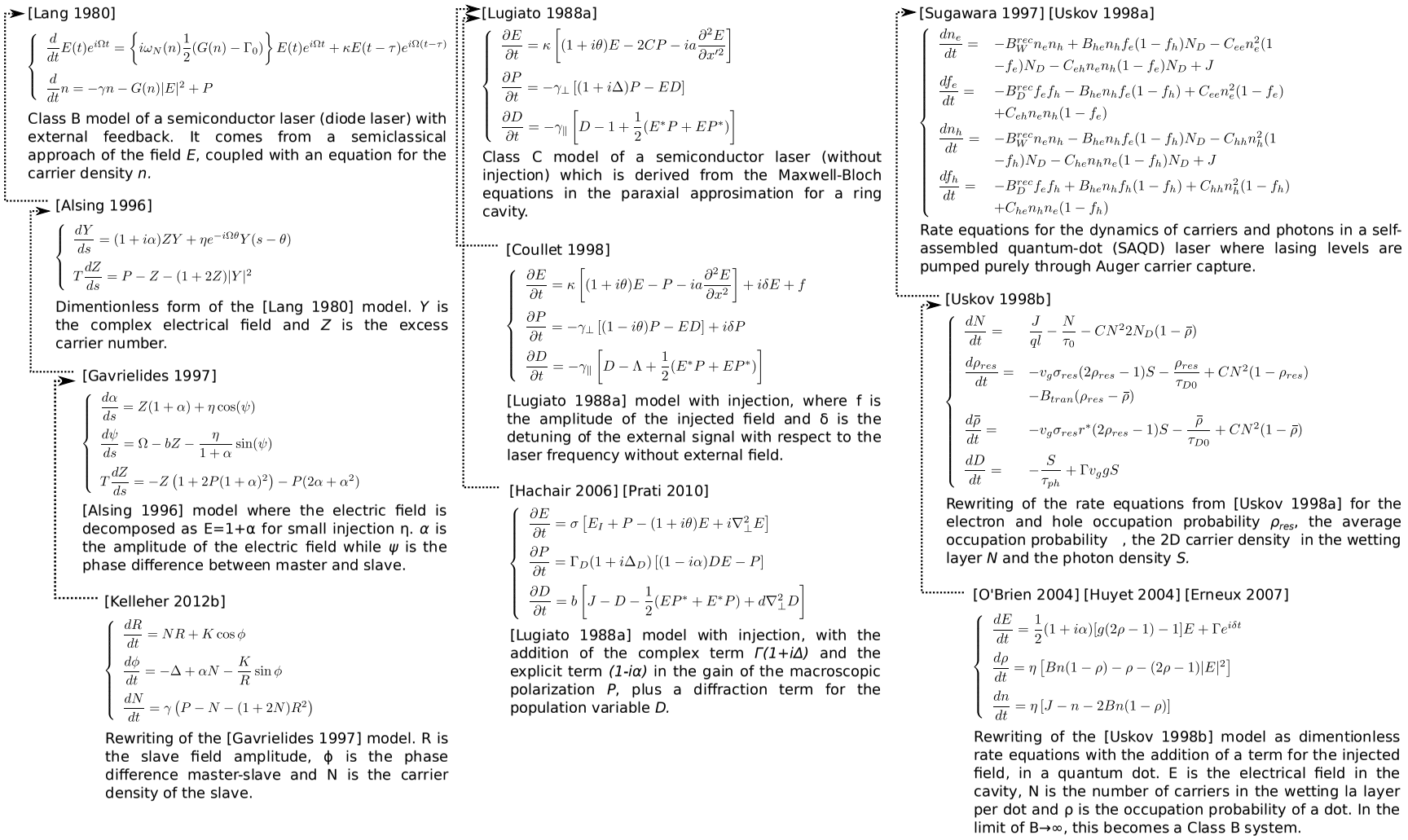

Figure 2.2: Examples of different semiconductor laser and LIS models that can be found in the literature, along with their genealogy.

2.2.2 Excitability of injection-locked semiconductor lasers with optical injection

Definition of excitability As was pointed out in the general introduction, excitability is a very general property that is shared by many nonlinear systems in various contexts, from biology, to chemistry to optics. Most notably, it plays a fundamental role in neuroscience where the elementary element, the neuron, is often taken as the epitome of an excitable system.

We remind here the definition of excitability: a system is said to be excitable if:

- given a perturbation whose strength is under a certain threshold, the system only relaxes following a response which is linearly dependent to the strength of the perturbation,
- given a perturbation whose amplitude is higher than the threshold, the system reacts with a large-amplitude nonlinear response, whose shape and amplitude are almost independent from the input perturbation.

This can be summarized as an all-or-none type of response to an input perturbation: the system is either mostly unaffected or it generates a large response when the perturbation overcomes the threshold.

We have also already described how this property is shared by many different optical systems: from lasers with saturable absorbers [Dubbeldam 1999, Larotonda 2002], to semiconductor ring and microdisk lasers [Campenhout 2007, Alexander 2013], to photonic crystal nanocavities [Yacomotti 2006, Brunstein 2012] and lasers with optical feedback [Fischer 1996, Giudici 1997, Garbin 2015b] or injection-locked semiconductor lasers [Goulding 2007, Kelleher 2009, Turconi 2013] and injected semiconductor amplifiers [Barland 2003]. For an extensive overview on the subject, we refer the reader to the review article [Prucnal 2016]. In the rest of this section we will introduce the case of injection-locked semiconductor lasers with optical injection, along with a brief historical survey on the subjection.

Excitability of locked LIS systems The optical excitability of injection-locked semiconductor lasers with optical injection is widely studied theoretically and experimentally. The first theoretical intuition that, under some approximations (namely, small detuning between slave and master and small injected power) a laser with injected signal could behave as an excitable medium was proposed by [Coullet 1998]. Under the aforementioned approximations, the authors are able to reduce the dynamics of a Class C semiconductor laser with injection to the phase equation

$$\frac{\partial \Theta}{\partial t} = \Delta - \sin(\Theta) + \frac{\partial^2 \Theta}{\partial x^2} - \Upsilon \left(\frac{\partial \Theta}{\partial x} \right)^2 \tag{2.13}$$

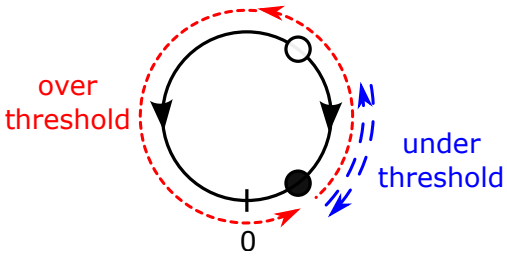

Figure 2.3: Excitability of the Adler model. Given a perturbation under threshold (blue long-dashed arrow), the system will just relax back to the stable point. If instead the perturbation is over the threshold (red short-dashed arrow), the system will perform a 2π phase rotation (an excitable event), before relaxing back to the stable point.

where Θ represents the relative phase of the laser with respect to the external field, Δ is the detuning and Υ is the ratio between diffraction and diffusion. If we ignore the evolution on the transverse direction we recover the Adler equation:

$$\frac{d\Theta}{dt} = \Delta - \sin\Theta \tag{2.14}$$

We have already shown how the dynamics of this equation is governed by a saddle-node bifurcation on a circle as depicted in Figure 2.1. What we have not emphasized is that this very simple model also behaves in an excitable way when inside the locking region. In fact, starting from the stable point and applying a positive phase-displacement perturbation on the system (as shown in Figure 2.3) then the system reacts in two possible ways:

- If the angle is small, the system gets displaced between the saddle and the node, so it will just relax back to the stable node. Note that the response is linear with respect to the perturbation in this case.
- If instead the angle is greater than the angular distance between the saddle and the node, the system will overcome the position of the saddle and it will complete a 2π phase rotation (the excitable event) before reaching the node.

The Adler model can then be viewed as an excitable one, and given its simplicity it is often taken as an example when describing excitable systems. Moreover, there is a strong connection between this model and the so-called θ-model [Ermentrout 1986, Izhikevich 2007][6]:

$$\frac{d\theta}{dt} = (1 - \cos\theta) + (1 + \cos\theta)\, I(t) \tag{2.15}$$

[6]The θ-model is actually just the same as the Adler model when $I(t)$ is considered as a constant. See Appendix A for a derivation of the Adler model from the θ-model.

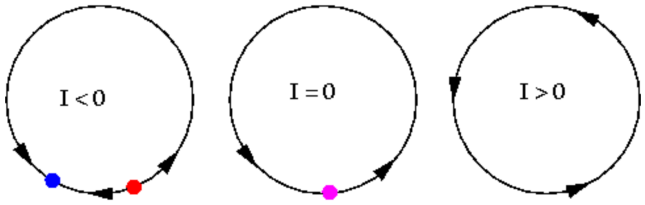

Figure 2.4: Saddle-node on a limit cycle bifurcation (SNIC) for the θ-model 2.15. Reprinted from [Ermentrout 2008][7].

which is a popular biological neuron model used in many fields of computational neuroscience. The angle variable θ represents the state of the neuron in radiants, and the input function $I(t)$ (often taken to be periodic) is the parameters which controls the bifurcation. The dynamics of this model also takes place on a circle where it is governed by a saddle-node bifurcation, where the parameter I is the bifurcation parameter. The bifurcation point is located at $I = 0$, while when $I < 0$ the system is excitable and when $I > 0$ the system gives rise to a limit cycle (as shown in Figure 2.4). The neuron is said to spike when $\theta = \pi$.

The theta model is also the locally canonical model for the saddle-node on a limit cycle bifurcation (SNIC), which means that every system that undergoes a SNIC bifurcation can be locally transformed (often with a change of variable) into this canonical model [Hoppensteadt 1997, Izhikevich 1999]. As an example, in Appendix A we derive the Adler model from the θ-model by applying a change of variable and of timescale. Near the transition, it can also be shown that the local dynamics follows the quadratic integrate-and-fire neuron which has the form [Ermentrout 1996, Ermentrout 2008]:

$$\frac{dx}{dt} = x^2 + I \tag{2.16}$$

In the case of $I > 0$, the solutions to this differential equation "blows up" in finite time and supposing that we reset $x(t)$ to $-\infty$ when it blows up at $+\infty$, then the total transit time is:

$$T_{per} = \frac{\pi}{\sqrt{I}} \tag{2.17}$$

This means that the frequency goes to zero as the I parameter approaches zero from the right. If we now recall the distinction between Class 1 and Class 2 neurons, as already explained in subsection 1.1.2, we remark that this property (the fact that action potentials can be generated with arbitrary low frequency) is the defining feature of Class 1 neurons. In fact, it was this observation that led Rinzel Ermentrout to remark that this bifurcation corresponded to Hodgkin's Class 1 excitable membranes while the more familiar Andronov-Hopf bifurcation corresponded to Class 2 excitability.

[7]Licensed under CC BY-NC-SA 3.0

This canonical model is then very useful as it can then shed some light on any neuronal model that displays Class 1 excitability. Nevertheless, one must be cautious when comparing other neuronal models to the canonical one because the transformation that converts a particular model into the canonical is guaranteed to exist only near the SNIC bifurcation: that is, when frequency of the action potential approaches zero, so that the periods of the interspikes become very large.

Given the strong connection between the LIS system, the Adler equation and the θ-model, it is reasonable to expect that a laser with injection can behave in an excitable way. Furthermore if we go back to the phase equation 2.13 that can be derived from the LIS system and we set $\Delta = \Upsilon = 0$ (weak detuning and weak dispersion), we can reduce it to the sine-Gordon equation:

$$\frac{\partial \Theta}{\partial t} = -\sin(\Theta) + \frac{\partial^2 \Theta}{\partial x^2} \tag{2.18}$$

that possesses a particular stationary 2π kink solution:

$$\Theta_{K_\pm} = \pm 4 \arctan(e^x) \tag{2.19}$$

As explained in the [Coullet 1998] article, this phase kink appears as a pulse when one looks to physical quantities such as the light intensity and for small detuning and dispersion this solution behaves as a travelling pulse of the form:

$$\Theta(x,t) = \Theta_K(x - ct) + ... \tag{2.20}$$

where the ellipses represent higher order corrections and the velocity c is given by:

$$c = \frac{\pi}{4}(\Delta - 2\Upsilon) \tag{2.21}$$

It is then possible to obtain excitable pulse solutions of the Maxwell-Bloch equations in the LIS system. These phase kinks will appear as discrete pulses in the circulating optical intensity.

Starting from this and other theoretical insight where it was suggested the possibility of excitability in other optical systems other than the LIS, as in the semiconductor élon [Rzhanov 1993] and the two-level Lorenz-Haken laser [Yu 1999], a lot of work has been carried out in search of the experimental realization of these excitable pulses.

In the case of semiconductor optical devices, an excitable behaviour that follow the van der Pol–Fitzhugh–Nagumo (VPFN) model has been observed in Semiconductor Optical Amplifiers (SOA) [Barland 2003, Marino 2004] and in Semiconductor Microcavities (a 2D excitable medium) [Marino 2005] where they observed self-confined optical waves. The VPFN model is one of the fundamental paradigms of for an excitable behaviour in many biological, chemical or electronic systems and it displays a firing activity that can be regulated

by noise when operating slightly beyond the supercritical Hopf bifurcation [Makarov 2001]. In these systems the excitable events were in fact triggered either by noise or thermal oscillations.

A first experimental realization of excitability in a LIS system of a quantum dot semiconductor laser was demonstrated in [Goulding 2007], and again in this case the excitable intensity pulses were noise-triggered. Later a first step towards the control of these pulses was made when it was realized how these excitable pulses could be triggered by perturbing the system with an external incoherent injected laser [Garbin 2014]. It was also later realized how each intensity pulse was accompanied by a 2π phase slip [Kelleher 2009] that could by either positive or negative depending on the sign of the detuning. This discovery has led to a clearer understanding of the nature of the excitable pulses as primarily phase phenomena, where the coupling between phase and amplitude comes into play due to the non-zero value of the α parameter (the linewidth-enhancement factor). A further development of an interferometric phase measurement technique used to construct phasor plots has again confirmed the phase-amplitude dynamics of these excitable events [Kelleher 2010].

A first demonstration of the control of the excitable pulses in an injection-locked semiconductor laser has been achieved by [Turconi 2013], where they managed to apply a phase perturbation to the master signal with variable amplitude in order to get an excitable response. This technique has an efficiency that reaches almost 100% when increasing the amplitude of the perturbation, while the shape of the pulses remains constant. The same type of technique has been used in our experiment, with different types of phase-perturbations. Furthermore, it was shown in [Garbin 2015b] how these excitable responses could be regenerated by the system when a delayed feedback loop is added to the optical injection system. Given the nature of these pulses as phase-slips of 2π that propagate in a spatio-temporal system without distortion, they have also been called topological solitons, as they bear a close resemblance to the Sine-Gordon solitons. In the same paper it was also demonstrated how these solitons can be individually nucleated and cancelled, thus opening their use as phase information units in next-generation coherent communication systems.

At the same time, a clearer theoretical understanding of the dynamics present in the LIS system has been achieved through a thorough theoretical and bifurcation analysis [Krauskopf 2003, Erneux 2010, Olejniczak 2010, Kovanis 2010, Kelleher 2011], usually separating the case of quantum dot and quantum well devices. The most complete theoretical report of the complex nonlinear behaviour of a semiconductor laser with injection can be found in [Wieczorek 2005a].

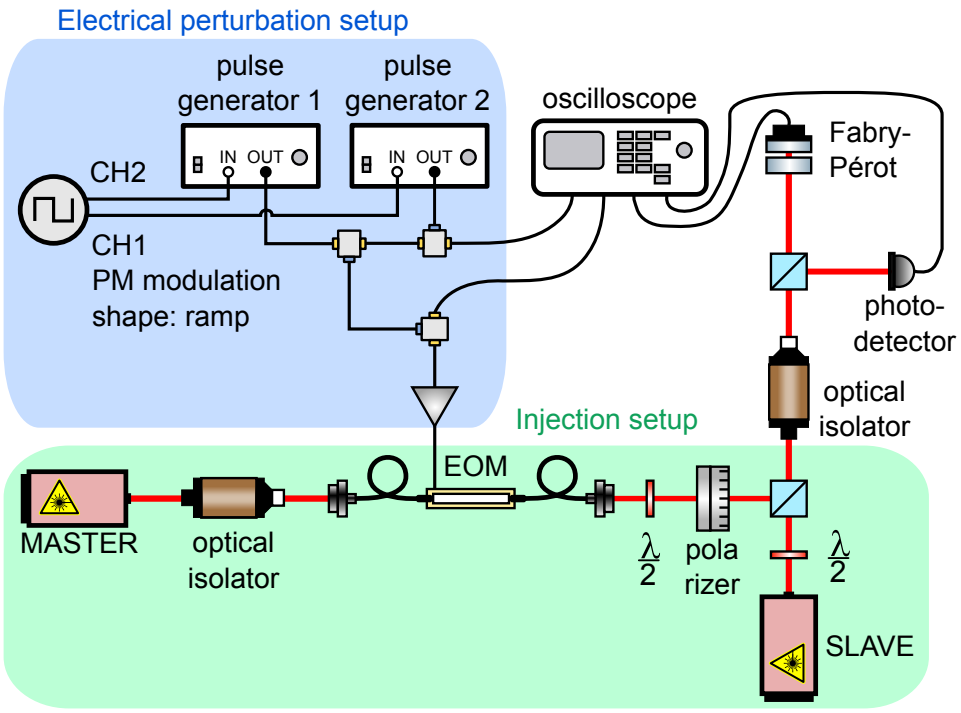

Figure 2.5: Experimental setup of a laser with injected signal. The electrical perturbation setup allows us to apply a double-pulse phase perturbation to the master signal with arbitrary delay.

2.3 Experimental results

This section will describe more in detail the experimental setup that we have used to probe the excitability properties of the LIS laser. After that, we will discuss and examine the experimental results that we obtained from the experiment.

2.3.1 Experimental setup

The experimental setup is shown in figure 2.5 and it basically consists on a laser with injected signal. A more schematic and visually pleasing version of the same setup is shown in 2.6. It is the same setup used in [Turconi 2013], with the addiction of a new electrical perturbation setup. The backbone of the experiment consists of two lasers which are coupled together in an unidirectional way. The master laser is the one whose signal we inject inside the other laser, called a slave laser. Before being injected, the master signal passes through an EOM (Electro-Optic Modulator) that allows us to apply a phase perturbation to the master signal.

The particular shape of this perturbation is determined by the settings of the electrical perturbation setup shown in the figure, which include two pulse generators. We then analyse the output of the system via a real-time oscilloscope

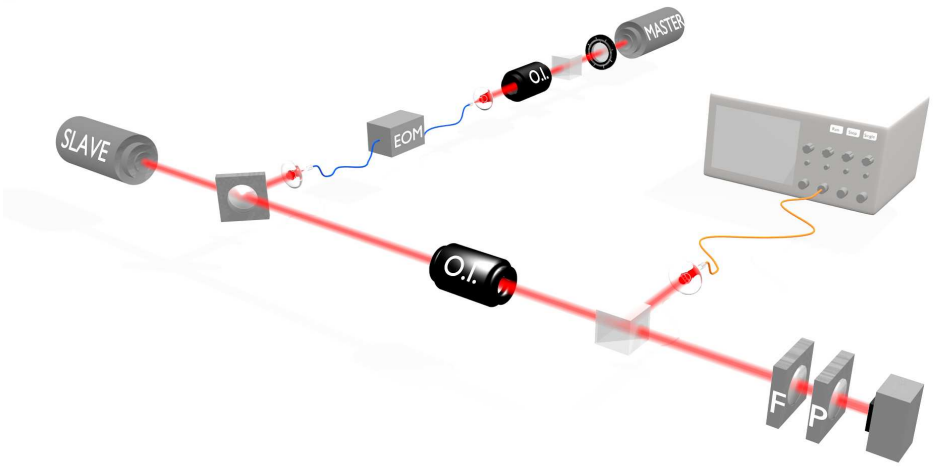

Figure 2.6: Schematic of the experimental set-up. MASTER: in- jection laser, SLAVE: injected laser, EOM: electro-optic mod- ulator, O.I.: Optical isolator,FP: Fabry-Pérot interferometer. Reprinted with permission from [Garbin 2017a].

and a Fabry-Pérot. We will now explain more in detail the different parts of the setup.

Electrical perturbation setup This section of the setup is needed in order to generate an electrical perturbation with a particular shape which will then be converted into a phase perturbation by the EOM. During this work we focused on double pulse perturbations, as the one which is depicted in figure 2.8(a), although we also used other types of pertubation, usually a combination of step-up or step down perturbations, either by themselves or in addition with pulse perturbations. In that case, the perturbation setup would be slightly different, but the overall structure would be very similar. Here we describe in particular the case for a double-pulse perturbation. A more detailed description of the electrical perturbation setup in this case is shown in Figure 2.7.

To generate the two pulses we employ two pulse generators: the Alnair Labs EPG-200B-0050-0250 (first pulse generator) and the Alnair Labs EPG-210B-0050-S-P-T-A (second pulse generator). The two pulse generators have a very similar use and they only differ in the fact that the second generator has a built in amplifier, so that we need to reduce the amplitude of the second pulse using attenuators in order to be able to combine the two pulses with similar amplitudes. They both respond to an input raising front with an amplitude of 400 mVpp by generating a pulse with constant amplitude and tunable width. The duration of the pulses can be set between 30 - 350 ps, with a rising/falling time of 30 ps. The amplitude of the signal for the first generator is 300-400 mVpp, while for the second is 5-7 Vpp, where the actual amplitude varies slightly depending on the chosen time duration.

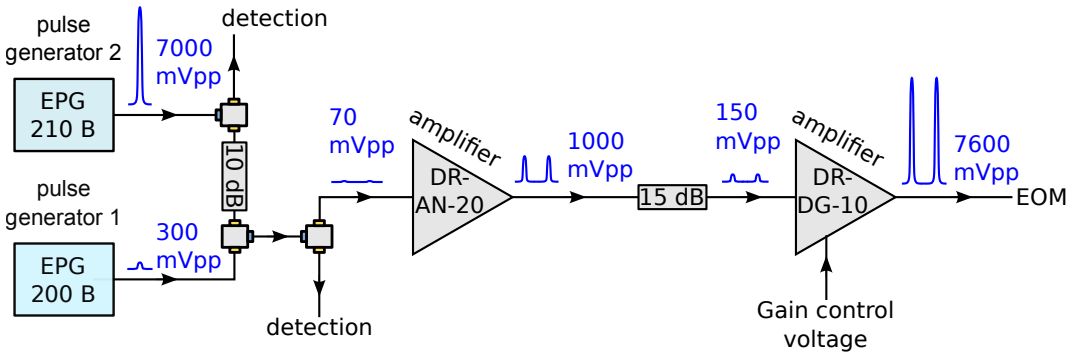

Figure 2.7: Detailed representation of the electrical perturbation setup (as in Figure 2.5) used in order to generate a two-pulses perturbation with arbitrary delay. The amplitude of the signals shown here represent an approximate typical experimental value.

The trigger signal for the two pulse generators is produced by a signal generator (Keysight 33600A) with two channels. We trigger the first pulse generator with a 50 MHz square wave with 400 mVpp amplitude, and the second pulse generator with another 50 MHz square wave. Since the two channels are synchronized, the two pulses are created at the same time. We can then control the delay between the two pulses by applying a phase delay (or a phase modulation) to one of the channels. Using this technique we can generate two very narrow pulses with arbitrary delay with a repetition frequency of 50 MHz.

In order to join the two pulses together and to amplify them close to the value of operation of the EOM, we employ a series of power splitter in addiction with two amplifiers as depicted in Figure 2.7. The power splitters that we used (either in a summing configuration or a splitting configuration) are Mini-Circuits power splitters ZFRSC-183-S+DC18000 MHz or DC12000 MHz. We also used power attenuators as to level the voltage between the two pulses from the two pulse generators to be almost equal. After the two pulses are joined, we obtain a signal which is of order 70-150 mVpp, that we need to amplify up to 6-9 Vpp to be in an useful range for the operation of the EOM. The apparatus that we use to achieve this consists of two amplifiers: the Photline DR-AN-20-MO wideband RF amplifier module designed (cut-off frequency of 20 GHz) and the Photline DR-DG-10-MO-NRZ Medium Output Voltage Driver Module (cut-off frequency of 28 GHz). We had to resort to use two amplifiers instead of one because the DR-DG-10 amplifier needs a signal of 100-300 mVpp if we want an output signal of the order of 6-9 Vpp.

The end result of this process is a double-pulse signal as shown in Figure 2.8(a). In the (b) panel of the same figure we also show the amplitude of the output signal when changing the gain control voltage, and in panel (c) we plot the full width at half maximum of one pulse as we increase the gain control voltage for three different experimental realization.

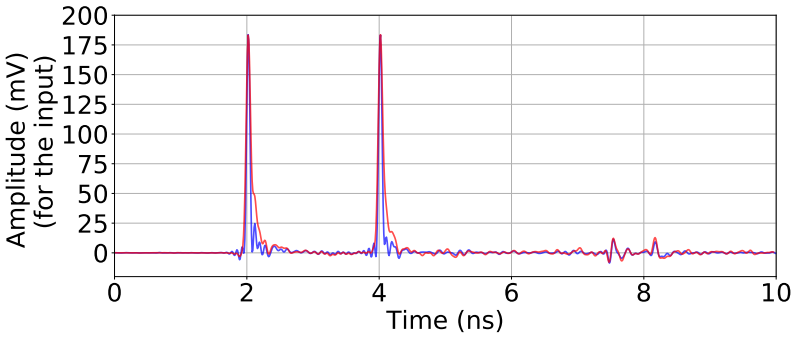

(a) Input signal (blue) and output signal (red) of the amplifier. The output signal is normalized to the input maximum.

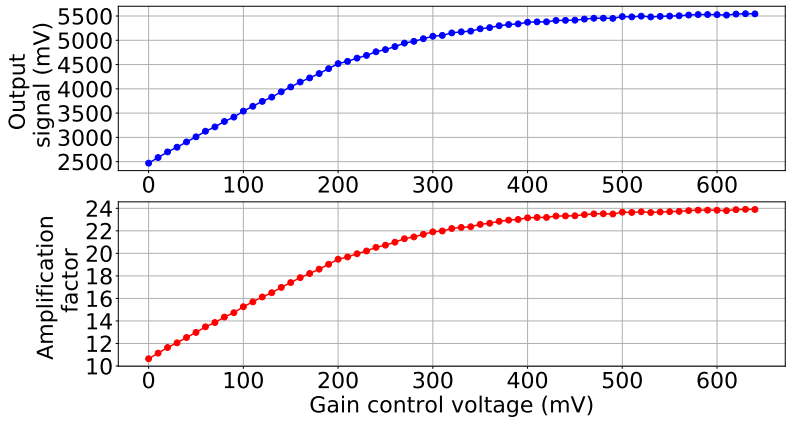

(b) Amplitude of the maximum of the output signal (top) and amplification factor (bottom) with increasing gain control voltage in the case of an input signal with amplitude = 236 mV.

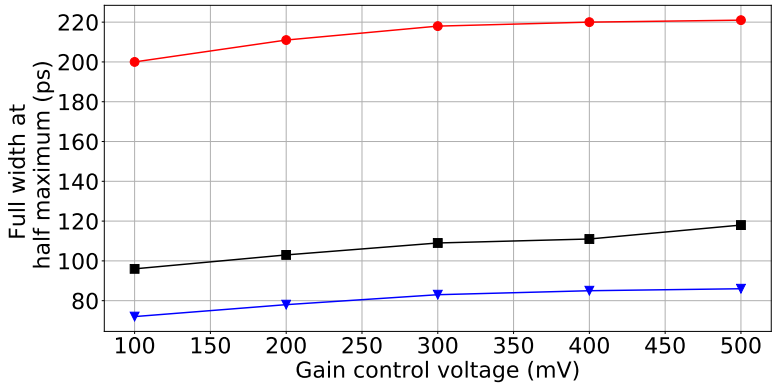

(c) Width of a single pulse with increasing gain control voltage for three different experimental realizations (changing parameters of the pulse generator and the amplifiers).

Figure 2.8: Shape and amplitude of the input-output signals of the DR-DG-10 amplifier for a double-pulse perturbation, before being injected into the EOM.

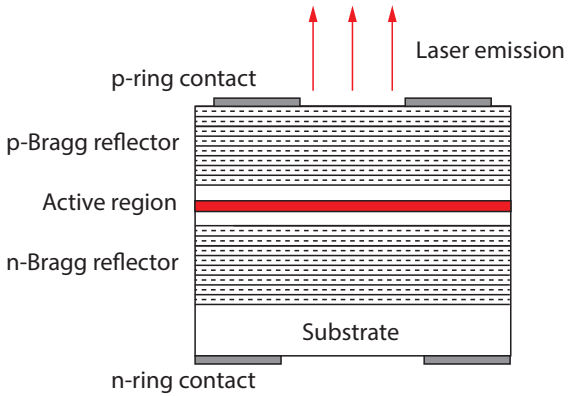

Figure 2.9: Schematic representation of a typical vertical-cavity surface-emitting laser (VCSEL) consisting of an active layer sandwiched between Bragg mirrors. Reprinted with permission from [Dolcemascolo 2015].

Injection setup This part of the setup is at the heart of the experiment and it includes two lasers, a master laser and a slave laser, which are coupled together in an unidirectional way. The master laser is an external grating tunable laser which emits on a single mode of its external cavity, and its frequency can be set by discrete steps through the alignment of the diffraction grating. The slave laser is a VCSEL, a Vertical-cavity Surface-emitting Laser (ULM980-03-TN-S46) that consists of an active layer sandwiched between Bragg mirrors, as shown in figure 2.9. The signal coming from the master laser is injected into the slave laser after having applied a phase perturbation through the EOM (Electro-Optic modulator).

The EOM is a Photline (polarization preserving) fiber coupled Lithium Niobate phase modulator with 10-GHz bandwidth. The phase perturbation of the EOM itself is controlled by an electrical signal that comes from the electrical perturbation setup, which is generated by the procedure that we already discussed in the previous section. Figure 2.10 shows a calibration curve of the EOM when applying phase perturbations with a square impulse shape of different amplitude and then measuring the intensity of the output light of the master. From a sinusoidal fit we calculate that in order to obtain a phase perturbation that corresponds to π radians, we need an electrical signal with amplitude 11.34 V.

The unidirectionality of the injection is insured by an optical isolator placed in the path of the master. The injection is performed through a 10% reflection beam splitter and the beam is collimated using a high numerical aperture 4.5-mm focal length lens with suitable antireflection coating. The same lens is used for the collimation of the output beam of the VCSEL laser. Before the injection, a polarizer aligned with the vertical axis is used to align the polarization of the master signal with that of the slave laser, and a zero-order half-wave plate allows to rotate the polarization axis of the master in order to

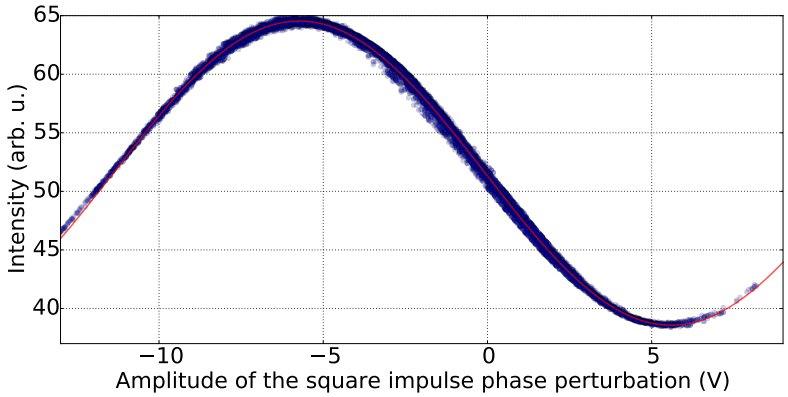

Figure 2.10: Intensity of the laser light coming out of the slave when we apply phase perturbations of different amplitudes to the master signal. From a sinusoidal fit, we obtain a value of the volt amplitude that corresponds to a π phase perturbation to be $\Delta V_\pi = 11.34\,V$.

control the intensity of the injection.

Detection The output signal coming out of the slave laser (which comprises a combination of the slave signal and the master signal) is analysed using a Fabry-Pérot interferometer and a real time oscilloscope. We also employ an optical isolator in order to avoid any unwanted reflection on the measurement instruments. The Fabry-Pérot, which is used to reconstruct the spectrum of the signal, has a free spectral range of 72 GHz and a finesse which is usually greater than 100. The real time detection is performed via a fiber-coupled photodetector, with a bandwidth greater then 9.5 GHz, and a real time oscilloscope (either a Tektronix DPO71254C with a bandwidth of 12.5 GHz or a Teledyne Lecroy HDO4024 with a bandwidth of 200 MHz). If needed, an RF amplifier (mini-circuit, ZX60-14012L-S+ with bandwidth 300 kHz - 14 GHz) that removes the DC component of the signal will be added to amplify the amplitude of the electrical signal after the photodetector.

2.3.2 Characterization of the VCSEL laser with injection

Let us now describe more in detail the characteristics of our injection setup in the context of the laser with injected signal. The main characteristics of the slave VCSEL laser are summarised in Figure 2.11.

The first (A) panel shows the emission power for the two axes of polarization. In this type of laser it is known that the output power is distributed on two polarization axes [Martin-Regalado 1997]. In the case of the polarization axis with higher power (blue line), we observe the appearance of a threshold at $I = 0.21\,A$. This laser threshold corresponds to a Hopf bifurcation of the

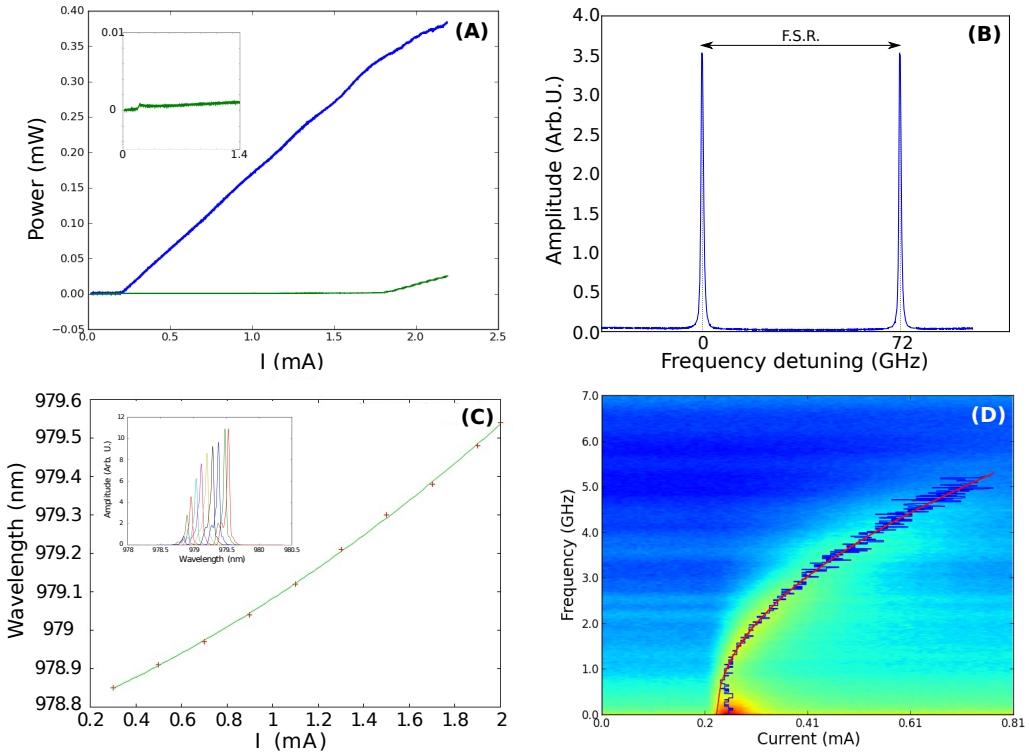

Figure 2.11: Characterization of the VCSEL slave laser. (A) Plot of the power emission as a function of the pumping current for the two axes of polarization. The inset shows a zoom of the weak polarization. (B) Optical spectrum obtained from the Fabry-Pérot interferometer (72 GHz of free spectral range). (C) Evolution of the wavelength of the laser emission as a function of the pumping current. The different spectra are shown in the inset, while the position of their maxima is fitted with a quadratic function. (D) Evolution of the frequence of the relaxation oscillations with pumping. The red line represents a square root fit of the blue points obtained experimentally. Reprinted with permission from [Garbin 2015a].

electric field and it appears when the laser output is dominated by stimulated emission rather than by spontaneous emission. After the threshold, the power evolves linearly when increasing the current. The inset shows instead a zoom of the lower power polarization axis, that is insignificant up to $1.8\,mA$.
The (B) panel shows the optic spectrum as seen from the Fabry-perot interferometer. We can clearly distinguish a single peak, which shows that the laser is monomode, that repeat itself every free spectral range (here of 72 GHz).
In the (C) panel we can then observe the evolution of the wavelength of the laser for different pumping currents above threshold, which exhibits a quadratic trend towards the red part of the spectrum. This behaviour is principally due to a Joule effect.
Finally the (D) panel displays the evolution of the frequency of the relaxation oscillations of the laser as a function of the pumping current. These oscillations

arise from the different characteristic relaxation times of the carriers and the field, and they are characteristic of many slow-fast systems. Here they follow a square root law as predicted theoretically.

The laser with injection has three control parameters:

1. The detuning Δ between the two lasers, defined as the frequency difference between the slave (the VCSEL) and the master (the external grating tunable laser):
$$\Delta = \nu_S - \nu_M \tag{2.22}$$
We can control this parameter either by changing the master frequency via the alignment of the external diffraction grating, or by changing the slave pumping current, since the frequency of the slave changes when changing the current (as already shown in Figure 2.11(C))

2. The injection strength of the master P_{inj}, that can be controlled by rotating the $\lambda/2$ waveplate placed before the polarizer in the master path,

3. The slave pumping current I_{sl}, which is set by a current controller.

When the detuning is weak enough the two lasers are locked in frequency with a constant relative phase. In the case of low power, for a large detuning the system will exit from the locking region via a saddle-node (SN) bifurcation. Both the size of the locking region and the kind of unlocking bifurcation depend on the injection strength [Wieczorek 2005a]. It is convenient to map the locking region in the Injected Power - Detuning ($P_{inj} - \Delta$) plane, as shown in Figure 2.12. The left part (a) shows the experimental points that corresponds to the transition from locking to unlocking for different injection powers when changing the detuning. We can see how the locking region has a "v" shape that starts from zero detuning and then opens up as the injected power increases. This is coherent with theory: starting from the rate equations for injection when spontaneous emission is disregarded one can show that [Tartwijk 1995] [Mogensen 1985] a necessary condition for locking to occur reads:

$$|\Delta| \leq \Delta_L = \kappa\sqrt{1+\alpha^2}\sqrt{\frac{P_{inj}}{P_{sl}}} \tag{2.23}$$

where κ is the feed-in rate, α is the linewidth enhancement factor, and P_{inj}/P_{sl} is the ratio of the injected power over the slave laser output power. This relationship would give us a square root function for the boundary of the locking-unlocking transition in the $P_{inj} - \Delta$ plane, with a vertex at $\Delta = 0$. This is only a first approximation, since both experimentally and theoretically the SN boundary depends on all the other physical parameters [Wieczorek 2005a].

To compare the experimental results with the theory, we can plot a numerical bifurcation diagram of the same plane. The right part (b) of Figure 2.12 shows the bifurcation diagram obtained via numerical continuation performed on the

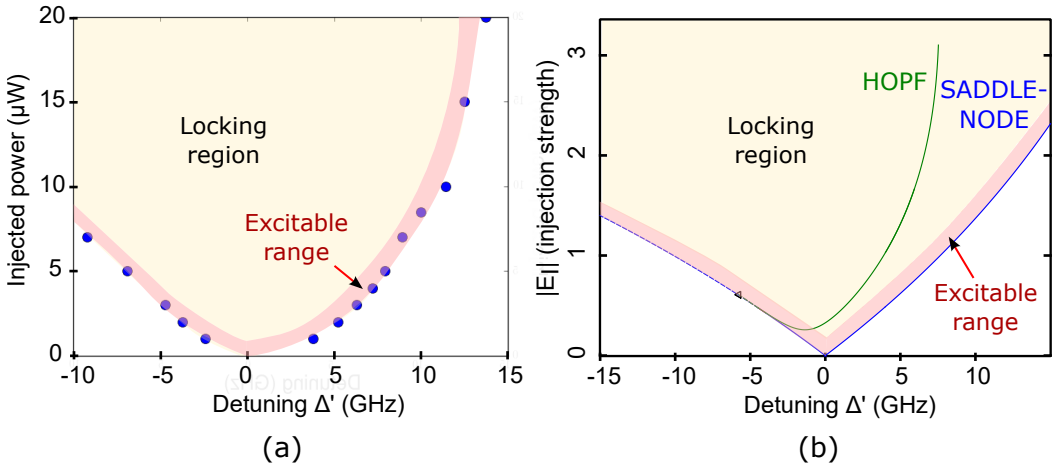

Figure 2.12: Experimental and numerical bifurcation diagram of principal codimension 1 bifurcations. The red region represents the approximate parameter range where the system is excitable when perturbed by a phase perturbation. (a) Experimental bifurcation diagram for $I_{sl} \approx 6.5\, I_{th}$. Modified from [Garbin 2015a]. The Hopf curve is not shown here. (b) Numerical bifurcation diagram calculated from the model of Equation 2.24, with $\alpha = 4$, $\mu = 15$, $\sigma = 50$ using the Knut software [Szalai 2013].

Knut software [Szalai 2013] for the injected laser. In particular, the model that we used to reproduce the dynamics of the system with injection is a Class B laser model (the same used in [Garbin 2017a]) that is a simplified version of the [Hachair 2006, Prati 2010] model after the adiabatic elimination of the atomic polarization variable:

$$\begin{cases} \dfrac{dE}{dt} = \sigma \left[E_I + (1 + i\alpha) DE - (1 + i\theta) E \right] \\ \dfrac{dD}{dt} = \mu - (1 + |E|^2) D \end{cases} \tag{2.24}$$

where E is the slowly varying envelope of the electric field and D is the population variable proportional to the excess of carriers with respect to transparency. The physical parameters are as follows:

$$\begin{aligned} &\alpha = 4 && \text{(linewidth-enhancement factor)} \\ &\mu = 15 && \text{(injected current)} \\ &|E_I| \in [0.0, 3.2] && \text{(amplitude of the injected field)} \end{aligned} \tag{2.25}$$

where E_I is the dimensionless complex amplitude of the externally applied field and μ is the pump parameter of the slave laser proportional to the excess of injected current I_{sl} with respect to the threshold I_{th}. The timescale is set by the σ parameter, defined as the ratio of the non-radiative interaction time

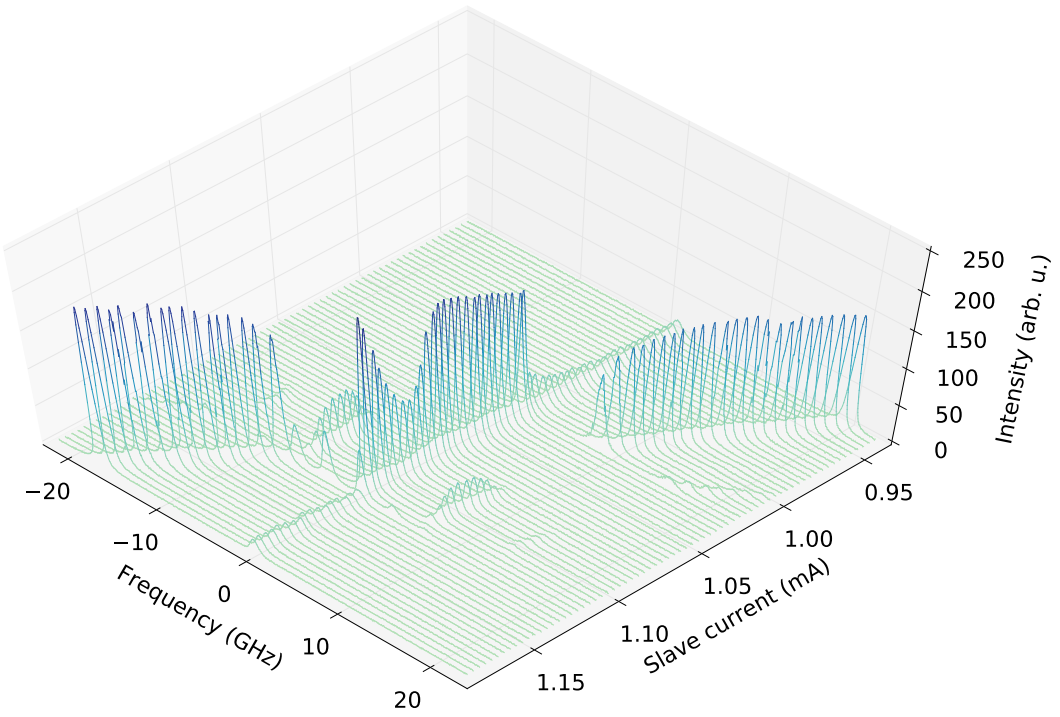

Figure 2.13: Evolution of the experimental spectrum acquired from the Fabry-Pérot in the proximity of the locked region, with injected power $P_{inj} \approx 5\ \mu W$. Each curve is collected for a different value of the slave current. Same experimental realization as in Figure 2.14

($\tau_c \approx 1\,ns$) and the mean lifetime of a photon inside the cavity ($\tau_p \approx 20\,ps$), that is $\sigma = \kappa/\gamma_{nr} = \tau_c/\tau_p = 50$. The detuning between slave ad master is taken into account by the θ parameter, defined as:

$$\theta = -\alpha + 2\pi\Delta\,\tau_p = -\alpha + \frac{2\pi\Delta'}{\sigma} \tag{2.26}$$

assuming $\tau_c = 1\ ns$, where Δ' is just the detuning measured in GHz.

Looking at the bifurcation diagram we notice that we recover the general v-shape of the locking region, which is delimited by two saddle-node branches that intersect at zero detuning. We also observe a Hopf bifurcation that starts from a point on the SN branch (which is a Bogdanov-Takens codimension 2 bifurcation point) and then extends inside the locking region. Even though this Hopf bifurcation is not plotted in the experimental plot, it is still present in the system, as shown in Figure 2.13. This figure represents the different experimental spectra that are measured by the Fabry-Perot when we change the detuning of the system by changing the slave current. Since we keep the injection power constant and all of the other physical parameters are fixed, we are basically scanning the system along an horizontal line in the $P_{inj} - \Delta$ plane.

Starting from left to right, we can observe how the two peaks of the master (the small peak centered at zero frequency) and the slave (the big peak) are separated at first. When we then increase the detuning (by decreasing the slave current), we observe the first appearance of another frequency which is due to the presence of an invariant limit cycle of the saddle-node on a circle bifurcation. Later we enter into locking region and we cross almost immediately a Hopf bifurcation. We can identify this bifurcation by the birth of two symmetric peaks that are born and die at a finite frequency which does not change with the detuning. We then exit the cycle region with another Hopf bifurcation, and we are well inside the stable locking region. Here we observe only one peak, as the frequency of the slave is locked to the frequency of the master. Increasing the detuning again, we exit from the locking region with another SN bifurcation. A more detailed view of the spectra and time traces that are visible during this scan is shown in Figure 2.14.

Apart from allowing us to understand the dynamics of the system, having in mind the shape of the bifurcations on the $P_{inj} - \Delta$ plane is greatly useful experimentally. This is because when we want to excite the locked system with a positive-slope phase perturbation in order to generate a pulse, we need to be in a region of parameters which is close to the saddle-node bifurcation that is present at positive detuning (inside the red region in Figure 2.12). With a negative-slope phase perturbation we should instead place ourselves close the bifurcation but at negative detuning. We then need to "navigate" this diagram by changing the injection power and the slave current in order to place the system in this region. We will explain this procedure more in detail in the following sections.

Finally it is also important to note that the shape of the bifurcations that are present on a $P_{inj} - \Delta$ plane in general can be very complicated, and depends substantially on the physical parameters of the system (especially the value of α). [Wieczorek 2005a] has a huge collection of such diagrams for different parameter ranges.

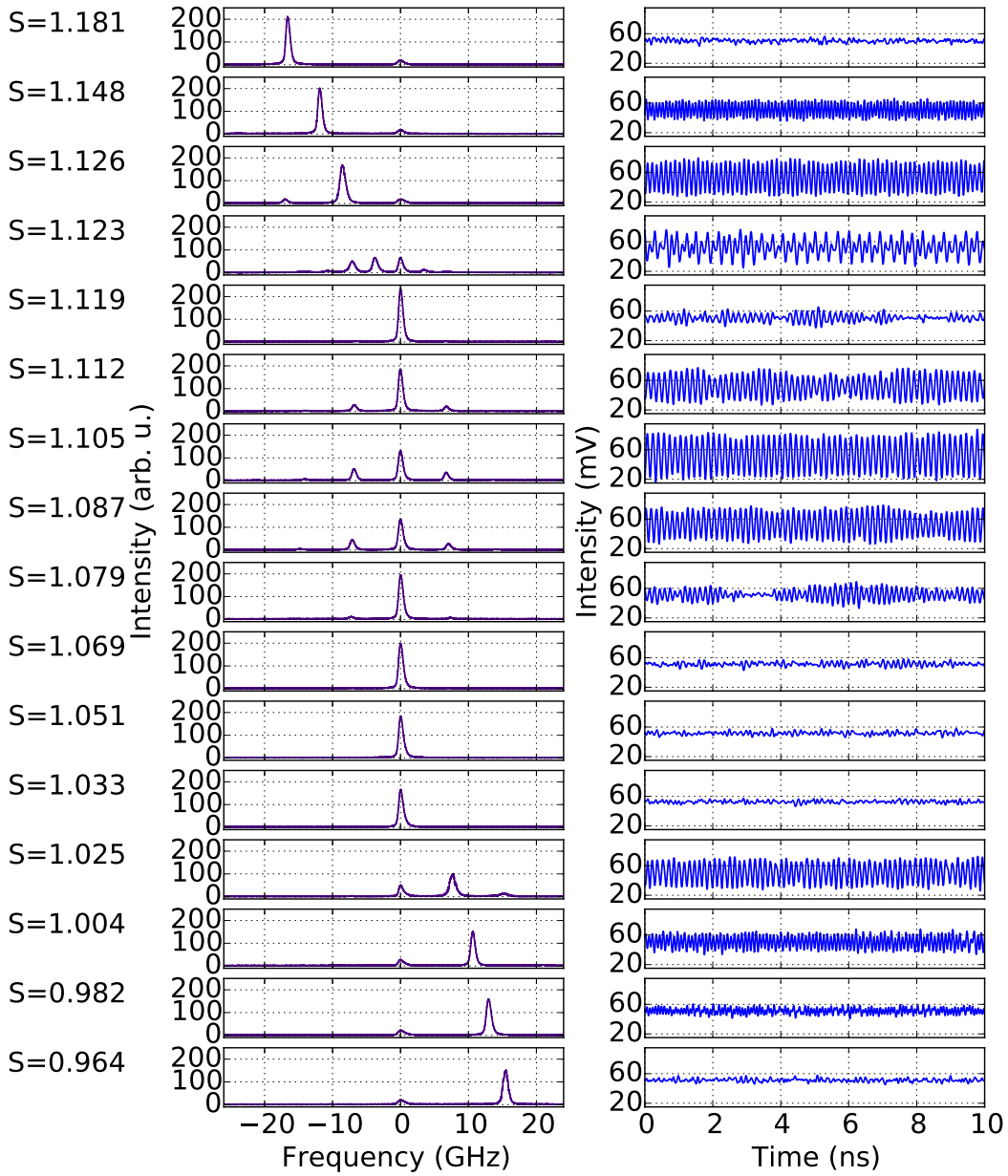

Figure 2.14: Examples of experimental spectra (left) and time traces (right) when changing the Slave laser current S (same as I_{sl}) in the vicinity of the locked region, with injected power $P_{inj} \approx 5\ \mu W$. Here S is measured in mA. The zero is set on the frequency of the master laser (the smaller peak). From top to bottom, one can observe:
i) The appearance of a first saddle-node bifurcation (with the rise of a new peak at the negative sum of the two frequencies) around $I_{sl} = 1.126$ mA.
ii) There is a small period doubling region at $I_{sl} = 1.123$ mA.
iii) We then we enter into the locked region, from $I_{sl} = 1.119$ mA to $I_{sl} = 1.033$ mA.
iii) From $I_{sl} = 1.112$ mA to $I_{sl} = 1.087$ mA (still inside the locked region) there is a limit cycle, which is born and dies with a Hopf bifurcation.
iv) Finally, we exit from the locked region with another saddle-node bifurcation around $I_{sl} = 1.025$ mA.
A global view of the evolution of the spectra can be seen in Figure 2.13

2.3.3 Single perturbation: excitable response

In the previous sections we have introduced the concepts of excitability in the case of a locked LIS system. In our case, the excitability is best apparent when we perturb the system with a phase-perturbation. In the experimental section we have already shown how we constructed the setup in order to probe the system with different phase-perturbations in the master signal. These perturbations can be of various shapes but in our case they are usually in the form of series of step-up functions or pulses. In this section, we will describe in particular how the system reacts to a single perturbation, that is, a single positive-slope phase-perturbation that is capable of producing a response.

Phase dynamics and triggering of excitable pulses In section 2.2.2 we explained how in the case of the locked LIS in the limit of small detuning, small injected power and weak dispersion the dynamics could be simplified to that of the Adler equation, as stated in equation 2.14. The system can then be thought to be one-dimensional where the dynamics is only present in the phase difference between the master and the slave and is completely confined to a circle. The control parameter is the detuning Δ (frequency difference between the slave and the master), which will determine the position of a saddle and a node on the circle, as depicted in Figure 2.1. The behaviour of the system is then very simple to predict: it will either oscillate when Δ is large and there are no fixed points, or converge toward the stable point when Δ is small. In addition, when the system is perturbed from its stable point by a phase perturbation, in can either relax to the stable point or exhibit a 2π phase rotation that is interpreted as an excitable event, as shown in Figure 2.3.

This simple picture is obviously a simplification of the real system, but it can help understand the basic behaviour of the locked LIS system. We will later describe in detail a more complex dynamic starting from an analytical and numerical study of the LIS model in section 2.4, but for the moment this simple model will suffice. One thing to keep in mind though is that, in the case of the real excitable events, each 2π phase slip will be associated with a pulse in the output intensity of the slave laser because of the coupling between phase and amplitude. In our experiment we will always detect the excitable responses as intensity pulses since it is an easier and more versatile method to detect these responses. A detection of the phase dynamics is however possible using the technique described in [Kelleher 2010].

With this picture in mind, it seems almost obvious that the system would respond most efficiently to phase-perturbations, as the dynamics is mostly related to the phase. This is indeed the case, and in this study we only perturbed the system using phase-perturbations applied to the master signal, as explained in the setup section 2.3.1. However, other types of perturbations are possible. In [Garbin 2014] and [Garbin 2015a] they showed how it was possible to trigger excitable pulses when applying an incoherent perturbation coming

from an external laser that is injected into the slave laser. Furthermore still in [Garbin 2015a] they managed to observe excitable responses by applying perturbations in the pumping current of the slave laser and in the power of the injected master laser. We refer the interested reader to this last reference for more details on the setup and on the efficiency of these alternative techniques.

Imaging of the saddle and node points on phaser plots The fact that the dynamics at small detuning and injection is basically governed by a saddle and a node points in the phase space can actually be verified experimentally. Using the technique previously mentioned, described in [Kelleher 2010], it is possible to image the evolution of the phase difference between the slave and the master and to plot the evolution in 2D phasor plots in the complex plane of the electric field.

In Figure 2.15 it is shown how it is possible to image indirectly the position of the saddle and the node point in the complex electric field plane using such technique. The procedure is the following: by switching on and off the master laser sufficiently fast and recording the evolution during the transient time before the locking between the master and laser occurs, one can trace many different trajectories of the evolution of the phase of the master with respect of the phase of the slave on the complex plane, as shown in Figure 2.15(A). Since each time the initial condition of the master laser is chosen at random by the system, this basically consists in watching the evolution of the phase of the master from a large number of randomly chosen initial conditions. The space of possible initial conditions consists of a circle whose radius is determined by the power of the master laser, which is set to be constant for each realization.

During each realization, the system will try to converge towards the stable point following a phase dynamic along the circle. By plotting all of the realizations at once, it is then possible to see the node point on the complex plane where all of the trajectories try to converge to (marked in Figure 2.15(A) by a red dot) and the saddle point, where all of the trajectories try to escape from (marked with a black arrow). It is also possible to follow the evolution of the saddle-node bifurcation by following the position of these points when changing the detuning. By plotting the difference in phase between the positions of the stable and unstable points as shown in Figure 2.15(B) as a function of the detuning, we get Figure 2.15(C). The phase difference is calculated supposing that the stable point remains fixed at angle zero.

We observe that this phase difference is mostly negative for negative detuning and positive for positive detuning. This can be seen qualitatively from the Adler model. If the system actually followed a dynamic strictly determined by the Adler equation 2.14, the evolution of the stable and unstable points would be given by:

$$\Theta_+ = \arcsin(\Delta), \qquad \Theta_- = -\arcsin(\Delta) + \pi \tag{2.27}$$

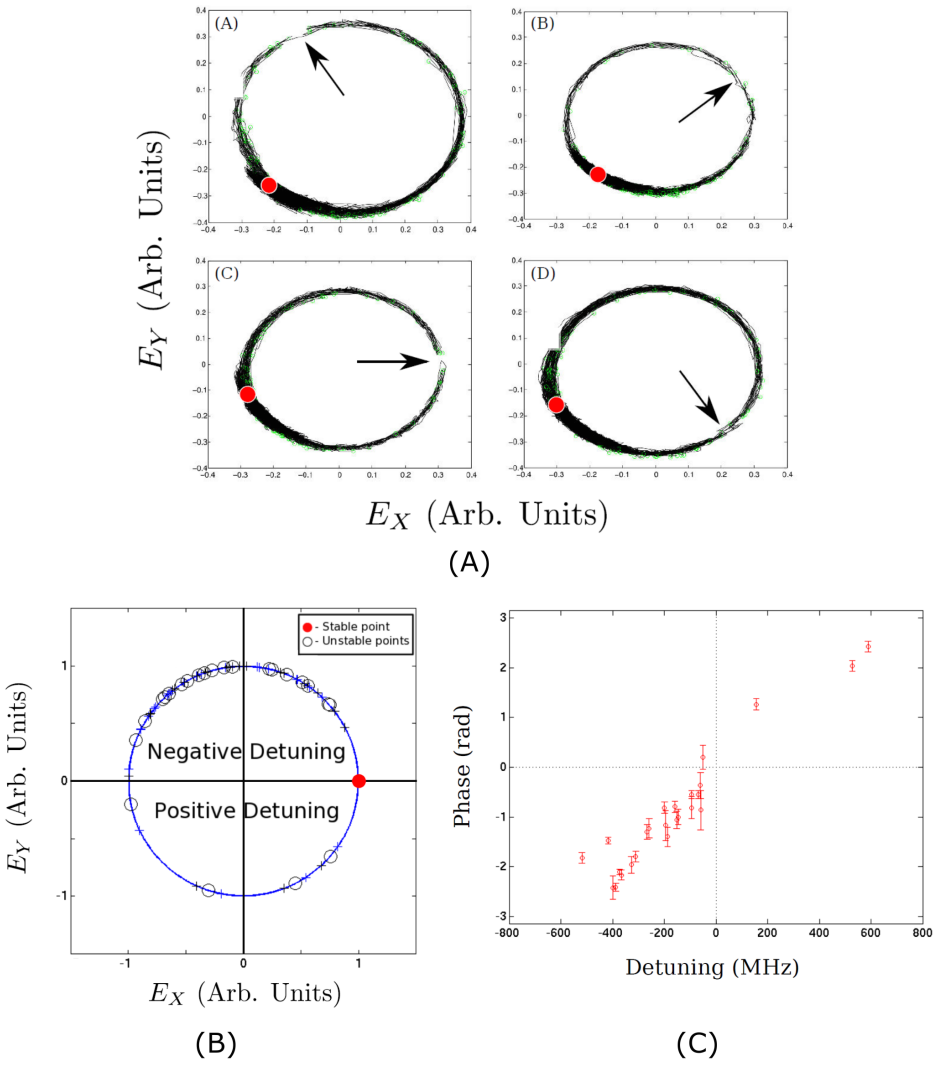

Figure 2.15: Experimental imaging of the saddle-node points. *(A)* Evolution of a large number of trajectories starting at different initial positions on a circle centered on zero in the Argand plane of the electric field; each panel at a different detuning. The trajectories are repelled from the saddle (marked with an arrow) and converge towards the node (the red point). *(B)* Summary of many different positions of the saddle-node points at different detunings. The stable node point is fixed at angle zero, and the saddle points are plotted at different positions on the circle, along with their error bar. *(C)* Evolution of the phase difference between the two points as a function of the detuning, supposing that the stable node is fixed at angle zero. Reprinted with permission from [Garbin 2015a].

where Θ_+ is the stable point and Θ_- the unstable one. Figure 2.1(b) represents a schematic plot of these two solutions as function of Δ. Starting instead from a Class B model for an optically injected laser, it is possible to show [Kelleher 2012b] that the relationship between phase and detuning for the sta-

ble point is given by:

$$\Delta = \frac{-K}{R}\sqrt{1+\alpha^2}\sin(\Theta_+ + \arctan\alpha) \tag{2.28}$$

where K is the injection rate, R is the slave field amplitude and α is the linewidth enhancement factor which represents the coupling strength between the amplitude and the phase of the electric field. Notice how this expression reduces to the Adler model 2.27 when $\alpha = 0$, $K/R = 1$. In any case, both models are consistent with the experimental trend seen in Figure 2.15(C).

Triggering of excitable pulses We have seen how the dynamics of the unperturbed system follows to a first approximation the Adler model. We will now describe more in detail how to trigger the excitable responses.

The first thing we need to do is to place the system in the parameters regime where it is excitable. From a theoretical point of view, the system is excitable when we are inside the locked region, so that the dynamics is governed by the two fixed points as in Figure 2.3. Furthermore, we need to be close enough to the locking-unlocking transition so that the angle between the two fixed points will be small, and a phase perturbation will then be capable of triggering a 2π phase rotation. Practically, we need to be in the red region of Figure 2.12. Experimentally, we then have to change the value of the injected signal by changing the angle of the half-wave plate in the path of the master signal, and the value of the detuning by changing either the frequency of the master using the diffraction grating or the pumping current of the slave I_{sl} (we remind that the frequency of the slave depends on the pumping current as in Figure 2.11(C)). By looking at the experimental spectra and at the time traces from the photodetector as in Figure 2.14, we are able to determine the approximate position of the system in the $P_{inj} - \Delta$ plane, and to place it in the excitable parameter range.

One thing to note is that, depending on the sign of the detuning, the relative position of the fixed points will change. For a positive detuning there will be a positive angle between the stable point and the node, so that in order to trigger a response, the phase of the perturbation will have to increase (we will refer to this as a *positive-slope perturbation*). For a negative detuning instead, the angle between the stable point and the node will be negative, so that the perturbation will have to decrease in phase (a *negative-slope perturbation*). The shape of the perturbation itself is not very important, and we can trigger a response both with a pulse-perturbation and with a step-perturbation.

Figure 2.16 represents the efficiency curve for the generation of a response when we perturb the system with a step-up or a step-down perturbation, depending on the sign of the detuning. The shape of the step-up perturbation can be seen in Figure 2.20, panel (a), following the pulse perturbation. A step-down perturbation would have the same shape but with a negative phase-jump.

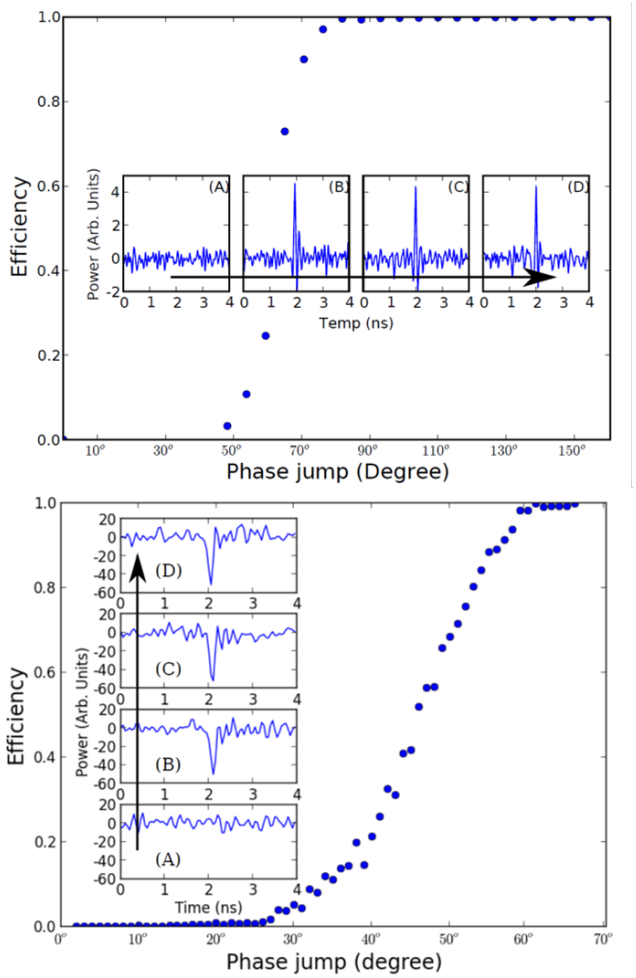

Figure 2.16: Efficiency curves for the generation of an excitable response given a step-up or step-down perturbation with increasing amplitude, calculated for the two cases of positive and negative detuning. The efficiency percentage is computed over more than 3000 events, and the time traces are acquired with a sample rate of 10 ps per points or more.
(Top) case $\Delta > 0$, applying a step-up perturbation, with parameters $I_{sl} \approx I_{th}$, $P_{inj} \approx 2.5\,\mu W$. The inset panel shows the intensity response of the system corresponding to the amplitudes $A \approx 48°$, $B \approx 48°$, $C \approx 65°$, $D \approx 160°$. We can observe the excitable response as a positive intensity pulse for amplitudes B, C and D.
(Bottom) case $\Delta < 0$, applying a step-down perturbation, with parameters $I_{sl} = 1.714\,mA$, $P_{inj} = 12.8\,\mu W$. The inset panel shows the intensity response of the system corresponding to the amplitudes $A \approx 32°$, $B \approx 32°$, $C \approx 48°$, $D \approx 66°$. We can observe the excitable response as a negative intensity pulse for amplitudes B, C and D. Reprinted with permission from [Garbin 2015a].

The perturbations are generated by a signal generator (HP8133a) with 31.2 MHz repetition rate and 100 ps rise/fall time. Its output is amplified by a RF amplifier (photline DR-DG-10MO-NRZ), to get high perturbations (8 V max). This electrical perturbation is then sent to the EOM as in Figure 2.5

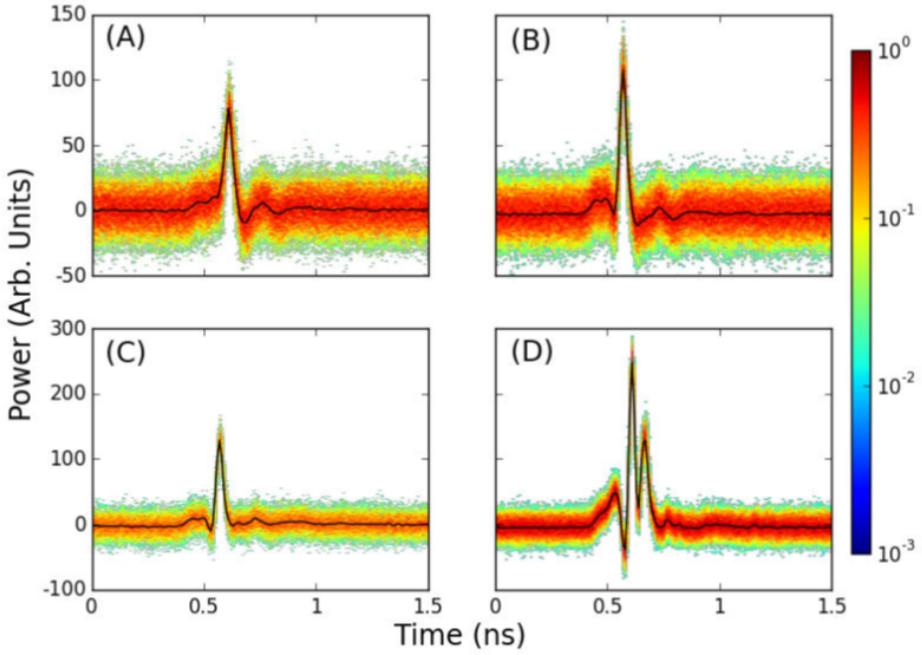

Figure 2.17: Histograms of the time-traces of the responses, traced from 350 to 600 excitable responses. The color scale is logarithmic. The black line represent the average of the histogram. (A) $\Delta = 6.6$ GHz. (B) $\Delta = 9.2$ GHz. (C) $\Delta = 12.5$ GHz. (D) $\Delta = 25.5$ GHz. Reprinted with permission from [Garbin 2015a].

that converts the electrical perturbation into a phase perturbation.

In order to construct this figure, we have increased the amplitude of the step-perturbation for both detuning, and we have recorded the number of trial where we get an excitable response over the total number of trials, for more than 3000 events. Converting this number into a percentage, we get the efficiency for the generation of a response for each amplitude. To detect a response, we set an appropriate threshold on the power of the response signal, and we detect signals that overcome this threshold as an excitable response. As we can see, for both cases the efficiency curve starts at zero for a small amplitude, and then increases following a sigmoid-like shape until reaching 100% efficiency. We can define in both cases a threshold for the generation of a response as the phase-jump value where the efficiency reaches 50%, which is around 60° in the case of $\Delta > 0$ and step-up perturbations and around 48° in the case of $\Delta < 0$ and step-down perturbations. In the insets of the figure we report the shape of the excitable responses, which remains more or less constant for each perturbation strength. In the case of $\Delta > 0$ the response appears as positive pulse in the intensity, while in the case of $\Delta < 0$, it appears as a negative intensity pulse.

To better appreciate the shape of the responses in the $\Delta > 0$ case, we can aver-

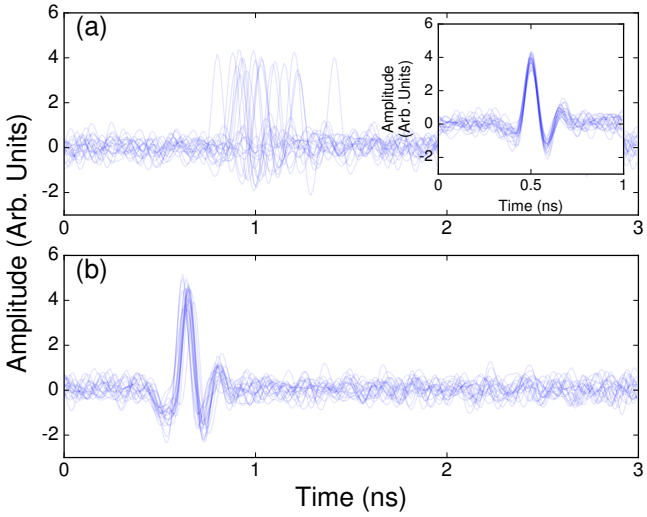

Figure 2.18: Superposition of 20 excitable responses for different perturbation with $I_{sl} = 5\, I_{th}$, $P_{inj} = 2.5\, \mu W$, and $\Delta = 5.8\, GHz$. *(a)* Perturbation amplitude of about 60°, triggered on the perturbations. Inset: same as (a), triggered on the maximum of the responses. *(b)* Perturbation amplitude of about 160°, triggered on the perturbations. Reprinted with permission from [Garbin 2017a].

age them over a great number of realizations. Figure 2.17 shows the histograms of the time-traces of the responses, along with the average of the response for different values of Δ. We can observe how the average shape changes slightly both in amplitude (due to the increased forcing) and in shape. In particular, the subplot (D) shows a response that presents a high second peak, which is the sign of a modified trajectory in phase space with respect to the trajectories at lower detuning. This is coherent with the fact that the Adler model is only valid for small injection values, and for higher values the dynamics of the excitable pulse can become more complicated.

Distribution of the delay times As our system is excitable, when we increase the strength of the perturbation the shape of the response will remain almost unaffected. However, what can change is the delay that we can expect from the onset of the perturbation and the appearance of the response. In particular, for perturbations of higher amplitudes the response will arrive quicker with respect to lower amplitude perturbations. This is a general property of excitable systems, and it was already observed in 1952 by Hodgkin and Huxley [Hodgkin 1952a] in the case of membrane action potentials from a giant nerve fibre of the squid.

Figure 2.18 shows a superposition of 20 excitable responses in the case of a low-amplitude perturbation (a) and a high-amplitude perturbation (b), both triggered on the onset of the perturbation. In the case of a low-amplitude per-

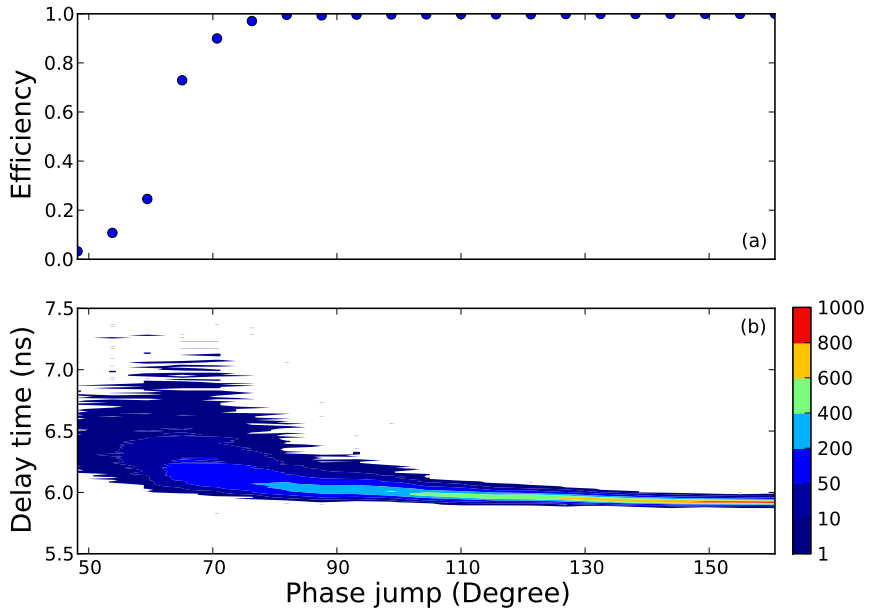

Figure 2.19: Perturbation efficiency and response time to external perturbations. Same parameters as in Figure 2.18. *(a)* Efficiency curve of the perturbation for more than 3000 events, defined as the number of excitable responses over the number of perturbations. *(b)* Associated evolution of the delay time histogram between the pulse and the trigger of the perturbation. Reprinted with permission from [Garbin 2017a].

turbation, we clearly see how the distribution of the responses is spread out in time and with a higher delay, while in the case of high-amplitude perturbation the distribution is much narrower, so that all of the responses neatly overlap.

A more quantitative study of the distribution of the delay times is visible in Figure 2.19. Plot (b) shows the histogram of the delay time between the onset of the response and the trigger of the perturbation when varying the strength of the perturbation (here a step-up perturbation with variable phase-jump amplitude). We can observe how the average of the delay time decreases (meaning a faster response) and also how the perturbation becomes narrower and narrower when increasing the strength of the perturbation. This is the typical histogram that one can expect from an excitable system, and it will be reproduced numerically from the simulations, as we will show in Figure 2.43. Plot (a) shows instead the efficiency curve for the generation of the excitable response, which is similar to what we have already shown in Figure 2.16 for the case of $\Delta > 0$. Also in this case, the efficiency curve has a sigmoid-like shape going from 0% efficiency to 100% efficiency, with a threshold at around 60° phase jump.

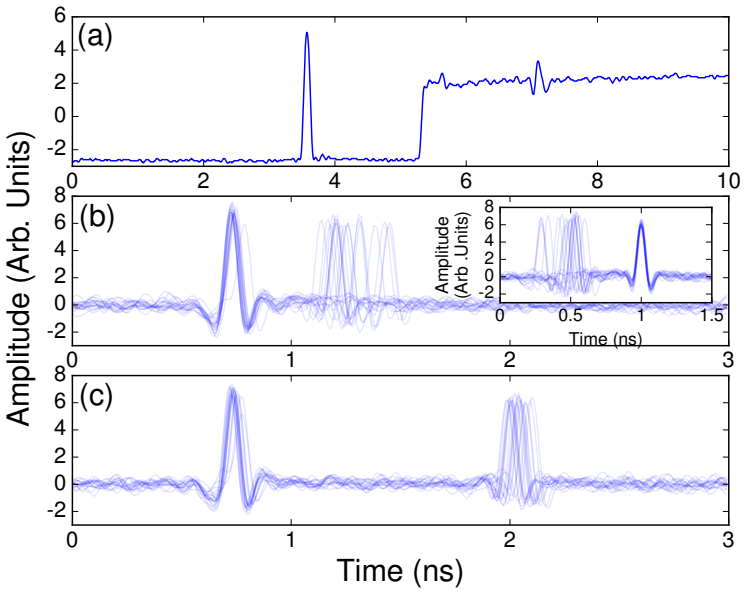

Figure 2.20: Temporal traces of the perturbation and excitable responses (only when two responses are observed) for $I_{sl} = 1.344\,mA$, $P_{inj} = 6.3\,\mu W$, $\Delta = 6.4\,GHz$. *(a)* Shape of the perturbation for the maximum delay used, 1.81 ns. *(b)* Superposition of 20 excitable events for a perturbation delay of about 0.34 ns, triggered on the perturbations. Inset: same pulses as (b), triggered on the maximum of the second responses. *(c)* Superposition of 20 excitable events for a perturbation delay of about 1.2 ns, triggered on the perturbations. Reprinted with permission from [Garbin 2017a].

2.3.4 Double perturbation: Refractory period

In this section we will describe how the system reacts to a double perturbation. In particular, we are interested in understanding if the system may display a refractory period after a first excitation.

The refractory period is a common property of an excitable medium, and it is defined as the period of time after a first excitable response where the system cannot be excited again. It is most commonly known in physiology in the case of neurons, where this period corresponds to the time that it takes for the membrane potential to depolarize and then repolarize during the formation of an action potential. It generally lasts one millisecond.

In the case of the LIS system, we can also expect to observe a refractory period. If we go back to the Adler excitability vision as in Figure 2.3, we can imagine how, after a first perturbation pushes the system over the threshold of the unstable saddle, the system will need some time to reach the stable point. During this time, a second phase perturbation in the same direction will not necessarily generate another excitable response as the system is now far away from the threshold. If we perturb the system with a double phase-perturbation

with two successive raising edges with an arbitrary delay between them, we can expect the efficiency of the response to go to zero when decreasing the delay between the two perturbations.

In order to measure the refractory period, we have then probed the system with a double phase-perturbation that consisted of a pulse, followed by a step-up as shown in Figure 2.20(a). The first pulse perturbation is generated by an electrical pulse generator (Alnair Labs, EPG-200B-0050-0250) with approximately 100 ps of duration. The second is the same step-up perturbation that was described in the previous section, which is generated by the signal generator HP8133a (31.2 MHz of repetition rate, 100 ps or raising/falling time). The sum of these electrical perturbations is then sent to the EOM, and the rest of the setup is (as always) the same of Figure 2.5.

When the delay between the two perturbations is large (about 1.2 ns) as in the case of Figure 2.20(c), then each perturbation will generate a response. By superimposing 20 excitable events we can see the responses that correspond to the first pulse, which overlap on the same spot, and later the ones that correspond to the step-up perturbation. In this second case, since the strength of the perturbation is lower, there will be a small spread of the distribution of the arrival times, so that the responses will not overlap perfectly. In this case we can suppose that the two perturbation are independent from one another, and each response is just the sum of the two independent perturbations.

However, when reduce the delay between the two perturbations, they will start to interact so that the response to the second perturbation will be affected by the presence of the first. This is visible in Figure 2.20(b), where in this case the delay between perturbations is small (about 0.34 ns). The distribution of the arrival times of the second responses is more spread out in this case. Furthermore, not in all cases we obtain 2 responses, as the efficiency for the generation of the second response starts to decrease when decreasing the delay.

This is more visible in Figure 2.21. This figure is composed of 4 panels, which correspond to 4 different experimental realizations of the same type of perturbation for different experimental parameters. What is important in particular, is that the value of the detuning is increasing when going from panel (a) to (d), as the detuning goes from (a) 6.4 GHz, to (b) 8.3 GHz, to (c) 9.2 GHz to (d) 10.6 GHz. The gray line with circles in each panel represents the efficiency for the generation of the second response, assuming that the first has been triggered. The horizontal white lines indicates 100% efficiency. As we decrease the delay between the two perturbations, we see how the efficiency starts to decrease and then goes to zero, at least for panels (a), (b) and (c). This means that, for a delay lower than a certain value (around 0.20 ns), a second response cannot be generated when perturbing the system with a double perturbation of this type. This is an experimental observation of the refractory system for our system.

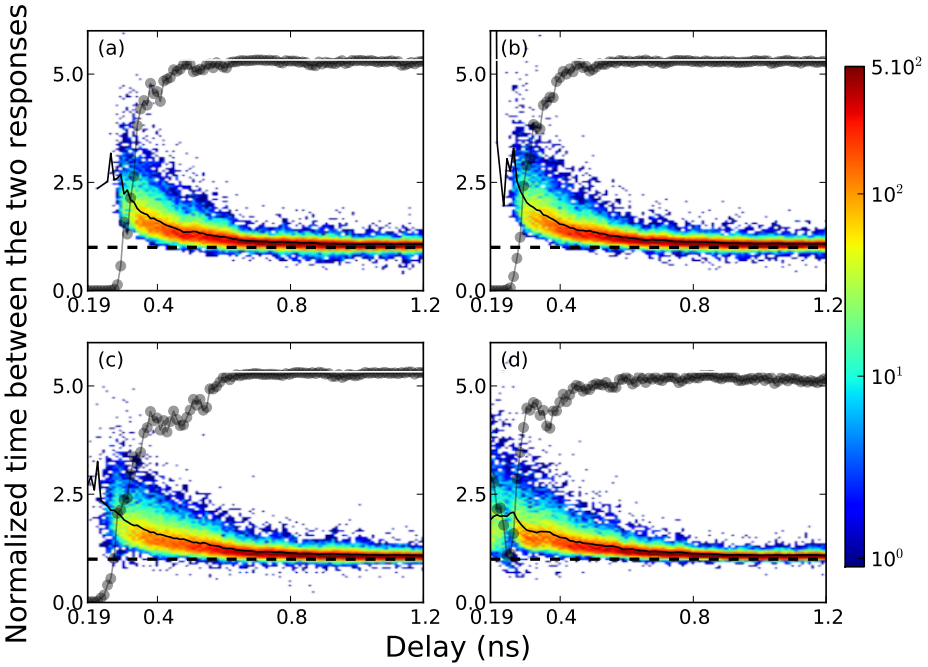

Figure 2.21: Evolution of the histograms of the interval delay times between the two responses (only when 2 responses are obtained) in logarithmic color scale, normalized to the delay times of the perturbations. In each panel about 1600 events for each of 163 values of the delay are shown, for different values of parameters. Solid black line: mean of the distribution. Black dashed thick line: time normalized to the delay between perturbations. Grey line with circles: efficiency curve of the second pulse added as a guide, assuming the first has been triggered, the horizontal white lines indicate 100% efficiency. *(a)* $I_{\mathrm{sl}} = 1.344$ mA, $P_{\mathrm{inj}} = 6.3$ μW, $\Delta = 6.4$ GHz. *(b)* $I_{\mathrm{sl}} = 1.338$ mA, $P_{\mathrm{inj}} = 8$ μW, $\Delta = 8.3$ GHz. *(c)* $I_{\mathrm{sl}} = 1.329$ mA, $P_{\mathrm{inj}} = 10.2$ μW, $\Delta = 9.2$ GHz. *(d)* $I_{\mathrm{sl}} = 1.321$ mA, $P_{\mathrm{inj}} = 12.7$ μW, $\Delta = 10.6$ GHz. Reprinted with permission from [Garbin 2017a].

The colourful histograms in each panel represent instead the distribution of the arrival times of the second response, normalized to the delay time between the two perturbations. The black dashed thick line represents the value of 1, which corresponds to the time between the responses equal to the time of the delay between the perturbations. A value higher than 1 means that the second response is generated some time later than the second perturbation, due to the interaction with the first response. By looking at the average of the distribution (the solid black line) we notice that for long delays (more than 0.8 ns) the average converges towards the value of 1, which means that the two perturbations are independent. When the delay gets closer, the presence of the first perturbation induces the second (when it is present) to be generated later in time. This is because we are entering into the refractory period, and in the Adler vision, the system needs more time to reach the threshold represented

as the saddle point as it is still travelling along the phase excursion caused by the first perturbation.

From these four panels we can extract some interesting properties about the system when we increase the detuning Δ (and consequently the injection power P_{inj}):

1. *The refractory period becomes shorter.* If we look at the efficiency curves, we note that the period where the curve stays at zero becomes shorter and shorter. We can explain this by the fact that the duration of the excitable pulses also decreases when increasing Δ [Garbin 2015a], so that the excursion in phase space that corresponds to the excitable event takes less time to complete and it is then possible to generate a second response faster.

2. *The interaction time between the perturbations is limited to around 0.8 ns.* Both the efficiency curve and the response time histogram in all four panels become almost constant after a delay between the two perturbations of around 0.8 ns. This is an indication that, after this time, the system has had the time to reach the stable point again after the first perturbation, so that the second perturbation is basically independent from the first.

3. *For high detuning we depart from the Adler model.* Panel (D) shows an efficiency curve which presents an unexpected increase when the delay goes towards the minimum value experimentally possible of 0.19 ns. This implies that is it not really possible to define a refractory period in this case. We can explain this behaviour by noting that in this case the value of the detuning and of injection is high enough for the Adler approximation not to be completely valid any more. This could be due to a richer dynamics where relaxation oscillations around the stable point are involved, which can determine a modification of the efficiency curve. We will describe this different behaviour more in detail in the numerical section on the Resonator property (subsection 2.4.5).

2.3.5 Double perturbation: Resonator property

In the previous sections we described the presence of a refractory period in the behaviour of our system. This is a property that is shared by many excitable systems, most notably neurons, and it can still be explained in the simple view of the Adler model as the time that it is needed by the system to reach the stable fixed point after a first excitation. In this section we investigate instead a property which is shared by Class 2 neurons (see subsection 1.1.2), that goes beyond the Adler-type of dynamics. For this class of neurons there is a preferred frequency of the perturbation pulses for the generation of an excitable response. As already explained, a possible dynamical explanation of such a behaviour can be found in the presence of a supercritical Andronov-Hopf bifurcation where, due to the presence of relaxation oscillations around the stable point, there is a preferred timing for the generation of an excitable response.

By choosing the right parameter range, we find that even in our system we can observe the presence of a resonator property. Since this property cannot be explained in the framework of the Adler-model, we will propose later a possible *ad hoc* phenomenological modelling that could describe this effect, namely adding a small inertial term to the Adler equation. We postpone this discussion to the section on the analytical and numerical study of the model (section 2.4), while here we will just describe the experimental results that were found.

The perturbation that we applied to probe the system is, again, a double perturbation which consists of two independent perturbations at different delays, but in this case it is composed by two successive pulses as shown in Figure 2.8(a). In order to obtain this kind of perturbation we have assembled an electrical setup that consists of two pulse generators: the Alnair Labs EPG-200B-0050-0250 (first pulse generator) and an Alnair Labs EPG-210B- 0050-S-P-T-A (second pulse generator) which respond to an input raising front by generating a pulse with constant amplitude and tunable width. Figure 2.7 shows in particular the electrical setup that we employed to obtain a sequence of two pulses with arbitrary delay and with approximately the same amplitude.

Since we wanted to probe the system with many double-pulse perturbations at different delays all at once, we devised a periodic electrical perturbation made of couples of pulses with increasing delay between them, as depicted in Figure 2.22. The couples are separated with a repetition time of 20 ns, and the delay between the pulses of each couple goes from a minimum of 0.10 ns to a maximum of 1.05 ns, with increasing steps of approximately 8 ps. The same electrical perturbation is repeated again after completion in a periodic manner. Practically we achieve this by triggering the first pulse generator with a 50 MHz square wave, and the second pulse generator by a second 50 MHz square wave with a 800 kHz phase modulation in the shape of a down-ramp. Since the two

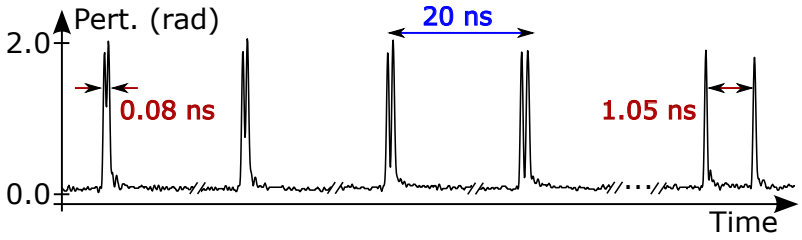

Figure 2.22: Simplified depiction of the shape of the periodic electrical perturbation sent to the EOM. Each couple of pulses is separated by its neighbours by a delay of 20 ns. The delay times between the couples increases gradually from a minimum of 0.10 ns to a maximum of 1.05 ns. The same perturbation is repeated periodically after completion, where each period takes 2.5 μs.

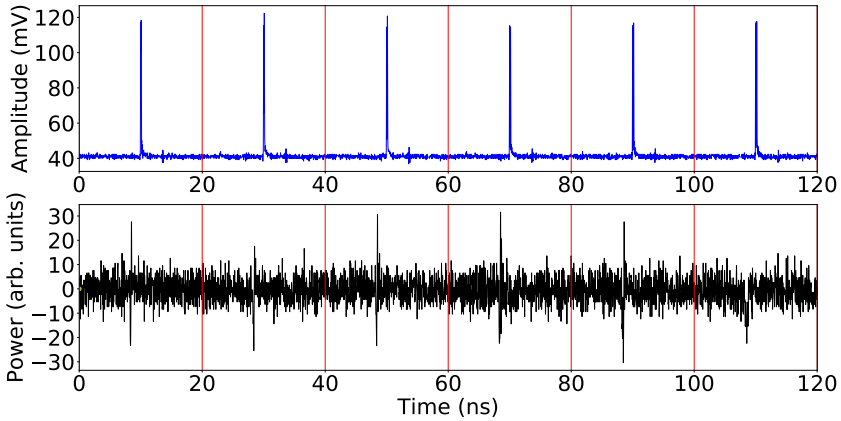

Figure 2.23: Example of how the long time traces of the periodic electrical perturbation (top trace) and the relative response (bottom trace) were analysed. Each trace is cut in many frames, each of 20 ns, each containing only one perturbation couple with a definite delay and the relative response. The statistics on one specific delay is performed on all the different frames with the same delay.

square waves are synchronized, this created a periodic shift between the two channels that translates into a delay between the creation of the two pulses by the pulse generators.

Once we acquire a long trace of many successive perturbations as previously described, we analyse the output power of the systems by bunching together the perturbation couples with the same delay. We do this as follows: we cut each perturbation and output trace in many successive *"frames"* of 20 ns each, as shown in Figure 2.23. Each frame contains a perturbation with a certain delay and the relative response. When making a statistic about a precise delay (let's say, to get an efficiency estimate), we will then consider only the frames with a perturbation with that particular delay.

Each pulse of the double-pulse perturbations that we are sending it's by itself under-threshold, which means that it's not able to trigger a response. This is

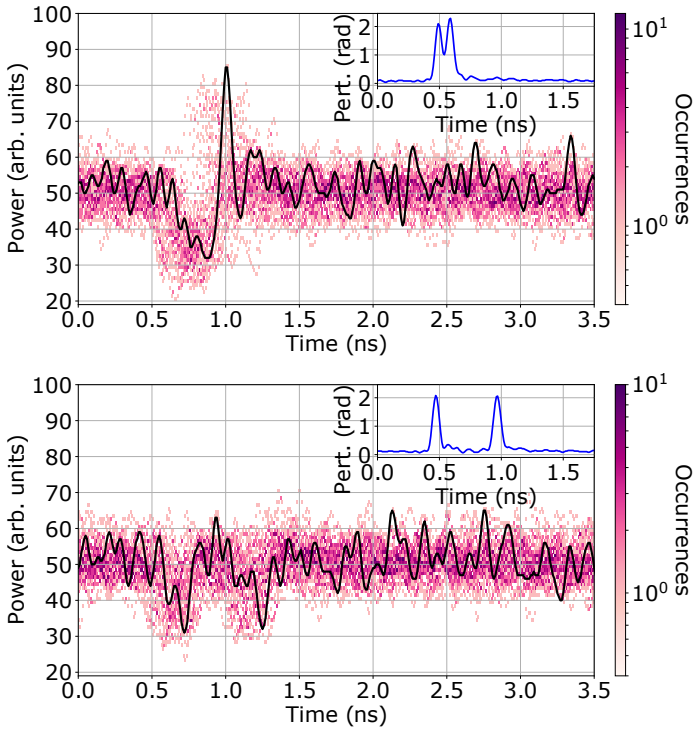

Figure 2.24: Experimentally measured time traces of the response of the system when the two perturbations are separated by 0.10 ns (top) and 0.50 ns (bottom). Insets: shape of the perturbations. The emitted power (dc level) is about 500 μW, the injected power is 4.6 μW and the pumping current is 1.023 mA. 40 realizations are superimposed and show that, on the bottom trace, no excitable pulse was observed. One example realization is shown as the black trace.

visible in the bottom plot of Figure 2.24, where the delay between the two-pulse perturbation was of 0.50 ns. Here we plot 40 responses of the system for the same type of perturbation as a color-coded persistence histogram and we see that each pulse is only able to produce a linear response. However, when the delay between the two-pulse perturbation becomes shorter, as in the top plot of the same figure, the sum of the two perturbations is capable of generating an excitable response. This would be coherent with an integrate-and-fire type of model, such as the Adler model, where the sum of two perturbations is capable of generating a response while a single perturbation is not. What cannot be explained by this model is that, for delays that are shorter than 0.12 ns, the efficiency for the generation of an excitable response actually decreases.

Figure 2.25 shows three efficiency curves for three different slave pumping currents for a delay between the pulses that goes from a minimum of 0.07 ns to a maximum of 1.05 ns, with increasing steps of 0.01 ns. We note that for long delays (more than 0.4-0.5 ns) the efficiency goes to zero, so that almost not response is observed. This means that the two perturbations, by themselves, are under-threshold. When the delay gets shorter than that, the efficiency rises

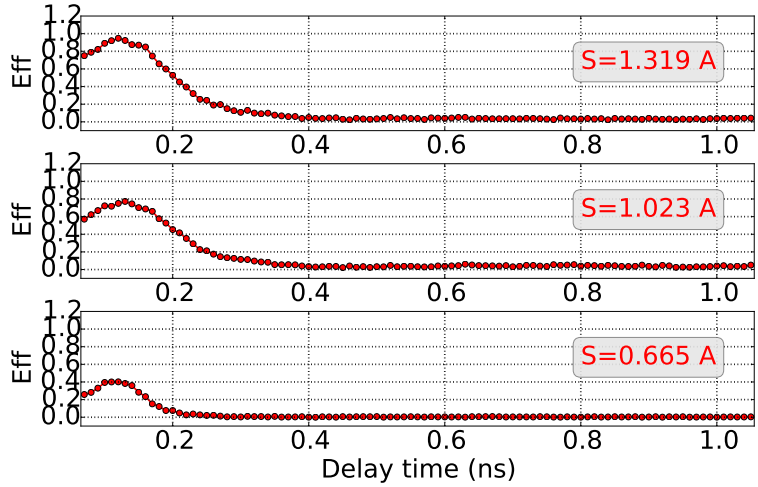

Figure 2.25: Experimental efficiency curves of the perturbation for around 1000 events for each delay. Taken at three different slave pumping currents S (same as I_{sl}). The efficiency is defined as the number of excitable responses over the number of perturbations applied.

to higher values, but then it decreases again for the very short delays. In all three curves, we observe a maximum of efficiency at around 0.12 ns. This type of behaviour can be explained by assuming that our system possesses a resonance time at around 0.12, which is able to trigger a response with a higher efficiency than if the timing is shorter or larger than that. Note that the height of the efficiency curves is not the same: this is due to the fact that the efficiency for a given experimental realizations depends strongly on how close we are to the saddle-node bifurcation (without crossing it), which is something that is difficult to estimate between different realizations. Furthermore, the amplitude in power of the excitable responses depends on the slave pumping current of the experimental realization, so that they have an higher amplitude for higher currents than for lower currents. Since we detect the excitable responses by setting a threshold, this means that in the case of lower-amplitude responses we could lose the responses with an amplitude comparable to the noise oscillations that are lower than our threshold, and this would reduce the efficiency curve. In any case, this is clear evidence that our system can display a resonator property, as is the case with Class 2 type of neurons. In the case of neurons, this property is related to the fact that there are membrane potential oscillations (or MPOs) [Bland 1988, Leung 1991] around the fixed point of the system, that have a definite frequency which is related to the resonance frequency. We will see later that this is analogous to what happens in this system, where the period of the resonance of 0.12 ns is related with the period of the relaxations oscillations of the laser system around its stable fixed point. This will be discussed more in detail in the analytical and numerical study (section 2.4).

Other interesting observations about the resonator property can be made if

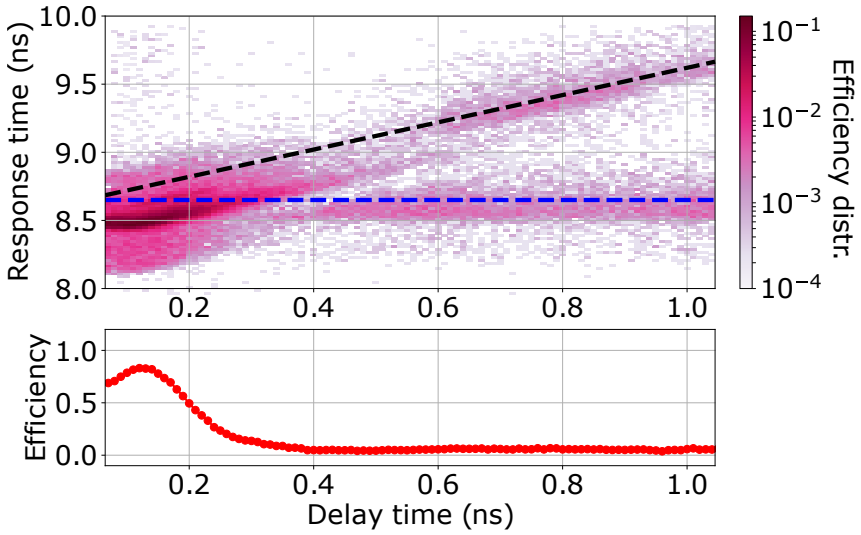

Figure 2.26: Experimental response time histogram and efficiency curve of the perturbation for around 4000 events for each delay. ($S = 1.023\,A$). The histogram is normalized so that each vertical slice for a single delay sums up to the corresponding efficiency value. For high delays, the dashed blue line (horizontal) is the average arrival time of an excitable response generated by the first pulse of the perturbation (which is constant), while the black dashed line is the average arrival time of a response created by the second pulse (which moves away as the delay increases).

we study more in detail the histogram of the response time of the excitable responses, as shown in Figure 2.26:

1. *The interaction time between the perturbations is limited to around 0.8 ns.* A first observation is that, for long delays (more than 0.8 ns), the two perturbations are independent. This is visible in the response histogram: since there is a slight chance that each perturbation will trigger a response, we can see that the response histogram is concentrated in two spots: around the blue line, which is the average time that one would expect to see a response from the first perturbation, and around the black line, which is the average time that one would expect to see a response from the second perturbation. Since for an arbitrary delay the first perturbation stays "in place" for each frame, while the second one "moves" according to the delay (as in Figure 2.23), the black line is slanted while the blue line is horizontal. The fact that the two perturbations do not interact after around 0.8 ns is coherent with a similar observations that we made in the case of Figure 2.20 where the perturbation was given by a pulse-plus-a-step.

2. *In the range of 0.4-0.6 ns, there is still a weak interaction.* Another observation is that, even though it is not visible in the efficiency curve, there is still some interaction between the two responses for delays between 0.4 and 0.6 ns. For this range, the response time histogram shows

gaps and lines that are not coherent with a single sum of the two perturbations as with longer delays. Although present, this interaction is not strong enough to generate efficiently a response, so that the efficiency stays almost flat in this range.

3. *The responses generated by the resonance of the two perturbations are created faster than with a single perturbation.* Finally for small delays we see a narrow range with a big spread in time for the arrival times of the response. This means that most of the responses arrive with a definite delay from the first perturbation. We note that the core of the distribution is at lower response times than the blue line (the average response time for the first perturbation). Therefore the excitable response that is generated by the resonance of the two perturbation pulses is created faster (with a lower delay from the perturbation) than in the case of a single perturbation. This is coherent with the general observation that a stronger perturbation can generate a response faster than a weaker perturbation, as already observed with a single perturbation such as in Figure 2.19.

2.3.6 Multipulse excitability

When perturbing the system with a single perturbation, it can happen that the response that follows is not a single pulse in intensity, but is instead composed of two or more consecutive pulses. In the Adler vision, this consists of performing two or more rotations in phase space before returning to the stable point. We will describe a more detailed dynamic of these response in the Analytical and Numerical section 2.4 after having introduced the physical model used in the simulations. While these multiple spikes have been already predicted theoretically [Wieczorek 2002] and generally observed in systems of semiconductor laser with optical injection, they have not been seen in response to controlled perturbations. Here we demonstrate that a single phase perturbation can nucleate multiple pulses, and that the probability to emit one, two or more consecutive spikes is controlled by the strength of the perturbation.

Figure 2.27 displays the different responses that one can obtain when perturbing the system with a single step-up phase perturbation with increasing amplitude. The panel on top shows the efficiency (i.e. the number of events where a condition is satisfied over the number of trials) for the generation of 0, 1, ... up to 5 pulses for a single perturbation, calculated over a total of 3800 perturbations with increasing amplitude. Looking at the efficiency for the generation of any pulse (the blue curve, labelled by "all") we notice how it displays a sigmoid shape when increasing the amplitude of the perturbation, which is similar to the efficiency curve of Figure 2.19. However, if we "decompose" the responses into groups of only 1, only 2, or more spikes, we see that the related efficiencies have peaks and lows at different strengths values. For instance, the efficiency of only 1 spike is higher at around 125° but it decreases after that. The efficiency of 2 spikes stays stable after 130°, while the efficiency of 3 spikes has instead a maximum at around 150°, while never reaching the value of the double spike. This shows that the number of pulses that one can expect for a given perturbation strength is different and varies depending on the amplitude of the perturbation.

The middle panel in Figure 2.27 shows at a glance the probability of the number of spikes that one can expect for a given amplitude. We observe here that the average of the distribution starts at 0 spikes for lower amplitudes, and then jumps to 1 and then rapidly to 2 for amplitudes greater than 130°. It is interesting to note that, even increasing the amplitude of the perturbation, the 2-spike response has the greater chance of being produced for higher amplitude perturbation. We also note that the distribution becomes wider, so that even 8- or 9-spike responses can be visible.

Finally the bottom panel displays an example of a multipulse response, which is overlaid on a background that reflects a two-dimentional histogram of the many possible responses of the system for the total of 3800 perturbations applied.

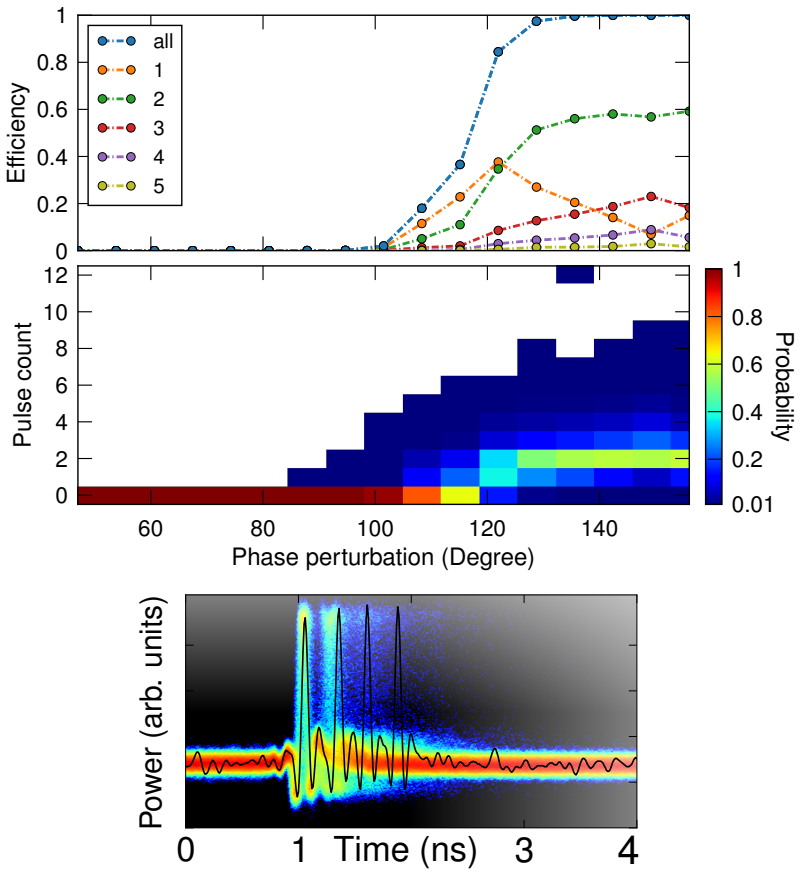

Figure 2.27: Multipulse response obtained when applying strong perturbations outside the integrator regime, constructed from 3800 perturbations. *(Top)* Efficiency curves for the generation of 0, 1, ... up to 5 spikes given a single step-up phase-perturbation of different amplitude. *(Middle)* Probability histogram of the number of responses that can be generated for a given amplitude. *(Bottom)* Example of a multiple response, overlaid over a background that display a two-dimensional histogram of all of the possible responses of the system. Note that larger perturbations cause larger number of spikes, but there is a clear stochastic component in the phenomenon. Beyond 140° all perturbations elicit a response but already at 120 ° the double-spike response is the most probable one.

2.4 Analytical and numerical study

In this section we will describe the system of the semiconductor laser with injection going beyond the simple Adler model description. In particular, we will introduce a proper model that comes from a reformulation of the Maxwell-Bloch equations, and we will make use of theoretical insight and of numerical simulations in order to explain all of the important features that were observed in the experiment, like the existence of a refractory period and the resonator property.

As we have already stated in the introduction on the laser with injection, this system has been studied theoretically intensely, both recently and in the past. While the first theoretical studies concentrated in determining the region of locking in parameter space [Petitbon 1986], especially in the plane of the injected field vs detuning (the one that we called $P_{inj} - \Delta$ plane), later studies revealed the amazingly complexity of the dynamics of the system. It was indeed shown how this system could display period doubling cascades [Lugiato 1984, Tredicce 1985, Politi 1986], quasiperiodicity [Tredicce 1985, Braza 1990], homoclinic orbits [Wieczorek 2002, Wieczorek 2005b], saddle-node bifurcations [Tredicce 1985, Politi 1986, Solari 1994], subcritical and supercritical Hopf bifurcation [Baugher 1989, Holzner 1987, Zehnlé 1992, Solari 1994] and chaos [Arecchi 1984, Brun 1985, Tredicce 1985].

In order to make sense of the effect of the different time-scales present in the system, a classification in three classes was proposed in [Tredicce 1985] Class A (fast atomic variables), Class B (fast polarization) and Class C. This and other parameters differences were exploited consistently to simplify the description of the system under study via such techniques as adiabatic elimination [Lugiato 1984, Oppo 1986], perturbative approach [Oppo 1986], multiscale analysis [Lugiato 1984] or averaging methods [Solari 1994, Jagher 1996, Krauskopf 1997, Zimmermann 2001, Mayol 2001].

In the following, we will mostly restrict our field of interest to the already mentioned [Hachair 2006, Prati 2010] model (which we will call [Prati 2010] model from now on), as in equation 2.6. We will then firstly review very quickly the most important features of this model in the next subsection 2.4.1, while in the following one we will move to the study of a simplified Class B version of this model, which is the one used in all of the numerical simulations.

2.4.1 Quick review of the [Prati 2010] model

Let us recap very briefly in this subsection the features of the [Prati 2010] model which are of most interest to us in this context. The model is the one

already described in 2.6, which we will rewrite here for convenience:

$$\begin{cases} \dfrac{\partial E}{\partial t} = \epsilon \left[E_I + P - (1 + i\theta)E + i\nabla_\perp^2 E \right] \\ \dfrac{\partial P}{\partial t} = \Gamma_D (1 + i\Delta_D) \left[(1 - i\alpha)DE - P \right] \\ \dfrac{\partial D}{\partial t} = b \left[\mu - D - \dfrac{1}{2}(EP^* + E^* P) + d\nabla_\perp^2 D \right] \end{cases} \tag{2.29}$$

We also remind the reader of the meaning of each variable:

1. $E \in \mathbb{C}$, $P \in \mathbb{C}$ and $D \in \mathbb{R}$ are the dynamical variables: E being the slowly varying envelope of the electric field, P the effective macroscopic polarization and D the normalized carrier density.
2. The physical parameters are given by (all Reals otherwise stated):
   - $E_I \in \mathbb{C}$ is the amplitude of the injected field;
   - μ is the normalized pumping current;
   - α is the linewidth enhancement factor;
   - d is the diffusion coefficient for the carriers;
   - $\Gamma_D = \Gamma(D)$ and $\Delta_D = \Delta(D)$ are two real functions of D that determine the shape of the susceptibility curve, which are set as $\Gamma(D) = 0.276 + 1.016D$ and $\Delta(D) = -\alpha + 2\delta(D)/\Gamma(D)$, where $\delta(D) = -0.169 + 0.216D$, as the best fit of gain curves calculated with a microscopic model.
   - $\theta = (\omega_C - \omega)\tau_p =$ detuning between the cavity longitudinal mode frequency and the frequency of the injected field
3. The different timescales are taken into account in the parameters:
   - $\epsilon = \tau_d/\tau_p = \kappa/\gamma_\perp$ (dephasing rate of the microscopic dipoles / photon lifetime);
   - $b = \tau_d/\tau_c = \gamma_\parallel/\gamma_\perp$ (dephasing rate of the microscopit dipoles / carrier nonradiative recombination time);

   while the time is scaled to the dephasing rate τ_d.

It will be useful for later to introduce the timescale parameter σ, defined as:

$$\sigma = \frac{\epsilon}{b} = \frac{\tau_c}{\tau_p} = \frac{\kappa}{\gamma_\parallel} \tag{2.30}$$

and it is also convenient to explicit the experimental detuning Δ, defined as the difference of frequency between the slave and the master as in Equation

2.22, by rewriting the θ parameter as:

$$\begin{aligned}\theta = \quad & (\omega_C - \omega)\tau_p = \frac{\omega_C - \omega}{\kappa} = -\frac{\omega_0 - \omega_C}{\kappa} + \frac{\omega_0 - \omega}{k} \\ & = -\alpha + \frac{2\pi\Delta}{k} = -\alpha + 2\pi\Delta\tau_p\end{aligned} \tag{2.31}$$

where we have made use of:

$$k = \frac{1}{\tau_p}, \qquad \alpha = \frac{\omega_0 - \omega_C}{\kappa}, \qquad \Delta = \frac{\omega_0 - \omega}{2\pi} \tag{2.32}$$

which are, respectively, the definition of the relaxation rate κ as in 2.9, the equation for the linewidth enhancement factor (see Section 16.5 of [Lugiato 2015] for a derivation), and the definition of the detuning. Assuming $\tau_c = 1\ ns$, we can rewrite this expression as:

$$\theta = -\alpha + \frac{2\pi\Delta'}{\sigma} \tag{2.33}$$

where Δ' is just the detuning measured in GHz.

Stationary solution The system of equations 2.29 admits a plane wave stationary solution that we will denote as $E = E_s$, $P = P_s$, $D = D_s$. This can be found by setting $\partial E/\partial t = \partial P/\partial t = \partial D/\partial t = 0$, and introducing the new notation:

$$\begin{aligned} x &\equiv |E_s|^2 \\ y &\equiv |E_I|^2 \end{aligned} \tag{2.34}$$

the equation that links the output intensity x to the input intensity y is given by:

$$y = x\left[\left(1 - \frac{\mu}{1+x}\right)^2 + \left(\theta + \frac{\alpha\mu}{1+x}\right)^2\right] \tag{2.35}$$

Figure 2.28 shows some examples of stationary solutions plotted for the parameters $\alpha = 4$, $\mu = 15$, $\sigma = 50$ at varying Δ values, which is equivalent to varying θ values. The parameters used here are the same that will be used for the numerical simulations.

This figure makes the most sense when looked sideways: given a value of y (the injected field), we can recover the corresponding value of the output intensity x that is stationary for the system. Most of these curves display an "S-shape", where given an horizontal line at a specific y value, there is more than one crossing point with the stationary curve. This means that the system is bistable, and in the case of the parameters selected here, this happens for $-315\,\text{GHz} < \Delta < 94\,\text{GHz}$. When the curve is bistable, there exists a negative slope branch which extends between two turning points x_A and x_B. Given a

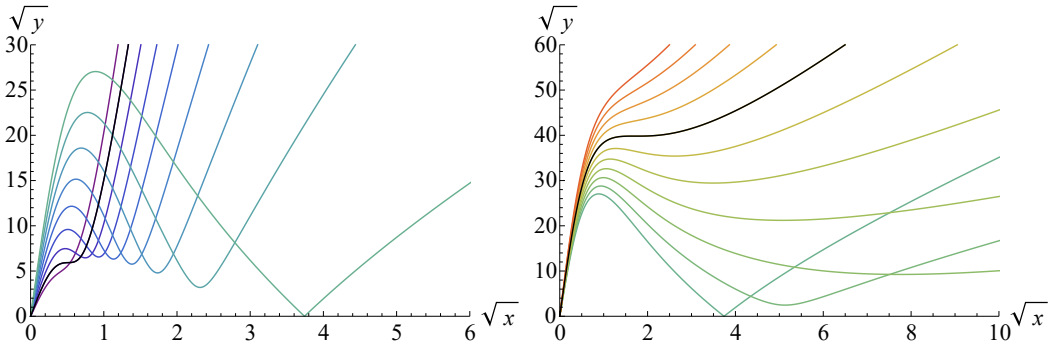

Figure 2.28: Stationary curves for $\alpha = 4$, $\mu = 15$, $\sigma = 50$, plotted for different Δ values, increasing from violet to red. The black curves represent the Δ values corresponding to the boundaries of the bistability. *(Left)* Stationary curves for negative Δ values equal to: -360, -315, -270, -225, -180, -135, -90, -45, 0 GHz. The black curve represents the value of $\Delta = -315$ GHz. *(Right)* Stationary curves for positive Δ values equal to: 0, 16, 31, 47, 63, 78, 94, 119, 125, 141, 157 GHz. The black curve represents the value of $\Delta = 94$ GHz.

value of θ, one can find the corresponding turning points coordinates with this expression:

$$\theta_{\pm}(x, \alpha, \mu) = -\frac{\mu\alpha}{(1+x)^2} \pm \frac{\sqrt{\mu^2 x^2(1+\alpha^2) - [(1+x^2) - \mu]^2}}{(1+x)^2} \tag{2.36}$$

Making use of this expression, we plot in Figure 2.29 the bistability curve for the same parameter range as Figure 2.28. Given that during the experiments we were always operating with a detuning in the range -20 GHz $< \Delta <$ 20 GHz, we observe how we are clearly well inside the bistability range.

In the [Prati 2010] paper, the authors perform a study on the Turing instability and the Hopf instability of the system, and they give analytical expressions for the results. While for the case of the Turing instability the expression that is found is the same that would be found for the simplified model that we are going to introduce, in the case of the Hopf instability the features that are found cannot be reproduced by the simplified model. In any case, we will study separately the stability of the stationary solution for the simplified model in the next subsection.

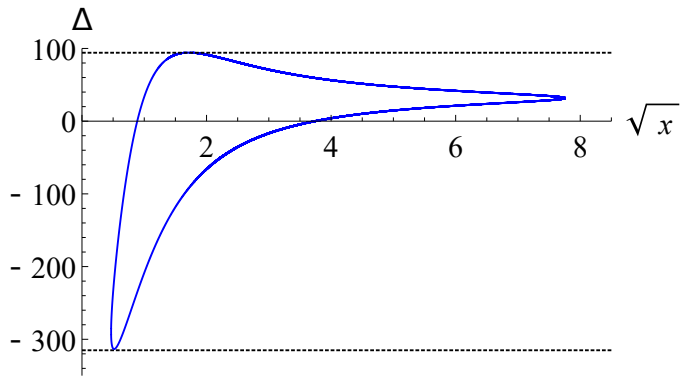

Figure 2.29: Bistability domains for $\alpha = 4$, $\mu = 15$ and $\sigma = 50$, as determined by Equation 2.36. Given these parameters, the bistability region exists for a detuning range of $-315\,\text{GHz} < \Delta < 94\,\text{GHz}$ (the range delimited by the black dashed horizontal lines).

2.4.2 Simplified Class-B [Prati 2010] model

In this subsection we will introduce the system of equations that were actually used in the numerical simulations. They are a Class-B model of a semiconductor laser with injection that comes from the standard adiabatic elimination of the P variable in the system of equation 2.29. Here we will firstly introduce the model, and then describe its dynamical features. We will also show how this system is basically equal to the ones already studied in References [Solari 1994, Tredicce 1985, Zimmermann 2001] and [Mayol 2001], and we will report some of the observations highlighted in these papers.

As shown in the [Prati 2010] paper, we can perform an adiabatic elimination of the P variable supposing that it is a fast variable (see Chapter 10 of [Lugiato 2015] for more details on the procedure), which consists of setting $\partial P/\partial t = 0$, so that the polarization is "slaved" to the other dynamical variables as:

$$P = (1 - i\alpha)DE \tag{2.37}$$

By substituting this equation back into the system, we get the simplified Class-B system:

$$\begin{cases} \dfrac{\partial E}{\partial t} = \epsilon\left[E_I + (1 - i\alpha)DE - (1 + i\theta)E + i\nabla_\perp^2 E\right] \\ \dfrac{\partial D}{\partial t} = b\left[\mu - D(1 + |E|^2) + d\nabla_\perp^2 D\right] \end{cases} \tag{2.38}$$

Some last few modifications are needed to arrive at the final form. Firstly, we will neglect the spacial terms $i\nabla_\perp^2 E$ and $d\nabla_\perp^2 D$, since in the experiment we are not measuring any spacial dependence of the field. Secondly, we introduce the new timescale τ:

$$\tau = \frac{t}{b} \tag{2.39}$$

such that, setting the dot notation to represent the derivative with respect of the new time τ, we can rewrite the simplified Class-B system as:

$$\begin{cases} \dot{\mathbb{E}} = \sigma\left[-(1+i\theta)\mathbb{E} + (1-i\alpha)D\mathbb{E} + \mathbb{E}_I\right] \\ \dot{D} = \mu - D(1+|\mathbb{E}|^2) \end{cases} \tag{2.40}$$

where we introduced the timescale parameter $\sigma = \epsilon/b$. All of the numerical simulations in this chapter will be performed using the model[8] as in Equation 2.40. Here we have changed the font of the electric fields as a blackboard bold font (*mathbb* style in LaTeX) to represent the fact that they are complex variables.

Typical parameters range The values of the parameters used in the simulation were selected so to be physically plausible and analogous to the experimental conditions. Some parameters, representing physical fixed quantities related to the system, were rarely changed, if at all. These are:

$$\begin{aligned} &\alpha = 4 && \text{(linewidth-enhancement factor)} \\ &\mu = 15 && \text{(normalized pumping current)} \\ &\sigma \equiv \frac{k}{\gamma_\parallel} = \frac{\tau_c}{\tau_p} = 50 && \text{(timescale of the system)} \end{aligned} \tag{2.41}$$

The choice of α is consistent with the experimental values that normally range from 1 to 5. For the timescale parameter σ, we suppose that the time of a non-radiative interaction is $\tau_c = 1$ ns, and that the mean lifetime of a photon inside a cavity is $\tau_p = 20$ ps. These values are coherent with [Barland 2005]. The value of the pumping current may seem high if compared to the experimental ratio J/J_{th} of the pump current to the threshold current, which is around 2-6. However, the injected current μ can be expressed in terms of the ratios J/J_{th} of the pump current to the threshold current and J_0/J_{th} of the transparency current to the threshold current as [Lugiato 2015], Equation (16.54):

$$\mu = \frac{\tilde{g}L}{T}\left(\frac{J}{J_0} - 1\right) = \eta\left(\frac{J/J_{th} - J_0/J_{th}}{J_0/J_{th}}\right) \tag{2.42}$$

where we introduced the gain-to-loss constant:

$$\eta \equiv \frac{\tilde{g}L}{T} \tag{2.43}$$

with $\tilde{g}$ the unsaturated gain per unit length, L the total length of the active region, i.e. $L = n_w L_w$ if the active region is made of n_w quantum wells of thickness L_w, and T the effective mirror transmittivity of the VCSEL, $T =$

[8] A/N: On a personal note, I'm thinking that I should tattoo this seemingly simple model on my arm as a memento of all the pain that it caused me during the last few years.

$1 - \sqrt{R_1 R_2}$, being $R_{1,2}$ the reflectivities of the two Bragg mirrors. We can estimate the value of η knowing that the VCSEL used in the experiment has $n_w = 3$ QW's of length $L_w = 80\,\text{nm}$, and the active material is $In_{0.2}Ga_{0.8}As$, for which a good estimation of the gain is $\tilde{g} \approx 2 \times 10^5\,\text{m}^{-1}$. Assuming that the effective transmissivity is $T \approx 5 \times 10^{-3}$, we obtain the gain-to-loss ratio η:

$$\eta \approx \frac{2 \times 10^5\,\text{m}^{-1} \times 3 \times 80 \times 10^{-9}\,\text{m}}{5 \times 10^{-3}} \simeq 10 \tag{2.44}$$

From the fact that $\mu = 1$ for $J = J_{th}$ we also know that:

$$\eta = \frac{J_0/J_{th}}{1 - J_0/J_{th}}, \qquad \frac{J_0}{J_{th}} = \frac{\eta}{1+\eta} \tag{2.45}$$

The second equation tells us that the value of η is connected to the value of the ratio J_0/J_{th}, so that for $\eta = 10$ we get $J_0/J_{th} = 10/11 \simeq 0.91$. Using the first equation we can also rewrite the pump as:

$$\mu = \frac{J/J_{th} - J_0/J_{th}}{1 - J_0/J_{th}} \tag{2.46}$$

so that $\mu = 15$ for the experimental value $J/J_{th} = 2.26$. This justifies the large value of μ adopted in the numerical simulations, with respect to the experimental value J/J_{th} of the injected current.

The control parameter which are most often varied are the ones that relate to the $P_{inj} - \Delta$ diagram: that is, the strength of the injected field $\mathbb{E}_I$ and the detuning parameter Δ. These were usually set so to be inside the locking region as shown in Figure 2.12, with the amplitude of the injected field which should be higher than the minimum of the stationary curve as displayed in Figure 2.31. Typical ranges are $\Delta \in [-10, 10]$ GHz and $|\mathbb{E}_I| \in [0, 1]$.

Stationary curve The stationary solution of the system 2.35 can again be calculated by setting $\dot{\mathbb{E}} = \dot{D}$. Doing so, one gets the same equation as for the stationary curve of the full model 2.29, which we report here along with the expressions for D_s:

$$\begin{aligned} y &= x\left[\left(1 - \frac{\mu}{1+x}\right)^2 + \left(\theta + \frac{\alpha\mu}{1+x}\right)^2\right] \\ x &= \frac{\mu - D_s}{D_s} \\ y &= \frac{\mu - D_s}{D_s}\left[(1-D_s)^2 + (\alpha D_s + \theta)^2\right] \end{aligned} \tag{2.47}$$

Some plots of the stationary curve in the $y-x$ plane for the range of parameters used in the simulations at different detunings are visible in Figure 2.28. The

numerical simulations will be performed for a detuning which is inside the bistability range. Given a value of the injected field which is in between the two turning points x_A and x_B, there will then be three intersection of the horizontal line at the injected field value and the stationary curve. These three points, called A, B and C, are the points around which all of the dynamics is organized. We will describe later their role and their position in the Argand plane after a study of the stability of the stationary curve.

Stability of the stationary curve Let us now analyse the stability of the stationary curve as in Equation 2.47. Here we will follow the same analysis that was already performed in the master's thesis [Dolcemascolo 2015]. A similar analysis can be found in [Tredicce 1985], where in this case the authors have derived analytical expressions in order to identify the stable and unstable branches of the stationary curve. However, we will not refer as much to this study if not for some final remarks. This is because we think that our formulation is easier to follow in this context, even though it is less general as it relies on numerics for a specific set of parameters. Furthermore, due to an approximation which is not valid in our case, the [Tredicce 1985] study fails to identify a crucial Hopf bifurcation point which is very important for the dynamics. In any case, we refer the interested reader to the [Tredicce 1985] paper for an alternative study, along with Appendix C for a "translation table" that allows to translate the results of this paper to our model.

To find the stability of the stationary curve 2.47, we first rewrite the system 2.40 by separating the real and the imaginary parts of the field:

$$\begin{cases} \dot{E}_1 = \sigma[-E_1 + \theta E_2 + (E_1 + \alpha E_2)D + E_{inj}\cos\phi_I] \\ \dot{E}_2 = \sigma[-E_2 - \theta E_1 + (E_2 - \alpha E_1)D + E_{inj}\sin\phi_I] \\ \dot{D} = \mu - D(1 + E_1^2 + E_2^2) \end{cases} \tag{2.48}$$

where $\mathbb{E} = E_1 + iE_2$ and $\mathbb{E}_I = E_{inj}e^{i\phi_I}$. The Jacobian of the system can then be written as:

$$\mathbf{J} = \begin{pmatrix} \sigma(D-1) & \sigma(\alpha D + \theta) & \sigma(E_1 + \alpha E_2) \\ -\sigma(\alpha D + \theta) & \sigma(D-1) & \sigma(E_2 - \alpha E_1) \\ -2DE_1 & -2DE_2 & -(1 + E_1^2 + E_2^2) \end{pmatrix} \tag{2.49}$$

The stability of the stationary solution is then given by the roots of the characteristic polynomial of the Jacobian matrix evaluated on the stability curve (that is, by substituting $D \to D_s$, $|\mathbb{E}|^2 \to |\mathbb{E}_s|^2 = x$), which can be written as:

$$\det(\mathbf{J} - \lambda\mathbf{I}) = \lambda^3 + c_1\lambda^2 + c_2\lambda + c_3 = 0 \tag{2.50}$$

where the three coefficients c_1, c_2 and c_3 are given by:

$$\begin{aligned} c_1 &= (1+x) + 2\sigma\left(1 - \frac{\mu}{1+x}\right) \\ c_2 &= \sigma^2\left(\frac{\mu}{1+x} - 1\right)^2 + \sigma^2\left(\frac{\alpha\mu}{1+x} + \theta\right)^2 + 2\sigma\left(1 + x - \frac{\mu}{1+x}\right) \\ c_3 &= \sigma^2\left\{(1+x)\left[\left(\frac{\mu}{1+x} - 1\right)^2 + \left(\frac{\alpha\mu}{1+x} + \theta\right)^2\right]\right. \\ &\quad \left. + \frac{2\mu x}{1+x}\left[\left(1 - \frac{\mu}{1+x}\right) - \alpha\left(\frac{\alpha\mu}{1+x} + \theta\right)\right]\right\} \end{aligned} \tag{2.51}$$

We will now find the conditions for when the stability curve is stable. According to Routh-Hurwitz stability criterion, a system with characteristic equation given by the third order polynomial $P(\lambda) = \lambda^3 + c_1\lambda^2 + c_2\lambda + c_3$ is stable (i.e. all the roots have real part less than zero) when the three following conditions are satisfied:

i) $c_1 > 0$

ii) $c_3 > 0$

iii) $c_1 c_2 - c_3 > 0$

Note that i), ii) and iii) imply $c_2 > 0$. Let us discuss them one by one in the case of the stationary solution.

i) $c_1 > 0$ If we apply this condition we get a closed inequality for x:

$$c_1(x) = (1+x) + 2\sigma\left(1 - \frac{\mu}{1+x}\right) > 0 \tag{2.52}$$

which, assuming that $\sigma > 0$ and $\mu > 0$, can be solved as:

$$-\sqrt{2\mu\sigma + \sigma^2} - \sigma - 1 < x < -1 \quad \vee \quad x > \sqrt{2\mu\sigma + \sigma^2} - \sigma - 1 \tag{2.53}$$

Since x cannot be negative, the only possible solution is:

$$x > \sqrt{2\mu\sigma + \sigma^2} - \sigma - 1 \simeq \mu - 1 \tag{2.54}$$

where the last approximation is valid whenever $\sigma >> 1$, as it is in our case. For the parameters $\sigma = 50$, $\mu = 15$, the exact condition is always satisfied for $x > 12.2$, while the approximated solution would be $x > 14$.

ii) $c_3 > 0$ It is easy to verify that the coefficient c_3 is related to the third equation of the stationary curve 2.47 by:

$$c_3 = -\frac{\sigma^2}{D_s}\frac{dy}{dD_s} \tag{2.55}$$

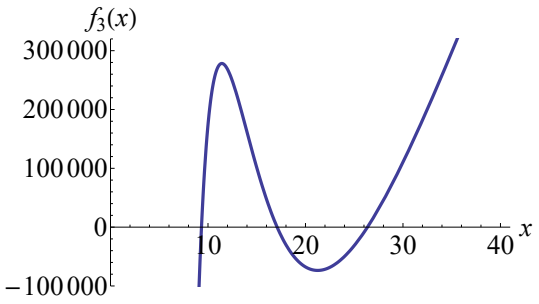

Figure 2.30: Plot of condition *iii)*, expressed as $f_3(x) > 0$, with the same parameters as in Figure 2.31. Note the intersection of the f_3 function with the x-axis at x=9.33, x=17.1 and x=26.4 which are respectively the X, W and Z points in Figure 2.31.

The second condition therefore implies that:

$$c_3 > 0 \qquad \Rightarrow \qquad \frac{dy}{dx} = \frac{dy}{dD_s}\frac{dD_s}{dx} = -\frac{\mu}{(1+x)^2}\frac{dy}{dD_s} > 0 \tag{2.56}$$

This means that when the derivative of y in the $y - x$ plane is negative (the curve is decreasing), the stationary state is unstable.

iii) $c_1c_2 - c_3 > 0$ When this condition goes from being false to being true (with $c_2 > 0$) a Hopf bifurcation will appear. This is when the real part of the eigenvalues λ of the characteristic equation goes from being negative to being positive.

In Figure 2.30 we can see a plot of the function:

$$f_3(x) \equiv c_1(x)\, c_2(x) - c_3(x) \tag{2.57}$$

for the parameters $\alpha = 4$, $\sigma = 50$, $\mu = 15$ and $\Delta = 4$ GHz (so that $\theta = -3.4973$. We can observe that the condition $f_3 > 0$ is satisfied for $9.33 < x < 17.1$ and for $x > 26.4$.

All these observations are summarized in Figure 2.31. In this Figure we have sketched the shape of the stationary curve, and we have plotted with different colors the different conditions of instability. We note that the stationary curve is unstable according to the three conditions i), ii) and iii):

i) For $|E_s|^2 < 12.2$ (green dashed line);

ii) In the negative-derivative branch (red dashed line);

iii) In the region $17.1 < |E_s|^2 < 26.4$ (blue dashed line) via a Hopf bifurcation.

We note that, even though we have truly evaluated the stability of the stationary solution only for a particular set of parameters, the observations that we have drawn remain valid in all of the set of parameters that we considered in the simulations. Furthermore, since the observations for the conditions i) and

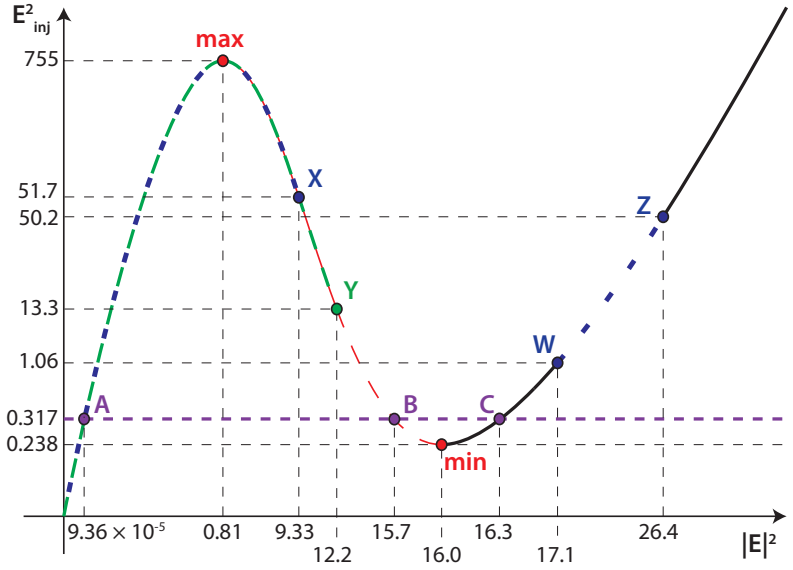

Figure 2.31: Sketch of the stationary curve, where it is shown where the curve is unstable according to the three conditions i), ii) and iii) (not to scale). The values on the $|\mathbb{E}|^2$ axis and the E_{inj}^2 axis are evaluated for the set of parameters $\alpha = 4$, $\sigma = 50$, $\mu = 15$ and $\Delta = 4$ GHz (so that $\theta = -3.4973$). Green dashed line: the curve is unstable according to i) (i.e. $f_1 < 0$). Blue dashed line: the curve is unstable according to iii) (i.e. $f_3 < 0$). Red dashed line: the derivative of the curve is negative, so that it is unstable according to ii). Black solid line: stable stationary solution. X, Y, W and Z represent the limit points of the instabilities, and A, B and C represent the intersection of the line $E_{inj}^2 = 0.317$. As we can see, for this choice of injected field C is the only stable point of the dynamics. Note that increasing the injection value to $E_{inj}^2 = 1.06$, the stable point C enters inside the Hopf instability. A numerical evidence of that is shown in Figure 2.32. Reprinted with permission from [Dolcemascolo 2015].

ii) are valid regardless of the parameters that are chosen, the only consideration that is not as general is the one regarding the Hopf bifurcation determined by the condition iii). In our particular case, the parameters for the Hopf bifurcation can be determined via a bifurcation analysis, which we will describe in the next paragraph. This study will remain valid for the set of parameters $\alpha = 4$, $\mu = 15$ and $\sigma = 50$, which have not been changed in the numerical simulations.

By comparison, in the [Tredicce 1985] paper they studied the stability of the stationary curve starting from the same characteristic polynomial as in Equation 2.50 (equation (15) of the paper) and, as in our case, they deduced that the system was unstable in the negative-derivative branch. However when studying the Hopf bifurcation, they first simplified the characteristic polynomial by assuming that $\alpha^2 << 1$ (which is not a valid approximation for our set of parameters), and then proceeded in analysing the reduced polynomial in the three branches of the stationary curve that one can obtain by cutting the sta-

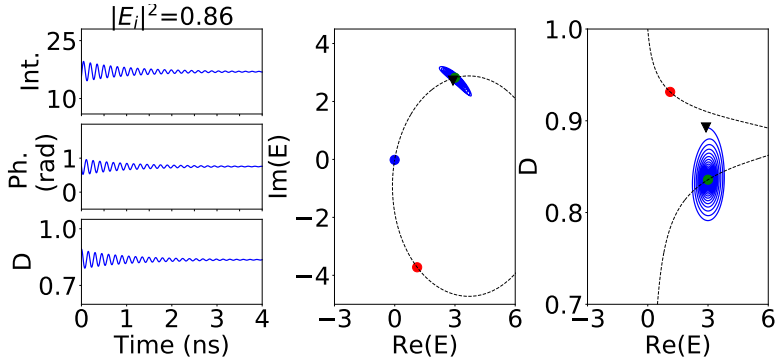

(a) E^2_{inj}=0.86, before the Hopf bifurcation

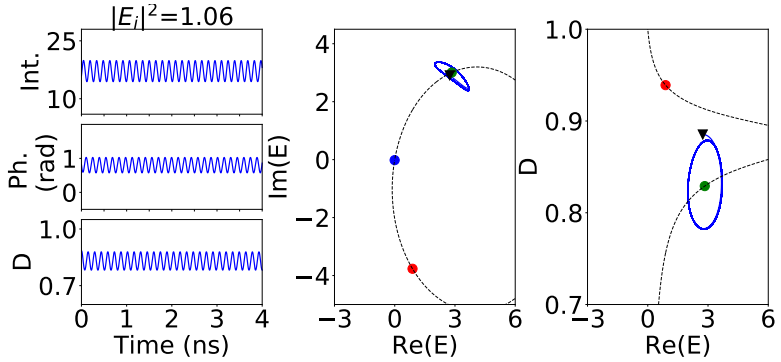

(b) E^2_{inj}=1.06, at the Hopf bifurcation

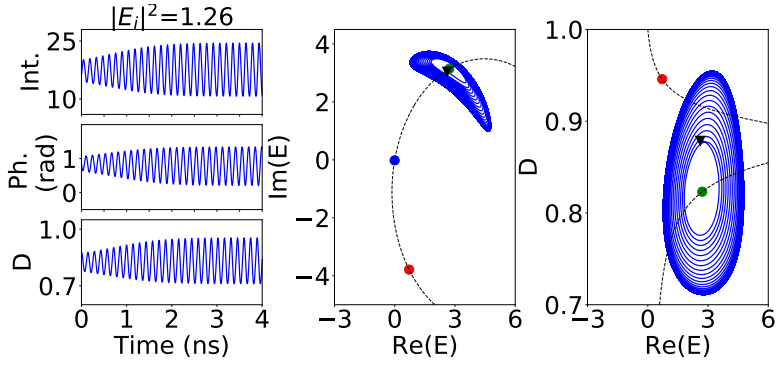

(c) E^2_{inj}=1.26, after the Hopf bifurcation

Figure 2.32: Numerical evidence of the Hopf bifurcation defined by condition *iii)*, in the same set of parameters as Figure 2.31. Each Figure (a), (b) and (c) represent a single numerical simulation, starting close to the point C of Figure 2.31, for different values of the injected field $E_{inj} = |\mathbb{E}_I|$. The blue, red and green point are respectively the A, B and C points of Figure 2.31. The black triangle represents the initial condition of the simulations. The black dashed curve is the Slow Manifold. *(Left panels)* Time evolution of the output intensity $|\mathbb{E}|^2$, the output phase, and the carriers D. *(Middle panels)* Simulation in the Argand plane. *(Right panels)* Simulation in the D-$\Re e(\mathbb{E})$ plane.

tionary curve at the turning points (the minimum and maximum points as shown in Figure 2.31). They then deduced that in the region of high output field, defined by:

$$\begin{aligned} |E_s|^2 &\gtrsim \mu - 1 \\ 0 < D_s &\lesssim 1 \end{aligned} \tag{2.58}$$

for $\mu > 2$ and small detuning, there was no Hopf bifurcation possible. This is in contradiction with the Hopf bifurcation that was found in our study (condition *iii)*). A numerical evidence of such a bifurcation for the same set of parameters as in Figure 2.31 can be found in Figure 2.32, where we show how the stable C point (the green point in the simulations) becomes unstable when crossing the injection value of $E_{inj}^2 = 1.06$, as expected.

Bifurcation diagram in the $P_{inj} - \Delta$ plane and averaged equations As already mentioned in the section on the characterization of the VCSEL laser (section 2.3.2), it is useful both for the experimental realizations and for the numerical simulations to be able to locate oneself on the $P_{inj} - \Delta$ plane. This plane scans two of the most used control parameters, the injection strength and the detuning, and is one of the best ways to capture visually the extension of the locking region and the saddle-node bifurcation which lies at its boundary. In the case of our particular model, Figure 2.33(a) shows again the same bifurcation diagram of Figure 2.12(b), which is calculated for the parameters $\alpha = 4$, $\mu = 15$, $\sigma = 50$ using the simplified [Prati 2010] model of equation 2.40 via the Knut software [Szalai 2013]. We can observe the extension of the locking region inside the saddle-node bifurcation, and also the existence of an Hopf bifurcation which lies inside the locking region. This Hopf bifurcation corresponds to what we called condition *iii)* in the previous paragraph. As already observed, the effect of increasing the injected field strength and entering the Hopf region is to make the stable C point defined in Figure 2.31 unstable.

The dynamics of the system for different regions of this diagram has been studied intensively in [Solari 1994]. Starting from a model of a Class B laser with injection which can be transformed in the same form as our model (see Appendix D), the authors performed an averaging method on the system of the rate equations by introducing a set of slow and fast variables, and by averaging the motion over the fast variable during a full period of the fast variables. Using this procedure, they derived the two-dimensional system of equations (3.4) in the paper, which can be rewritten in terms of our parameters as:

$$\begin{cases} r' = -\dfrac{r}{2}\left(\dfrac{\mu}{\sqrt{\sigma}} + \mathbb{K}\dfrac{\sin(\psi + 2\beta)}{\sin\beta}\right) \\ \psi' = -\dfrac{2\pi\Delta'}{\sqrt{\sigma}} - \mathbb{K}\dfrac{\cos(\psi)}{\sin\beta} - \mathbb{K}\dfrac{r^2}{4\sin^3\beta}\left(\cos\psi - 2\cos(\psi + 2\beta)\right) \end{cases} \tag{2.59}$$

with errors of order $O(r^3, \mathbb{K}^2, 1/\sigma)$, where the time in this case is measured in

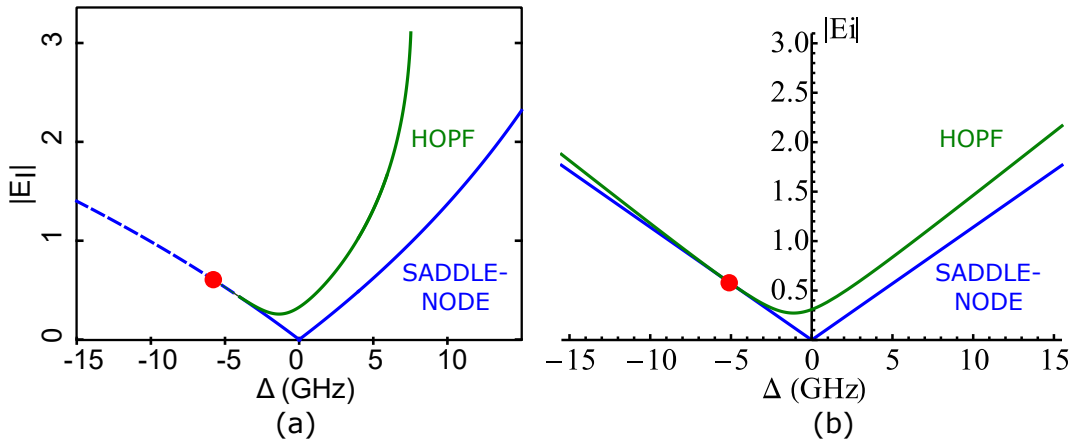

Figure 2.33: Numerical and analytical bifurcation diagrams of principal codimension one bifurcations for the simplified [Prati 2010] model as in Equation 2.40. Both diagrams are calculated for $\alpha = 4$, $\mu = 15$, $\sigma = 50$. *(a)* Numerical bifurcation diagram, evaluated using the Knut software [Szalai 2013]. *(b)* Analytical bifurcation diagram, evaluated using expression 2.64 for the saddle-node boundary and expression 2.65 for the Hopf bifurcation line. The red point when the two curves meet corresponds to a codimension two Hopf-saddle-node point, whose coordinates are given by 2.66.

units of time τ equal to:

$$\tau = \sqrt{\frac{1+\alpha^2}{\gamma_{\parallel}}\left(\frac{1}{\kappa}+\frac{1}{\gamma_{\perp}}\right)} \tag{2.60}$$

r is a new dynamical variable which describe the evolution of the slow envelopes of the V, U variables as:

$$\begin{aligned} V(t) &= r(t)\cos(\zeta) \\ U(t) &= r(t)\sin(\zeta) \end{aligned} \tag{2.61}$$

where $\zeta(t) = \sqrt{2(\mu-1)}\,t$ is the fast variable which disappears after the averaging procedure during a full period $2\pi/\sqrt{2(\mu-1)}$, and V, U are related to the old dynamical variables $\mathbb{E}, D$ of the system 2.40 by the change of coordinates:

$$\begin{aligned} \ln\left(\frac{\rho}{\sqrt{\mu-1}}\right) &= V - \frac{V^2}{3} - \frac{2}{3}U^2 \\ D &= \sqrt{\frac{2(\mu-1)}{\sigma}}\left(U + \frac{2}{3}UV\right) + 1 \\ \phi &= \psi - \alpha\ln\left(\frac{\rho}{\sqrt{\mu-1}}\right) + \beta \end{aligned} \tag{2.62}$$

where ρ and ϕ are the amplitude and phase of the electric field (i.e. $\mathbb{E} = \rho e^{i\phi}$)

and we have introduced the new parameters[9]:

$$\begin{aligned} \mathbb{K} &\equiv \frac{\sqrt{\sigma}\,\mathbb{E}_I}{\sqrt{\mu-1}} \\ \beta &\equiv -\arctan\left(\frac{1}{\alpha}\right) \end{aligned} \tag{2.63}$$

The last equation of the system 2.62 also describe the definition of the new phase variable ψ. In the paper, the authors later analysed the bidimensional system 2.59 using bifurcation analysis. The results are strikingly similar to the numerical bifurcation analysis performed on the full system 2.40. In particular, they derived an analytical equation for the saddle-boundary in the $P_{inj} - \Delta$ plane (equation (3.10) of the paper), which can be expressed using our parameters as:

$$|\mathbb{E}_I|^{SN}(\Delta) = \frac{2\pi|\Delta'|\sqrt{\mu-1}}{\sigma\sqrt{\alpha^2+1}} \tag{2.64}$$

and also an analytical expression for the line of the Hopf bifurcation (equation (3.11) of the paper):

$$|\mathbb{E}_I|^{H}(\Delta) = \frac{\sqrt{\mu-1}\sqrt{4\pi\Delta'\mu\sin\left(2\tan^{-1}\left(\frac{1}{\alpha}\right)\right)+4\pi^2(\Delta')^2+\mu^2}}{\sqrt{(\alpha^2+1)\,\sigma^2\cos^2\left(2\tan^{-1}\left(\frac{1}{\alpha}\right)\right)}} \tag{2.65}$$

Plotting these two conditions for the same set of parameters of the numerical bifurcation analysis of Figure 2.33(a) gives us the bifurcation diagram of Figure 2.33(b). As we can see, there is a very good qualitative agreement between the two diagrams, even though they somewhat differ quantitatively. We can attribute this difference to the effect of the averaging procedure, and to the approximations of small injection and detuning which are required for the procedure to be valid.

As visible in both diagrams, the saddle-node line and the Hopf bifurcation line are tangent on one point (the red point). This is not a coincidence but instead the evidence that the touching point corresponds to a codimension two Hopf-saddle-node bifurcation. The coordinates of this point are given by (equation

[9]One note of caution on the definition of the $\mathbb{K}$ parameter as in 2.63. In the paper [Solari 1994] the equivalent version of this parameter, written as κ, is set as $\kappa = \epsilon/A^2$ (equation (3.9) of the paper). During the conversion process to get equations 2.64 and 2.65, we have instead always set $\kappa = \epsilon/A$. Given that all of our observations, both numerical and theoretical, matches the equations here derived, and given that in the successive paper [Zimmermann 2001] they reviewed again the same bidimensional system 2.59 derived by the same procedure but setting $\kappa = \epsilon/A$, we believe that this may just be a typo in the paper [Solari 1994]. In any case, all the equations here reported should be correct for the system 2.40.

(3.12) of [Solari 1994], revisited):

$$\begin{aligned} \Delta' &= -\frac{\mu \csc\left(2\tan^{-1}\left(\frac{1}{\alpha}\right)\right)}{2\pi} \\ |\mathbb{E}_I| &= \frac{\mu\sqrt{\mu-1}\csc\left(2\tan^{-1}\left(\frac{1}{\alpha}\right)\right)}{\alpha\sigma\sqrt{\frac{1}{\alpha^2}+1}} \end{aligned} \tag{2.66}$$

The dynamics is organized around this point, in such a way that by turning around it one can experience many different flow types and attractors. The type of flows that one can obtain are different depending on the sign of α:

- For $\alpha < -\sqrt{3}$, the codimension two bifurcation will be of type II;
- For $-\sqrt{3} < \alpha < -1$, the codimension two bifurcation will be of type I;
- For $\alpha > -1$, the codimension two bifurcation will be of type III;

The study of the different flow type and attractors that one can experience is well explained in the rest of the paper. In our case, since we have a positive value of α, the flow will be of type II as in Figure 2 of the paper. In particular, as we will consider a set of parameters which is inside the locking region but outside the Hopf region, the flow type will be as in region A, where the attractor is a fixed point born in a saddle-node bifurcation with a companion saddle. We will describe more in detail the flow type of our system when describing the position of the three fixed points A, B and C in the Argand plane.

The system of averaged equations 2.59 has been further studied numerically in [Mayol 2001]. This study shows the complexity that can arise from this system, and describes the existence of a secondary Hopf bifurcation to a transversal and longitudinal periodic orbit, homoclinic orbits to the "off"-state of the laser, period doublings and other types of Hopf bifurcations. In our case, the main two bifurcations shown in Figure 2.33 will suffice to explain the dynamics.

Relaxation oscillations When the system is close to the Hopf bifurcation, but still in the stable locking region, the C point will still be stable, and the system will relax towards it with damped oscillation, as shown in Figure 2.32(a). Note that these oscillations, even though they are called "relaxation oscillations" in laser physics, do not show the typical features of what are called "relaxation oscillations" in slow-fast relaxation oscillators. See Appendix B for a discussion on the terminology. The damping rate and frequency of these oscillations at the steady-state solution (point C) for a Class B laser (so that $\kappa >> \gamma_\parallel$) have been derived in the [Tredicce 1985] paper in both the case of a Class B laser and in the case of a Class B laser with injection. Written in terms of our parameters, the dumping rate Γ_{RO} and the frequency Ω_{RO} are

given by:

$$\begin{aligned}\Gamma_{RO} &= \frac{\gamma_{\parallel}\mu}{2} = \frac{\mu}{2\tau_c} \\ \Omega_{RO} &= \sqrt{2\kappa\gamma_{\parallel}(\mu-1)} = \sqrt{\frac{2\sigma}{\tau_c^2}(\mu-1)}\end{aligned} \tag{2.67}$$

while adding the injection term, the expression for the relaxation frequency is modified as:

$$\begin{aligned}\Omega_{RO}^{I} = \quad & \sqrt{2\kappa\gamma_{\parallel}(\mu-1)+\kappa^2(\theta+\alpha)^2} \\ & \sqrt{\frac{2\sigma}{\tau_c^2}(\mu-1)+\frac{(2\pi\Delta')^2}{\tau_c^2}}\end{aligned} \tag{2.68}$$

where we have made use of the fact that $\kappa\gamma_{\parallel} = 1/(\tau_c\tau_p) = \sigma/\tau_c^2$, $\kappa = \sigma/\tau_c$ and Equation 2.33. The dumping rate Γ_{RO}^{I} for the laser with injection is the same as without injection Γ_{RO}.

By comparing Equations 2.67 and 2.68, we notice that the effect of adding an injected field is that of increasing the oscillation frequency, no matter the sign of the detuning. Since in our range of parameters $2\sigma(\mu-1) > (2\pi\Delta')^2$, the additional term for the injection can be considered as a (not insignificant) perturbation term to the frequency without injection. To make an example, for the parameters used in Figure 2.32, the values of Γ_{RO}, Ω_{RO} and Ω_{RO}^{I} (assuming that $\tau_c = 1$ ns) are:

$$\begin{aligned}\Gamma_{RO} &= \quad 7.5 \text{ ns}^{-1} \\ \Omega_{RO} &= \quad 37.41 \text{ ns}^{-1} \\ \Omega_{RO}^{I} &= \quad 45.07 \text{ ns}^{-1}\end{aligned} \tag{2.69}$$

It's clear that since $\Omega_{RO}, \Omega_{RO}^{I} > \Gamma_{RO}$ the oscillations undergo a slow damping, and the period of the relaxation oscillation is equal to $T_{RO} = 2\pi/\Omega_{RO} = 0.17$ ns without injection and to $T_{RO}^{I} = 2\pi/\Omega_{RO}^{I} = 0.14$ ns when considering the injection term, which is consistent with the oscillation period of $T = 0.14$ ns observed numerically.

An extensive analysis of the dumping rate of the relaxation oscillations along with numerical and experimental evidence can be found in [Kelleher 2012b]. It is shown how the dumping is modified through a nonlinear term so that it displays a higher dumping in the positive detuning side of the $P_{inj} - \Delta$ diagram as in Figure 2.33 and a lower dumping for similar level of detuning but on the negative side. The experiments and numerical simulations are performed at the positive-detuning side, so that the dumping will be relatively high and we do not see more that 4-5 oscillations following the spike in intensity.

Argand plane portrait As stated before, when we choose an injection value which is inside the bistability region and close to the turning point at the edge of the high output power branch, we obtain three fixed stationary points A, B

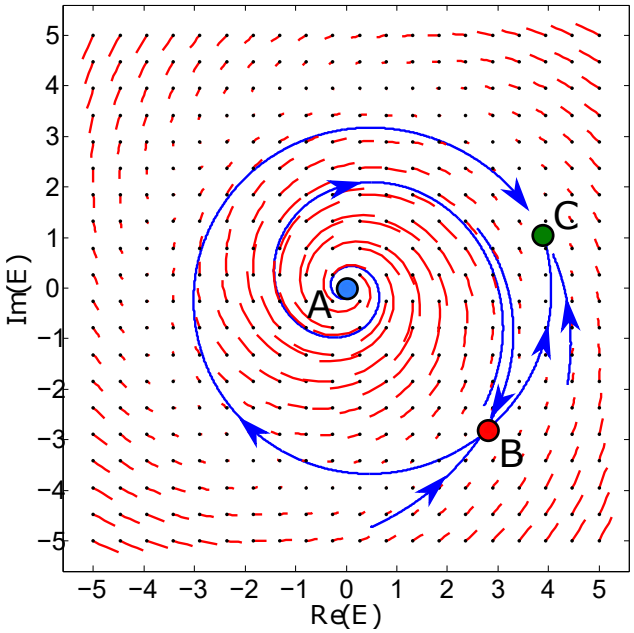

Figure 2.34: Argand plane portrait of the flow types and attractors. A is an ustable focus, B is a saddle and C is a stable node. Each small black point represents the initial condition of a numerical simulation, which has been let evolve for a small amount of time (the same for every point) on the plane $D = 1$. The red lines represent the simulations starting at those point. Same parameters as in Figure 2.31.

and C as described in Figure 2.31. Point A and B are always unstable, while point C is stable until the injection power is high enough to enter inside the Hopf region. It can be useful to visualize the position of these three points in the Argand plane, as the dynamics is organized around them.

Figure 2.34 shows a portrait of the flow type in the same parameter range as Figure 2.31. We have also plotted here the position of the stationary points A, B and C on the same plot. The phases of the three points can be calculated using the expression:

$$\phi_I - \phi_s = \text{atan2}\left(\theta + \frac{\alpha\mu}{1+|\mathbb{E}_s|^2}, 1 - \frac{\mu}{1+|\mathbb{E}_s|^2}\right) \tag{2.70}$$

where we have written the fields in polar coordinates as $\mathbb{E}_s = |\mathbb{E}_s|e^{i\phi_s}$ and $\mathbb{E}_I = E_{inj}e^{i\phi_I}$, which comes directly from the first equation of the stationary system 2.47. Atan2 is the four-quadrant inverse tangent that produces results in the range $[-\pi, \pi]$ that can be expressed in terms of the standard arctan

function with range $(-\pi/2, \pi/2)$ as follows:

$$\text{atan2}(y,x) \equiv \begin{cases} \arctan(y/x) & x > 0 \\ \arctan(y/x) + \pi & y \geq 0, x < 0 \\ \arctan(y/x) - \pi & y < 0, x < 0 \\ +\pi/2 & y > 0, x = 0 \\ -\pi/2 & y < 0, x = 0 \\ \text{undefined} & y = 0, x = 0 \end{cases} \tag{2.71}$$

The A point belongs to the branch of the stationary curve of high carrier density and low output field, and has coordinates approximately equal to:

$$\begin{aligned} |\mathbb{E}_A| &\simeq 0 \\ D_A &\simeq \mu \end{aligned} \tag{2.72}$$

It acts as an unstable focus, so if the system is place near it, it will try to repel it following a spiral. In the $\Re e(\mathbb{E}) - \Im m(\mathbb{E}) - D$ phase space, this point is placed at a very high D value, and very close to the origin. In our plots, it is marked as a blue dot. Even though it lives at high D values, its effect can be felt even at lower D values, as the system will be often pushed away from the origin.

The B and C points are born from a saddle-node bifurcation on a limit cycle. The B point is the saddle, while the C point is a stable node, at least for low injection powers. They appear in the system whenever we cross the saddle-node boundary described in Figure 2.33, and they disappear again when exiting the locking region. Their output field value is close to the local minimum of the stationary curve as in Figure 2.31, so their coordinates are approximately equal to:

$$\begin{aligned} |\mathbb{E}_B| &\simeq |\mathbb{E}_C| \simeq \sqrt{\mu - 1} \\ D_B &\simeq D_C \simeq 1 \end{aligned} \tag{2.73}$$

When changing the detuning for a fixed injection value, these two points move around the limit cycle in different directions, as one might expect from a SNIC bifurcation. It is possible to find an approximate analytical formula for the angles of the points B and C as a function of the bifurcation parameter z defined as:

$$z \equiv \frac{(\alpha + \theta)\sqrt{\mu - 1}}{E_{inj}\sqrt{1 + \alpha^2}} = \left(\frac{2\pi\Delta'}{E_{inj}}\right) \frac{\sqrt{\mu - 1}}{\sigma\sqrt{\alpha^2 + 1}} \tag{2.74}$$

z represents a normalized detuning with respect to the injected power, so that the Saddle-Node bifurcation happens at $z = \pm 1$, and $-1 < z < 1$ inside the locking region. In the approximation of small injected field (which, as we will

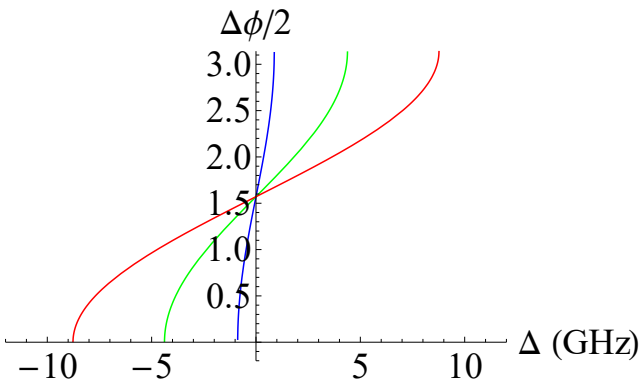

Figure 2.35: Half phase difference between the B and C points, as a function of the detuning, same parameters as Figure 2.33. The three curves are calculated for three different injection values $|\mathbb{E}_I|$ equal to 0.1, 0.5 and 1.0 respectively for the blue, green and red curve. The detuning range for each curve can be calculated with expression 2.64.

see in the last paragraph, corresponds to an Adler limit), we can write the phases of the B and C points as:

$$\phi_B \simeq \arcsin z + \arctan \alpha - \pi \tag{2.75}$$

and

$$\phi_C \simeq -\arcsin z + \arctan \alpha \tag{2.76}$$

See Appendix F for a full derivation. The half phase difference $\Delta\phi/2 = (\phi_B - \phi_C)/2$ then follows an arcsin function with argument z. By plotting it as a function of Δ for different injection values, we obtain Figure 2.35. We recognize the typical phase evolution of a stable node for a SNIC bifurcation, where the boundaries for the detuning for each injected field value are determined by Equation 2.64.

Figure 2.34 shows the position of the three points in the Argand plane, for the same parameters as in Figure 2.31. For this and future plots the B point will be marked in red and the C point will be marked in green, while the A dot will be marked in blue. We can see that in this plane the A point is very close to the origin, while the other two points B and C lie on a circle centred at zero with a radius $\simeq \sqrt{\mu - 1} = 3.74$. The C point is the only stable point. Note that the flow from B to C can be either clockwise (the long blue trajectory) or counter-clockwise (the short blue trajectory).

Another observation concerns the the rotation direction of the electric field, which we report here from [Rimoldi 2017]. When we recast the system of equa-

tions 2.40 into polar coordinates, we obtain the following system:

$$\begin{cases} \dot{\rho} = \sigma\left[\rho(D-1) + \rho_I \cos(\phi_I - \phi)\right] \\ \dot{\phi} = -\sigma\left[\theta + \alpha D - \dfrac{\rho_I}{\rho}\sin(\phi_I - \phi)\right] \\ \dot{D} = \mu - D(1+\rho^2) \end{cases} \tag{2.77}$$

where $\mathbb{E} = \rho e^{i\phi}$ and $\mathbb{E}_I = \rho_I e^{i\phi_I}$. Setting $\phi_I = 0$, we get the following equation for the phase of the output field:

$$\dot{\phi} = -\sigma\left[\theta + \alpha D + \frac{\rho_I}{\rho}\sin(\phi)\right] \tag{2.78}$$

which is an Adler-like equation as in 2.2. The ratio ρ_I/ρ in front of the sine is usually small, because of the A point near the origin that acts as a repeller. Then the dominant therm is $\theta + \alpha D$, so that we can mark the boundary when this term goes from negative to positive, which is correlated with the rotation direction that the field will follow. We can then define the critical value of $D_c = -\theta/\alpha$, which in our case is $D = 0.87$. Furthermore, if the D variable is fast enough to follow the electric field, we can also define a critical amplitude of the electric field through the stationary solution as $D_c = \mu/(1+\rho_C^2)$, which in our case gives $\rho_c = 4.02$. This is coherent with the flow plotted in Figure 2.34. We can observe that, for the black points that are outside a circle of radius approximately equal to 4, the rotation direction changes from clockwise to anticlockwise. In this study however we will not concern ourselves too much about the rotation direction of the field, as all of the excitable response will happen at D values greater than D_c, and they will all follow a clockwise trajectory which corresponds to a negative phase slip.

Slow Manifold The system of equations 2.40 is composed of two equations which in general can have two very different timescales. It is possible to exploit this difference in order to simplify the system by rewriting our model as a slow-fast system:

$$\begin{cases} \dot{\mathbb{E}} = -(1+i\theta)\mathbb{E} + (1-i\alpha)D\mathbb{E} + \mathbb{E}_I \equiv f(\mathbb{E}, D) \\ \dot{D} = \epsilon\left[\mu - D(1+|\mathbb{E}|^2)\right] \equiv g(\mathbb{E}, D, \epsilon) \end{cases} \tag{2.79}$$

where $\epsilon \equiv 1/\sigma = 0.02$ is a small parameter with our choice of parameters, and the dot derivatives now represents the derivatives with respect to the fast time $s = t/\epsilon$. In particular, it is known from Geometric Singular Perturbation Theory [Fenichel 1979, Berglund 2006], that whenever the slow manifold is stable (i.e. all of the eivenvalues of the Jacobian calculated on the manifold have negative real part), the system will asymptotically converge toward the

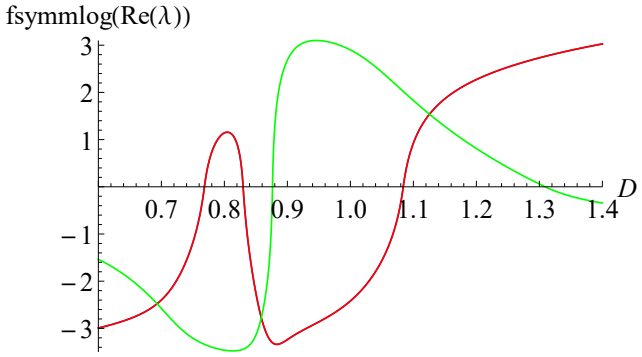

Figure 2.36: Numerical plot of the real parts of the eigenvalues along the slow manifold as in Equation 2.80 as a function of D for the same parameters as Figure 2.37. Two of the three eigenvalues are superimposed. Note that the points where the manifold changes stability occur at $D = 0.7684$, $D = 0.8298$ and $D = 0.8764$. fsymmlog is the function defined by $\text{fsymmlog}(x) \equiv \{\text{If } x \leq 0 : -\log(-x+1), \text{else: } \log(x+1)\}$

slow manifold. In our case, the critical manifold is defined by the parametric curve:

$$f(\mathbb{E}, D) = 0 \quad \rightarrow \quad \mathbb{E}(D) = \frac{\mathbb{E}_I}{(1+i\theta) - (1-i\alpha)D}\,, \tag{2.80}$$

The critical manifold here expressed can be considered as a zero-th order approximation in ϵ of the slow manifold, so in the following we will consider this expression as the one defining the slow manifold. For our usual choice of parameters, the slow manifold has the shape of a string going from negative values of D towards positive values of D close to the origin, that develops a circular loop for $D \simeq 1$. Figure 2.37 displays both a 3D plot of the slow manifold in the $\Re e(\mathbb{E}) - \Im m(\mathbb{E}) - D$ space, and in the Argand plane.

Although the slow manifold is usually used in slow fast systems as a way to simplify the dynamics to a lower dimensionality, the same cannot be realized in our case. This is because it is mostly unstable, and the regions where it is stable (as for low D values) are far from the stable C point, which is were most of the dynamics takes place. In any case, it will be useful to plot this structure in the numerical simulation firstly because of its relationship with the fixed points A, B and C, as all of the points have to lie on the slow manifold ($f(\mathbb{E}, D) = 0$ implies that $\dot{\mathbb{E}} = 0$); and secondly because, in the region were it is stable as near the stable point, the system will try to converge towards it possibly following some relaxation oscillations.

When plotting the slow manifold, its stability will be calculated numerically by calculating the Jacobian of the system as in equation 2.49 on the critical manifold, and then observing when the real parts of the eigenvalues are positive or negative. Figure 2.36 represent such a study for the same parameters as Figure 2.37. This stability analysis can then be directly translated to the slow manifold as, for small ϵ, the slow manifold will be stable provided that the

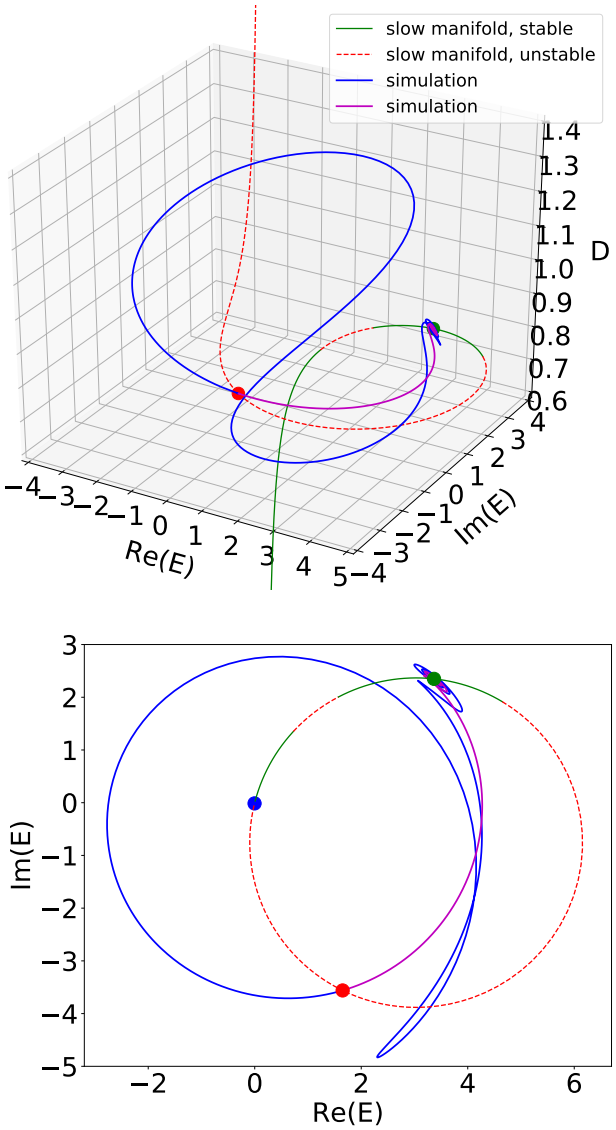

Figure 2.37: Slow manifold and two numerical simulations without noise, starting close to the B saddle point (red point in the Figure). The parameters are $\alpha = 4$, $\sigma = 50$, $\mu = 15$ as usual, and $\Delta = 4.2$ GHz, $|\mathbb{E}_I| = 0.8$. The blue simulation represents the phase excursion of an excitable response, while the magenta simulation represents the linear relaxation towards the stable C point (green point). The slow manifold is unstable whenever it's red dashed, according to the observations of Figure 2.36. *(top)* Plot in the 3D $\Re e(\mathbb{E}) - \Im m(\mathbb{E}) - D$ space. *(bottom)* Plot in the Argand plane.

critical manifold is stable.

Towards the Adler model and beyond When describing the bifurcation diagram, we introduced a bidimensional system of equations 2.59 which can be derived from the Class B model 2.40 by employing an averaging procedure. In the paper [Zimmermann 2001] they performed an order-by-order analysis of the averaging procedure that results in this system, so that by including terms of increasingly higher order, one can increase the complexity of the dynamics step by step with a perturbation approach. The results are the following:

1. Retaining only the first order terms in the expansion parameters $\mathbb{K}$, $1/\sqrt{\sigma}$, U and V and then performing the averaging, one obtains a decoupled system consisting of an oscillator plus a phase equation in the form of an Adler equation:
$$\psi' = -\frac{2\pi\Delta'}{\sqrt{\sigma}} - \mathbb{K}\frac{\cos(\psi)}{\sin\beta} \tag{2.81}$$
The system displays a saddle-node bifurcation for:
$$\frac{2\pi\Delta'\sin\beta}{\sqrt{\sigma}\mathbb{K}} = \pm 1 \quad \longrightarrow \quad |\mathbb{E}_I|^{SN}(\Delta) = \frac{2\pi|\Delta'|\sqrt{\mu-1}}{\sigma\sqrt{\alpha^2+1}} \tag{2.82}$$
which is what we already knew from [Solari 1994], as in Equation 2.64. This means that, to first approximation, the dynamics of this system is equal to the Adler model. This confirms the theoretical observation in [Coullet 1998] which derived an Adler-like equation for the phase-difference of master and slave for a Class C model of a laser with injection.

2. If we include the second-order term proportional to $1/\sqrt{\sigma}$ (assuming hence $|\mathbb{E}_I| \ll \sqrt{\mu-1}/\sigma$) we obtain an equation for r as:
$$r' \approx -\frac{\mu\, r}{2\sqrt{\sigma}} \tag{2.83}$$
so that the dynamics of r goes asymptotically to $r = 0$ after a short transient, and the Adler equation describes the motion in this submanifold.

3. For injection rate of the order of $|\mathbb{E}_I| = O(\sqrt{\mu-1}/\sigma)$, one has to consider the full equation for r' as in 2.59, so that the system becomes:
$$\begin{cases} r' = -\dfrac{r}{2}\left(\dfrac{\mu}{\sqrt{\sigma}} + \mathbb{K}\dfrac{\sin(\psi+2\beta)}{\sin\beta}\right) \\ \psi' = -\dfrac{2\pi\Delta'}{\sqrt{\sigma}} - \mathbb{K}\dfrac{\cos(\psi)}{\sin\beta} \end{cases} \tag{2.84}$$
Which means that the shape of the submanifold where the dynamics take place is no more $r = 0$ and now depends on the phase ψ. The Adler equation still describes the motion in this submanifold.

4. Finally the last step of this procedure would be to include the terms up to second order in U and V and first order in $|\mathbb{E}_I|$ and $1/\sqrt{\sigma}$, recovering the full equations 2.59. Normal form analysis reveals that these terms are necessary un unfold the most important bifurcations.

Simple explicit connection with the Adler model In the previous paragraph we have shown how the averaged model as in 2.59 has a clear connection with the Adler model. Let us now try to make a simpler explicit connection between the simplified Class B model used in the simulations 2.40 and the Adler model, without requiring an averaging procedure. As far as we are aware, this observation is an original work of this thesis. As discussed in the paragraph on the Argand plane portrait, the evolution of the phase of the output field can be written as:

$$\dot{\phi} = -\sigma \left[\theta + \alpha D + \frac{\rho_I}{\rho} \sin(\phi) \right] \tag{2.85}$$

It is clear from this equation that the evolution must be Adler-like, and we will show how to derive exactly an Adler model. We will use the same approximation used in Appendix F, which consists in considering a low injected field, so that the B and C points have amplitudes approximately equal to $\rho_{B,C} \simeq \sqrt{\mu - 1}$. We also suppose that the motion happens on a circle centred on zero in the Argand plane, so that for all points $\rho \simeq \sqrt{\mu - 1}$. This requirement seems justified by looking at Figure 2.40 which shows that, for the full system with low injection, the dynamics does happen on a circle-like manifold in three dimensions[10].

Given this requirement, Equation 2.85 for the phase dynamics of the field can be written as:

$$\left(\frac{\sqrt{\mu - 1}}{\sigma E_{inj}} \right) \dot{\phi} = -\frac{\sqrt{\mu - 1}(\theta + \alpha D)}{E_{inj}} - \sin(\phi) \tag{2.86}$$

where we have just renamed $\rho_I = E_{inj}$. Now, we will use an ansatz on the possible form of the Adler equation resulting from this phase equation. The Adler model should be of the form:

$$\dot{\phi} \sim -z - \sin\left(\phi - \arctan \alpha\right) \tag{2.87}$$

apart from global factors that can be taken into account in the time evolution. This is because we know that the Saddle-Node bifurcation parameter is the variable z defined as:

$$z \equiv \frac{(\alpha + \theta)\sqrt{\mu - 1}}{E_{inj}\sqrt{1 + \alpha^2}} = \left(\frac{2\pi \Delta'}{E_{inj}} \right) \frac{\sqrt{\mu - 1}}{\sigma \sqrt{\alpha^2 + 1}} \tag{2.88}$$

so that with this choice the bifurcation would happen at $z = \pm 1$, as expected. Furthermore, from Appendix F we know that, in the same limit of small injected field, the phases of the B and C points can be written as:

$$\begin{aligned} \phi_B &= \arcsin z + \arctan \alpha - \pi \\ \phi_C &= -\arcsin z + \arctan \alpha \end{aligned} \tag{2.89}$$

[10] Apart in the first row, where the evolution is not as linear. We think this is an effect of the initial conditions, which were chosen with a D value equal to the B (red) point, but slightly shifted in phase.

which means that the frame of reference of the phases is shifted by $\arctan\alpha$, in the sense that the B, C pair is born and dies at angles $\arctan\alpha - \pi/2$ and $\arctan\alpha + \pi/2$. This suggests that the final Adler model should be of the form 2.87. We will also suppose that the dynamics of the D variable only depends on the phase ϕ, and that it will be sinusoidal, as is it a projection of an Adler motion in 3D. We will come back on this assumption later. For the moment, let assume that:

$$D(\phi) = \mathsf{A}\cos\phi + \mathsf{B} \tag{2.90}$$

Putting together Equation 2.86 with the ansatz 2.87, we obtain the following equation that has to be satisfied:

$$-\frac{\sqrt{\mu-1}(\theta+\alpha D(\phi))}{E_{inj}} - \sin(\phi) = \mathsf{C}\left[-z - \sin\left(\phi - \arctan\alpha\right)\right] \tag{2.91}$$

where A, B and C are constants to be determined. By simplifying the right sinus function as:

$$\sin\left(\phi - \arctan\alpha\right) = \frac{1}{\sqrt{\alpha^2+1}}\sin\phi - \frac{\alpha}{\sqrt{\alpha^2+1}}\cos\phi \tag{2.92}$$

and replacing the expression for z and $D(\phi)$, one can easily find that this equation can be satisfied if:

$$\begin{aligned} \mathsf{A} &= -\frac{E_{inj}}{\sqrt{\mu-1}} \\ \mathsf{B} &= 1 \\ \mathsf{C} &= \sqrt{\alpha^2+1} \end{aligned} \tag{2.93}$$

which means that the equation for the phase 2.85 can be written as the Adler model:

$$\left(\frac{\sqrt{\mu-1}}{\sigma E_{inj}\sqrt{\alpha^2+1}}\right)\dot{\phi} = -z - \sin\left(\phi - \arctan\alpha\right) \tag{2.94}$$

as long as we can consider ρ to remain constant and equal to $\sqrt{\mu-1}$, and supposing that the evolution for the D variable is given by:

$$D(\phi) = -\frac{E_{inj}}{\sqrt{\mu-1}}\cos\phi + 1 \tag{2.95}$$

Figure 2.38 shows all of the possible locations of the saddle-node pair of the B, C points for the same parameters as the top row of Figure 2.40. It is constructed using the expressions 2.89 for the phases, and 2.95 for the related D value, at distance $\sqrt{\mu-1}$ from the origin. Notice the shape of the bifurcation, which ends at begins at the angles $-\arctan\alpha$ and $-\arctan\alpha + \pi$.

Figure 2.39 shows instead a numerical simulation using the Adler model from Equation 2.94 for the phases, and the related D value again from equation 2.95.

By comparing these simulations with the top row of Figure 2.40, we notice that, as long that we consider the Argand plane, the two types of simulations are almost indistinguishable. Only looking at the $D - |\mathbb{E}|^2$ plane one can see that, for the Adler model, the distance from the origin is fixed at $\sqrt{\mu - 1}$, while for the full model in Figure 2.40, there seems to be a clear linear-like relation between the D evolution and the $\rho^2 = |\mathbb{E}|^2$ evolution which means that the dynamics happen on a slanted deformed circle which is farther away from the origin for lower D values and closer to the origin for higher D value.

Given these observations, the equations:

$$\begin{cases} \rho &= \sqrt{\mu - 1} \\ \left(\dfrac{\sqrt{\mu - 1}}{\sigma E_{inj}\sqrt{\alpha^2 + 1}}\right)\dot{\phi} &= -z - \sin\left(\phi - \arctan\alpha\right) \\ D(\phi) &= -\dfrac{E_{inj}}{\sqrt{\mu - 1}}\cos\phi + 1 \end{cases} \tag{2.96}$$

where:

$$z = \frac{(\alpha + \theta)\sqrt{\mu - 1}}{E_{inj}\sqrt{1 + \alpha^2}} \tag{2.97}$$

can be considered as a first order analysis for the simplified [Prati 2010] model for low injection that results in the Adler model, in a very similar way to what was already done in the [Zimmermann 2001] paper in the case of the averaged equations. Also in this case, it could be interesting to extend this analysis to increasing orders, to find what are the correcting terms that further approximate the full model.

One first step could be to find what is the function $D(\phi, |\mathbb{E}|^2)$ were most of the dynamics seems to take place in Figures 2.40, thereby relaxing the condition of fixed amplitude ρ that was employed for the first order here shown. Alas, we have not managed yet to find other approximating terms of this equation, which may be a future task to be undertaken.

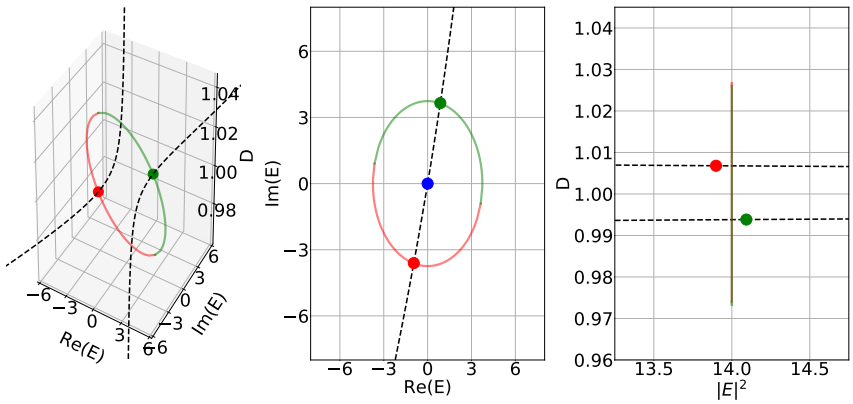

Figure 2.38: Representation of the location of the Saddle-Node pair of points B and C in the same parameters of Figure 2.40 when varying the bifurcation parameter z from -1 to $+1$, in the Adler limit. The points shown here represent the position of the B and C points for $\Delta = -0.010$ GHz, the same as the top row of Figure 2.40. Notice how the birth and death angles of the bifurcation happen at $\arctan\alpha - \pi/2$ and $\arctan\alpha + \pi/2$.

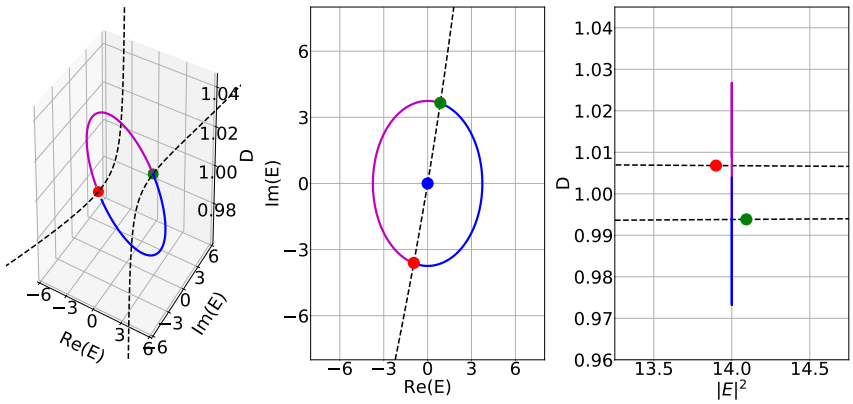

Figure 2.39: Numerical simulation of the system in the Adler limit, same parameters as the top row of Figure 2.40. The ϕ and D evolution is governed by the system 2.96. Note how in this case the distance from the origin is fixed and equal to $\sqrt{\mu - 1}$.

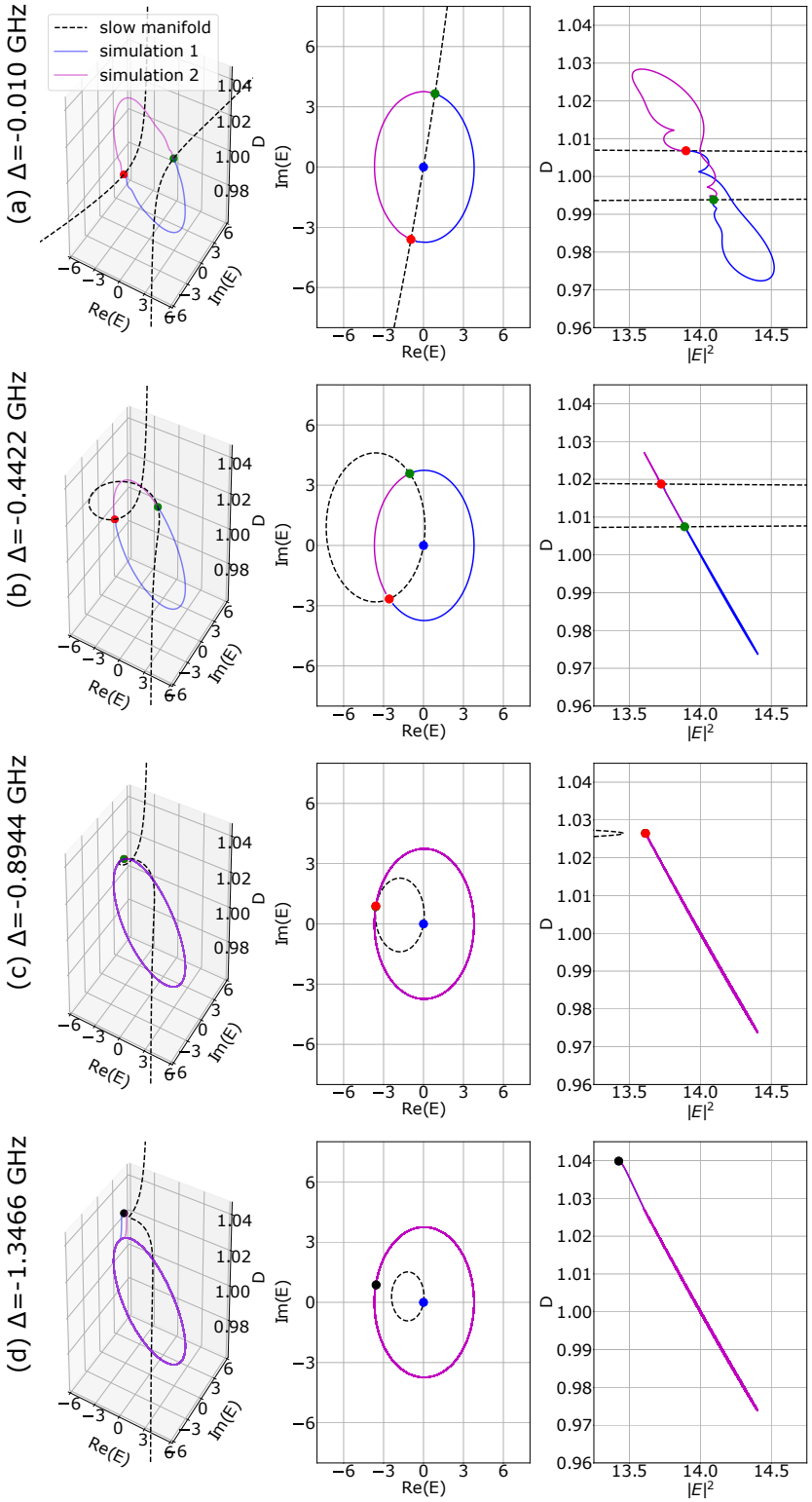

Figure 2.40: Evolution of the slow manifold and of the saddle-node pair for different Δ' values, with parameters $\alpha = 4$, $\sigma = 50$, $\mu = 15$ and $|\mathbb{E}_I| = 0.1$ (low injection), with numerical simulations of the full 2.40 model. Same type of plot as in Figure 2.37, with an added rightmost panel for the evolution in the $D - |\mathbb{E}|^2$ plane. In the last row, the black point is the start of the simulations (there are no saddle-node points).

2.4.3 Single perturbation: excitable response

In the previous section we have introduced and described in detail the model 2.40 of a Class B injected laser, and now it's time to use it for good. In this section, we will show how it is possible to trigger an excitable response from this system by applying a phase perturbation to the injected field, in exactly the same way as in the experiment.

During the description of the experiment, in Figure 2.15 we already introduced experimental phasor plots that describe the evolution of the system towards a stable point on a circle. The two points that determine the dynamics, the repeller and the attractor, can now be clearly identified with the B and C points that we described in the model section. In the experiment the plan to trigger an excitable response was the following: by letting the system converge to the stable point, and then applying a phase-perturbation capable of pushing the system over the unstable point, the system would then be forced to reach the stable point from the other direction, as shown schematically in Figure 2.3. Given that the phase excursion is not exactly circular, each excitable response will be characterized by a pulse in intensity, whose shapes can be seen in Figure 2.17.

In the following numerical simulations we will reproduce the same scheme: we will apply a phase perturbation to the phase of the injected field by modifying the first equation of system 2.40 as follows:

$$\dot{\mathbb{E}} \;=\; \sigma\left[\mathbb{E}_I e^{i\gamma(t)} + (1-i\alpha)\,D\mathbb{E} - (1+i\theta)\mathbb{E}\right] + \xi(t)\,, \tag{2.98}$$

where $\gamma(t)$ is a real function which will take the temporal shape of the perturbation (mostly step-functions and pulses), and $\xi(t)$ is a Gaussian source of noise with $\langle\xi(t)\rangle = 0$ and $\langle\xi^*(t)\xi(t')\rangle = \beta\sigma(t-t')$. We will not add any noise to the carrier variable as we have checked numerically that adding a noise term to the population inversion D is not useful for the modelling of the specific experiment, which agrees with the experimental observation that the excitable dynamics happens mostly in the phase, as demonstrated by the fact that a phase-perturbation is the most suitable type of perturbation in order to trigger a response [Garbin 2014]. Most of the figures and considerations in this section can be found in the paper [Garbin 2017a].

Step-up perturbation: efficiency and delay times The first perturbation $\gamma(t)$ we will use are step-up perturbations with different phase jump amplitudes, created using sigmoid functions with about 50 ps rise time. Two examples of such a perturbation are visible in Figure 2.42. They will mimic the same type of step-up phase perturbations used in the experiment. As observed experimentally and described in Figure 2.19, there is a threshold on the amplitude of the perturbation that is needed in order to obtain an excitable response. This can be now understood from the model as related to the phase

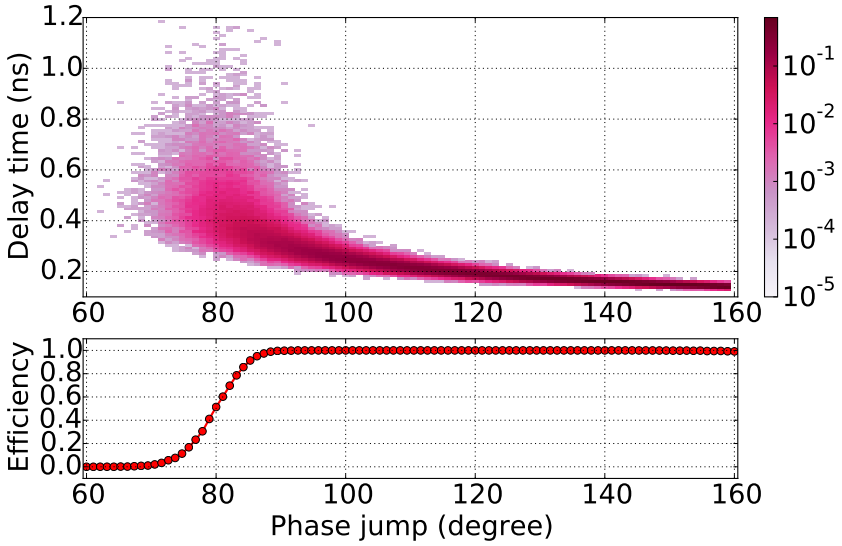

Figure 2.41: Effect of the perturbation amplitude on the efficiency for the generation of an excitable response and on the time delay between the perturbation and the excitable response, according to numerical simulations. The parameters are $\alpha = 4$, $\sigma = 50$, $\mu = 15$, $\Delta = 4$ GHz, $|\mathbb{E}_I| = \sqrt{0.317}$ (as in Figures 2.31, 2.34) and noise $\beta = 6.4 \times 10^{-3}$. *(Top)*: Delay time histogram. *(Bottom)*: Associated efficiency curve, defined as the number of excitable responses over the number of perturbations. Reprinted with permission from [Garbin 2017a].

angle between the B and C points. A perturbation which is able to push the system over the B saddle point, which represents the threshold, will trigger a response.

This is captured by Figure 2.41, which is the esperimental analogue of the experimental Figure 2.19. It is the result of 460 800 simulations with phase perturbations of different amplitudes uniformly distributed between 60° and 160°. Looking at the efficiency curve, we note that both the numerical and experimental figures jump from 0 efficiency to 100% efficiency when increasing the phase jump of the step-up perturbation, even though the threshold value, which we can define roughly as the phase jump at 50% efficiency, is about 80° in the numerical simulations and 65° in the experiment. If we now look at the delay distribution, we note how they are both greatly spread out for lower perturbation amplitudes, with a spread of around 1 ns, and then converges towards a narrow asymptotic value for large amplitudes. Here the delay is defined as the time between the middle of the rising edge of the step-up perturbation, and the maximum of the excitable response.

Figure 2.42 shows an example of 20 superimposed numerical simulations for the same parameters as Figure 2.41, in the cases of a lower-amplitude perturbation of 90° and a higher-amplitude perturbation of 160°. As we can see, while for a low amplitude perturbation the distribution of the arrival times of the excitable

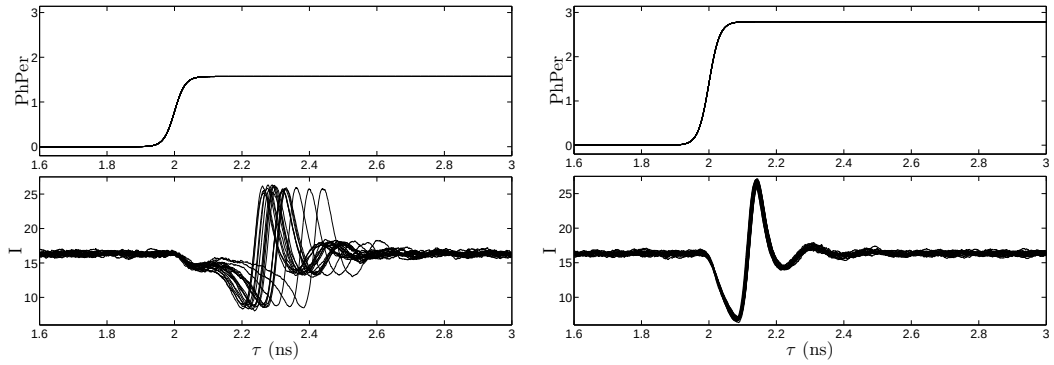

(a) Step-up perturbation amplitude of 90° (b) Step-up perturbation amplitude of 160°

Figure 2.42: Superposition of 20 excitable responses for two different step-up perturbation amplitudes. The parameters are $\alpha = 4$, $\sigma = 50$, $\mu = 15$, $\Delta = 4$ GHz and $|\mathbb{E}_I| = \sqrt{0.3172}$, with noise $\beta = 6.4 \times 10^{-3}$. *(a)* In the case of a low perturbation, the distribution of the arrival times of the impulses is broad. *(b)* In the case of a high perturbation, all the impulses are generated at almost the same time. Reprinted with permission from [Dolcemascolo 2015].

response is spread out, it is much narrower in the case of a high amplitude perturbation, so that all of the responses nicely superimpose.

We also show here Figure 2.43, which represents the superposition of 10 different excitable responses for phase amplitudes going from 90° to 160°, without noise. The different responses evolve with the amplitude of the perturbation, so that for a higher perturbation the response is faster. This is a clear feature of an excitable system, and it is interesting to note how this figure reminds us of the famous figures of the membrane action potentials at different depolarization values found in [Hodgkin 1952a].

Before passing on, we make a final remark on the definition of an excitable response in the numerical simulations: note that the detection of an excitable response in a given simulation has been performed, unlike in the experimental analysis, by setting a threshold on the phase evolution. This means that an excitable response is detected whenever there is a 2π phase slip (or approximate) between the initial condition and the final state of the simulation. This is slightly different than the experimental case, where the threshold was an amplitude threshold of suitable value on the intensity trace. We employed this different method because in the simulations we have access to the phase evolution of the output electric field, which is not the case in the experiment, and the phase-threshold detection is a clearer evidence of an excitable response that doesn't suffer as much from intensity noise.

Effect of the phase-perturbation on the A, B, C points in the Argand plane The type of dynamics that we can observe from the numerical simu-

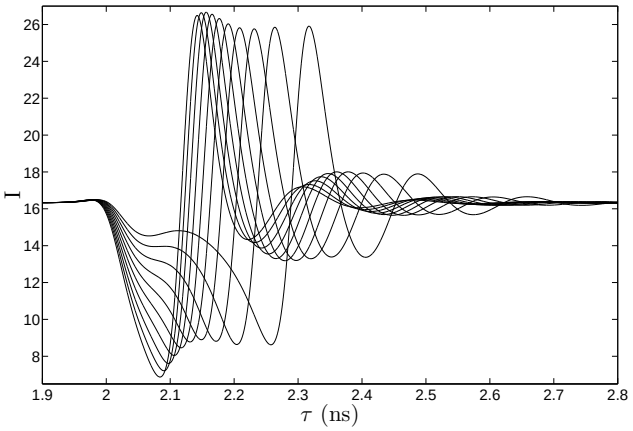

Figure 2.43: Superposition of 10 different excitable responses computed for 10 different phase amplitudes (in the case of a step-up perturbation), from a minimum of 90° to a maximum of 160°, evenly spaced. Same parameters as Figure 2.42, without noise. As the phase amplitude increases, the delay of the response from the perturbation decreases. Reprinted with permission from [Dolcemascolo 2015].

lations can be neatly interpreted by looking at the evolution of the position of the A, B, C points on the Argand plane over the course of the perturbation. The effect of the phase-perturbation on the phases of these points is to rotate them counteclockwise according to:

$$\phi_{A,B,C}(t) = \phi^0_{A,B,C} + \gamma(t) \tag{2.99}$$

where $\phi^0_{A,B,C}$ is the phase of the stationary points before the onset of the phase perturbation that one can obtain from 2.70 for $\phi_I = 0$. Given a step-up perturbation, these points will then be moved to a new position A', B' and C' at the end of the perturbation, where this position will depend on the amplitude of the phase jump.

Figure 2.44(a) shows the trajectory in the complex plane when we apply a 40° phase perturbation. During the onset of the perturbation, the three point will move toward their final position at the end of the perturbation, marked as A', B' and C' on the figure. Given that this phase jump is less than the angular difference between the B and C points, the new position of the B point (B') will happen to be in between the B and C position. This means that the system will not feel the effect of the threshold that corresponds to the saddle B point, but instead will just move from the C position to the C' position, following the movement of the stable C point. Since the motion happens along a circle, the intensity remains essentially constant as the phase jumps to the new stationary value, as shown in the lower panels of the figure. In this case, the system will not experience an excitable response.

Figure 2.44(b) shows instead the case of a higher amplitude perturbation, of 110°. In this case, this angle is greater than the angular separation between

node and saddle, and the new position of the B saddle (B') will be over (counterclockwise speaking) the C position. As the movement between the old and new positions happens faster than the system has time to follow, during its trajectory the B point will overcome the position of the system, which will be then pushed away in the other direction. This explains the "U-turn" that the red trajectory performs in between the C and B' positions in the figure. Once the new primes positions have been reached, the system will try to converge towards the new position of the stable C node (C') going clockwise, and performing in this way a phase negative phase jump. In this case, the phase jump will be lower than 2π since the new C' position doesn't coincide with the old C position. Before reaching its final destination in C', the system will perform some relaxation oscillations. This trajectory is translated in the intensity trace as an intensity pulse followed by some oscillations, with a shape mush similar to the experimental one, and with a negative phase jump for the evolution of the phase of the electric field. This is the trajectory that corresponds to an excitable response for our system given our step-up phase perturbation.

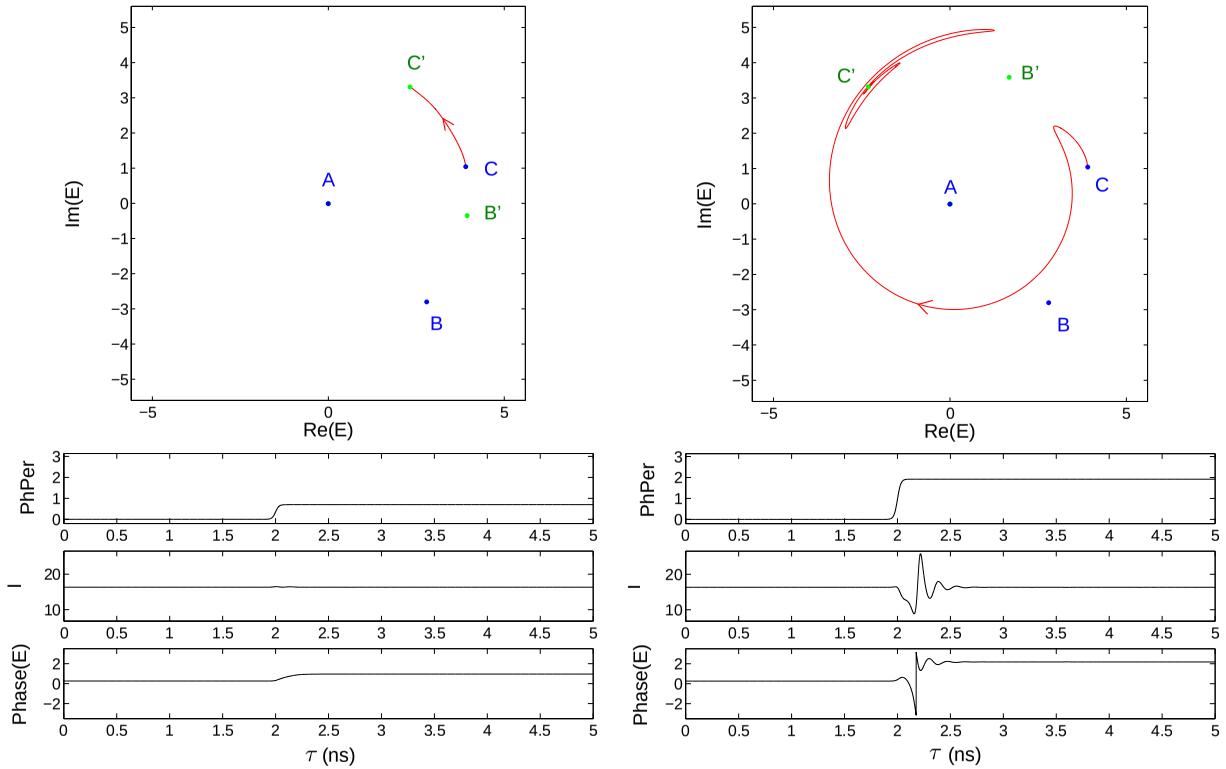

(a) Step-up perturbation with phase amplitude of 40° (b) Step-up perturbation with phase amplitude of 110°

Figure 2.44: Examples of typical numerical simulations for a step-up phase perturbation, below (a) and above (b) the excitability threshold. The parameters are $\alpha = 4$, $\sigma = 50$, $\mu = 15$, $\Delta = 4$ GHz and $|\mathbb{E}_I| = \sqrt{0.3172}$ (so that $\theta = -3.4973$) with no noise. All the simulations start from the stable point C and end at the new stable point C'. The plot of the phase space (E_1, E_2), the phase perturbation, the intensity and the phase of the field $\mathbb{E}$ are shown from top to bottom. Reprinted with permission from [Garbin 2017a].

2.4.4 Double perturbation: Refractory period

In the experimental part (see Figure 2.20) we observed the existence of a refractory period when perturbing the system with a double perturbation. This is the period of time after a first perturbation where the system cannot be excited again, and in the experiment it was found to be of the order of 0.20 ns. In the Adler model vision, this was the time that was needed to complete the excitable orbit in phase space, before coming back to the stable point. In this subsection we will describe how such a refractory period can emerge from our system following the evolution of the fixed A, B and C points in the Argand plane during the phase perturbation. By performing numerical simulations, we will observe a refractory period for our usual choice of parameters which is of the order of 0.22 ns, in accordance with the experiment.

Double perturbation: Efficiency and Response time Evidence for the refractory period was obtained by performing the same type of numerical simulations as described in the last subsection, but with a phase perturbation $\gamma(t)$ which is composed by a pulse, followed by a step up perturbation, as it was done in the experiment. The pulse is a short Gaussian impulse with 100 ps full width at half maximum and height $\Delta\phi = 150°$, while the step-up function is the same sigmoid function used before, with a fixed height of $\Delta\phi = 105°$, which is well inside the region were the efficiency reaches 100% for a single perturbation. Two examples of the phase-perturbation used are visible in the phase-perturbation time-trace panels of Figure 2.47.

Figure 2.45 is the analogue of the experimental Figure 2.20, and it shows both the efficiency curve for the generation of the second excitable response (note that the response to the first pulse perturbation is always present in all of the simulations), and the distribution of the response time, normalized to the delay time. The delay time is the time between the two perturbation, while the response time is the time between the two responses. A definition of the two times is visible in Figure 2.46. This figure is the result of 460 800 numerical simulations with noise, with a delay time spanning from 0.1 to 1.2 ns.

Looking at the efficiency, we note that, also in this case, the efficiency reaches the value of 1 for higher values of the delays, where there is no more interaction between the two perturbations. This means that, by themselves, each perturbation is capable of generating a response 100% of the time. However, when the delay between the two perturbations approaches the value of 0.22 ns, the efficiency of the generation of the second pulse goes to zero, which means that only one pulse is generated in this case. This is the effect of the refractory period which follows from the first excitable response. It is also interesting to note that the efficiency has a small bump at 0.1 ns: this is similar to what was also observed in the experimental efficiencies of Figure 2.20, and we attribute it to the effect of relaxation oscillations around the stable point after the first excitation. We will study the effect of these oscillations in more detail in the

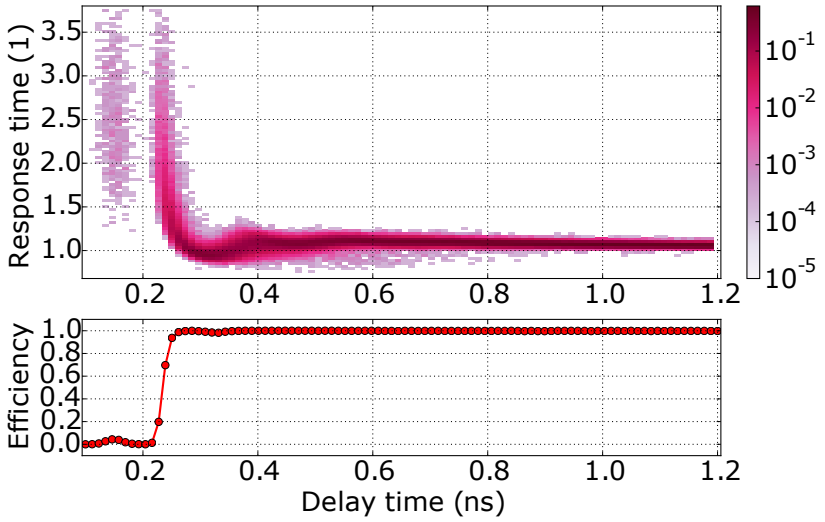

Figure 2.45: Efficiency and response time histogram of the second excitable response (the one triggered by the step-up function) varying the delay time, according to numerical simulations. The parameters are $\alpha = 4$, $\sigma = 50$, $\mu = 15$, $\Delta = 4$ GHz, $|\mathbb{E}_I| = \sqrt{0.317}$ (as in Figures 2.31, 2.34) and noise $\beta = 6.4 \times 10^{-3}$. For a delay smaller than 0.22, a refractory time is clearly visible. *(Top)*: Normalized response time histogram. The response time is normalized to the delay time. *(Bottom)*: Associated efficiency curve for the generation of the second response, defined as the number of excitable responses over the number of perturbations. Reprinted with permission from [Garbin 2017a].

next subsections.

Regarding the response time histogram, its distribution starts broad for a small delay, and then becomes narrower for larger delays, as seen experimentally. For large delays, it reaches the normalized value of 1, which means that the delay time and the response time become almost the same. It is also interesting to note that, even though the efficiency curve reaches 100% around a delay of 0.25 ns, the response time histogram actually shows some other small bumps and oscillations up to 0.4 ns, and it reaches its final asymptotic state around 0.8 ns. This is the same interaction time between two consecutive perturbations that has been inferred from the experiments.

Effect of the double-phase-perturbation on the A, B, C points in the Argand plane The existance of a refractory period can be understood from the motion of the the fixed points A, B, and C on the Argand plane due to the phase perturbation. We already demonstrated how the effect of the phase perturbation is to rotate the fixed points counterclockwise around the origin. Let us now describe in detail the two cases represented in Figure 2.47, which are calculated for a delay which is smaller (a) and larger (b) than the refractory period. We remark that in both cases, A, B, and C mark the position of the

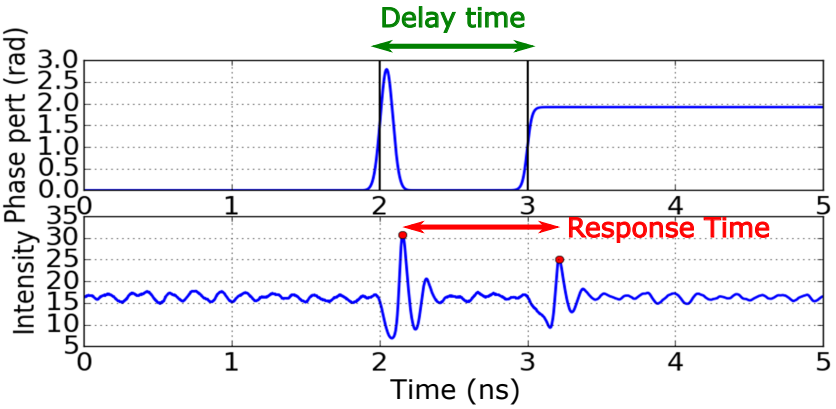

Figure 2.46: Definition of the delay time and of the response time. The delay time is the time interval between the middle of the rising edge of the pulse and the middle of the rising edge of the sigmoid function. The response time is the time interval between the two maxima of the excitable responses.

fixed points before the start of the perturbation; A'', B'' and C'' mark the position of the fixed point at the maximum of the first pulse perturbation, and A', B' and C' mark their final position at the end of the step-up perturbation. The movement of the fixed point is then as follows:

1. They start at their A,B,C position at the beginning of the simulation;
2. The first pulse perturbation moves them to the A'', B'', C'' position counterclockwise for the first half of the pulse, before going back to the A,B,C position at the end of the pulse;
3. The step-up perturbation moves them again from the A,B,C position to the final A',B',C' position counterclockwise.

The dynamics will be as follows:

- *Time delay larger than the refractory period, Figure 2.47 (b)* The dynamics in this case can be separated into two separate trajectories corresponding to the two perturbations. During the first trajectory, the system starts at the stable C point and then, as in the case of a single perturbation described before, it is overcome by the movement of the unstable B saddle which makes it make and "U-turn", followed by a clockwise excitable response which brings it back to the C point with a couple of large relaxation oscillations. Here the system rests for a few moments, before the start of the second perturbation. When it comes, the system is overcome again by the B saddle, makes a "U-turn" and performs another clockwise excitable response, ending this time at the new stable position C', following some oscillations. In this case, the two perturbations are separated enough that there is time for the system to reach the stable C point again after the first perturbation, before being perturbed again.

- *Time delay shorter than the refractory period, Figure 2.47 (a)* In this case the dynamics in the Argand plane displays only one excitable response, which brings the system from the initial C point to the final C' point. The difference in this case with respect to figure (b) is that, during the large first relaxation oscillations that follows the first excitable response, the system finds itself "captured" in between the moving saddle-node pair B,C, which escort the system to the final position C'. In this case, there is not enough time for the system to reach again the C position after the first pulse as in was in case (b).

In conclusion, the refractory time stems from the fact that the system needs some time to reach the stable point C after a first perturbation, during which it cannot be excited again with another phase perturbation.

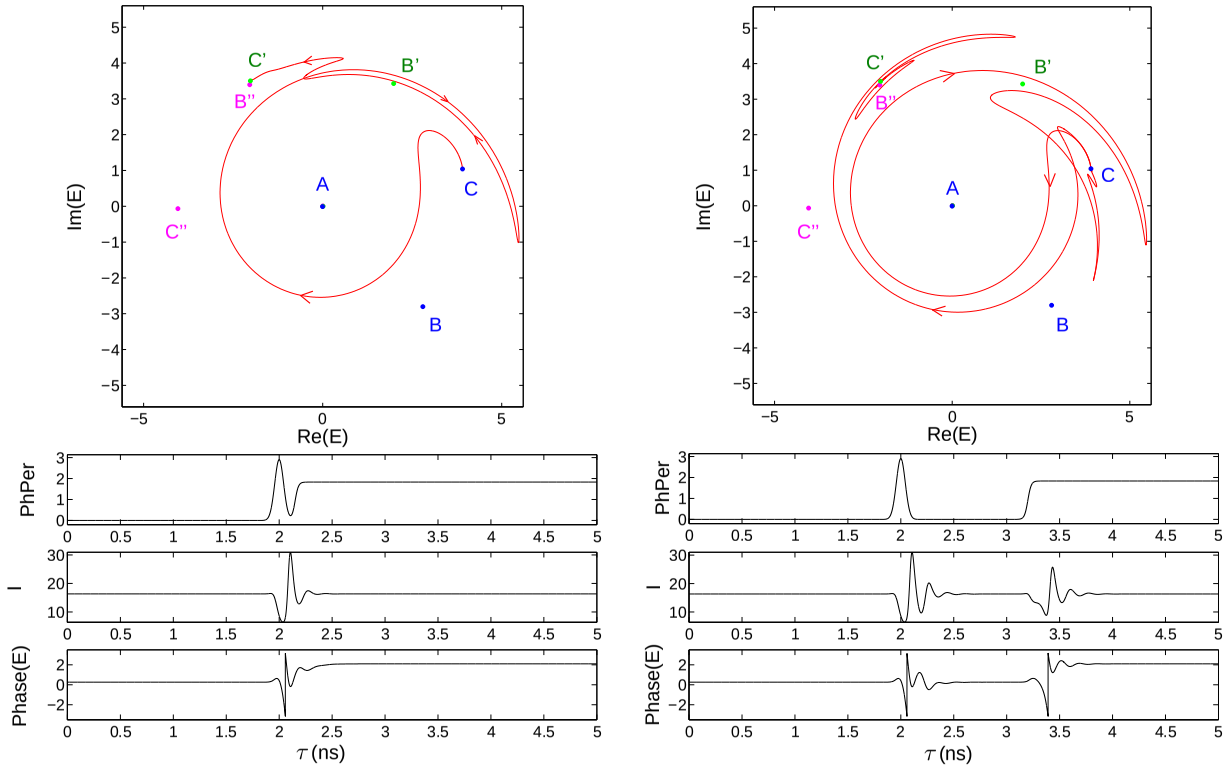

(a) Impulse and step-up perturbation with a delay of 0.15 ns.

(b) Impulse and step-up perturbation with a delay of 1.2 ns.

Figure 2.47: Examples of typical numerical simulations for an impulse plus step-up phase perturbation, below (a) and above (b) the threshold for the delay. The parameters are $\alpha = 4$, $\sigma = 50$, $\mu = 15$, $\Delta = 4$ GHz and $|\mathbb{E}_I| = \sqrt{0.3172}$ (so that $\theta = -3.4973$) with no noise. All the simulations start from the stable point C and end at the new stable point C'. The plot of the phase space (E_1, E_2), the phase perturbation, the intensity and the phase of the field $\mathbb{E}$ are shown from top to bottom.

2.4.5 Double perturbation: Resonator property

In the experimental section we described how the system, when perturbed with a double pulse perturbation under-threshold, can actually generate a single response with an efficiency that shows a maximum for a value of around 0.12 ns. We hypothesised that this resonator effect could be due to the relaxation oscillations that the system performs before reaching its stable state. In the Adler model vision, this is because if the system oscillates around the stable point, there will be times when a second perturbation would be more efficient than others, namely, when the system is oscillating towards the unstable point.

In this section we will explore more in detail the relationship between these oscillations and the resonator period by analysing in detail the dynamical properties of the simplified Class B model 2.40, and we will propose a simple *ad hoc* modification of the Adler model that displays a resonator property as observed in the experiment. By choosing the right parameter range, we can also show numerically that our system can transition from an integrator type of system (as in Class 1 type of neurons) to a resonator type of system (as in Class 2 type of neurons), which displays the resonator property. We will propose a dynamical explanation of this transition by describing the separatrix for the system, which is the surface that separated the excitable regions of phase space from the non-excitable regions.

The integration algorithm is the Euler-Maruyama method with Gaussian white noise $\langle \xi(t) \rangle = 0$, $\langle \xi(t)\xi(t-\tau) \rangle = \beta\delta(\tau)$ with $\beta = 0.01$ as the weight parameter of the random variables.

Integrator behaviour We start by choosing a range of parameters where the Adler approximation is more appropriate: that is, at lower injection values. Looking at Figure 2.48, we set $|\mathbb{E}_I| = 0.3$ and $\Delta = 2.45$ GHz, so as to be close to the saddle-node boundary at positive detuning. The result is visible in Figure 2.50.

In all of these simulations, we perturb the system with a double-pulse perturbation with a delay between the two pulses that varies from 0.2 ns to 0.8 ns, in a similar way as it was done in the experiment. The top two rows of this figure represent two different numerical simulations at two different delay times between the two pulses of the perturbation: the first row at 0.2 ns and the second row at 0.6 ns. For each simulation, the first column shows the time traces of: the phase perturbation $\gamma(t)$, the intensity of the output field $|\mathbb{E}|^2$, the phase evolution of the field, and the population inversion D; the middle column represent the trajectory in the Argand plane, and the third column the trajectory in the $D - \Re e(\mathbb{E})$ plane.

Looking at the efficiency curve we note that, for large delays, there is no excitable response in the system. This means that the two perturbations, by themselves, are underthreshold. However, when reducing the delay, the two

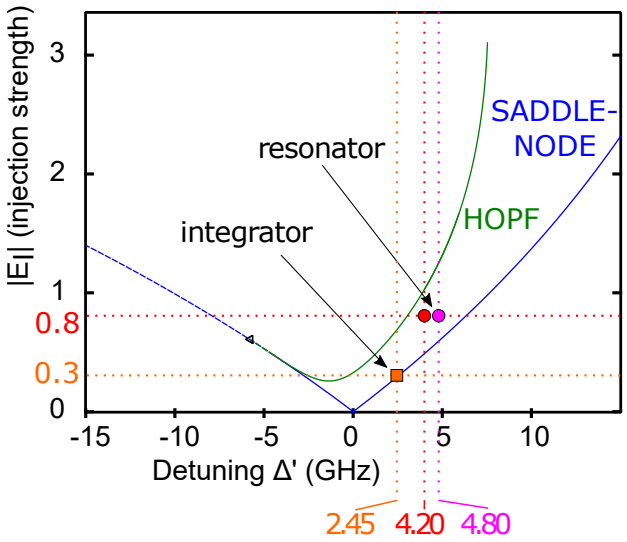

Figure 2.48: Numerical bifurcation diagram of principal codimension 1 bifurcations for the model 2.40, with $\alpha = 4$, $\sigma = 50$ and $\mu = 15$, evaluated with the Knut software [Szalai 2013]. The diagram shows a Fold-Hopf bifurcation, where a saddle-node and a Hopf bifurcation collide on a single point. The parameters for the simulations are chosen in the region in between the Hopf and SN bifurcation.

perturbations get integrated by the system, which is able to generate an excitable response, as with the first simulation with a delay of 0.2 ns. The efficiency curve increases almost monotonically from larger delays to shorter delays, which indicates that the closer the two perturbations are in time, the more efficient is the generation of the response, reaching 100% for delay shorter than 0.35 ns. This type of efficiency curve is the same that one would get from an integrate-and-fire type of neuron, and is a clear evidence of an integrator behaviour.

Since in this case the phase perturbations are two pulses, the trajectory of an excitable response in the Argand plane is that of a clockwise phase excursion which starts from the stable C point and ends at the same point after a negative 2π phase slip.

Resonator behaviour We now change the parameter range in order to excite more prominently some relaxation oscillations. To do that, we place ourselves at $|\mathbb{E}_I| = 0.3$ and $\Delta = 4.20$ or $\Delta = 4.80$ GHz, as shown in Figure 2.48, so that we are closer to the Hopf bifurcation. We perturb the system with a double-phase perturbation in exactly the same way as before. The results are visible in Figures 2.51 and 2.52.

Also in the case of $\Delta = 4.20$ (Figure 2.51), the efficiency goes to zero at larger delays, which means that the two pulse-perturbations are underthreshold by themselves. However in this case the efficiency curve shows 3 different bumps

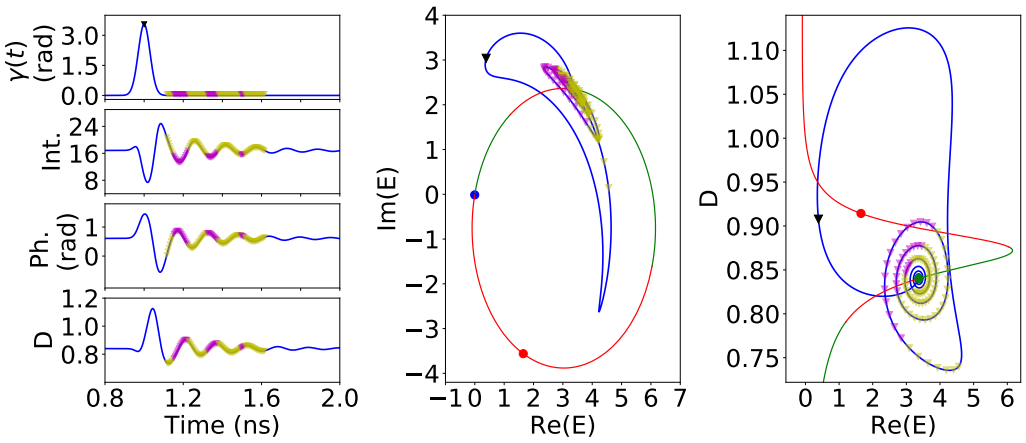

Figure 2.49: Display of the right timings that are required after the first pulse perturbation in order to trigger an excitable response, parameters as in 2.51, without noise. The magenta triangles represent the spots where a second perturbation triggered on that spot would result in an excitable response. The yellow triangles represent instead the spots where a response would not be seen. Looking at the $D-\Re e(\mathbb{E})$ plane, the magenta triangles correspond to the places where the relaxation oscillations bring the system closer to the unstable B saddle point (red point).

with centers that are equally spaced in the Delay time, with a fourth one barely visible at around 0.75 ns. The spacing between them is around 0.13-0.14 ns. If we now look at the two numerical simulations of the first two rows, we notice that, even though there is no excitable response for a smaller delay of 0.35 ns, there is an excitable response for a larger delay of 0.42. The explanation for this difference comes from the relaxation oscillations around the stable C point after the first pulse-perturbation, as visible in the Argand plane and more clearly in the $D-\Re e(\mathbb{E})$ plane. Even though the first perturbation is not enough to trigger a response, it displaces the system away from the stable C point and sets in motion some relaxation oscillations. Depending on the timing of the second pulse, the efficiency to reach the threshold either increase or decreases, which gives rise to those equally spaced bumps in the efficiency curve. To make a comparison, the period of these oscillations according to expression 2.68 should be:

$$T_{RO}^{I}=\frac{2\pi}{\Omega_{RO}^{I}}=\frac{2\pi}{\sqrt{\frac{2\sigma}{\tau_c^2}(\mu-1)+\frac{(2\pi\Delta')^2}{\tau_c^2}}}=0.137\text{ ns} \tag{2.100}$$

which is consistent with the spacing of the bumps.

Another proof that the timing to get an excitable response is related to the relaxation oscillation period comes from Figure 2.49. Here we have performed the same simulations as in Figure 2.51 (without noise in this case), and we have

marked both on the time-traces and on the phase planes with magenta triangles all of the spots where a second pulse perturbation starting on that spot would have produced an excitable response, and in yellow triangles the spots were it would not have produced a response. As visible in the time-traces, the magenta triangles seem to "ride the wave" of the relaxation oscillations, in the sense that, for instance in the phase trace, they always happen close to the peaks of the relaxation oscillations. Looking at the $D - \Re e(\mathbb{E})$ plane, we also notice that we could draw a diagonal line that separates the magenta triangles from the yellow ones, which indicates that the spots where the system is brought closer to the B saddle (red) point by the relaxation oscillation "wave", are the ones that have a higher chance of producing an excitable response.

Figure 2.52 shows the same type of study, but with a detuning parameter which is a bit farther apart from the Hopf bifurcation, as with $\Delta = 4.80$. If we look at the efficiency curve, we only notice one bump because in this case the amplitude of the relaxation oscillations doesn't allow for more than one "wave-front" for the system, using the same surfing analogy as before. However, even in this case, the fact that the efficiency starts closer to zero for smaller delays and then rises again at 100% for larger delays is the evidence of an underlying resonator effect in the system. This case is actually closer to what we can observe in the experiment, as also in that case the efficiency displayed just one efficiency bump with one maximum at a delay of around 0.12 ns.

One note on the values of the efficiency greater than one: when adding the noise in the numerical simulations, is turns out that there are cases were the system performs more than one excitable response for a single perturbation. These multipulse events can increase the efficiency since they increase the total counting of the excitable responses for a given number of perturbations. We will describe more in detail those events in subsection 2.4.6.

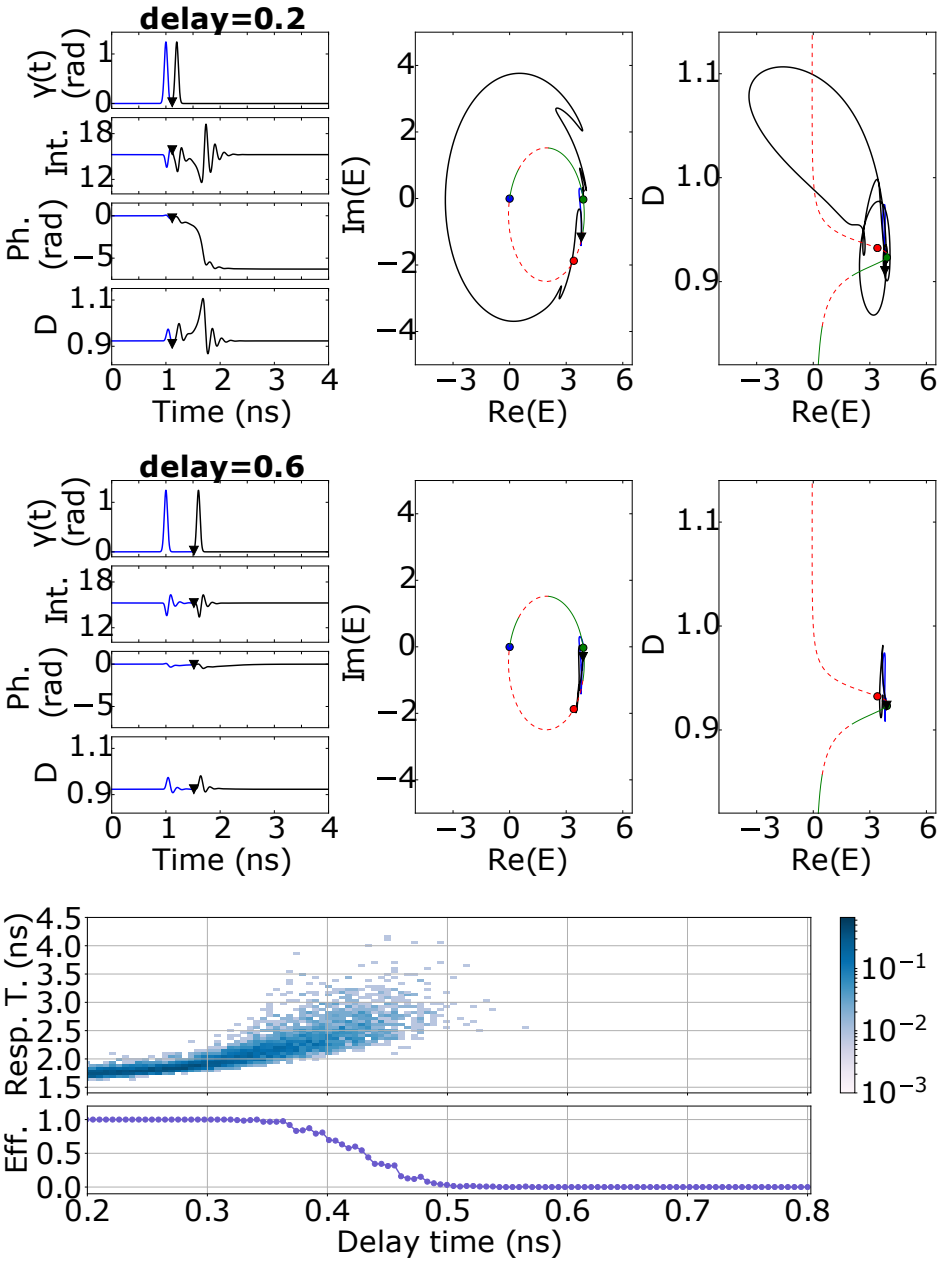

Figure 2.50: Example of an integrator behaviour, numerical simulations, with parameters $|\mathbb{E}_I| = 0.3$ and $\Delta = 2.45$ GHz (the others are as in Figure 2.48). The first two rows of figures represent two different numerical simulations at different delays (without noise), while the last row represents the efficiency curve for the generation of an excitable response, and the related response time histogram (with noise $\beta = 0.01$). For each of the two numerical simulations, the first column represents the time-traces of: the phase perturbation $\gamma(t)$, the intensity of the output field $|\mathbb{E}|^2$, the phase evolution of the field, and the population inversion D; the middle column represent the trajectory in the Argand plane, and the third column the trajectory in the $D - \Re e(\mathbb{E})$ plane (black line). The black triangle is the onset of the second perturbation, and the blue, red and green points are the A, B and C points respectively. The slow manifold is shown as a green line when stable and as a dashed red line when unstable. Note that while for a delay of 0.2 ns the system displays an excitable response, this is not the case for a delay of 0.6 ns.

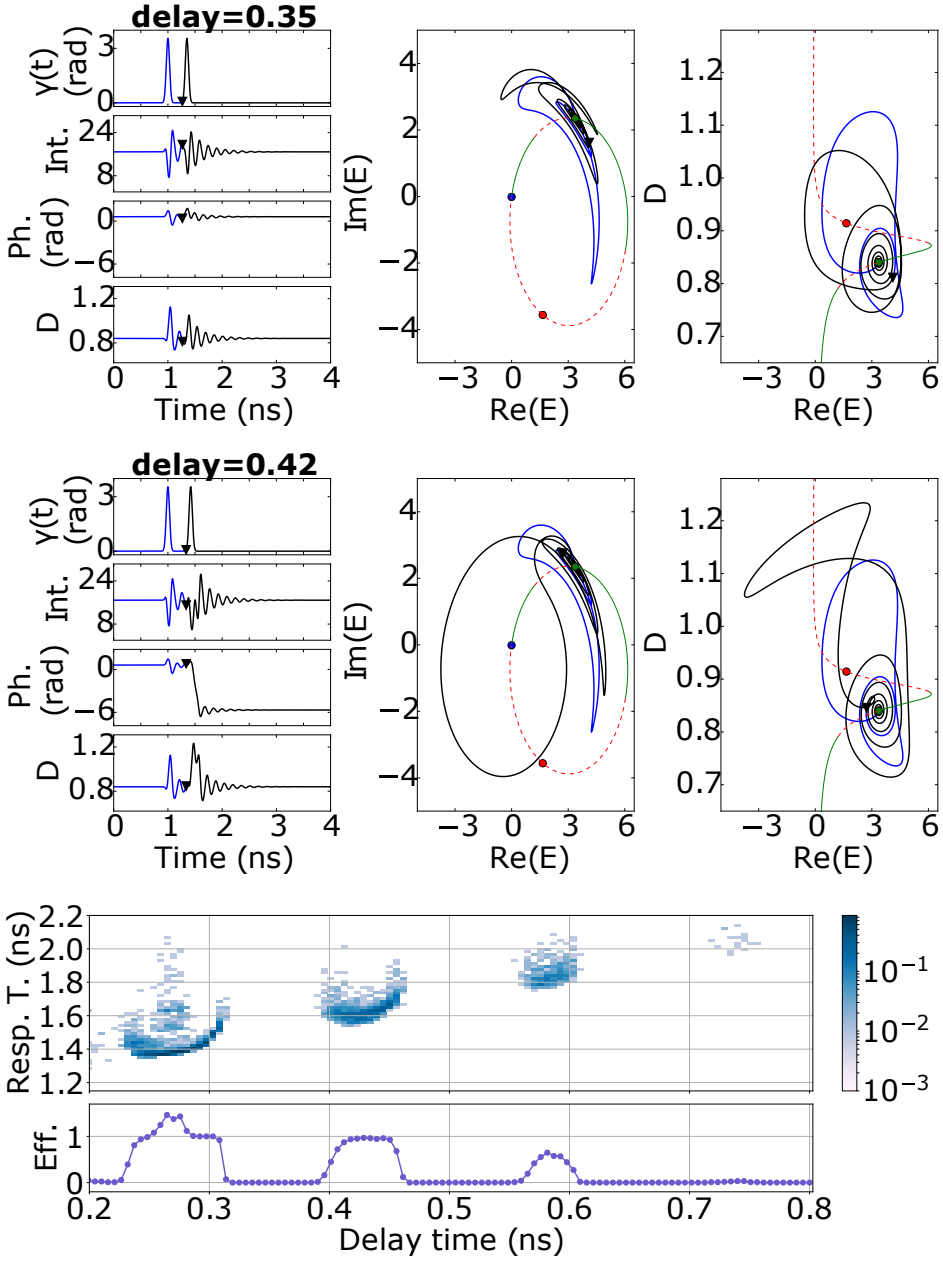

Figure 2.51: Example of an resonator behaviour, numerical simulations, with parameters $|\mathbb{E}_I| = 0.8$ and $\Delta = 4.20$ GHz (the others are as in Figure 2.48). The first two rows are numerical simulations, while the last row represent the efficiency curve and response time histogram, as in Figure 2.50. Note that while for a smaller delay of 0.35 ns the system doesn't displays an excitable response, it does for a larger delay of 0.42 ns.

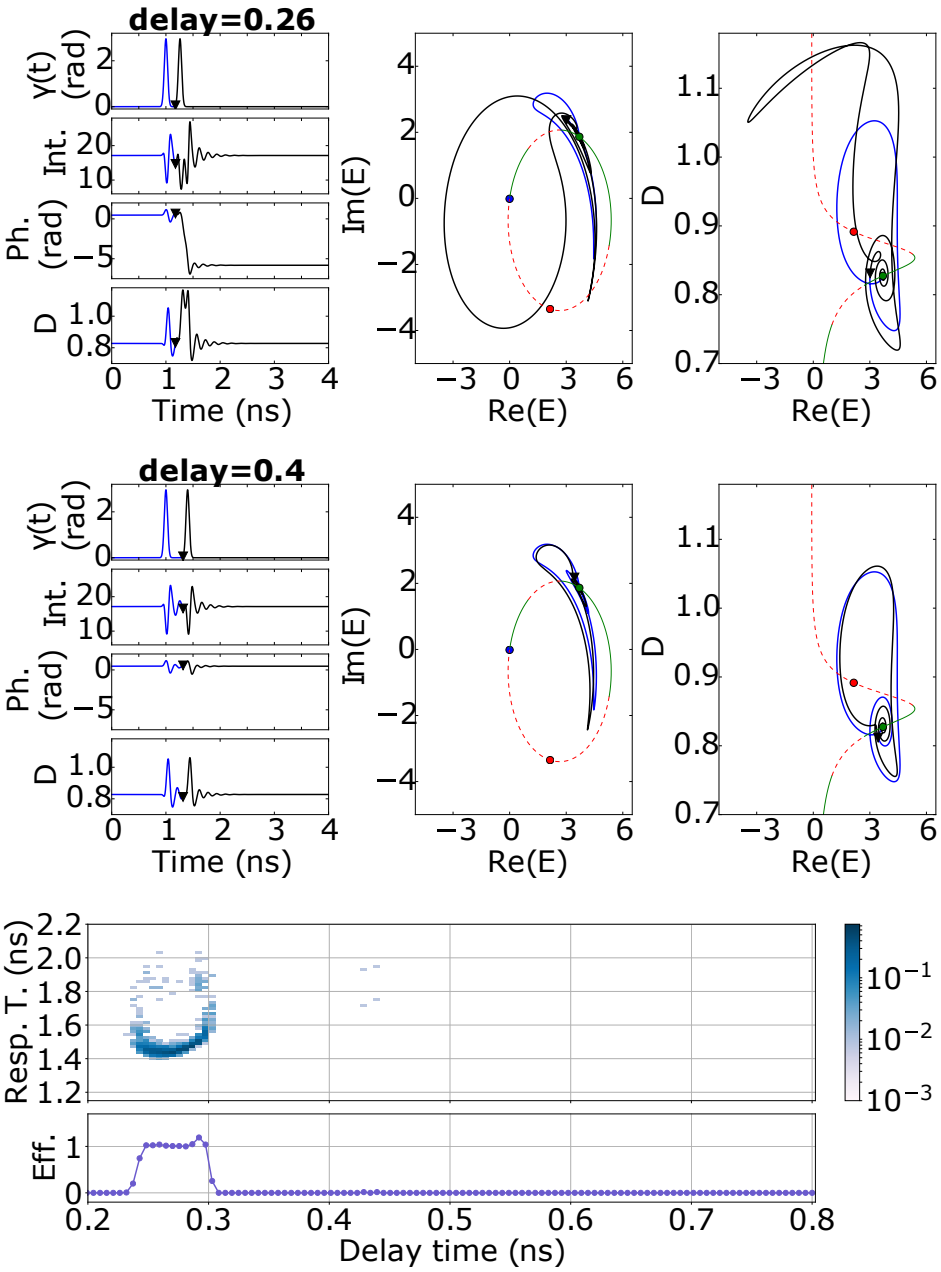

Figure 2.52: Example of an resonator behaviour, numerical simulations, with parameters $|\mathbb{E}_I| = 0.8$ and $\Delta = 4.80$ GHz (the others are as in Figure 2.48). The first two rows are numerical simulations, while the last row represent the efficiency curve and response time histogram, as in Figure 2.50. Note that while for a smaller delay of 0.26 ns the system doesn't displays an excitable response, it does for a larger delay of 0.40 ns.

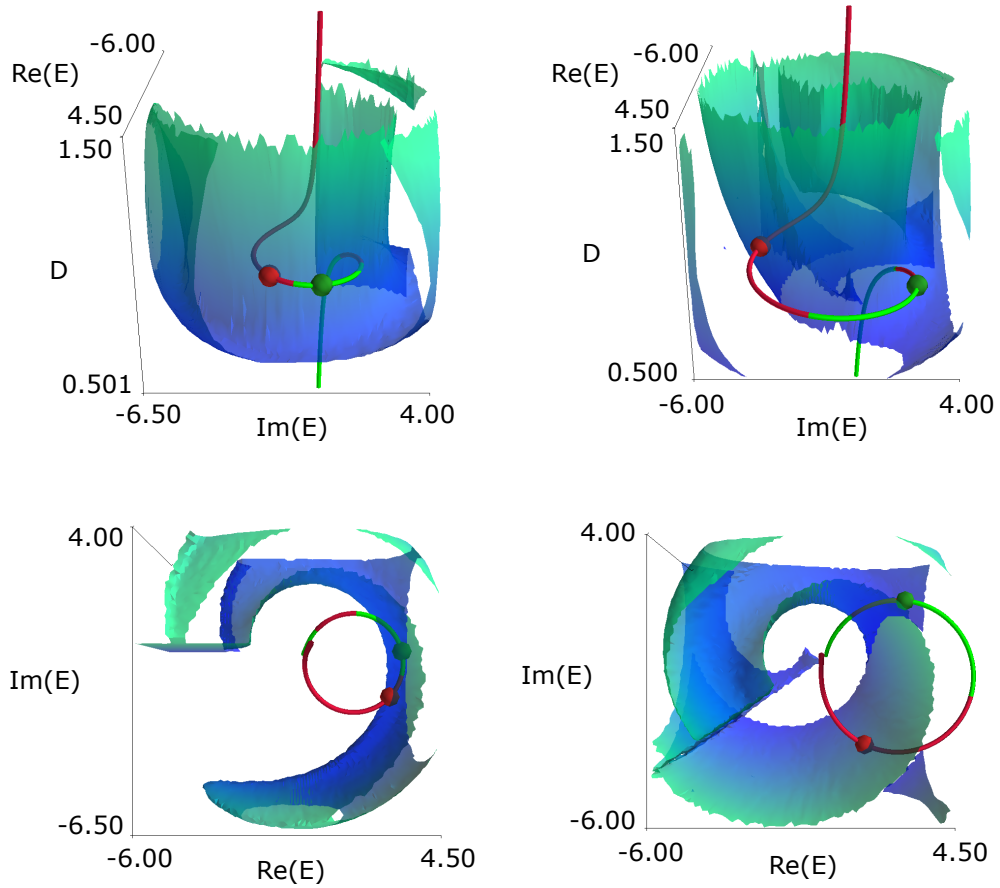

(a) Integrator regime ($|\mathbb{E}_I| = 0.3$, $\Delta = 2.45$ GHz)

(b) Resonator regime ($|\mathbb{E}_I| = 0.8$, $\Delta = 4.20$ GHz)

Figure 2.53: 3D-plot of the slow manifold, saddle-node pair and the separatrix in phase space $\Re e(\mathbb{E}) - \Im m(\mathbb{E}) - D$ for the integrator *(a)* and resonator *(b)* regime of parameters. Bottom figures are a top-down view of top figures. The other parameters are as in Figure 2.48. The color coding of the surface is proportional to D to improve readability in the $\Re e(\mathbb{E}) - \Im m(\mathbb{E})$ plane.

Separatrix We have seen in Figure 2.49 how there seem to be a clear distinction in phase space from the regions where a perturbation can lead to an excitable response from the regions where it cannot. In this paragraph we take this spacial analysis a step further by introducing the numerical shape of the separatrix, which in this context is the 2D-surface in the 3D phase space $\Re e(\mathbb{E}) - \Im m(\mathbb{E}) - D$ that separates the excited regions from the not excited ones. Note that in this case we define a region of phase space as excited if the system, starting from inside the region, converges naturally to an excitable response. In particular, whenever the system starts from a not-excited region and then crosses the separatrix, soon after it will emit one or more excitable responses.

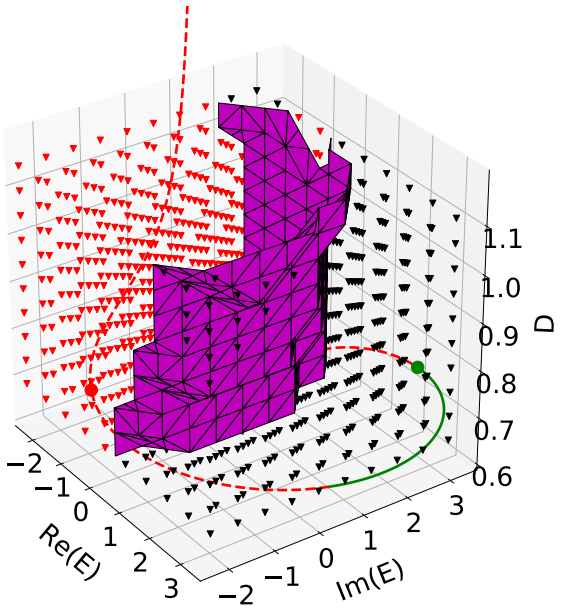

Figure 2.54: Visual description of the procedure to find the separatrix. Starting from a grid of initial conditions, we separate the excited ones (red triangles) from the not excited (black triangles). By employing a Marching Cubes algorithm, we extract the polygonal mesh of the isosurface that separates the two sets and plot is as a magenta surface. Note that, due to a known issue of the Matplotlib library which is used here for the 3D plot, the plot does not render appropriately the intersections and the overlap of different structures, so that some of the black triangles seem to be behind the magenta surface while in fact they should be in front.

Figure 2.53 displays the part of the separatrix structure which is close to the saddle-node pair where most of the dynamics takes place. The separatrix here shown are calculated for the integrator (a) and the resonator (b) set of parameters. It is computed by following the evolution of a large number of initial conditions (in this case $85^3 = 614\,125$ initial conditions) arranged in a 3D-grid. We refer to Figure 2.54 for a visual clue of the procedure, which is applied here for a much smaller grid of $10^3 = 1\,000$ initial conditions. After running the numerical simulations from each point on the grid (without perturbation or noise), we separate the ones that display at least an excitable response from the ones that don't. In the example of Figure 2.54, they correspond to the red triangles and the black triangles respectively. Each point of the grid will then be labelled with either a 1 or a 0 depending on the result, so that by the end of this procedure we obtain a 3D discrete scalar field. By employing a Marching Cubes algorithm[11] [Lorensen 1987], we can extract the polygonal mesh of the

[11]This is an algorithm which is commonly used in Computer Graphics in order to reconstruct polygonal meshes of isosurfaces in 3D data. It is usually employed to plot 3D medical data as with computed tomography (CT), magnetic resonance (MR), and single-photon emission computed tomography (SPECT).

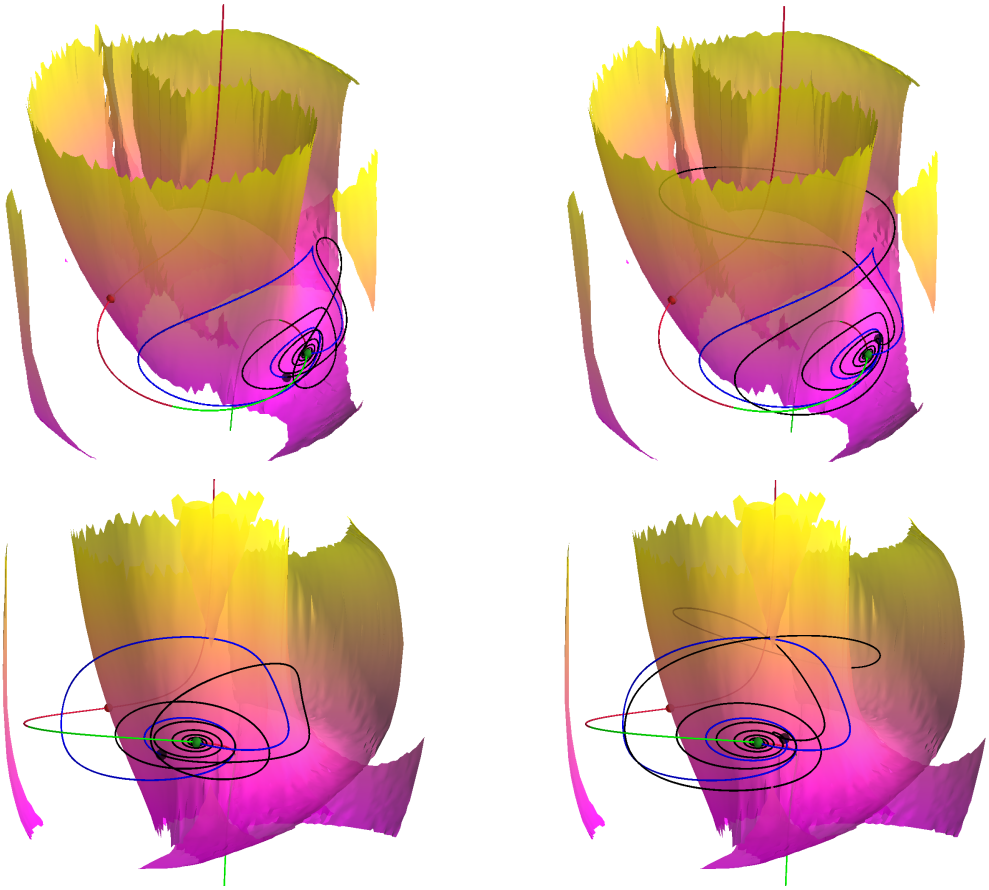

(a) Delay of 0.35 ns (b) Delay of 0.42 ns

Figure 2.55: 3D-plot of the slow manifold, saddle-node pair and the separatrix in phase space $\Re e(\mathbb{E}) - \Im m(\mathbb{E}) - D$ for the resonator regime ($|\mathbb{E}_I| = 0.8$, $\Delta = 4.20$ GHz). The color coding of the surface is proportional to D to improve readability. *(a)* Numerical simulation with delay 0.35 ns between the two pulses of the perturbation while *(b)* Simulation with delay of 0.42 ns. These are the same two numerical simulations as in the two top rows of Figure 2.51. In the (b) case the trajectory crosses the separatrix and an excitable response follows.

isosurface that separates the two sets, and plot it as a 2D surface. This is the magenta surface of Figure 2.54. We finally process geometrically the obtained polygonal mesh and we remesh it into a simpler shape using the Python module PyMesh [Zhou 2018] in order to obtain the the surfaces plotted in Figure 2.53.

If we compare the shape of the separatrix of Figure 2.53 with respect to the saddle-node pair, we can better interpret the behaviour of the system as an integrator or a resonator. For both cases, the separatrix has the shape of an open tube that envelops the slow manifold, at least close to the saddle-node pair (the red and green points). Since the system will stay on the stable point

when unperturbed ans it does not travel too far from the slow manifold when perturbed, the most important part of the separatrix is the surface near the stable point, which can be approximated by a curved section of a cylinder with an axis oriented along the D direction. In the case of the integrator regime (a) this section is very close to the stable node, so that a perturbation in the right direction can easily push the system over the separatrix and generate an excitable response. Furthermore, the relaxation oscillations have a very small amplitude, so that, given two perturbations, they will not add more efficiently for a particular delay.

By comparison in the resonator regime, the part of the separatrix closest to the stable point is slightly far from the point itself. Figure 2.55 shows in particular the effect of a double-pulse perturbation with respect to the position of the separatrix in the resonator case. The left (a) part of this Figure and the right (b) part display exactly the same two numerical simulations for a delay of 0.35 ns and 0.42 ns that were already plotted in Figure 2.51, but here in 3D and with the separatrix.

In the case of a smaller delay of 0.35, we can see the the blue relaxation oscillations after the first pulse-perturbation happen outside of the excited region that is enveloped by the separatrix. Then when the second pulse-perturbation kicks in (the black point here is the same as the black triangle in Figure 2.51), the system is displaced from the relaxation oscillation plane away from the separatrix, before relaxing again to the stable point. We see that in this case, the system trajectory does not cross the separatrix, and as a consequence we do not observe an excitable response in this case.

In the case instead of a larger delay of 0.42 ns, the second pulse perturbations is instead able to push the system towards the separatrix, and by crossing it, an excitable response is triggered. We can clearly see from these two examples that the role of this structure is indeed as a separatrix between the trajectories that display an excitable response from the trajectories that don't.

This idea is confermed by the study of Figure 2.56. Here we reproduced the same type of numerical simulations as in Figure 2.51 but without noise, and for each simulation we measured weather or not it displayed an excitable response, and we also recorded what was the minimum distance in 3D space $\Re e(\mathbb{E}) - \Im m(\mathbb{E}) - D$ that the trajectory ever got to with respect to the separatrix structure. We can see that the number of responses oscillates between 0 and 1 (red curve) following the same behaviour as the efficiency curve of Figure 2.51 but without noise. And if we look at the minimal distance (black curve), we notice how the delay times that correspond to an excitable response correlates pretty well with the delay times when the minimal distance between the trajectory and the separatrix goes to zero, meaning that the trajectory has crossed the separatrix. We can further note that, for a delay between 0.7 ns and 0.8 ns, the trajectories do get closer again to the separatrix, but since they

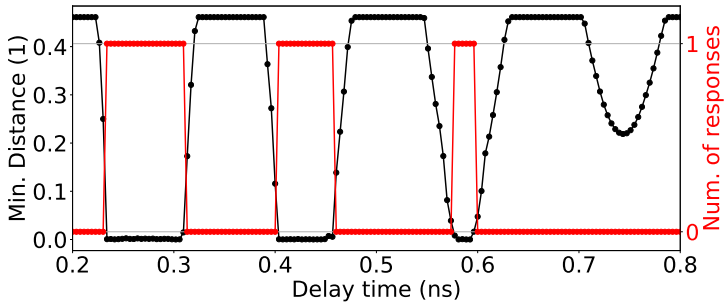

Figure 2.56: Distance between the separatrix and the trajectories in the 3D $\Re e(\mathbb{E}) - \Im m(\mathbb{E}) - D$ space, and number of excitable responses observed, for different delays. Same type of simulations and parameters of Figure 2.51, without noise. Notice that when the distance reaches zero (the trajectory crosses the separatrix), an excitable response follows.

do not cross it in this case, there is no excitable response present.

To conclude, the separatrix structure showed in Figure 2.53, along with the amplitude and spatial extension of the relaxation oscillations, can explain why for some choice of parameters it is possible to observe a resonator behaviour, while for similar others it is possible to observe an integrator behaviour.

***Ad hoc* modelling: beyond the overdamped pendulum.** In the previous sections we have referred multiple times to the Adler model (as expressed in equation 2.2) as a simple explanation for many dynamical properties of the system. Features like the presence of a saddle-node pair of fixed points, the locking range for the detuning parameter, the excitability of the system and the refractory period could all be explained qualitatively starting from the simple dynamical picture of an overdamped pendulum with constant torque subject to a phase perturbation. The connection between a laser with injection and the Adler model comes, from one side, from the observations in the [Coullet 1998] paper where they demonstrated that a Class C model of a laser with injection can be reduced to the Adler equation for low injection and detuning; and from another side, from our observations reported in the last two paragraphs of subsection 2.4.2.

Given its connection to the θ-model, the Adler model should behave as an integrate-and-fire type of neuron which is typical of Class 1 neurons. However, in this paragraph we propose an extension to the Adler model which is able to reproduce the resonator property as observed in the experiment. By introducing a small inertial term to the Adler model we will be able to observe an oscillation in the efficiency curve as evidence of a resonator behaviour, which is typical of Class 2 type of neurons. In the pendulum analogy explained in [Coullet 2005], this consists in considering a pendulum which is damped but not overdamped, so that we cannot drop the second derivative of θ in equation

2.4. It has already been shown in [Eguia 2000] that adding this term corresponds to increasing the dimension of the phase space from that of a circle to an infinite cylinder, where oscillations around the stable focus can take place. In the paper they showed how the broadening of the phase space has the effect of to heavily impact the interspike time distribution in the case of an excitable system with noise. In the pendulum analogy, we are modelling the fact that the pendulum, after a first pulse perturbation, does not simply relax to the stable fixed point but instead oscillates around it a few times. If we can time the second perturbation so that it kicks the pendulum when it oscillates closer to the unstable point, then it is more likely that an excitable response will be triggered. This will influence the efficiency curve for the generation of a second response, which will result in the same shape with repetitive and equally spaced bumps as seen in the modelling (see Figure 2.51).

Let us now turn to the numerical simulations for a confirmation of these hypotheses. As a first step, we check numerically that the Adler model acts as an integrate-and-fire type of system by perturbing it with a double pulse perturbation. The integrated equation can be written as:

$$\dot{\phi} = \omega + \Delta\omega(t) - \sin\phi + \xi(t) \tag{2.101}$$

where ϕ is the dynamical variable, $\Delta\omega(t)$ is the applied perturbation in the shape of two Gaussian with different delays and $\xi(t)$ is the added noise. Each of the two Gaussians has an amplitude of 2.8 Hz and standard deviation of 0.35. Note that in this case the perturbation is applied to the detuning parameter ω which, in a similar way as the phase-perturbations used in the full model 2.98, has the effect of moving the position of the saddle-node pair along the limit circle. All the simulations shown in this paragraph are performed using the Euler-Maruyama method of integration with Gaussian noise $\langle\xi(t)\rangle = 0$, $\langle\xi(t)\xi(t-\tau)\rangle = \beta\delta(\tau)$ with $\beta = 0.08$ as the weight parameter of the random variables.

Figure 2.59 shows different realizations of the simulations at different delays, with $\omega = 0.01$. For each simulation, the top panel represents the time-trace of the perturbation, while the bottom panel represents the histogram of the results of 20 000 simulations with the same delay. The black lines correspond to the position of the stable node while the red lines to that of the unstable saddle, which for this value of the detuning are almost π radiants apart. If we first consider a long delay of 3.0, we note that all the simulations start from the stable node, and they they get perturbed by the phase perturbation which has the effect of displacing the system towards the threshold of excitability represented by the saddle point. In this case the two perturbation are too far apart in time, and after each pulse the system relaxes monotonically towards the stable state. By decreasing the delay time, we can add the effect of the two perturbations. If with a delay of 2.0 the system has almost reached the threshold, by lowering it further the system can finally overcome it, first only

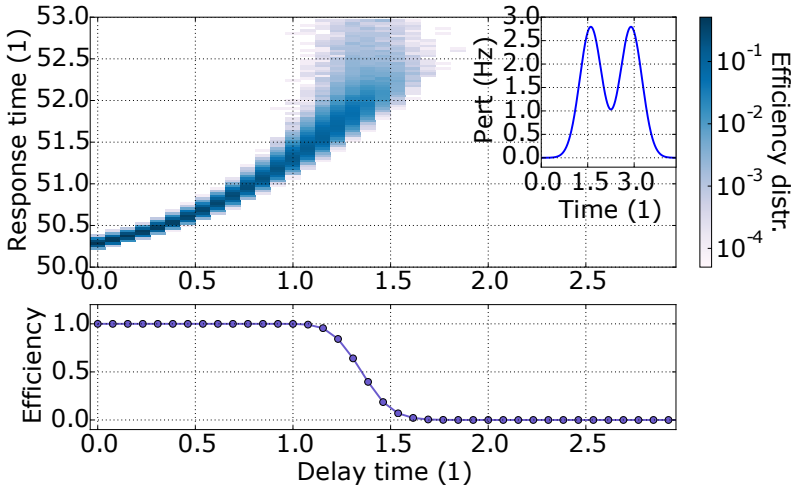

Figure 2.57: Numerical response time histogram and efficiency curve of the Adler model with noise 2.101 with added detuning-perturbation $\Delta\omega(t)$. Same type of simulations and parameters as in Figure 2.59, constructed from 10 000 events for each delay. *(Inset)* Shape of the perturbation for a delay of 1.3 (at approximately 50% efficiency).

in a few simulations as with a delay of 1.5, and then for all of the simulations as with a delay of 1.0. In this final case all of the simulations experience an excitable response that consists of a 2π phase rotation.

All of these results are summarized in the efficiency curve of Figure 2.57, which is constructed from 10 000 simulations for each delay with the same parameters as before. The efficiency curve starts off at zero for long delays, and then increases monotonically towards 100% for shorter delays. This shape is the typical feature of an integrate-and-fire type of system. Looking at the histogram of the response time of the excitable response, we note how the response is generated quicker and with less dispersion for a lower delay (which means a stronger overall perturbation), as expected from an excitable system. Both the efficiency curve and the response time histogram are very similar to the results displayed in Figure 2.50 obtained with the full model, confirming that this simple model can explain most of the dynamical features of the system with integrator parameters.

We now extend the Adler model by adding an inertial term I to the equation 2.101, which basically means that we cannot drop the second derivative of θ in equation 2.4. We can write the model as:

$$I\ddot{\phi} + \dot{\phi} = \omega + \Delta\omega(t) - \sin\phi + \xi(t) \tag{2.102}$$

where $\Delta\omega(t)$ is the same type of detuning-perturbation as before in the shape of two pulses. In this case, the amplitude of the two Gaussians is 0.96 Hz and their standard deviation is 5.65.

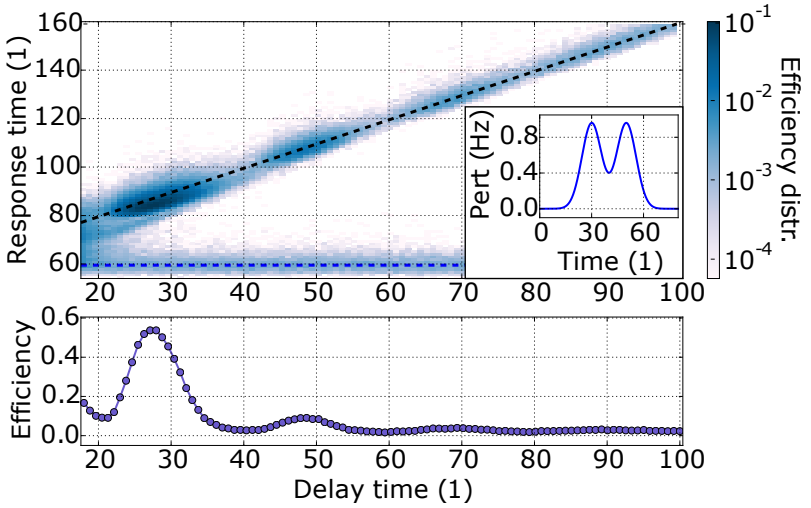

Figure 2.58: Numerical response time histogram and efficiency curve of the modified Adler model with noise 2.102 with added detuning-perturbation $\Delta\omega(t)$ and inertial term I. Same type of simulations and parameters as in Figure 2.60, constructed from 10 000 events for each delay. *(Inset)* Shape of the perturbation for a delay of 20.

We perform also in this case different simulations at different delays, as shown in Figure 2.60, with $\omega = 0.01$ and $I = 10$. As before, for each delay the top panel represent the time-trace of the detuning-perturbation, while the the bottom panel represents the histogram of the results of 20 000 simulations with the same delay. Looking at the case of a long delay of 80, we note that each perturbation displaces the system from the stable the stable node, and then returns towards it when the perturbation stops following some relaxation oscillations around the stable node. Depending on the choice of the delay, the system can then either "ride" the relaxation oscillations, as with a delay of 48 or 27, so that it has an higher chance of producing an excitable response; or be opposed to them, as with a delay of 40 and 20, thereby reducing the number of excitable responses.

These observations are summarized in the efficiency curve of Figure 2.58, which is constructed from 10 000 simulations for each delay with the same parameters as before. The efficiency curve shows a series of bumps which corresponds to the delay times where the relaxation oscillations bring the system closer to the threshold. The response time histogram shows instead that, while some of the excitable responses are generated by the first pulse perturbations (the distribution around the horizontal blue line), most of the responses happen due to the second pulse (the distribution around the slanted black line) and are concentrated around the local maxima of the efficiency. Again, we can compare this Figure with the results displayed in Figure 2.51 which were obtained with the full model. We note that, by only adding an inertial term to the Adler model, we have recovered most of the features of the resonator behaviour that the full system exhibit.

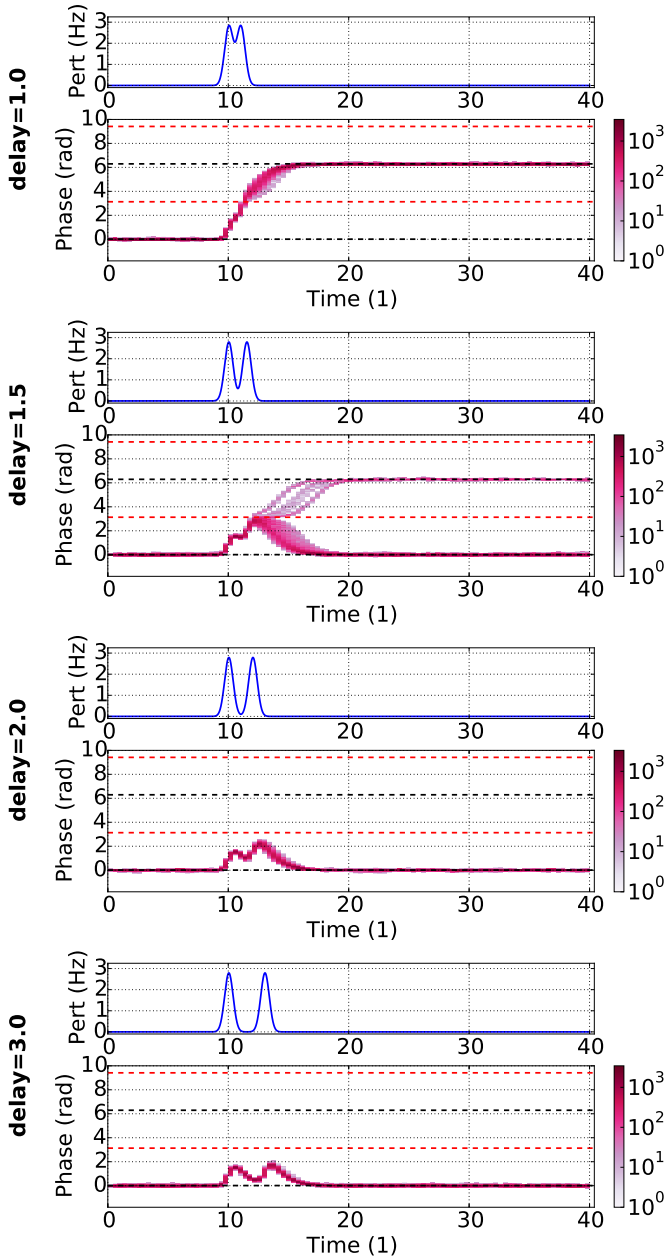

Figure 2.59: Numerical simulations of the Adler model with noise 2.101 with added detuning-perturbation in the shape of two pulses, with $\omega = 0.01$ and $\beta = 0.08$. The delay between the two pulses are 1.0, 1.5, 2.0 and 3.0 from top to bottom. For each delay, we show the time-trace of the perturbation (top panels) and the histogram of 20 000 simulations with the same delay (bottom panels). Note that, while no excitable response is present for a delay of 3.0 and 2.0, some are present for a delay of 1.5 and for a delay of 1.0 all of the simulations display an excitable response.

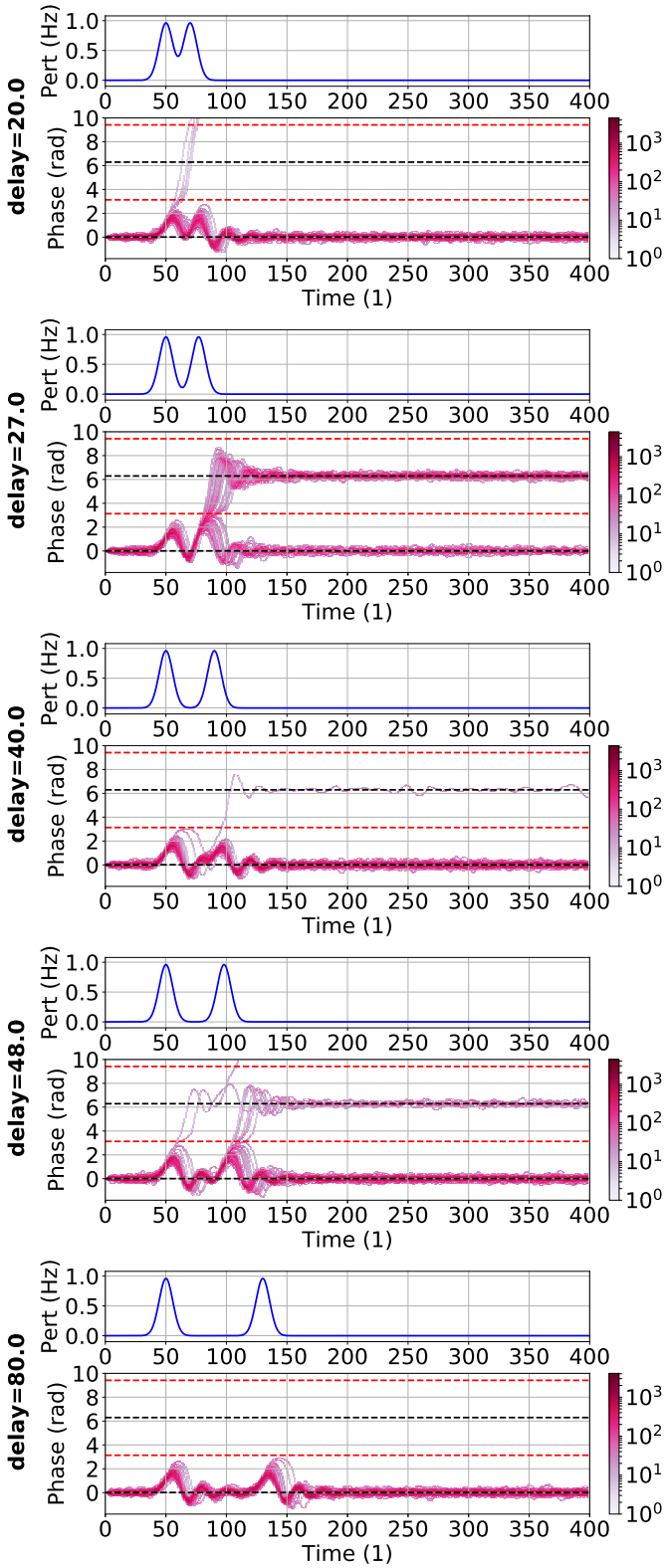

Figure 2.60: Numerical simulations of the modified Adler model with noise 2.102 with added detuning-perturbation $\Delta\omega(t)$ in the shape of two pulses and inertial term I, with $\omega = 0.01$, $I = 10$ and $\beta = 0.08$. The delay between the two pulses are 20, 27, 40, 48 and 80 from top to bottom. For each delay, we show the time-trace of the perturbation (top panels) and the histogram of 20 000 simulations with the same delay (bottom panels). Note that, while few excitable responses are present for delays of 80, 40 and 20, much more are present for delays of 48 and 27.

2.4.6 Multipulse excitability

In the experimental section we have shown that the system can respond to a single perturbation with more than one spike in intensity. If we refer to our physical model as in Equation 2.40, this means that for a single perturbation there will be more than one full-rotation-excursion in the Argand plane (as in Figure 2.34), and each of these excursion will be associated with a spike in intensity and a 2π phase rotation, before going back to the stable C point.

In the paper [Wieczorek 2002] they show how the regions in the $P_{inj} - \Delta$ plane where multipulse responses can be found are located inside what are called homoclinic teeth that are placed inside the locking region and touch the saddle-node bifurcation at the negative ω detuning boundary. By crossing the boundaries of different bifurcation tongues, one can observe one, two or more spikes following a single perturbation.

Figure 2.61 shows instead the case of multipulse responses that are generated from a double-perturbation. Here we are in the same condition as Figure 2.51, so that we are perturbing the system with a double-pulse phase perturbation with a fixed delay of 0.27 ns, which corresponds to the delay in Figure 2.51 where the efficiency curve is greater than one. We show in Figure 2.61 three different simulations (a), (b) and (c). In the case of simulation (a), we can observe only one excitable response, while we can see two responses for simulation (b) and three responses for simulation (c). Even if the only thing that changes between these simulations is the randomness in the noise we can still observe two or more excitable responses instead than only one. This means that we are perturbing the system to be close to a region where multiple responses are possible, so that just the noise level can bring the system to experience two or more pulses.

These types of multiple responses are a further evidence that the system can depart from an Adler-type dynamics (in the integrator regime) and go towards a more complex type of dynamics which can display a resonator property (in the resonator regime) or multipulse excitability.

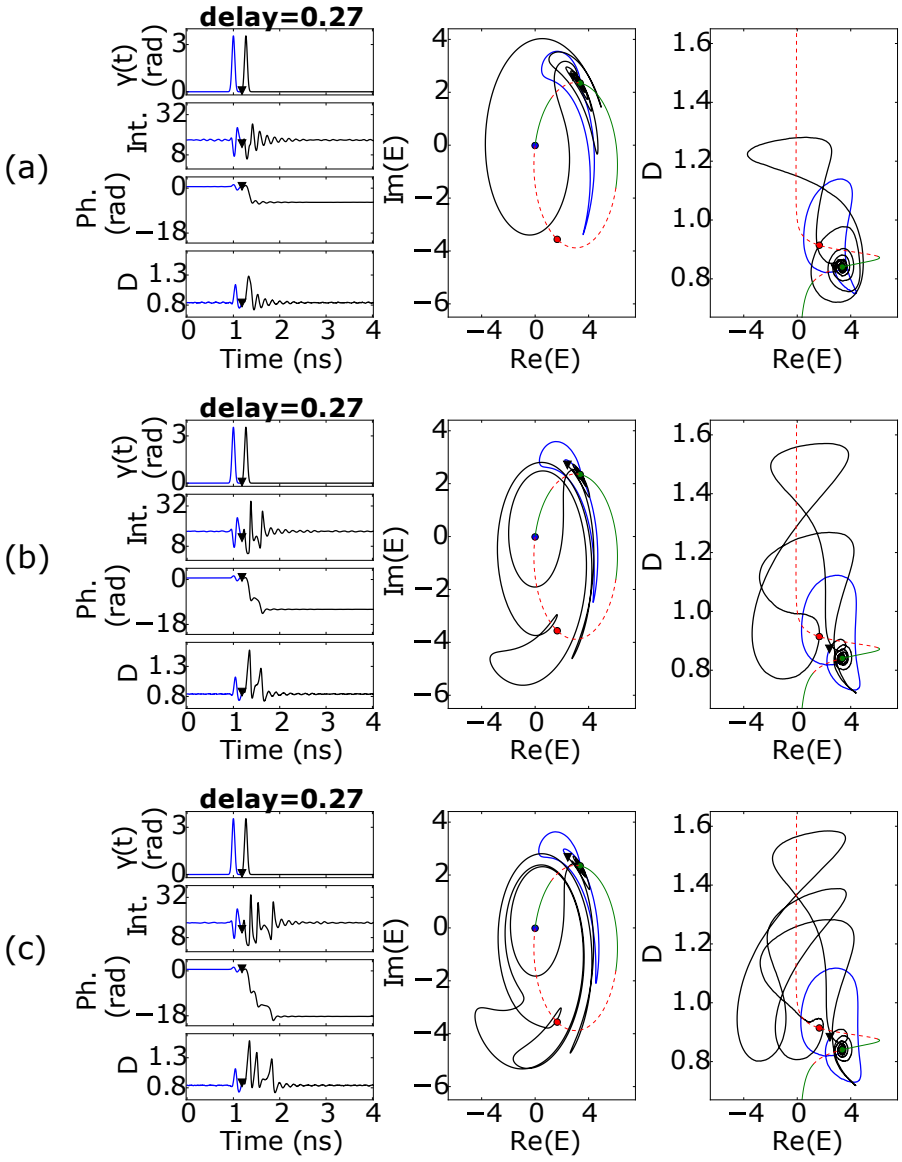

Figure 2.61: Multiple responses consiting of 6π phase rotation in response to a double-pulse perturbation. Same type of simulations and parameters as in Figure 2.51, with noise $\beta = 0.01$. *(a)* One response. *(b)* Two responses. *(c)* Three responses.

2.5 Conclusions and perspectives

The system under study in this chapter was that of a quantum-well semiconductor laser with injection. Under certain conditions, this system can be made to be excitable, so that it responds to an input phase perturbation in the master signal with an excitable response which consists of a 2π phase rotation and a corresponding spike in intensity. The excitability shown by this system is analogous to the one displayed by the most famous excitable system, i.e. the neuron. Furthermore, the formulation of the Adler model, which is the first order approximation of the behaviour of our system for low injection and small detuning, is the same as the neuronal θ-model, which is a popular biological neuron model used in neuroscience, and is a typical Class 1 type of neuron.

Following this analogy, we have probed our system with different types of phase perturbations, either single or double, in order to understand the limit of the Adler description, and to find what other properties this system shares with neuronal systems. The following properties were observed experimentally:

- A *refractory period* of around 0.20 ns which follows from a first excitation;
- A *resonator property* when perturbing the system with a double perturbation under-threshold with delay of 0.12 ns;
- *Controllable multipulse excitability*, where the number of responses (from 1 to around 10) depends on the strength of the single perturbation.

While the Adler model suffice to explain qualitatively the existence of a refractory period, this is not the case for the resonator property and multipulse excitability. In this case, we have to go beyond the simple Adler description and instead rely on the full physical model which comes from a rearrangement of the Maxweel-Bloch equations [Arecchi 1965]. In particular, the Class B model that can be derived from the [Prati 2010] system of equations is able to reproduce qualitatively and quantitatively the experimental observations, and to give some insight on each property. It was found that the regime where these properties are more noticeable is the same as where the relaxation oscillations are more prominent. These oscillations are due to the proximity to a Hopf bifurcation, and their frequency depends on the pumping value and the detuning [Tredicce 1985, Kelleher 2012b]. An *ad hoc* extension of the Adler model, namely by adding an *inertia term* as in the case of a simple pendulum with torque [Eguia 2000], is capable of reproducing a comparable efficiency figures as in the full Class B model in the case of two successive under-threshold perturbations. It has been recently shown that adding the same inertial term to a network of Kuramoto oscillators can lead to complex hysteretic transitions from synchronized to desynchronized states [Olmi 2014].

Going back to the neuroscience analogy point of view, this means that the quantum-well semiconductor laser under study can behave more like a Class 2

neuron than a Class 1 [Izhikevich 2007]. They are a class of neurons where the transition between non-spiking and spiking, when increasing the perturbation strength, happen at a finite frequency, so that there exists a discontinuity in the frequency-current curve. This point also matches the experimental observations reported in [Turconi 2013] where they showed that the unlocking transition for the laser with injection happen at a non-strictly zero frequency. The models that are usually used in order to reproduce the behaviour of a Class 2 neuron are those which exhibit a Hopf bifurcation, as in the case of the Fitzhugh-Nagumo model. The existence of a discontinuity in this type of model comes from the fact that fact that, at the bifurcation point, there is a change in dynamics from a stable point to a spiking limit cycle, which is born with a finite frequency. Common types of resonator neurons include most cortical inhibitory interneurons, including the FS type, and brainstem mesencephalic V neurons and stellate neurons of the entorhinal cortex [Izhikevich 2007]. Following the emission of an excitable spike, such systems relax back to their stable point via oscillations which allow for a resonance effect. In biology, this type of oscillations can be observed experimentally as Membrane Potential Oscillations [Leung 1991, Bland 1988].

In this work we observed that both integrator and resonator dynamics can be obtained depending on the parameters. When looking at the bifurcation diagram in the injection strength-detuning plane ($P_{inj} - \Delta$), we observe that the dynamics is in fact organized around a Saddle-Node-Hopf bifurcation of codimention 2 [Solari 1994], and the type of dynamics depends on the selected parameters. The same type of switch from an integrator to a resonator has also been observed in neurons. For example in [Prescott 2008] it has been observed how pyramidal neurons can switch from being integrators in vitro to resonators under in vivo-like conditions, and in [Zeberg 2015] it has been shown how a particular parameter (the density of voltage-gated potassium channels) was able to shift the dynamics of the model of the same neurons from a Class 1 to a Class 2. It has been proposed that the transition between Class 1 and Class 2 can be explained by the existence of important codimention-2 bifurcation points (Bautin, Bogdanov-Takens, resonant homoclinic and saddle-node homoclinic) which organize the bifurcation landscape [De Maesschalck 2015].

The long term vision of this study would be to detect the properties of this system that may be relevant to their application in spike processing. We know that spike encoding, apart from being widely accepted as the information medium underlying the brain, is a type of processing of information that can be robust to errors, expressive and power efficient [Paugam-Moisy 2012, Tait 2013]. It could then be possible to combine these advantages with the possibility of a scalable photonic network able to process information in an ultrafast and adaptive way as a way of reaching high processing speeds and capability. For instance, the integrator property may be used to provide temporal summation [Selmi 2015] for phase encoded data and the resonator effect may be used to

provide advanced coincidence detection feature while multipulse excitability may be employed for analog to spike signal conversion. As a further example, when an excitable system is coupled to itself after a long delay [Garbin 2015b], we expect a pure refractory time to give rise to repulsive interactions between spikes [Terrien 2018], while a resonator feature may be at the origin of clusters [Garbin 2017b].

In the following chapter we will go beyond the study of a single element and instead we will explore a first attempt at constructing an optical spiking network of many coupled laser elements, with size ranging from 1 to around 500 elements. We will observe how a large number of laser systems can interact via an all-to-all opto-electronic type of coupling, and we will describe the role of the selected population on the observed dynamics.

Chapter 3

System of many lasers with optoelectronic coupling as a network of spiking elements

3.1 Introduction to the chapter

As mentioned in the general introduction, there is great interest in the scientific community in studying physical systems that can implement a network of coupled spiking elements, both as a model of neuronal dynamics and for neuro-inspired applications. However, in the case of optical systems, realizing a large and scalable systems that can be easily manipulated (e.g. by changing the coupling strengths) is still quite challenging.

In this chapter we will introduce a system of many lasers (up to 451) that can be coupled in an all-to-all configuration thanks to an optoelectronic type of feedback. The basic idea consists in realizing an optical mean field of a matrix of lasers onto a detector, and then translating the optical signal into an electrical one and transforming it through a nonlinear function before injecting it back into the pumping current of the laser matrix itself.

The dynamics that results from this setup can be a *stable stationary dynamics*, or it can be *periodically oscillating*, or display *chaotic spiking*. Throughout the different types of dynamics, all of the lasers will be synchronized when following the slow manifold, so that only small amplitude deviations in the output power of single lasers can be observed. By studying the dynamics of different populations of lasers, we will be able to relate the type of dynamics observed in different populations to a property of the selected population (i.e. the average threshold of the LI curves of the selected lasers), and we will test this hypothesis for populations of many different sizes. Furthermore, as the population size increases, the type of dynamics will converge towards a

simplified case which will depend on the statistical properties of the whole population (the average threshold).

The chapter is then organized as follows: we will firstly introduce the reader in section 3.2 to the concepts of dimensionality reduction and collective phenomena in networks of oscillators and also to the type of optoelectronic system here employed, which is a generalization from [Al-Naimee 2009]. Then we will report the experimental results, both in the case of this setup in section 3.3 and in the case of similar ones in section 3.4. Later in 3.5 we will describe theoretically and numerically the system by using a $(2N+1)$-dimensional model of N coupled lasers, which will fit our experimental observations very nicely. Finally, we will draw our conclusions in section 3.6.

The experimental and numerical results reported in this chapter are envisioned to be the subject of a paper:

- Axel Dolcemascolo[1], Romain Veltz[2], Francesco Marino[3] and Stéphane Barland[1]. *"Mean field dimensionality reduction of coupled lasers"* (Title subject to change), (2019) [Dolcemascolo 2019]

which will be submitted to publication soon (expected to appear in print in 2019).

[1]Université Côte d'Azur, CNRS UMR 7335, Institut de Physique de Nice, 1361 Route des Lucioles, F-06560 Valbonne, France

[2]Inria Sophia Antipolis, MathNeuro Team, 2004 route des Lucioles - BP93, 06902 Sophia Antipolis, France

[3]Dipartimento di Fisica, Università di Firenze, Via Sansone 1, I-50019 Sesto Fiorentino, Firenze, Italy

3.2 Introduction to networks of oscillators

3.2.1 Networks of pulse-coupled oscillators, dimensionality reduction and collective chaos

In the general introduction we already mentioned a part of the great wealth of studies on the topic of synchronization of coupled oscillators, which can be thought of as a first step towards the study of networks of more biologically-oriented spiking elements. The field of spiking neural networks is indeed of great interest in neuroscience, and among the many studies on the subject we can cite [Brunel 2000, Roxin 2005, Fournier 2016, Schwalger 2017, Rosenbaum 2017, Pyle 2017].

However in order to achieve a first understanding on such networks, here we will restrict our studies to the simpler case of coupled oscillators. The Kuramoto model in particular has been extensively studied as one of the simplest models that can describe the dynamics of globally coupled networks. Even though the study of these networks is vast and ongoing (e.g. a first proof of the synchronization of pulse-coupled oscillators is as old as the author of this manuscript [Mirollo 1990]), given the high complexity of the problem it would be useful to find a way to obtain a reduction in the dimensionality of the system. Many attempts to achieve this reduction have been successful, as in the case of N identical Josephson junctions [Watanabe 1994], a macroscopic field version of a network of modified theta-model neurons [Kotani 2014], and a pair of coupled oscillating networks of FitzHugh-Nagumo elements [Nakao 2018].

The Ott-Antonsen ansatz and its applications A major breakthrough in this sense has come from what is now commonly referred to in the literature as the *"Ott-Antonsen" ansatz*, or manifold (OA for short) [Ott 2008, Ott 2009, Ott 2011]. This ansatz allows to cast the system of Kuramoto oscillators in the thermodynamic limit ($n \to \infty$) into a reduced, low dimensional system of ordinary differential equations that define a *reduced manifold* towards whom the system is attracted.

The gist of the argument is as follows (reduced version from [Pietras 2016]): adopting the notation as in [Montbrió 2015], one can write the kuramoto-like models as:

$$\dot{\theta}_j = \omega_j + \Im m\left[He^{-i\theta_j}\right] \qquad j \in \{1, \dots, n\} \tag{3.1}$$

where ω_j is the natural frequency of the j-th oscillator, and H is a driving complex-valued field, which represent the coupling, that can depend on parameters such as the time t, the mean field or other auxiliary variables. In the thermodynamics limit, one can introduce the quantity $\rho(\theta, \omega, t)\, d\theta\, d\omega$ which represents the fraction of oscillators whose phases are in the range $[\theta, \theta + d\theta]$ and have natural frequencies in $[\omega, \omega + d\omega]$ at time t. The OA ansatz consists in assuming that the form of the distribution of the density-of-oscillators variable

ρ is of the type:

$$\rho(\theta,\omega,t) = \frac{g(\omega)}{2\pi}\left\{1 + \left[\sum_{n=1}^{\infty}\alpha(\omega,t)^n e^{in\theta} + c.c.\right]\right\} \tag{3.2}$$

where $g(\omega)$ is a continuous frequency distribution function of non-zero width; *c.c.* stands for complex conjugate and $a_n = \alpha(\omega,t)^n$ is the n-th coefficient of a restricted Fourier representation. Note that with this ansatz the problem is shifted from finding the right evolution of the density function $\rho(\theta,\omega,t)$ to finding the function $\alpha(\omega,t)$ that determines all of the Fourier coefficients a_n. Inserting this expression back into a continuous version of the Kuramoto equation 3.1, we obtain a set of ordinary differential equations for α:

$$\frac{\partial\alpha(\omega,t)}{\partial t} + i\omega\alpha(\omega,t) + \frac{1}{2}\left[H\,\alpha(\omega,t)^2 - H^*\right] = 0 \tag{3.3}$$

which can be readily analysed using numerical bifurcation analysis. As an example of application, in [Panaggio 2015], section 3, for a network with two clusters of N identical oscillators, they derive a 2D dynamical system (equation 10) that is capable of displaying chimera states.

The low-dimensional manifold described by this procedure has been shown to be globally attracting for a broad class of Kuramoto oscillators [Ott 2009, Ott 2011]. Later, even for *parameter-dependent systems* (where the natural frequency may deviate from ω_j and depend on another parameter η and where H may also depend on the same parameter) the OA manifold was also conjectured to be attractive [Montbrió 2015]. The case of "weak" parameter-dependence has been recently proved in [Pietras 2016]. Note that the parameter-dependent case is analogous to a network of *theta neurons*, which is a model of spiking elements described by equation 2.15. This extends the OA ansatz to networks of *quadratic integrate-and-fire (QIF)* neurons, as described in [Luke 2013, Montbrió 2015, Pietras 2016], and including gap-junction coupling in [Laing 2015]. Finally, the same ansatz has been applied to the biologically realistic Winfree model [Winfree 1967], as described in section 9.1 of [Ashwin 2016], and more recently in networks of recurrently coupled spiking neurons [Schmidt 2018]. A recent overview on this topic can be found in [Pietras 2016].

Chaos synchronization and collective chaos The issue of the emergence of chaotic phenomena is of great interest in the study of networks of coupled elements. Broadly speaking, we can divide this topic into two categories: *chaos synchronization* and *collective behaviour*.

Chaos synchronization deals with coupled elements that by themselves can exhibit a chaotic behaviour, as in the case of a Lorentz oscillator or a Rössler oscillator, but as they are coupled together they can display more complicated

types of dynamics. In particular, they can become synchronized between each other, display coherence resonance or even suppress their chaotic behaviour. A seminal study in the coupling of two chaotic oscillator is [Pecora 1990], where it was shown how two chaotic systems linked with a common signal can become synchronized. This condition was analysed through sub-Lyapunov exponents. In [Zhou 2002] the authors studied a lattice network of 100x100 Rössler oscillators, and they found that local weak coupling and global noise could induce phase synchronization and coherence resonance in the system. On the other hand, in [Masoller 2005] it was shown how an array of coupled chaotic logistic maps with time-delayed coupling can display a synchronized state which is a homogeneous steady state, so that the chaotic dynamics of each element is suppressed. A similar result of chaos suppression was found in [Gonzalez-Miranda 2002] in the case of two Rössler oscillators coupled by a bidirectional diffusive link with weak periodic forcing.

In the case of simpler types of oscillators, as with theta-neurons or Kuramoto-like oscillators, a chaotic macroscopic or collective dynamics can be a result of the increase in the dimensionality of the system induced by the coupling, even if the single oscillators are not chaotic by themselves. In this case one usually talks of collective chaos. In the case of a network of Kuramoto oscillators, collective chaos via period-doubling cascades has been shown to occur in a population subjected to global coupling with periodic time variations [So 2011], and in the case of identical oscillators with a symmetric natural frequency distribution [Bick 2011], thereby disclaiming the fact that either inhomogeneities or asymmetries are necessary for collective chaotic dynamics to appear. Collective chaos was also observed in the case of theta-neurons with global pulse-like coupling [So 2014], two symmetrically coupled populations of identical leaky integrate-and-fire neurons [Olmi 2010], identical inhibitory integrate-and-fire neurons with time-delayed coupling [Pazó 2016], and Ginzbourg-Landau oscillators [Hakim 1992, Nakagawa 1994].

3.2.2 Coupled semiconductor laser arrays

Semiconductor laser arrays have been studied and utilized in coupled configurations for the last 30 years or so. The interest around these types of devices initially rose thanks to the idea of constructing arrays of phase-locked lasers that could deliver high coherent powers in narrow, diffraction-limited beams for applications such as free space optical communications [bot 1994]. As an example of a "back of the envelope" calculation, it is well known that, given N individual mutually coherent lasers, the power density at the central spot can be proportional to N^2, thus rapidly increasing the spot power [Golubentsev 1987].

Historically, one of the first attempted techniques for the implementation of global coupling within an array of lasers has been by employing *Talbot self*

imaging [Antyukhov 1986, Latimer 1993], which consists in placing a normal partly-reflecting mirror at d^2/λ distance from the face of the array, where d is the period of the array lattice and λ is the wavelength of the lasers. This distance is such that the Fraunhofer diffraction pattern generated by the laser array lattice is imaged onto the face of the array. In doing so, each diffraction spot is imaged on each laser element, hence creating an all-to-all type of coupling. Other methods include using adaptive optics (optical resonator, coherent optical recombination, beam steering, and beam focusing) to coherently recombine many multiline laser beams [Wang 1978] and the use of a common injected signal into each of the lasers in order to achieve phase locking [Dunn 1983, Bourdet 1987]. A review of these techniques can be found in [Likhanskiĭ 1990, bot 1994] while a theoretical treatment of this subject is described in [Oliva 2001] and all the references therein.

Despite these earlier investigations, few experimental studies have managed to implement a large, scalable network of optical emitters where the parameters of the network, such as its coupling topology, can be easily controlled. Recent works in this direction include [Trela 2013], where gratings are used to lock the wavelengths of all elements within an array of lasers; [Nixon 2011, Nixon 2012] where chains of 7 and 16 laser in a loop have been coupled through their far field; [Nixon 2013], where up to 1700 lasers have been coupled through far field diffraction in a nearest-neighbour configuration and [Brunner 2015], where a network based on a 8x8 laser array is coupled through a novel optical diffractive scheme which allows for self- and neighbour coupling.

3.2.3 Single laser with optoelectronic feedback as a chaotic spiking element

As mentioned in the previous subsection, it is not experimentally easy to construct a network of locally or globally connected lasers. The setup that we employed in order to achieve this goal is that of a laser matrix with optoelectronic feedback, as it will be described later. This type of setup allows us to realize an all-to-all type of coupling in a population of N lasers, where N that can go from 1 to 451. This setup is a generalization of a very similar optoelectronic setup already utilized in the study of a single semiconductor laser by the group of Kais Al-Naimee[1,2], Francesco Marino[3], Marzena Ciszak[1], Sora F. Abdalah[1,4], Riccardo Meucci[1] and F. Tito Arecchi[1,3] based in Florence and Baghdad and in the following we will compare both the experimental observations and the modelling introduced in the pa-

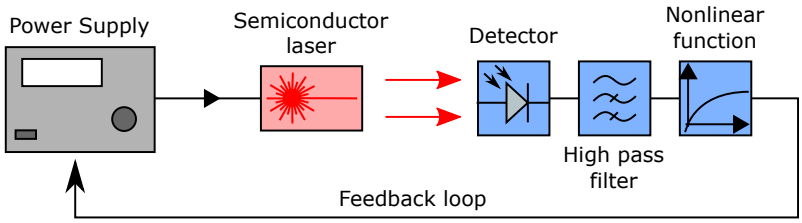

Figure 3.1: Schematic setup of a single semiconductor laser with optoelectronic feedback. The signal coming from the laser is firstly converted into an electrical signal by the detector and then transformed through a high pass filter and a nonlinear function before being injected back into the power supply.

pers [Al-Naimee 2009, Al-Naimee 2010, Marino 2011].

Chaotic spiking and excitability Let us then describe briefly the experiment in question and its results. It consists of a semiconductor laser with optoelectronic feedback, as shown in the schematic of Figure 3.1. Here the output laser light is sent to a photodetector which produces a current proportional to the optical density. This current is then filtered by a high-pass filter with a cut-off frequency that can be varied between 1 Hz and 100 Hz. Then the signal is sent to a variable gain amplifier characterized by a nonlinear transfer function of the form $f(w) = Aw/(1 + sw)$, where A is the amplifier gain and s a saturation coefficient, and then fed back to the injection current of the laser. Note that this injected current will be added on top of a stable DC value of the pumping current that can be set by a DC current adjuster (a function generator, not shown in the Figure for simplicity and for coherence with the following setups schematics in this chapter).

The dynamics of the photon density S, the carrier density N and the high-pass-filtered feedback current I (before the nonlinear amplifier) can be described by the usual single-mode semiconductor laser rate equations [Chow 1994]:

$$\begin{cases} \dot{S} = & [g(N - N_t) - \gamma_0]\, S \\ \dot{N} = & \dfrac{I_0 + f_F(I)}{e\,V} - \gamma_c N - g(N - N_t)S \\ \dot{I} = & -\gamma_f I + k\dot{S} \end{cases} \tag{3.4}$$

which are appropriately modified in order to include ac-coupled feedback loop. As the pumping current I_0 is varied, a transition between a stationary state and

[1]Consiglio Nazionale delle Ricerche (CNR), Istituto Nazionale di Ottica, Largo E. Fermi 6, I-50125 Firenze, Italy
[2]Department of Physics, College of Science,University of Baghdad, Al Jadiriah, Baghdad, Iraq
[3]Dipartimento di Fisica, Università di Firenze, Via Sansone 1, I-50019 Sesto Fiorentino, Firenze, Italy
[4]High Institute of Telecommunications and Post, Al Salihiya, Baghdad, Iraq

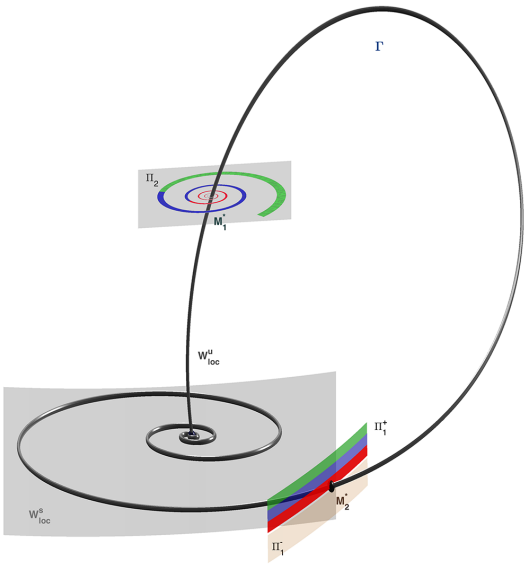

Figure 3.2: Homoclinic loop of a saddle-focus in the case of a Shilnikov bifurcation. Reprinted from [Shilnikov 2007][5].

a periodic self-oscillation state in the dynamics of the light intensity measured at the photo-detector can be observed both experimentally and numerically [Al-Naimee 2009]. At the transition point between the two states, the system displays a *chaotic spiking regime*, which consists in a series of erratic spikes on top of small-amplitude chaotic oscillations. Notice that as the model is three dimensional, all three variables S, N and I are required in order to observe chaos. These dynamics has been explained as the result of an *incomplete homoclinic Shilnikov scenario*, which can mimic trajectories close to a Shilnikov bifurcation. This bifurcation consists in a homoclinic bifurcation of a saddle-focus equilibrium state that can elicit the onset of complex dynamics near homoclinicity whenever the saddle-focus, with linearized eigenvalues $(\mu, -\rho \pm i\omega)$, $(\rho, \mu > 0)$, satisfies the condition $|\rho/\mu| < 1$ [Shilnikov 2007]. Figure 3.2 shows a homoclinic loop of a saddle focus. This bifurcation can lead to the formation of a *spiral chaotic attractor* characterized by large pulses separated by time intervals in which the system displays small-amplitude chaotic oscillations, as can be seen in the case of the Lorentz model [Shil'nikov 1995, Afraimovich 2014].

However, the original Shilkinov scenario does not explain in general the appearance of chaotic spiking. In particular, each spike could be generated not only by a homoclinic orbit, but also by other types of reinjection mechanism that, in particular in slow-fast systems, could include a Hops bifurcation followed by a period doubling cascade producing a sequence of small-periodic and chaotic excitable attractors, that develops before relaxation oscillations arise. As the mean amplitude of the chaotic attractors grows, some fluctuations of the chaotic background spontaneously trigger spikes in an erratic

[5]Licensed under CC BY-NC-SA 3.0

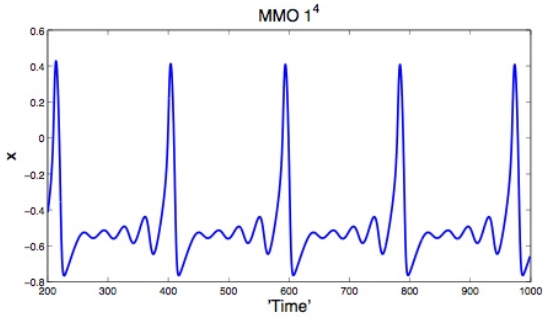

Figure 3.3: Example of periodic Mixed Mode Oscillations (MMOs) consisting of a switch between small and large amplitude oscillations. The MMOs here shown are realized via a generalized canard phenomenon. Reprinted from [Wechselberger 2007][6].

but deterministic sequence [Marino 2007, Al-Naimee 2009]. Furthermore, these spikes are *excitable* as it is possible to generate one at will by applying an external perturbation to the pumping current in the shape of a sharp pulse [Al-Naimee 2010].

Mixed-mode oscillations The dynamics of the optoelectronic system here described displays an alternation between oscillations of distinct large amplitude (i.e. the spikes) and of small amplitude (i.e. the small-amplitude chaotic oscillations). These type of oscillations are called *mixed-mode oscillations* (MMOs) and they were first discovered in the van der Pol equations [Benoît 1981, Eckhaus 1983]. Figure 3.3 displays an example of MMOs. Such MMOs have been observed in a large variety of chemical, biological and physical systems as in the case of surface chemical reactions, electrochemical systems, neural systems, electrocardiac dynamics, laser dynamics and more [Brøns 2008]. They can usually be found in slow-fast systems, where there is a switch between a slow and small type of motion and a fast and large type of motion. Other mathematical mechanisms that can produce MMOs include slow passage through a Hopf bifurcation, breakup of an invariant torus, loss of stability of a Shilnikov homoclinic orbit and subcritical Hopf-homoclinic bifurcation. A review on experimental system that display MMOs can be found in [Brøns 2008], while a more mathematical description of their characteristic features in the context of multiple time scales include [Krupa 2008, Desroches 2012].

In the case of the system of a laser with optoelectronic feedback, in [Marino 2011] the authors demonstrate experimentally and theoretically the occurrence of complex sequences of periodic mixed-mode oscillations, and they construct the complete transition diagram between periodic and chaotic mixed-mode states, and study the role of the noise on the experimental transition diagram.

[6]Licensed under CC BY-NC-SA 3.0

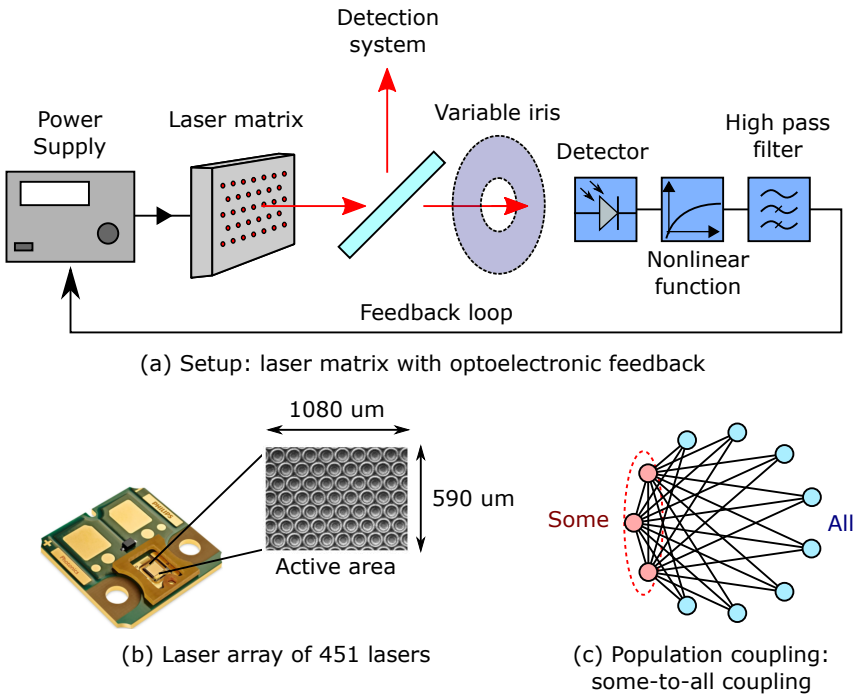

Figure 3.4: Simplified setup of a laser matrix with optoelectronic feedback. *(a)* Simplified setup with the most important elements for the dynamics. *(b)* Picture of the laser array, with 451 laser VCSELs inside the active area. *(c)* Type of population coupling employed with this setup: some-to-all coupling. The population size is selected by the aperture of the iris.

3.3 Experimental results

Let us now describe in detail the experimental setup that we have employed in order to study a newtwork of spiking laser elements. After that, we will discuss and examine the experimental results that we obtained from the experiment.

3.3.1 Experimental setup

In order to construct a network of coupled spiking elements, we employed a setup as shown in Figure 3.4, which is a similar type of optoelectronic-feedback setup that was used in [Al-Naimee 2009], described in the previous subsection 3.2.3. It consists on a laser matrix whose pumping current is controlled by an optoelectronic feedback loop, where the signal from the matrix itself is firstly converted into an electrical signal, transformed, and then injected back into the power supply.

At the heart of the experiment is a Philips VCSEL array visible in Figure 3.4(b). The laser matrix is mounted on a ceramic substrate and this assembly is mounted on Metal Core Printed Circuit Board. Inside its active area of 1080 μm $\times$ 590 μm there are 451 VCSEL lasers manufactured in a semiconductor process on GaAs wafers and arranged in an hexagonal-lattice matrix structure.

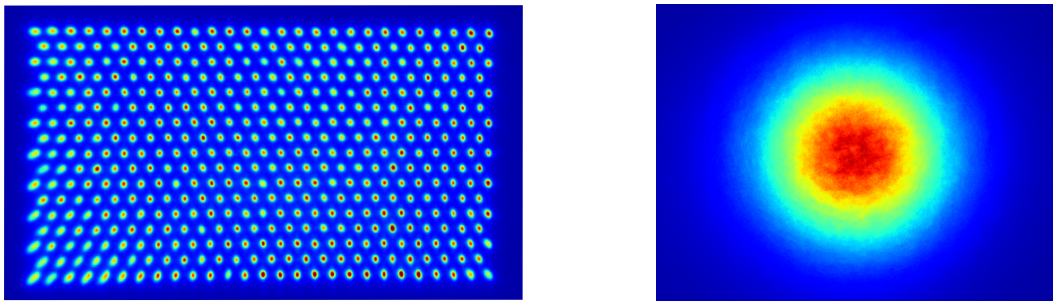

(a) Near field (NF) (b) Far field (FF)

Figure 3.5: Imaging of the Near field and Far field of the light output from the laser matrix.

The typical emission wavelength of the total light emitted by the device is of about 980 nm, with a total emitted power that can go up to 2 Watts. We will study more in detail the optical properties of the population of lasers in the next subsection 3.3.3. This device is pumped by a Thorlabs Laser Diode Current Controller LDC220C, ±2 A (from now on, the "power supply") and is mounted on a Thorlabs Temperature Controlled, Laser Diode Mount TCLDM9 in order to control its temperature. The near field of this laser matrix is an imaging of its hexagonal-lattice structure, as seen in Figure 3.5(a), while the far field is an almost perfectly Gaussian intensity distribution, as seen in same Figure, (b) panel.

A schematic of the complete setup is visible in Figure 3.6. The signal coming from the laser matrix is split into two main branches by a beam splitter: a detection branch and a feedback branch (the one that participates to the optoelectronic feedback loop). Let us describe them individually.

Detection branch This is the part of the signal coming down from the beam splitter in Figure 3.6. The series of lenses 1 and 2 allows to realize the Near Field, and in this plane (or close to it) we select the ouput of single lasers with an iris. We also split this branch in two, so as to be able to monitor two separate lasers at the same time. The two signals are later collected by two photo-detectors whose electrical response will be recorded onto an oscilloscope (Teledyne Lecroy HDO4024 with a band-width of 200 MHz).

Optical feedback branch This is the part of the signal going right from the beam splitter in Figure 3.6. The series of lenses 1 and 3 allows to realize the Near Field at the position where an iris is placed, to be able to select only a portion of the laser population. It is in fact the aperture of this iris that controls the number of lasers that are selected to participate in the feedback loop, while the others will be excluded. After the selection, a flip mirror allows us to switch to a secondary branch that realizes the Near Field again (now after the iris

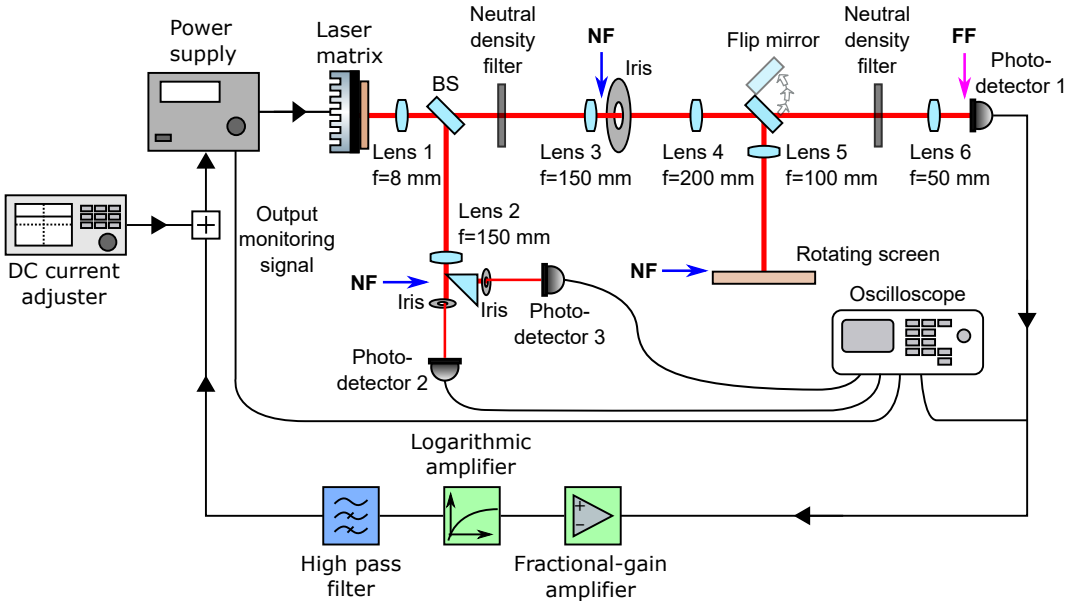

Figure 3.6: Complete setup of a laser matrix with optoelectronic feedback. NF is the location where the Near Field is realized, while FF is the location of the Far Field.

selection) onto a rotating screen. During the experiment, we take pictures of this screen with a fixed camera equipped with an objective so that we can image and later reconstruct what exactly is the population of lasers selected by the iris. When the flip mirror is down, the optical signal goes instead to a photodetector, after possibly being filtered by neutral density filters. The photodector is placed at a position where the Far Field is realized thanks to lenses 4 and 6, so that the spatially extended Near Field after the iris, with extension of a few cm^2, gets reduces to a spot of a few mm^2 that can all fit inside of the sensor area of the photodetector. This photodetector also has a in-built amplifier, with 4 available configuration which we will call *Dpos* in the following, characterized by the following conversion factor of the light signal into an electrical signal:

- $Dpos = 1$: 0.466 mV/μW;
- $Dpos = 2$: 2.47 mV/μW;
- $Dpos = 3$: 21.8 mV/μW;
- $Dpos = 4$: 211 mV/μW;

The rest of the electronic feedback loop will be described in the next paragraph.

Electrical feedback branch From this point on, a series of devices are charged with the task of applying specific transformations to the electrical signal, before it is injected back into the power supply by a feedback loop. The overall effect of these tranformation is to first apply a nonlinear transfer

function of the type $f_F(I) = B\ln(1+\beta I)$, followed by an high pass filter of the current, as shown in Figure 3.4(a). These transformations will be taken into account when constructing the physical model for the system, as it will be shown later. The actual devices that are used for this purpose are: a logarithmic amplifier, followed by a fractional-gain amplifier and an high pass filter, as displayed in Figure 3.6. We will characterize their behaviour in particular in the following paragraphs.

After the transformation, the electrical signal is injected as an external analog modulation of the power supply. The current modulation formula depending on the external voltage U_{mod} that arrives at the power supply is given by:

$$I = I_{MX} + \frac{U_{mod}}{2.5\,\Omega} \tag{3.5}$$

where I is the pumping current of the laser matrix and I_{MX} is the DC value of the current (which in the following we will also call just "MX") that can be set manually by turning the knob of the power supply. As an example, for an external modulating voltage with peak-to-peak amplitude of 100 mV, the oscillations of the pumping current around its DC value I_{MX} will be of 40 mA.

Type of population coupling The size of the population of lasers that are allowed to participate to the opto-electronic feedback loop is determined by the size of the aperture of the iris placed in the optical feedback branch. The total signal of the selected population is later collected onto the photodetector that participates to the electronic feedback loop. This signal can be interpreted as the mean field of the population, as all of the lasers participate equally, and as it will be normalized to the size of the population by a procedure which we will describe later. The mean field electrical signal is later transformed and then injected into the pumping current of the whole laser matrix device. This means that each laser will feel the effect of the change in intensity of all of the lasers that are selected by the iris through a change in the pumping current. The type of coupling realized here is then an all-to-all type of coupling for the population of selected lasers. The lasers outside of the selected population still feel the same mean field but they are not part of the mean field themselves, and furthermore their dynamics can be measured by the detection branch independently from the population selection. The whole system can then be described as having a some-to-all type of coupling, as depicted in Figure 3.4(c), where a selected population (with all-to-all coupling) is also coupled to the rest of the population, but not vice versa.

3.3.2 Characterization of the electrical feedback loop

Let us now characterize more in detail the properties of the electronic elements used in the electronic feedback branch.

Characterization of the logarithmic amplifier Let us now describe more in detail the practical usage of the logarithmic amplifier. This device applies a transfer function on the input current of the type $f_F(I) = B\ln(1+\beta I)$, where the β value can be modified by turning a knob on the device. The knob is graduated on a scale that goes from 0 to 2 with the possibility of reading up to two decimal places. We will call this experimental variable L.

Figure 3.9 shows the effect of changing the L variable on the output signal for the same type of input signal. Here the input signal has pulse-like periodic shape with a frequency of 20 kHz and amplitude of around 150 mV. This signal comes from the photodetector, and it has this shape because it is detecting the light coming from the laser matrix (iris all open) when the power supply is modulated by an external sinusoidal signal with frequency of 20 kHz and a peak-to-peak amplitude of 400 mVpp and the base current of the power supply is MX = 180 mA (no feedback loop is present in this case). The fact that on the detector the signal is no more sinusoidal is an effect of the global threshold for the output power of the laser matrix. We have chosen this modulation to reproduce what *a posteriori* will be the amplitude of the modulations observed on the photodetector when closing the optoelectronic loop, which will be of the order of 100-200 mV, and a frequency which is inside the band of relevant frequencies for the system (more on that in the following paragraph). Given this amplitude range, we can observe the different IN-OUT curves of the device when changing the L variable in the panels from (b) to (e). Note how the output is amplified 40-70 times (depending on L), but also modified in the shape of a logarithmic function. During the the experiment, we will usually work in the regime of $L \in [0.10, 0.30]$ where the logarithmic curve is more pronounced for our range of oscillations. We also notice that for $L > 1$, the IN-OUT curve "opens-up", because of a low pass filter effect in addition to the logarithmic function. We will avoid working at these values.

Characterization of the fractional-gain amplifier The fractional-gain amplifier is placed after the logarithmic amplifier and, as its name suggests, its purpose is to reduce the signal coming from the logarithmic amplifier. One can change the amplification factor for the voltage by rotating a graduated knob on the device on a scale that goes from 0 (which means 0 amplification) to 10 (which means around 1/2 amplification). We will call this control variable A.

Figure 3.10 shows the IN-OUT curves of the amplifier for signals in the range of relevant frequencies from 10 kHz to 80 kHz when $A = 10$ (the maximum value). As we can see, the IN-OUT relationship stays linear for all frequencies, with an amplification factor of around 1/2.

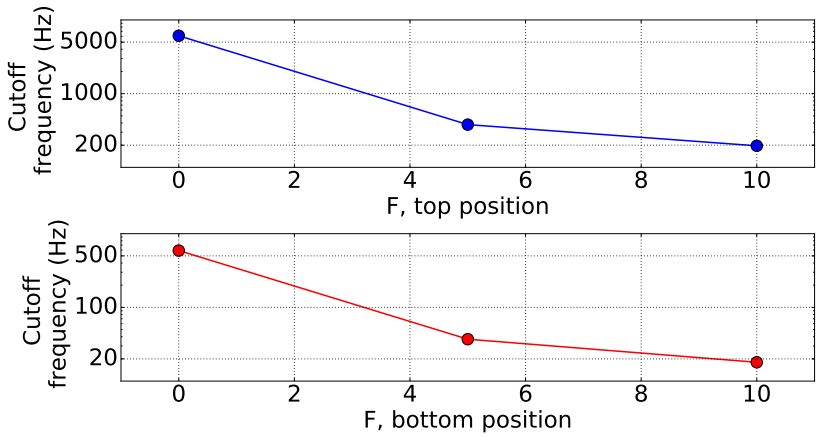

Figure 3.7: Cutoff frequency of the high pass filter, depending on the control variable F, top and bottom scale.

Characterization of the high-pass filter The high pass filter is placed at the end of the electronic branch and it applies an high pass filter to the electric signal that comes from the fractional-gain amplifier. It has a cutoff frequency which can be changed by varying a graduated knob with two different scales that go from 0 to 10. One can change between the two scales by flipping a switch up or down, so that we will refer to these two scales by "top position" and "bottom position". We will call this control variable F top position and F bottom position respectively.

Figure 3.7 shows the cutoff frequency (defined as the half-power point) for the high-pass filter when changing this control variable. For the top scale, the cutoff frequency goes from 6.1 kHz to 196 Hz, while for the bottom scale it goes from 590 Hz to 18 Hz. During the experiment, we will often use position $F = 5$ top, which corresponds to a cutoff frequency of 380 Hz.

Characterization of the total electrical feedback branch Let us now try to have a general idea on the type of transformations that one can apply to the electrical signal coming from the photodetector. This is visible in Figure 3.11 which shows the IN-OUT curves of the logarithmic amplifier, fractional-gain amplifier and high pass filter, for the same type of input used for the logarithmic amplifier and $L = 0.15$, $F = 5$ top and variable A. We can see that the effect of the high-pass filter at a cutoff of 380 Hz is to slightly open the IN-OUT curves. By changing the value of A one can therefore amplify or deamplify the amplitude of the output, while by changing the L variable one can modify the shape of the logarithmic curve to be more or less pronounced.

Summary: control parameters We will now summarize the control parameters for this optoelectronic system:

1. The DC baseline of the power supply I_{MX} or just MX, which is either

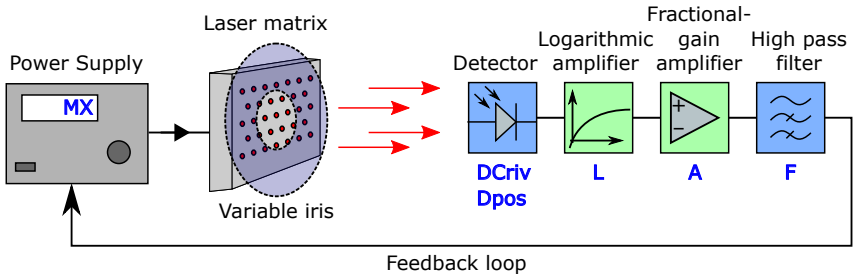

Figure 3.8: Simplified setup, with all of the control paramters specified. MX is the base value of the power supply, Dpos is the level of amplification of the photodetector, DCriv is the DC level when the feedback loop is not present, L and A are two variables that determine the shape and amplitude of the transfer function $f_F(I) = B\ln(1+\beta I)$ and F is related to the cutoff frequency of the high pass filter.

set by hand by turning the knob on the power supply, or by changing the offset of the external modulation that is injected into the power supply;

2. The amplification factor of the photo-detector of the feedback loop, determined by the position $Dpos \in \{1, 2, 3, 4\}$;
3. The DC value registered on the photodetector when the feedback loop is not present for a fixed MX value. This is related to the amount of light that arrives on the photodetector, which can be changed by either changing the iris size or by changing the neutral density filters in front of the detector;
4. The shape of the logarithmic transfer function $f_F(I) = B\ln(1+\beta I)$, which depends on the value of $L \in [0,\ 2]$;
5. The amplitude of the transfer function, which depends on the value of $A \in [0,\ 10]$;
6. The cutoff frequency of the highpass filter, which is determined by the value of $F \in [0,\ 10]$ top/bottom.

A depiction of the different control paramters is visible in Figure 3.8.

An observation on the relevant frequencies at play An important observation on the type of oscillations that we can expect from this optoelectronic feedback setup comes from the extension of the frequency range that this system can support. We know that low frequencies will not contribute to the dynamics of the current, as the high-pass filter will eliminate them. However, at some point there will be an electronic limit on how fast the devices can oscillate, which will result in a low-pass filter. In particular, we find that the bottleneck that determines the highest supported frequency is the power supply, which displays a low-pass filter at around 150 kHz. This means that, supposing that we set the high pass filter at 380 Hz, the range of frequency

that can enter the dynamics will be in the range 380 Hz − 150 kHz, which corresponds to oscillations in the range 6 μs − 2.5 ms. All the dynamics outside this range will not come into play in the description of the current in the electronic branch.

Note however that this discussion is valid only for the electronic branch of the setup, as in the case of light/matter dynamics, their characteristic time-scale is much faster than the frequencies here considered. Remarkably, one cannot eliminate adiabatically the faster variables, as doing so would render the system bi-dimensional and therefore unable to generate chaos. All three timescales are therefore needed for a proper description of the dynamics.

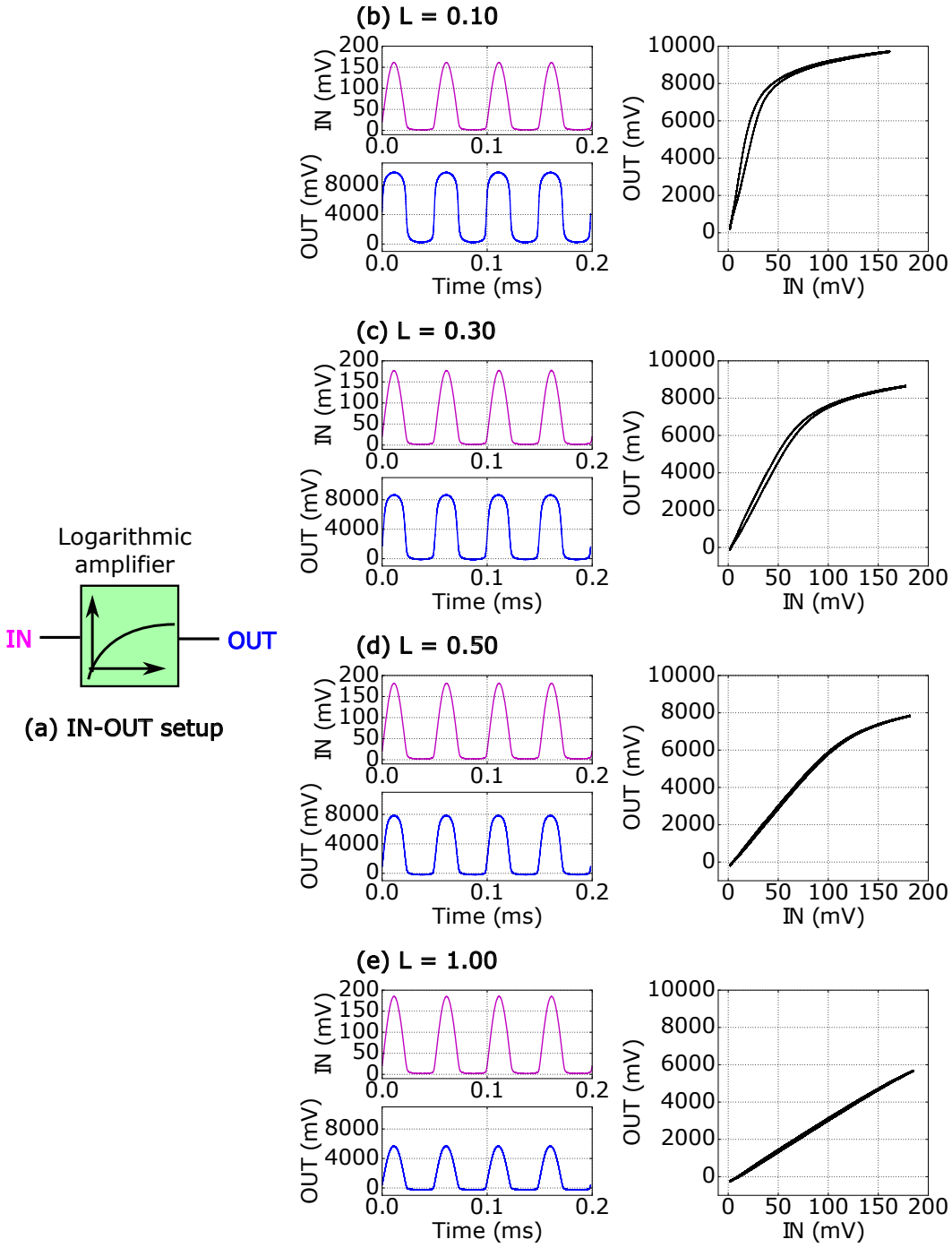

Figure 3.9: IN-OUT curves of the logarithmic amplifier, changing the experimental control variable L. *(a)* Setup employed in the recording of the IN and OUT signals, where the IN signal comes from the photodector when the power supply of the laser matrix (iris all open) is modulated by a 400 mVpp - 20 kHz sinusoidal signal at a base value of MX=180 mA (no feedback loop present). *(b)(c)(d)(e)* IN-OUT curves at different L values for the same type on input.

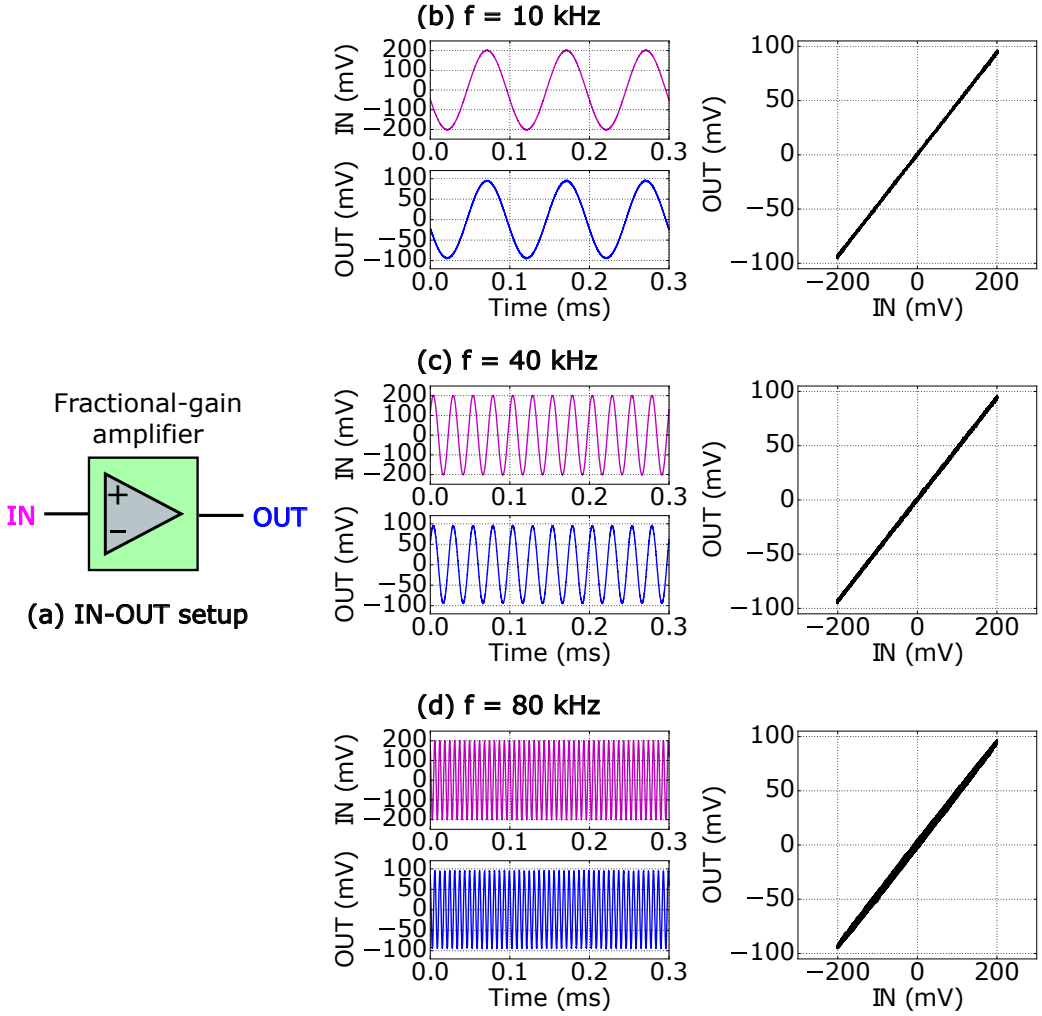

Figure 3.10: IN-OUT curves of the fractional-gain amplifier, changing the frequency of the input signal. *(a)* Setup employed in the recording of the IN and OUT signals, where the IN signal is a 400 mVpp sinusoidal at different frequencies. *(b)(c)(d)* IN-OUT curves at different frequencies of the input, with $A = 10$.

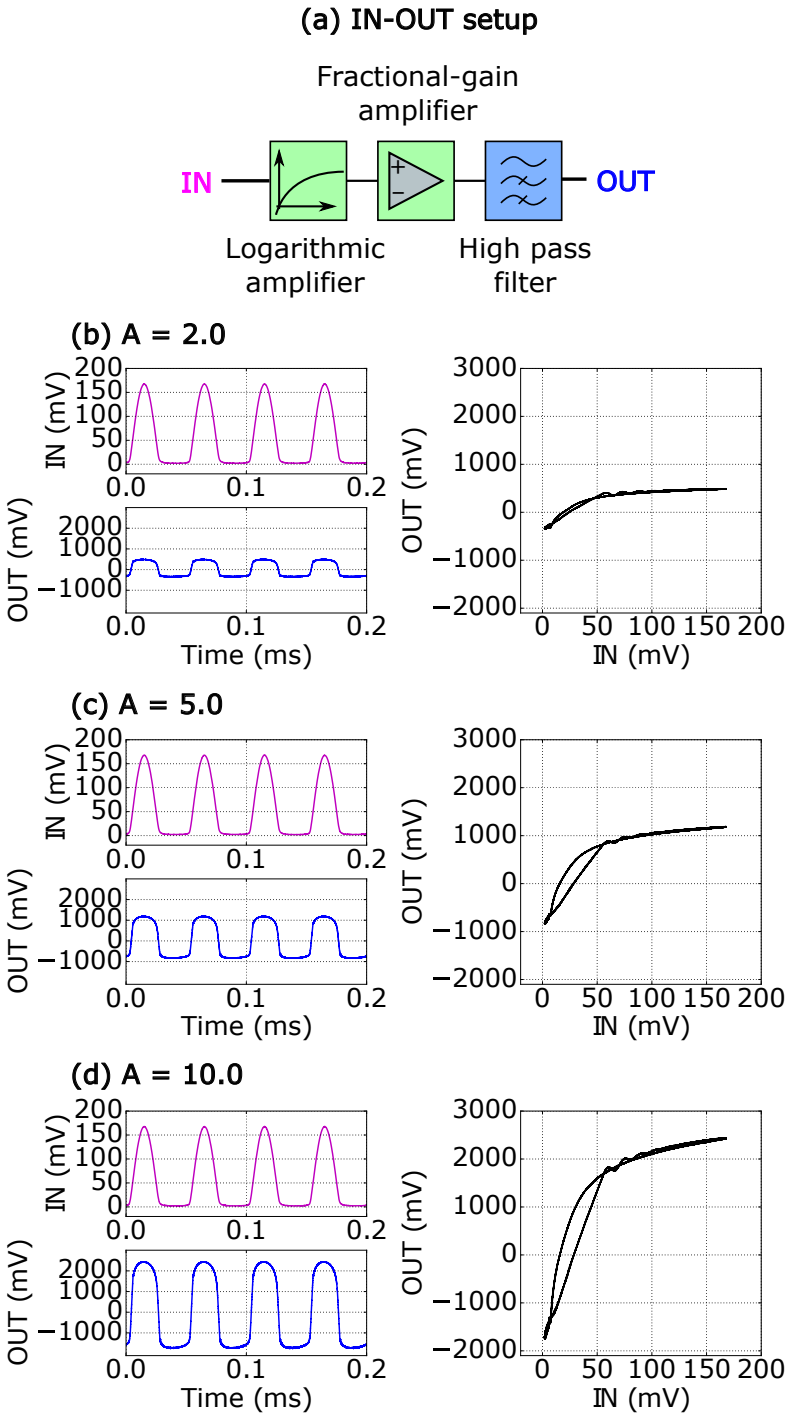

Figure 3.11: IN-OUT curves of the electrical branch of the setup. *(a)* Setup employed in the recording of the IN and OUT signals, where the IN signal comes from the photodector when the power supply of the laser matrix (iris all open) is modulated by a 400 mVpp - 20 kHz sinusoidal signal at a base value of MX=180 mA (no feedback loop present). *(b)(c)(d)(e)* IN-OUT curves at different A values for the same type on input, with $L = 0.15$, $F = 5$ top.

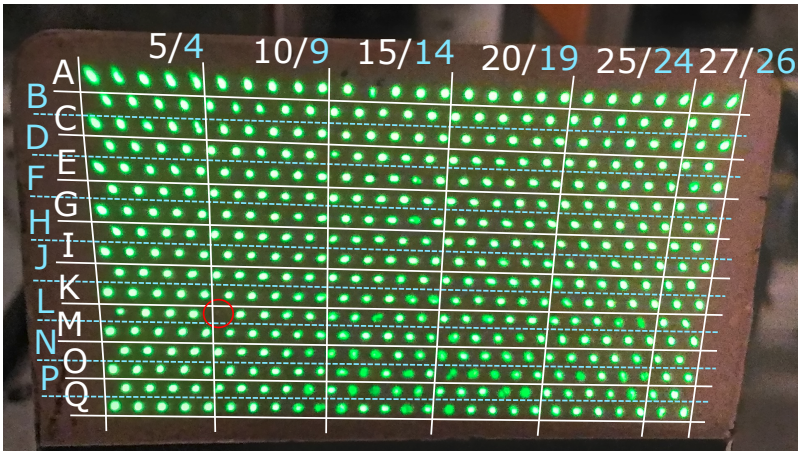

Figure 3.12: Coordinate system for the laser matrix, superimposed on a picture of the far field of the matrix reproduced on a NIR Detector Card when only employing the collimating lens (Lens 1 in Figure 3.6), at DC-pumping current MX=279 mA. The "laggard laser" $L05$ (circled in red) is not yet visible by eye.

3.3.3 Characterization of the population of laser devices

The laser matrix that we are using in the experiments contains 451 VCSEL lasers on a GaAs substrate. Even though they are all pumped at the same current, there can be differences between one laser and the next (for instance in the wavelength, polarization and threshold) which can ultimately affect the dynamics of each laser. Since, for what the current in the electrical branch is concerned, the only thing that distinguishes one laser from its neighbour is its intensity as recorded on the photodetector, the threshold distribution of the selected population will be the only characteristic that can influence the current dynamics. There can however still be dynamical differences between the different device in the carrier density and fast oscillations in the emitted electric field. In the following, we will describe more in detail the different characteristics of the population of lasers devices, with a special interest in the threshold distribution.

Coordinate system for the laser matrix Before starting with the study of the population of laser devices, it is convenient to introduce a coordinate system for the laser matrix in order to be able to specify each element individually if necessary. We therefore introduce the coordinate system as in Figure 3.12. This is a picture of the near field of the laser matrix reproduced on a NIR Detector Card when only employing the C240 collimating lens. On this picture we have superimposed a series of 17 rows, from A to Q, and 26/27 columns (depending if the row is even or odd respectively) labelled from 1 to 26/27. We have chosen this arrangement because this was one of the first pictures of the near field of the laser matrix that we took, and later measurements were calibrated according to this reference. It is easy experimentally to verify the

orientation of the near field according to this reference frame when reproduced on other screens. It suffice to look for the laser $L05$ (circled on the Figure), which is the last laser that can be seen to light up by eye (looking on the Detector Card) when increasing the pumping current. The location of this "laggard laser" can tell us quickly if the reference coordinate frame has been flipped due to the lenses or camera imaging. Note that the laggard laser is not necessarily the one with the highest threshold, since this picture is taken at MX=279 mA, which is far higher than the global threshold at 183 mA that we will calculate later. This is just a transition from "insibile by eye" to "visible by eye" that happens at higher values of pumping currents than the actual threshold.

Wavelength distribution The wavelength distribution for the whole population of lasers is broad, going from 980 nm to 984 nm approximately. Figure 3.13 shows the distribution for different population sizes at the same pumping current of MX=400 mA. We can observe a reduction of the wavelength distribution when decreasing the size, which suggests that each laser has a wavelength that differs slightly from the one of its neighbours.

This is even clearer when looking at Figures 3.14 and 3.15, which represent the wavelength distribution of all of the lasers that belong to the Q row at MX=400 mA, when measured individually. We can see that each laser emits at different modes, and that the principal mode differs in wavelength from the other lasers of the same row. This is what ultimately limits our ability to couple the different lasers coherently, which is why we have employed an optoelectronic type of feedback that does not depend on the wavelength distribution of the population.

Figure 3.16 shows a test of a coherent interaction between different lasers and an injected monomode laser field coming from an external grating tunable laser (the Master laser of the previous chapter). Here the black curve represents the spectrum of the single element, the blue curve the spectrum of the injected master laser and the red curve the spectrum of the device when the master laser is injected into the whole matrix. We can observe that the red curve is slightly different than the sum of the blue and black curves, with certain parts of the black spectrum that rises or decreases when the injected signal is present. This is evidence of a coherent interaction. However, in order to see the interaction of one element with the injected field one has to tune the frequency of the master laser on a particular value, which is not the same for neighbouring elements on the matrix. Given this and other preliminary tests of possible coherent types of coupling of the laser device, we have opted for an optoelectronic type of coupling which is indifferent to the wavelength distribution.

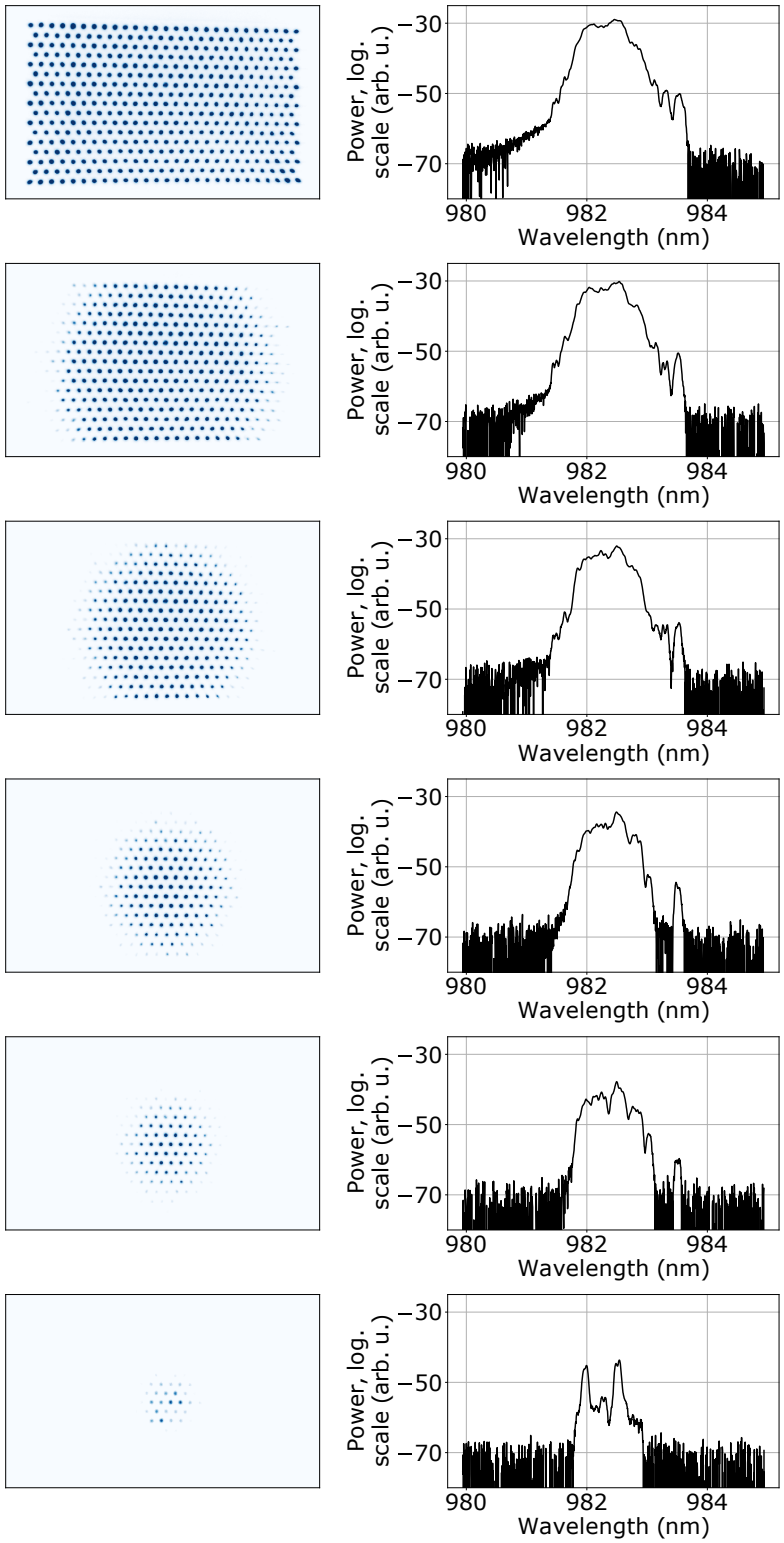

Figure 3.13: Wavelength distribution of lasers populations of different sizes, for MX=400 mA. *(Left)* Imaging of the population selected by the iris. *(Right)* Wavelength distribution of the selected population on the left.

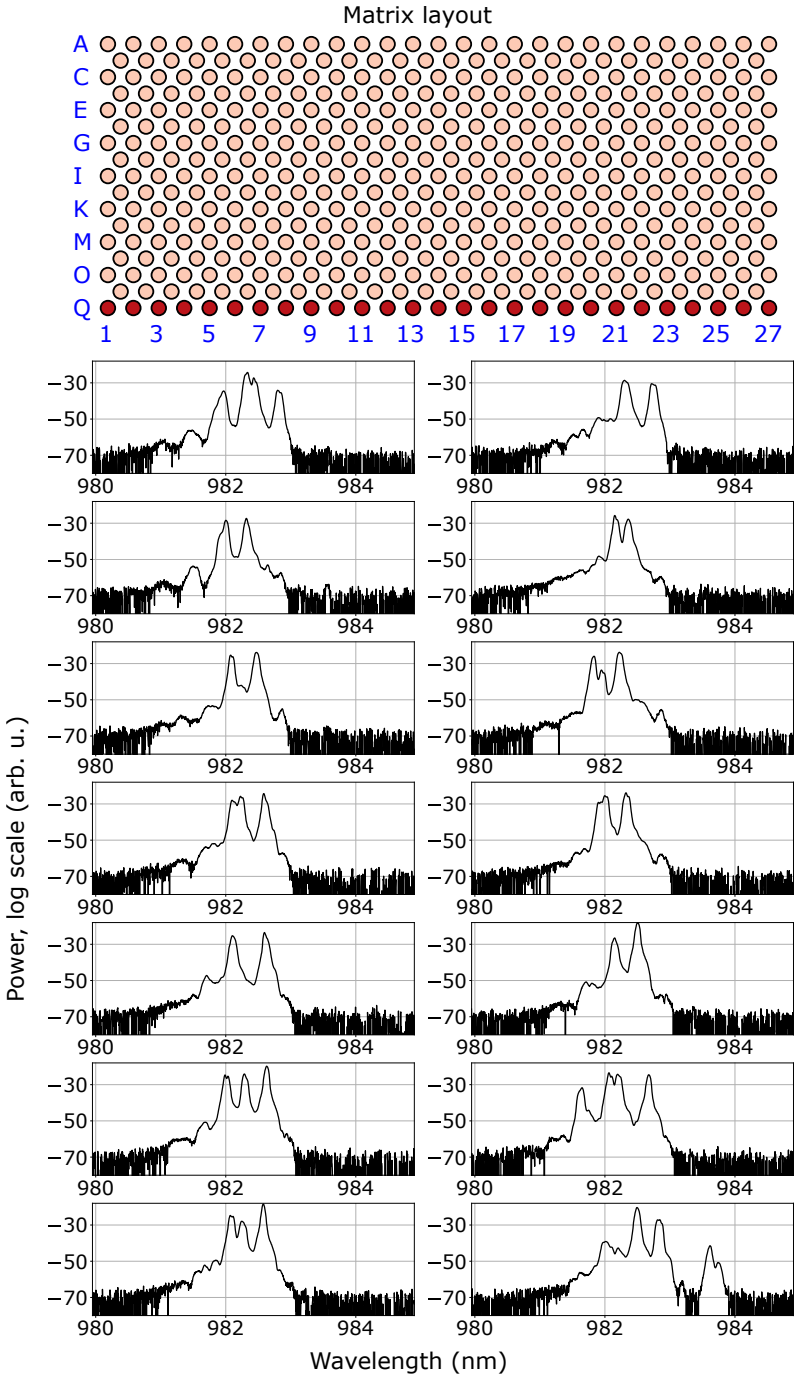

Figure 3.14: Wavelength distributions of different separate lasers, for MX=400 mA. *(Top)* Representation of the selected lasers, which are the ones that belong to the Q row. *(Bottom)* Wavelength distribution, from $Q01$ to $Q14$ in natural reading order. Continued in Figure 3.15

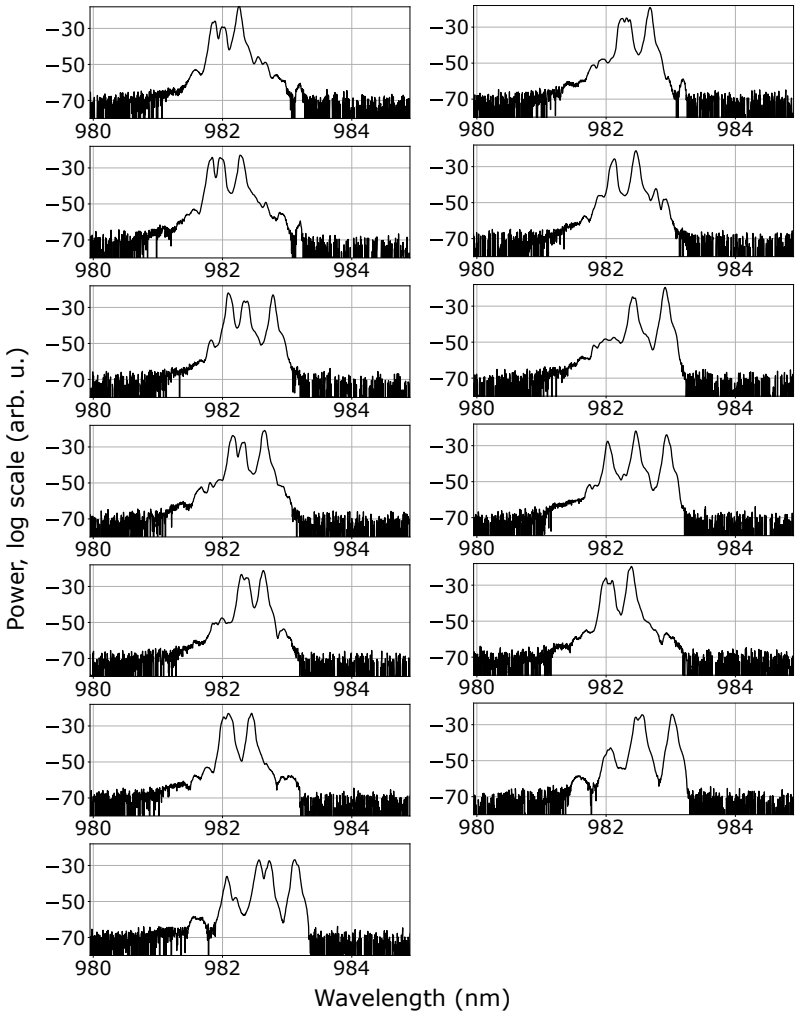

Figure 3.15: Continuation of Figure 3.14. Wavelength distribution, from $Q15$ to $Q27$ in natural reading order.

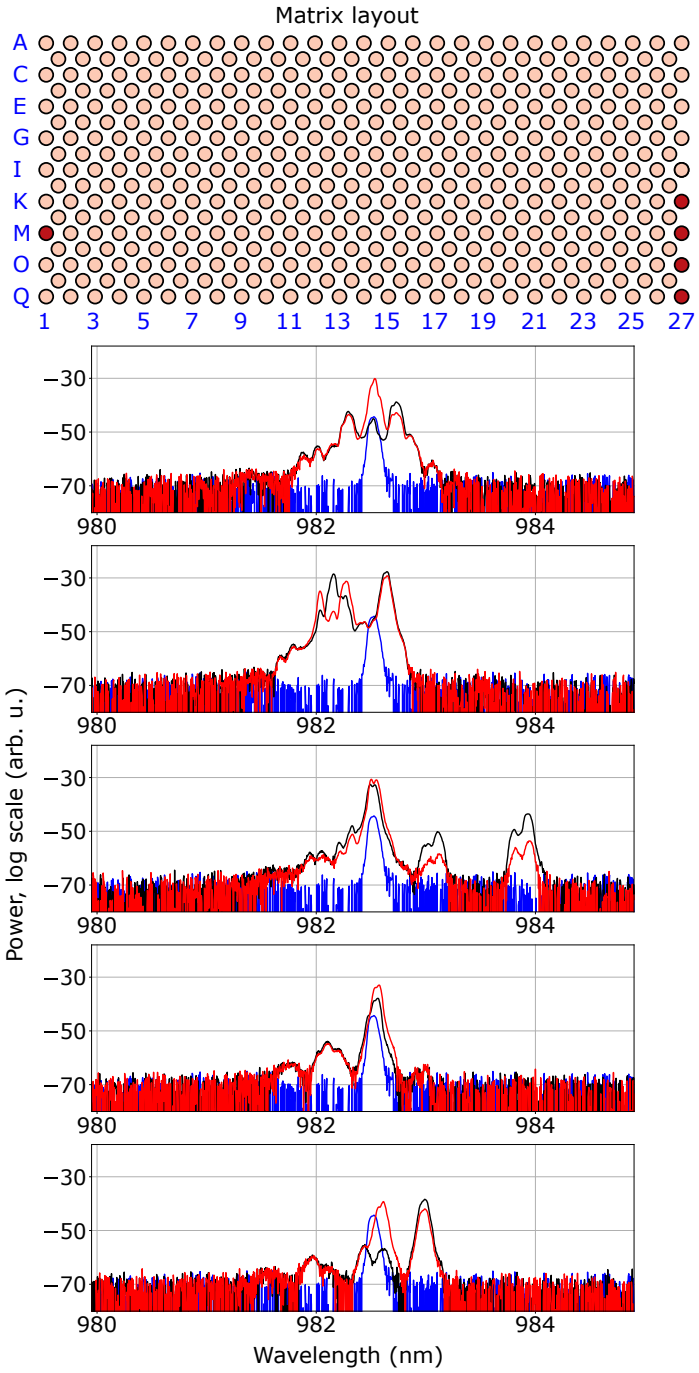

Figure 3.16: Wavelength distribution for selected lasers, with and without injection of an external field. *(Top)* Representation of the selected lasers, which are $K27$, $M01$, $M27$, $O27$, $Q27$ with pumping currents MX equal to 170, 170, 170, 132, 147 mA respectively. *(Bottom)* Wawelength distribution for the isolated laser (black), the injected field (blue) and when the external field is injected in the device (red). Notice how the red curve is different than the simple sum of the black and blue curves, meaning an interaction is taking place.

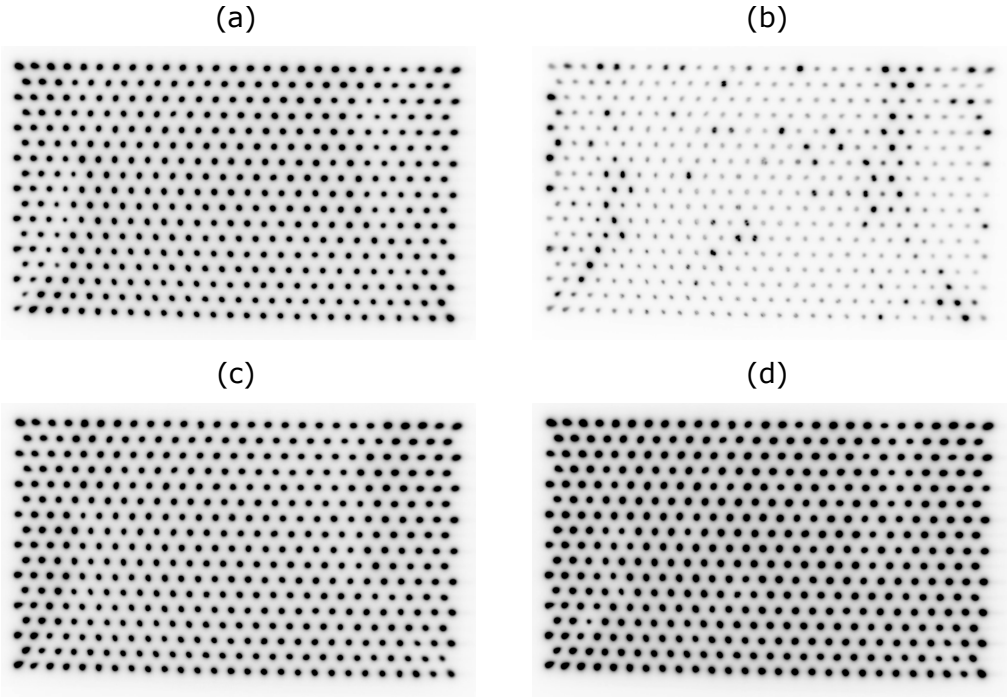

Figure 3.17: Imaging of the near field of the laser matrix for an imaging setup which includes the collimating lens C240, a half-wave plate and a polarizing beam splitter. *(a), (b), (c), (d)* correspond to different rotation angles of the half-wave plate, which are respectively 0°, 22.5°, 45° and 67.5°. Black pixels correspond to high intensity.

Polarization distribution Let us now describe qualitatively the polarization distribution of the laser population. In order to observe the laser intensity emitted at different polarization angle, we have employed a simple imaging setup which consists of the collimating lens C240, a rotating half-wave plate, a polarizing beam splitter and a screen. By imaging the near field of the laser matrix onto the screen at different rotation angles of the half-wave plate while maintaining fixed the polarization angle of the beam splitter, we can have a qualitatively idea of what is the polarization distribution of the matrix. Figure 3.17 represents four different angles of the half-wave plate, going from 0° to 67.5°. We note how most of the devices seem to have a similar principal axis of polarization, even though case (b) clearly shows that this is not the case for all of the population. This would be another obstacle in trying to couple these devices in a coherent way by injecting their output lights into themselves, as the polarization angle would need to be taken into account. Another advantage of employing an optoelectric type of feedback is that in this case the polarization distribution is irrelevant.

Threshold distribution The threshold distribution of the laser population has been studied thoroughly, as it will be relevant for the dynamics. This distribution has been analysed starting from different near field images of the

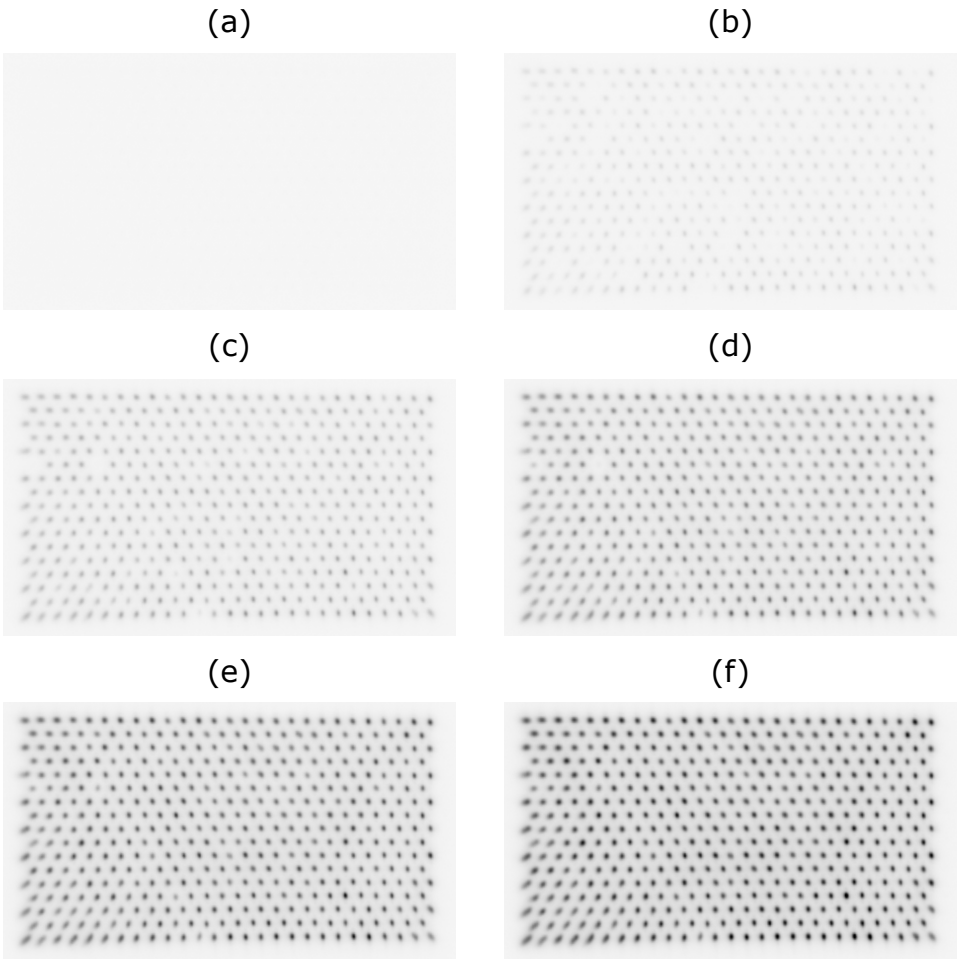

Figure 3.18: Imaging of the near field of the laser matrix for different pumping currents. From *(a)* to *(f)*, the pumping currents are 157, 206, 255, 304, 352, 402 mA. Black pixels correspond to high intensity.

laser matrix at different pumping currents, as shown in Figure 3.18. This figure represents the near field image taken at 6 different pumping currents, from 157 mA to 402 mA. We note that the intensity of the different elements increases with increasing pumping, but the intensity is not uniform for all of the devices, meaning that each laser will have a different intensity threshold, defined as the transition from the "off" state to the "on" state. These pictures represent a sample of a dataset of 930 pictures with pumping ranging from 0.3 mA to 402.0 mA.

From this data, we can analyse the intensity of each device. Figure 3.19 displays an home-made application where one can load a sample picture in order to align a grid of 451 circles on top of the picture. By this procedure, we can easily generate a grid of identical circles where each circle includes the output light of one laser device. By recording the average pixel intensity inside the various circles for all the dataset, we can construct an L-I curve (laser intensity vs

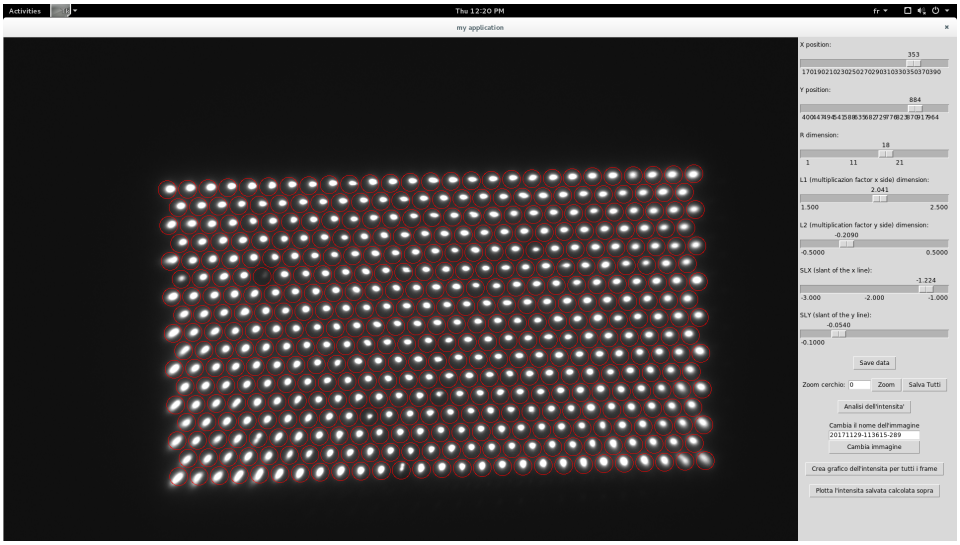

Figure 3.19: Screenshot of the home-made application used to align a grid of 451 circles onto one sample picture of the near field of the laser matrix for the dataset.

pumping current) for all of the devices at once.

Figure 3.20 shows 4 different L-I curves of 4 lasers ($A01$, $A27$, $L05$, $Q27$) constructed in this way. For each curve we have defined a threshold corrent using the following procedure:

1. We fit the data of the L-I curve that belongs to the range [10, 100] mA with a linear fit (red dashed line in the figure);
2. We find the kink point at current x_0 of the curve as the first point where the first derivative overcomes a well-defined threshold;
3. We then fit the L-I curve in the range [x_0+8.6, x_0+51.6] with another linear fit (magenta dashed line in the figure);
4. Finally we define the threshold as the current coordinate of the intersection point (green triangle) between the two lines.

We had to employ this sort of elaborate procedure because, as seen in the figure, the L-I curves of the different devices can have slightly different types of shapes, with more than one kink point as in the "laggard" $L05$ laser, or with intensities that are not exactly linear after the first kink point.

In order to see at a glance all the distribution of all of the different L-I curves, we constructed Figure 3.21. Here we have created a 2D histogram dividing the plane into different "pixels" and counting the number of L-I curves passing through the pixels (in a similar way to a persistence figure). The black curve represents the mean of the distribution, while the red curves represent the limit of $\pm 1\, stddev/2$ from the mean, $stddev$ being the standard deviation of the curves, as shown in the bottom panel of the figure. Looking at the

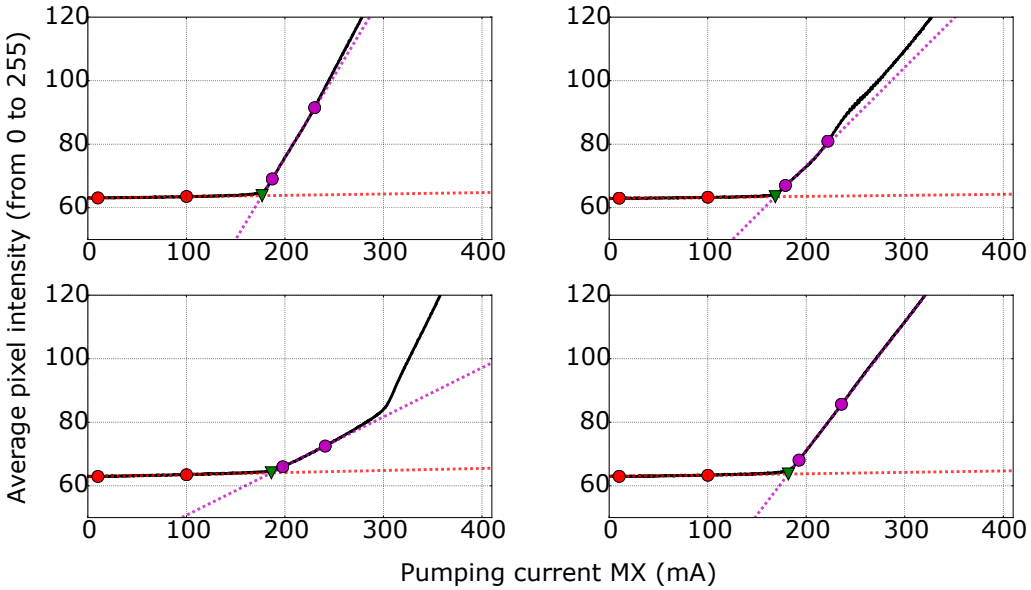

Figure 3.20: L-I curves of four different lasers: $A01$, $A27$, $L05$, $Q27$ shown in natural reading order. The red points mark the current range $[10, 100]$ mA, the magenta points mark the current range $[x_0 + 8.6, x_0 + 51.6]$ mA, where x_0 is the first kink point of the L-I curve. The respective red and magenta lines are the best linear fit of the L-I curve in those ranges. The intersection between the two lines (green triangle) defines the laser threshold for our analysis.

mean of the distribution, we can recognize a general threshold for the whole device that takes place between 170 and 190 mA, and then a linear-like trend after that. However, even if the distribution remains very narrow below the general threshold, it starts to widen more and more as the pumping current increases. When performing the experiment, we will operate the laser matrix in the neighbourhood of the global threshold, so that the only difference between the different L-I curves that will be taken into account for the dynamics to first approximation will be the position of the threshold current point.

Going back to the threshold distribution, the two figures that can summarize our analysis are Figure 3.22 and 3.23. Figure 3.22 shows the spatial distribution of the threshold of each laser, plotted on an hexagonal grid of 451 circles, each representing a different laser element. The laser thresholds are distributed approximately from 160 to 200 mA, and what is interesting is that we cannot see any clear pattern for the distribution, which means that the threshold spatial distribution can be considered as specially random. When selecting a certain population of lasers with the iris, one can then expect an average threshold for the selected population that can span between 160 to 200 mA. Figure 3.23 shows instead the histogram of the different thresholds currents. We can note that the distribution is more or less Gaussian-shaped, with an average global value of $\mathcal{I}_{451} = 183.3$ mA, and a standard deviation of 5.8 mA.

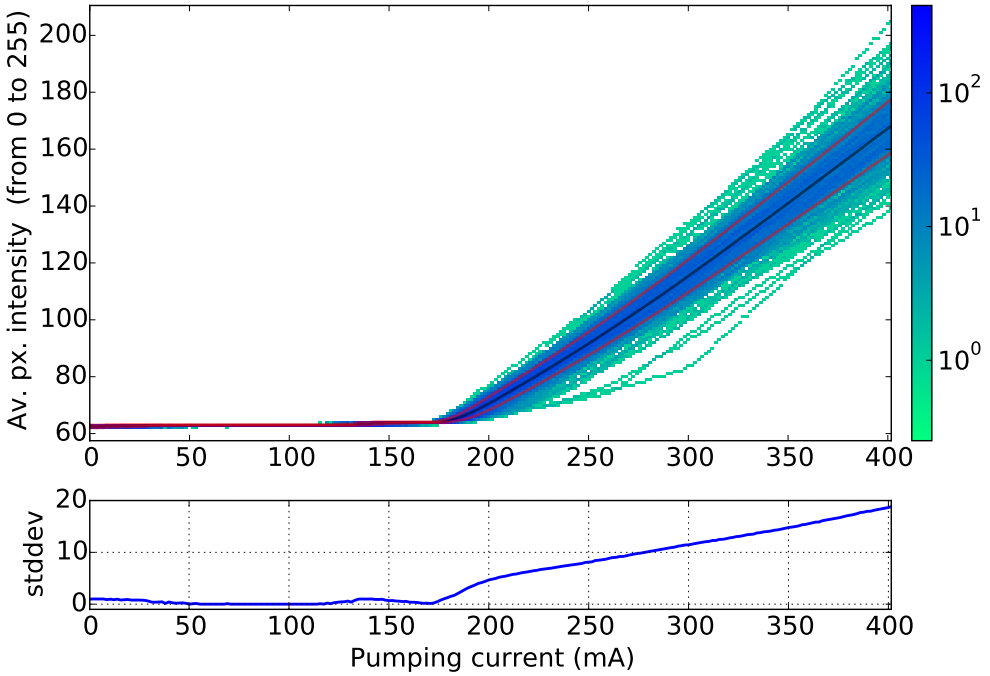

Figure 3.21: L-I curve of the laser matrix. *(Top)* 2D histogram of the L-I curves for all 451 elements of the laser matrix. Black curve: mean of the distribution; red curves: limits at $\pm 1 stddev/2$ distance from the mean. *(Bottom)* Standard deviation of all the curves at different pumping currents.

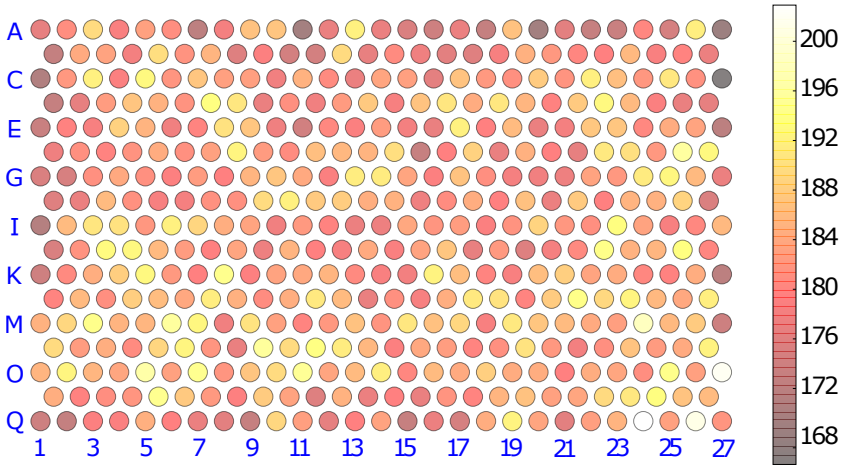

Figure 3.22: Spacial distribution of the thresholds of the laser matrix. The distribution span approximately from 160 mA to 200 mA.

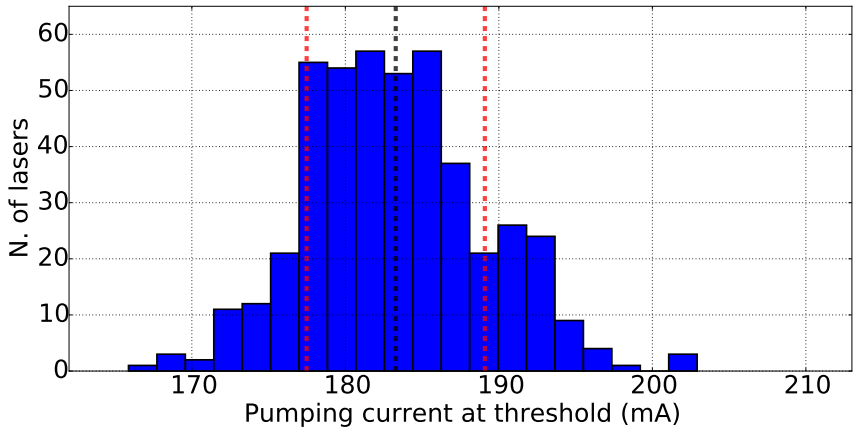

Figure 3.23: Histogram of the distribution of the pumping currents at threshold. The black dashed curve represent the mean of the distribution at $\mathcal{I}_{451}$=183.3 mA and the two red dashed curves represent the two limits at $\pm 1\, stddev$ distance from the mean, where $stddev = 5.8$ mA.

3.3.4 Type of dynamics observed

After having described the properties of the population, we will now show what is the type of dynamics that we have observed when closing the opto-electronic feedback loop as in Figure 3.4(a). This system has 6 different control parameters that we can change, the ones shown in Figure 3.8, plus one if we also consider the size of the population selected by the iris. 4 of these parameters ($DCriv$, $Dpos$, L and A) determine the shape of the transfer function $f_F(S) \equiv A\ln(1+\alpha' S)$ that transforms the optical power S as seen from the detector into the feedback current as measured just before the high-pass filter, while one parameter (F) determines the cutoff frequency of the high-pass filter (γ_f). Finally the last parameter MX is the base value of the current of the power supply as defined in Equation 3.5, which will be often varied in a range close to the global threshold of the device at $\mathcal{I}_{451} = 183.3$ mA.

Varying these parameters, one can usually observe in the dynamics measured at the detector of the feedback loop either a stable condition, characterized by a flat value; or an oscillating condition, characterized by non-sinusoidal oscillations with amplitude of 50-200 mV and with a timescale of the order of ms; or, in rare cases, a chaotic spiking dynamics where each single spikes has the same time and amplitude orders as one period of the periodic oscillations. This was not unexpected as we know from [Al-Naimee 2009] that a similar opto-electronic feedback applied on a single semiconductor laser can result in these types of dynamics. Other more exotic types of dynamics have been observed with this setup for sets of control parameters that have not been explored in depth. For simplicity, in this section we will restrict ourselves to the set of control parameters where mostly the three types of dynamics consisting of stationary state, periodic oscillations and chaotic spiking were observed and characterized. We refer to section 3.4 for an overview of different types of observed dynamics.

Our goal was to be able to observe a full transition between the different dynamics when varying the DC value of the pumping current MX, which will be considered as our bifurcation parameter when fixing all of the other parameters as constant. To do so, we have been guided by the shapes of the IN-OUT curves of the electric feedback as in Figure 3.11. We selected the right parameters in order to have a reasonably logarithmic response and with an amplitude that would allow for oscillations of the order or 30-60 mA of the pumping current when operating with a DC value MX close to the threshold value of around 183 mA. The cutoff frequency was instead varied between 20 Hz and 200 kHz, as done in the [Al-Naimee 2009] paper.

By following a trial and error process, we arrived at specific parameters values where we managed to observe the whole range of the bifurcation when changing MX. In table 3.1 we report the selected parameters used to acquire different datasets, which we have named from “m01” to “m07” (the “m” stands

Name	Date	Parameters	Selected population
m01	18 Gen 2018	1. MX variable 2. $Dpos = 2$ 3. $DCriv$@220 mA= 22.70 mV 4. $L = 0.15$ 5. $A = 1.68$ 6. $F = 8.00$ Top	Laser $J16$
m02	19 Gen 2018		All lasers
m03	22 Gen 2018	1. MX variable 2. $Dpos = 3$ 3. $DCriv$@220 mA= 196.5 mV 4. $L = 0.14$ 5. $A = 0.68$ 6. $F = 5.00$ Top	Laser $J16$
m04	22 Gen 2018		All lasers
m05	30 Gen 2018	1. MX variable 2. $Dpos = 3$ 3. $DCriv$@220 mA= 252.0 mV 4. $L = 0.14$ 5. $A = 0.68$ 6. $F = 5.00$ Top	16 single lasers
m06	06 Feb 2018		19 groups of increasing size, from 1 to 451
m07	07 Feb 2018		25 groups of 7 lasers
m08	09 May 2018	1. MX variable 2. $Dpos = 3$ 3. $DCriv$@220 mA= 167.9 mV 4. $L = 0.14$ 5. $A = 0.68$ 6. $F = 5.00$ Top	Laser $J16$
m09	09 May 2018		All lasers

Table 3.1: Experimental parameters for the different datasets of acquired data.

for measurement). For all the data, we have scanned the value of the base current MX and recorded the corresponding dynamics, when selecting laser populations of different sizes with the iris. Note that, experimentally, if we want to keep all of the control parameters the same when changing the size of the selected population (i.e. when opening or closing the iris), we need to keep constant as well the value of $DCriv$, that is, the DC offset set on the feedback detector. This is because the value of this parameters, which is measured when the feedback loop is not present, depends on the intensity of the light that the detector receives at a fixed pumping current value. Only changing the population selected by the iris would inevitably change the total ouput power and

therefore its DC value and correspondingly the shape of the transfer function f_F would be different. Each time we change the selected population, we also need to adjust the intensity of the light that arrives at the detector so that its DC value at a particular pumping current (usually 220 mA) is kept constant. We do this by applying or removing a combination of neutral density filters in order to reach the desired power.

Because of this re-normalization process, the signal that comes from the feedback detector can be considered as a *mean field* of the selected population, as it collects all of the different power signals of the lasers selected by the iris normalized to the $DCriv$ value. This will allow us to compare different mean field values for different population sizes but similar control parameters.

Dynamics of single lasers Let us first consider the case when only a single laser is selected by the iris. This case is the closest to what was already described in [Al-Naimee 2009], with the possibility of observing a transition between a stable state, a chaotic state and an oscillating state when changing the pumping current. Figure 3.25 shows some examples from dataset m05, where 16 single lasers were measured, one after the other, by keeping all of the control parameters the same. We note that, for currents in the range $[175, 210]$ mA, we can observe different types of dynamics, which are the ones represented in panels (i) to (v) in the Figure 3.25. Figure 3.24 represents similar dynamics in case of dataset m03. In these cases, increasing the DC-pumping current we observe:

(i) A stationary steady state with small oscillations of order of 2 mV principally due to electronic noise;

(ii) A first bifurcation, which lasts around 1 mA, where the dynamics resembles that of a 2D excitable system with noise-triggered spikes, similar to a 2D FitzHugh-Nagumo system with noise. The DC-pumping value MX where this dynamics take place will be called lower-bound bifurcation current, and denoted with I^l.

(iii) Periodic self-oscillations with increasing amplitude;

(iv) Another bifurcation which lasts around 1 mA or less, where a chaotic spiking regime can be observed. It is characterized by mixed-mode oscillations, where the large oscillations have an amplitude and timescale which is comparable with the self-oscillations just before the bifurcation point. The DC-pumping value MX where this dynamics take place will be called upper-bound bifurcation current, and denoted with I^u.

(v) Finally at higher currents we observe another stationary steady state, which is at higher values of the mean field and increases when increasing the DC-pumping current as this value now follows the $L - I$ curve for the laser.

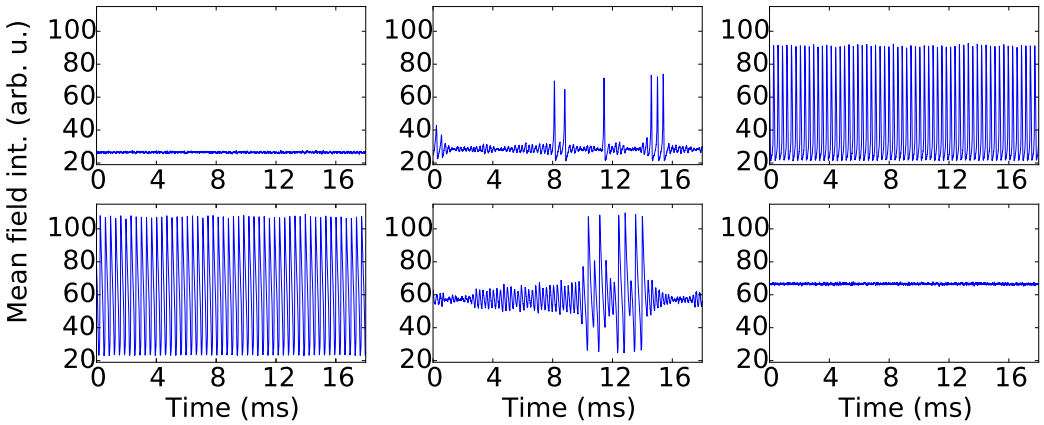

Figure 3.24: Examples of timetraces showing the different types of observed dynamics. Data from dataset m03, with only laser $M02$ in the feedback. In natural reading order, the DC-pumping current values are 182.9 mA (stationary steady state), 184.8 mA (2D FitzHugh-Nagumo-like with noise), 187.4 mA (periodic self-oscillations), 195.4 mA (periodic self-oscillations), 196.5 mA (chaotic spiking regime) and 198.5 mA (stationary steady state).

Even though here we described only few cases with single lasers participating to the feedback, the same type of dynamics can be observed with any other single laser selected, apart from small differences in the amplitude of the oscillations. In particular, the general behaviour of a double bifurcation which follows dynamics (i) to (v) stays the same for any laser. The most important difference between two different lasers is the exact location of the lower (I^l) and upper (I^u) bound bifurcation DC-pumping currents. Figure 3.25(a)(b)(c)(right) shows the 2D histogram of the extrema (maxima and minima) of the mean field traces when changing the DC-pumping current for three different lasers: (a) $O21$, (b) $O20$ and (c) $L18$. This type of figure allows us to see at a glance the whole bifurcation, and it can also be used to identify I^l and I^u (the vertical black dashed lines). What we can observe is that, even though the general shape of the bifurcation is the same, I^l and I^u happen at very different DC-pumping current values, from 175 to 185 mA for I^l and from 190 to 205 mA for I^u.

The fact that these current values can vary from one laser to the next is a consequence of the slightly different $L-I$ curve of each laser, and in particular of its threshold values. We will see later how these values are correlated to the threshold, so that lasers with similar values of I^l and I^u, also have a similar threshold value.

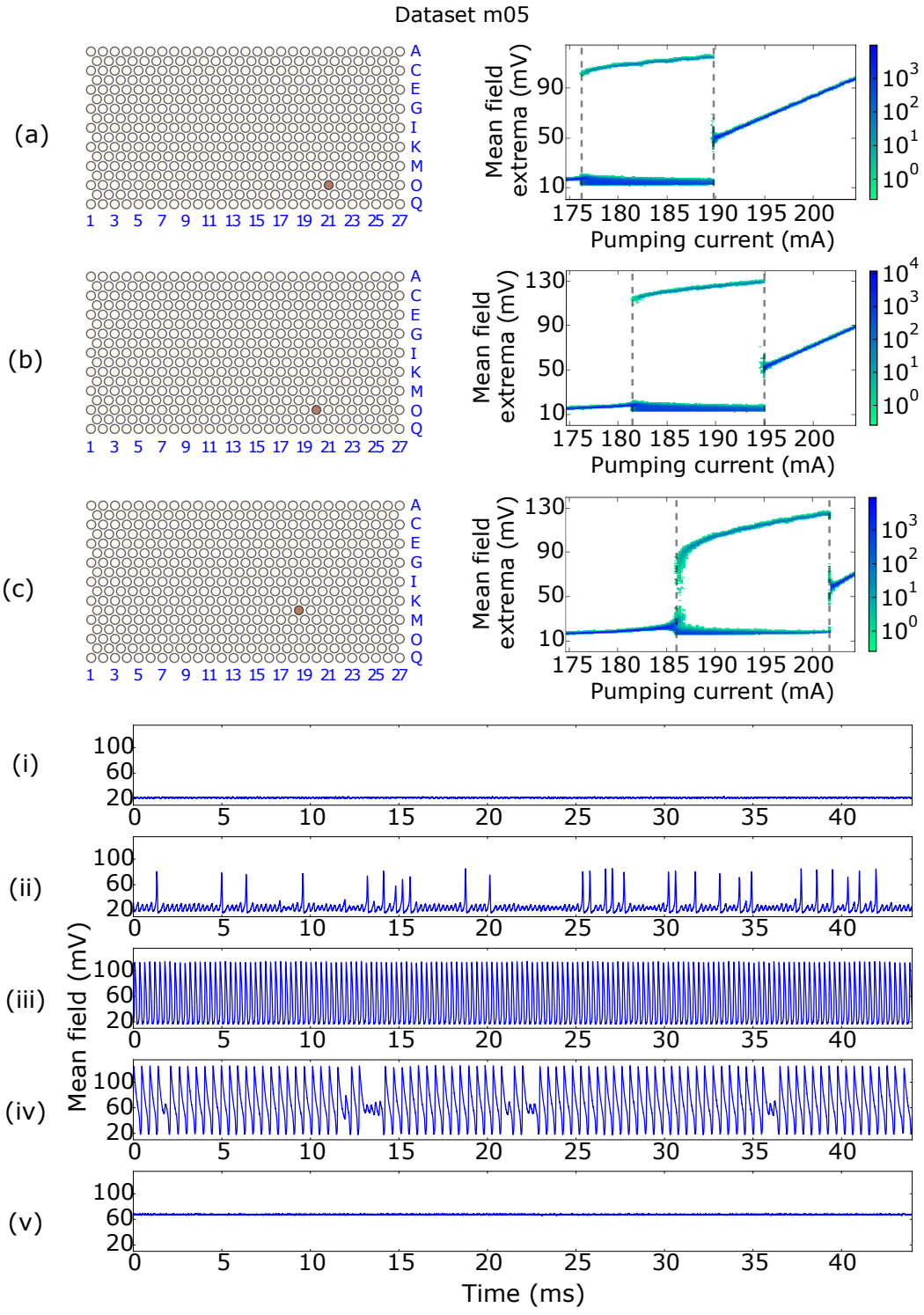

Figure 3.25: Dynamics of single lasers. Selected results from dataset m05. The experimental parameters are described in Table 3.1. The panels represent: *(a)(b)(c)* Left: Representation of the selected laser ($O21$, $O20$ and $L18$ respectively). Right: 2D histogram of the mean field extrema when varying the DC-pumping current. The vertical black dashed lines mark the lower and upper bound bifurcation currents. *(i)(ii)(iii)(iv)(v)* Examples of Mean field traces for laser $L18$ (case (c)) at DC-pumping currents MX equal to 185, 187, 195, 202, 204 mA top to bottom.

Comparison between the dynamics of only one selected laser and the dynamics of a large population of lasers As already explained, the size of the population of lasers under study can be varied by changing the aperture of the iris placed before the feedback detector. When a certain population is selected, the lasers that belong to the selected population are coupled with the mean field as they are all driven by the current that comes from the electric feedback loop that starts with the feedback detector, where the mean field is realized. This means that each laser is coupled with the power that comes from all of the other lasers inside of the population selected by the iris, in an all-to-all type of coupling. The lasers outside of the selected population still feel the same mean field but they are not part of the mean field themselves, so that the whole system can be described as having a some-to-all type of coupling as depicted in Figure 3.4(c).

Figure 3.26 shows the comparison for the dynamics displayed by a single element and the dynamics of the whole population, when keeping all the control parameters the same. Figure 3.27 shows again the same type of comparison but for a different set of parameters (namely, with $DCriv$ greatly increased). Panels (i) and (ii) display the imaging of the selected population by the iris, while panels (iv)(v)(vi) are examples of mean field traces and intensity traces of a particular laser. Finally, panels (iii) show the same type of 2D histogram of the mean field extrema as described before. What we can observe in both cases is that there is not much difference in the type of dynamics that we can observe, be it for the FitzHugh-Nagumo-like type of regime, for the periodic self-oscillations regime or for the chaotic spiking regime. The most clear difference between the two cases (one laser vs all of the lasers) seem to be in the 2D histogram of the mean field extrema, which can change in amplitude, but most importantly, can display an upper an lower bound bifurcations currents at different DC-pumping current values.

Starting from these and other similar experimental realizations, whenever we change the selected population from one single laser to a group of lasers, we notice the following observations:

1. The mean field dynamics remains similar, so that we still observe the double bifurcation with dynamics going from (i) to (v) of Figure 3.25 when increasing the DC-pumping current;
2. When measuring the intensity traces individually of each laser, they all display a dynamics with is almost identical to the mean field, both for the ones inside and the ones outside the selected population. In short: they are all synchronized between themselves and to the mean field.
3. The value of the lower (I^l) and upper (I^u) bound bifurcation currents are proportional to the average threshold value of the population selected by the iris.

Observations 1. and 2. tell us that the dynamics of the mean field can be reduced to that of a single laser, even though in this case the dimensionality of the system has greatly increased. Furthermore, each laser has a dynamics in the emitted power which is basically identical to the mean field. We can explain these experimental facts empirically by the following considerations:

- The type of coupling at the moment does not allow for a partial de-synchronization of the population due to the opto-electronic setup. This is because the coupling is mediated by the mean field which is then translated into oscillations of the pumping current for the whole matrix, so that all of the lasers are affected by the current in the same amount. The coupling between the different elements can then only be set to be so weak so that the population is not affected, or so strong so that it doesn't allow for any partial or total de-synchronization of the population.
- The slower possible dynamics detectable in the system is of the order of 6 μs. This comes from the band-pass limitation on the feedback current dynamics. The lower boundary of the band-pass filter comes from the cutoff frequency of the high-pass filter, while the higher boundary comes from the maximum response of the slower electronics, which is around 150 kHz. This means that fluctuations shorter then around 6 μs are averaged by the system, and as a result the output power of the laser is slaved to the slower current dynamics.
- We do not have access to the fast evolution of the output power, nor to the carrier dynamics.

In summary, the strong coupling constant doesn't allow for a de-synchronization of the population, and even if the lasers may be de-synchronized in the faster oscillations of the electric field or carrier dynamics, these are averaged out in the opto-electronic feedback and in the detection so that they are not visible to us.

Nevertheless there can still be examples of de-synchronization effects in the shape of the output intensity of individual lasers. As we will see after, even though in the chaotic regime the spike events are recognizable in each single laser, their shape can be different depending on the laser under consideration. This is the evidence of a possible de-synchronization of the fast variables of the system. Furthermore, in Section 3.4 we will present slightly different realizations of the same type of opto-electronic setup where the differences of different intensity traces for different elements can be more pronounced. In any case, a possible theoretical reasoning behind the synchronization of the population will be put forward in the theoretical section 3.5.

In the case of Observation 3., the proportionality between the upper and lower bound bifurcation currents and the average value of the threshold for a population with be explored more in detail in subsection 3.3.5, while a theoretical

explaination will be put forward in the analytical and numerical section 3.5.

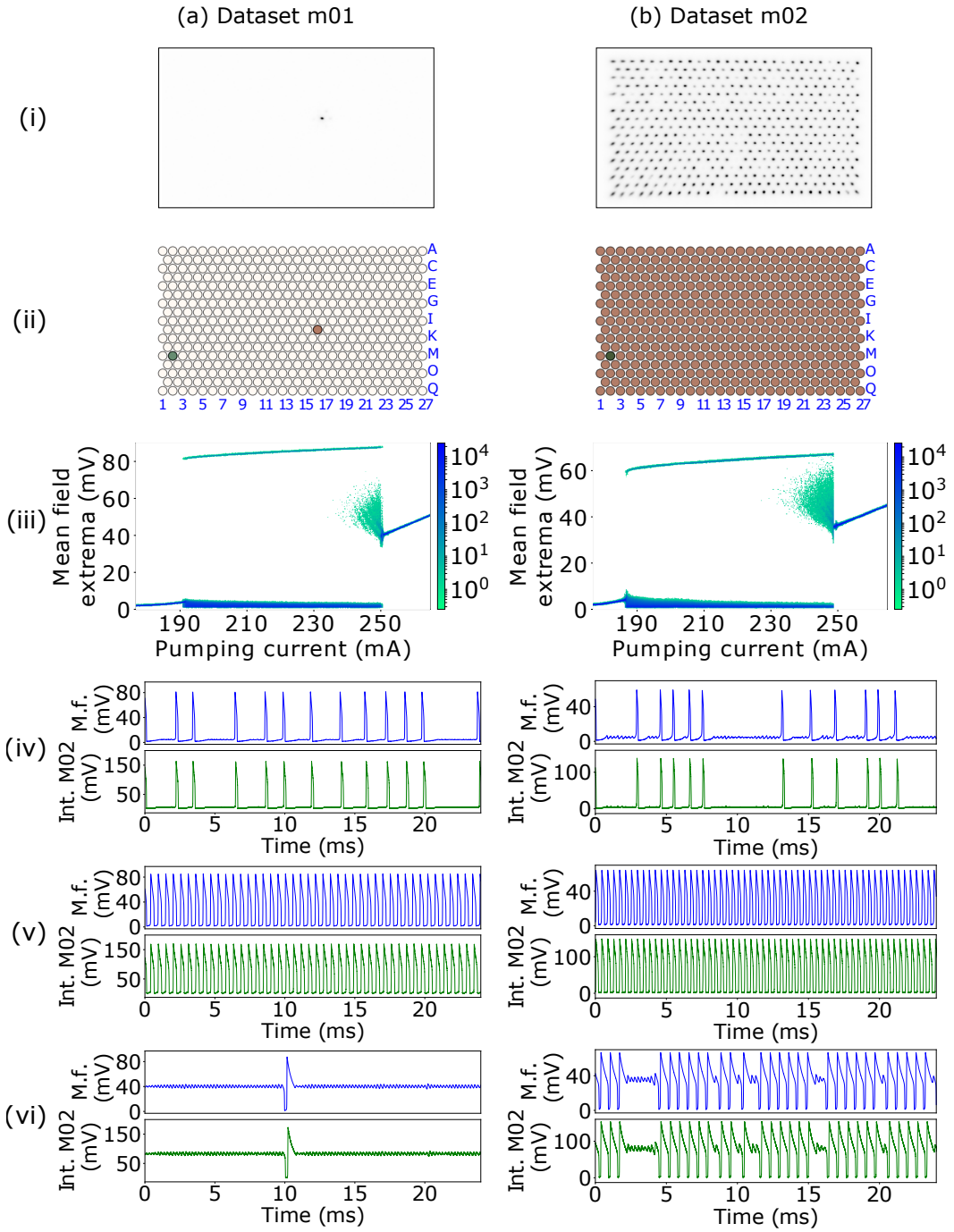

Figure 3.26: Summary results from datasets *(a)* m01, population size 1, and *(b)* m02, population size 451. The experimental parameters are described in Table 3.1. For each dataset the panels represent: *(i)* Image of the near field after the iris, MX=220 mA. *(ii)* Representation of the selected laser population. Laser $M02$ whose intensity is detected is highlighted in green. *(iii)* 2D histogram of the mean field extrema when varying the DC-pumping current. *(iv)(v)(vi)* Examples of Mean field traces and intensity traces of laser $M02$ at DC-pumping currents MX equal to (a) 192, 221, 251 mA and (b) 187, 218, 249 mA, top to bottom.

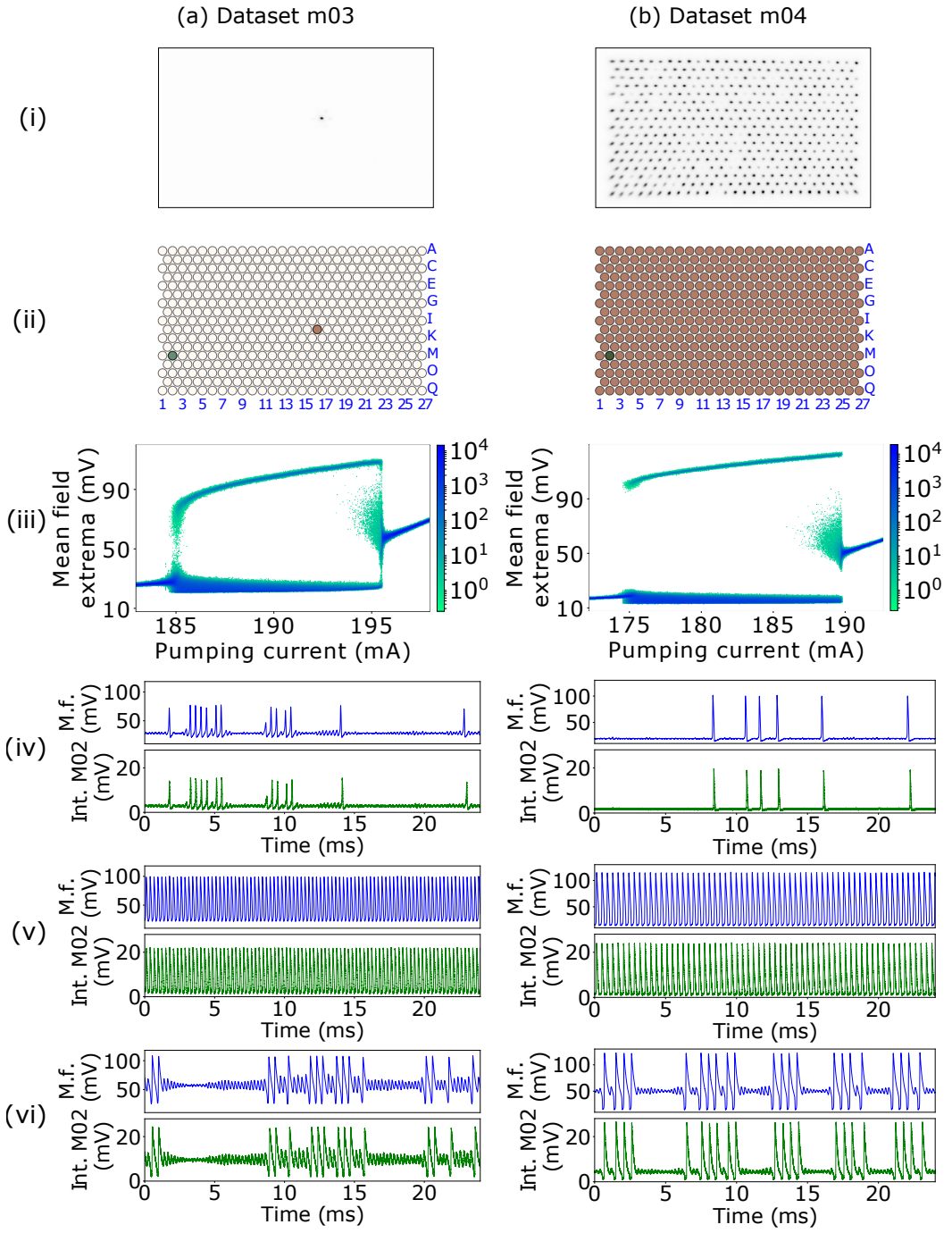

Figure 3.27: Summary results from datasets *(a)* m03, population size 1, and *(b)* m04, population size 451. The experimental parameters are described in Table 3.1. For each dataset the panels represent: *(i)* Image of the near field after the iris, MX=220 mA. *(ii)* Representation of the selected laser population. Laser $M02$ whose intensity is detected is highlighted in green. *(iii)* 2D histogram of the mean field extrema when varying the DC-pumping current. *(iv)(v)(vi)* Examples of Mean field traces and intensity traces of laser $M02$ at DC-pumping currents MX equal to (a) 185, 191, 196 mA and (b) 176, 183, 190 mA, top to bottom.

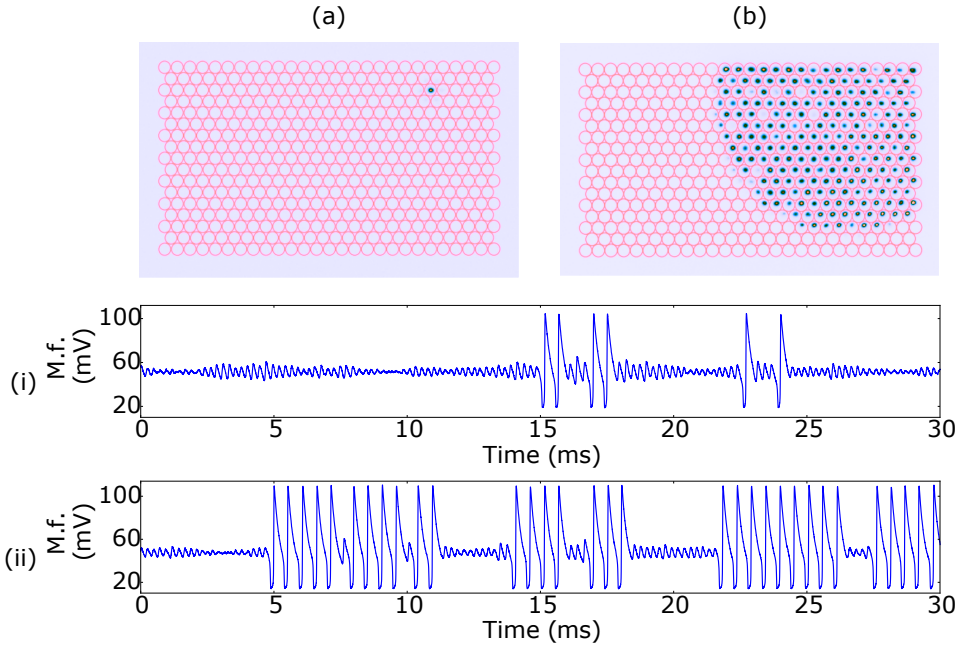

Figure 3.28: Comparison between similar chaotic dynamics when selecting only 1 laser VS many lasers. Selected data from datasets m05 (a)(i) and m06 (b)(ii). *(Top Images)* Imaging of two populations with sizes 1 (a) and 216 (b). *(i)* Mean field dynamics corresponding to case (a), MX=194.52 mA. *(ii)* Mean field dynamics corresponding to case (b), MX=192.09 mA.

Chaotic spiking regime In this paragraph we will concentrate on the description of the chaotic spiking regime, which for our choices of parameters always happen at transition between the periodic self-oscillations regime and the stationary steady state at higher currents. Figures 3.33 and 3.34 show the transition between periodic self-oscillations and chaotic spikes when increasing the DC-pumping current. It is the same type or chaotic spiking already observed in [Al-Naimee 2009] for a single quantum-well laser diode with optoelectronic feedback. This regime happens for any population size selected by the iris: from one laser (as in Figure 3.33) to all lasers (as in Figure 3.34).

Figure 3.28 shows two examples of this chaotic spiking regime for the same control parameter but laser populations of different sizes. Case (a)(i) displays the mean field trace for a single laser, while case (b)(ii) displays the mean field trace for a population of around 200 lasers. We can observe in both cases a dynamics which exhibit mixed-mode oscillations: small oscillation of varying amplitude around a fixed DC value, and big oscillations (the spikes) that happen at random times, all with the same shape and amplitude. This type of dynamics will be explained and reproduced in the Analytical and numerical section 3.5 by a 3D dynamical model that takes into account the evolution of the field, the carriers and the current.

Even though it seems clear from the modelling (as we will see) that this type

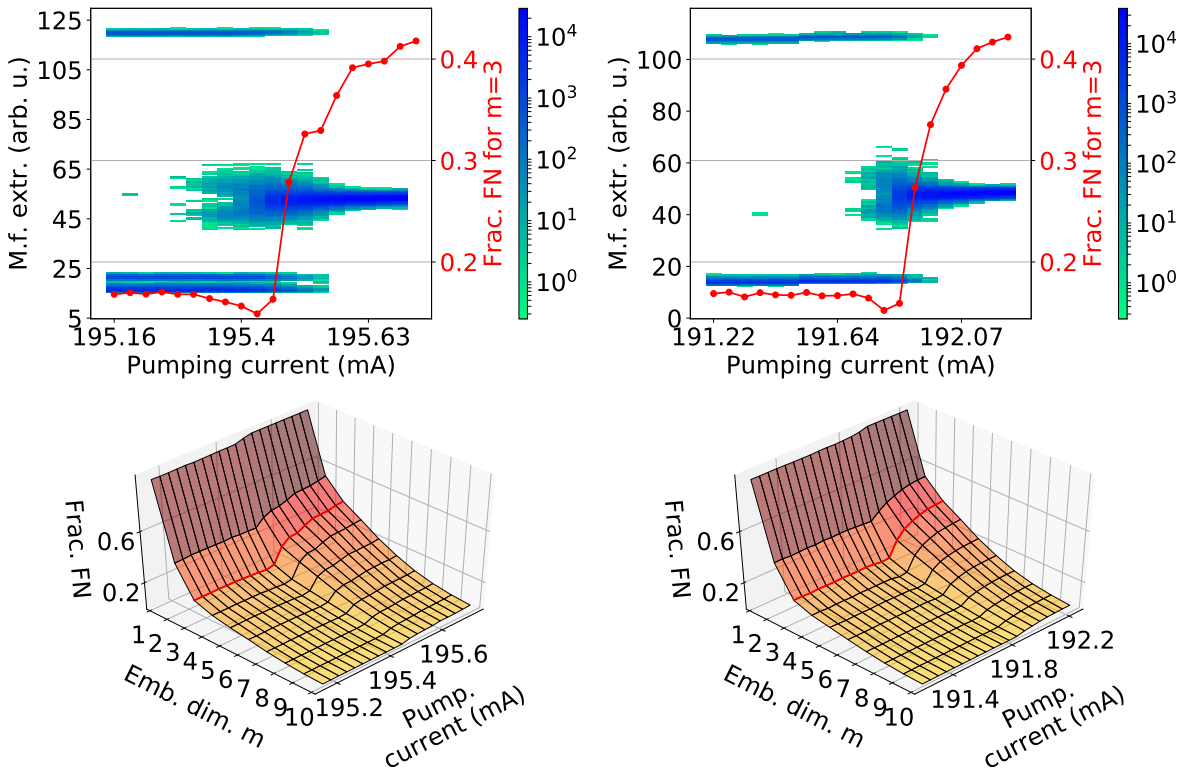

(a) Single laser $J16$ (b) All lasers

Figure 3.29: Analysis of the fraction of false neighbours (FN) depending on the embedding dimension, using the *false_nearest* program of the TISEAN software [Hegger 1999]. Data from dataset (a) m08, single laser $J16$ and (b) m09, all lasers. *(Top)* Evolution of the fraction of FN for a 3-dimensional embedding, as a function of the DC-pumping current, superimposed on the 2D histogram of the mean field extrema. *(Bottom)* Fraction of FN at different embedding dimensions as a function of the DC-pumping current.

of oscillations is indeed the result of a deterministic 3-dimensional chaotic process, it would be useful nevertheless to characterize the dimensionaliy of the dynamics. To do so, we analyse the spiking chaotic traces by employing the *false_nearest* neighbours program provided by the TISEAN software [Hegger 1999]. This program is an implementation of the algorithm described in [Kennel 1992] that allows to determine the proper embedding dimension when applying the Ruelle–Takens embedding technique on a timetrace. Given a data point in an m-dimensional embedding, the program will look for all of its nearest neighbours and it will iterate their position one delay-step into the future. If the new distance between one of the neighbours becomes smaller than the standard deviation of the data divided by a given threshold, the point is marked as a false neighbour (FN). The output of the program is the fraction of the FN over the whole data. We apply this algorithm with a delay of $\tau = 40\,\mu$s

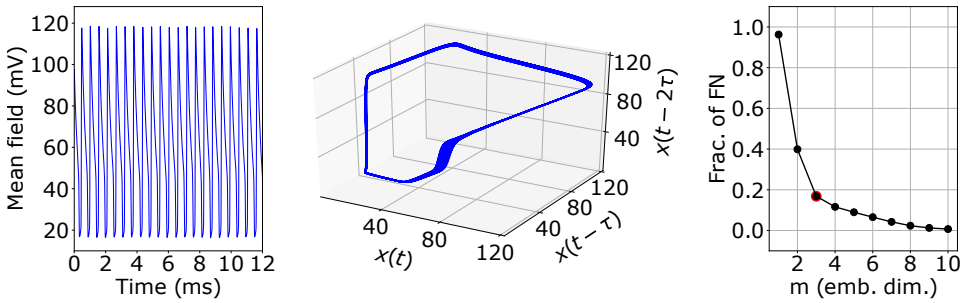

(a) MX=195.279 mA

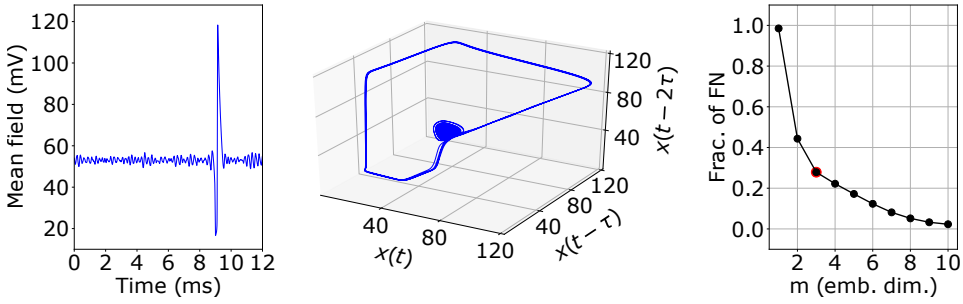

(b) MX=195.286 mA

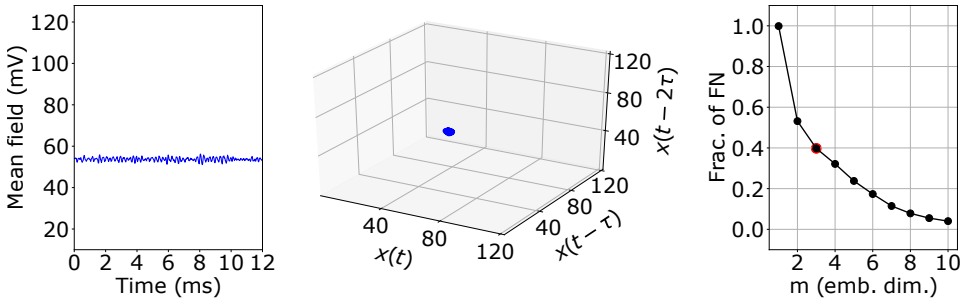

(c) MX=195.664 mA

Figure 3.30: Single laser case. From left to right: mean field timetraces, attractor reconstruction in 3D embedding space with $\tau = 40$ μs and fraction of false neighbours (FN) at different embedding dimensions. Each row corresponds to a different DC-pumping current value MX. Same data as in Figure 3.29(a).

on the timetraces of the mean field, after filtering the data with a Gaussian filter with $\sigma = 10$ (σ is the standard deviation for the Gaussian kernel). Figure 3.29 shows the results of the analysis for a limited range of DC-pumping currents in the vicinity of the transition from periodic oscillations to stationary state, in the case of a population composed by a single laser (a) and all the lasers (b). The top panels represent in both cases the evolution of the fraction of false neighbours (FN) in the case of a 3-dimensional embedding.

In both cases, we observe an increase in the number of FN for a 3-dimensional embedding when crossing the transition between the periodic self-oscillations regime and the stationary state. This means that, even though there is an in-

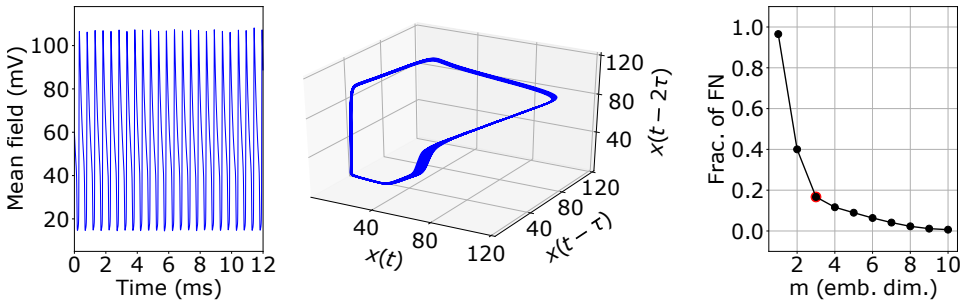

(a) MX=191.644 mA

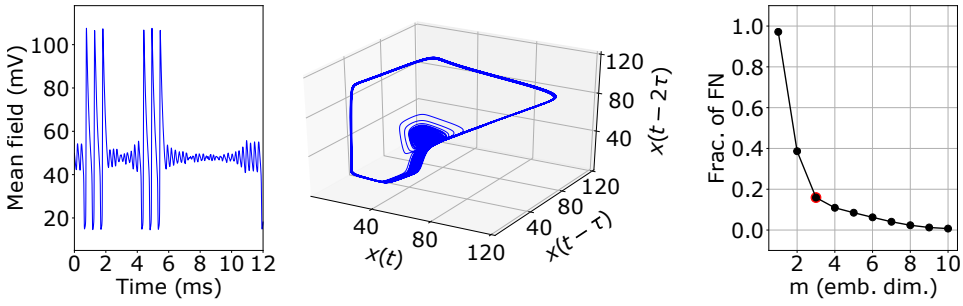

(b) MX=191.856 mA

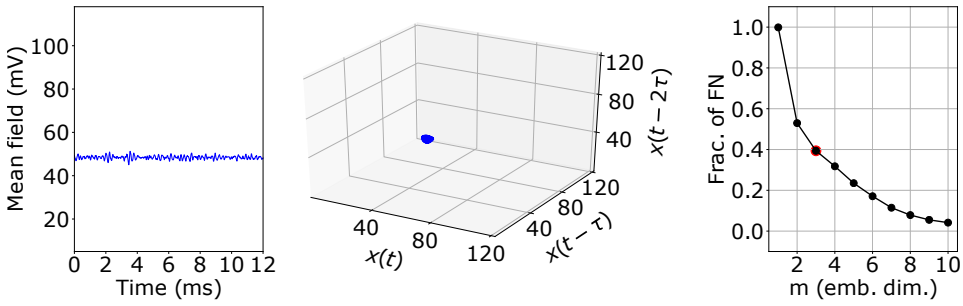

(c) MX=192.067 mA

Figure 3.31: All lasers case. From left to right: mean field timetraces, attractor reconstruction in 3D embedding space with $\tau = 40$ μs and fraction of false neighbours (FN) at different embedding dimensions. Each row corresponds to a different DC-pumping current value MX. Same data as in Figure 3.29(b).

crease in the dimensionality of the system when going from the self-oscillations to the chaotic regime, the final stationary state seems to have an even higher dimensionality than the chaotic spiking regime. We can conclude that we are unable to observe exactly the transition from the periodic self-oscillations to the chaotic regime from the fraction of FN due to the effects of the noise in the stationary state which increases the FN value.

We can nevertheless check the randomness of the spike sequences in the chaotic spiking regime by looking at the distribution of the interspike interval for the traces, in a similar way to what was done in the now notorious [Al-Naimee 2009] paper. Figure 3.32 reports this type of study in the case of

all lasers selected, but a similar result can be found in the case of a single laser. Here we consider two traces, one in the periodic self-oscillations regime (a), and one in the chaotic spiking regime (b). We then detect all of the maxima of the timetraces (the red points) and we consider the distribution of the time differences between the maximum of one spike and the next. In the case of the periodic self-oscillations, we observe a distribution which is highly peaked at around 0.5 ms, which is the average distance between two spikes in this periodic trace. In the case of the chaotic spiking timetrace, the distribution displays a long exponential tail, as evidence of the erratic nature of the sequence, but with also a sequence of sharp peaks and gaps that repeats periodically after the first peak at 0.5 ms with a period of around 0.24 ms. As explained in the paper, this reveals the existence of unstable periodic orbits embedded in the chaotic attractor.

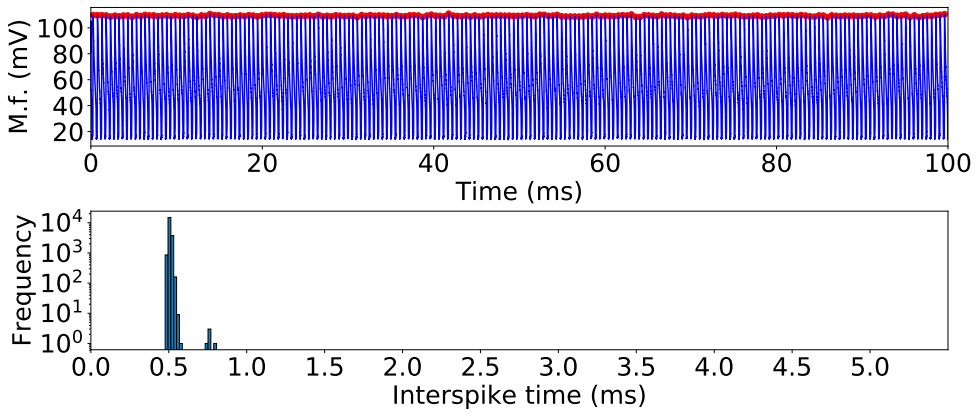

(a) MX=191.644 mA

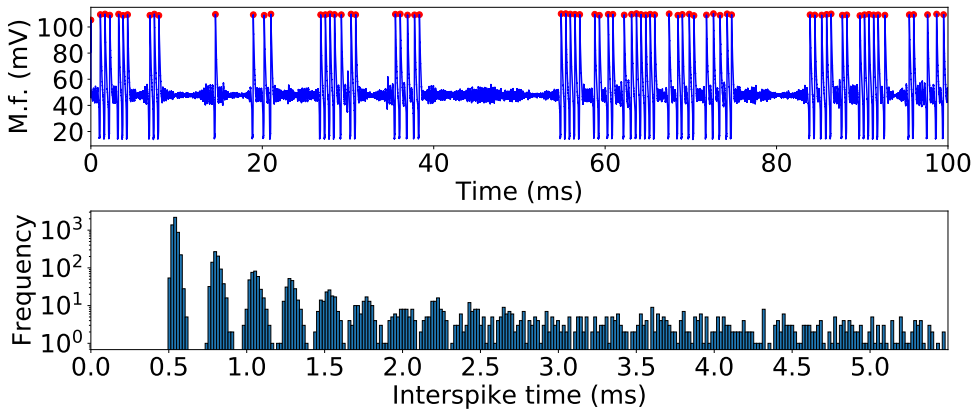

(b) MX=191.856 mA

Figure 3.32: Interspike distribution, all lasers case, at two DC-pumping current values corresponding to *(a)* Periodic self-oscillations, and *(b)* Chaotic spiking regime. The top panels represent the mean field timetrace while the bottom panels represent the interspike distribution frequency. Same data as in Figure 3.29(b) and as the first two rows of Figure 3.31.

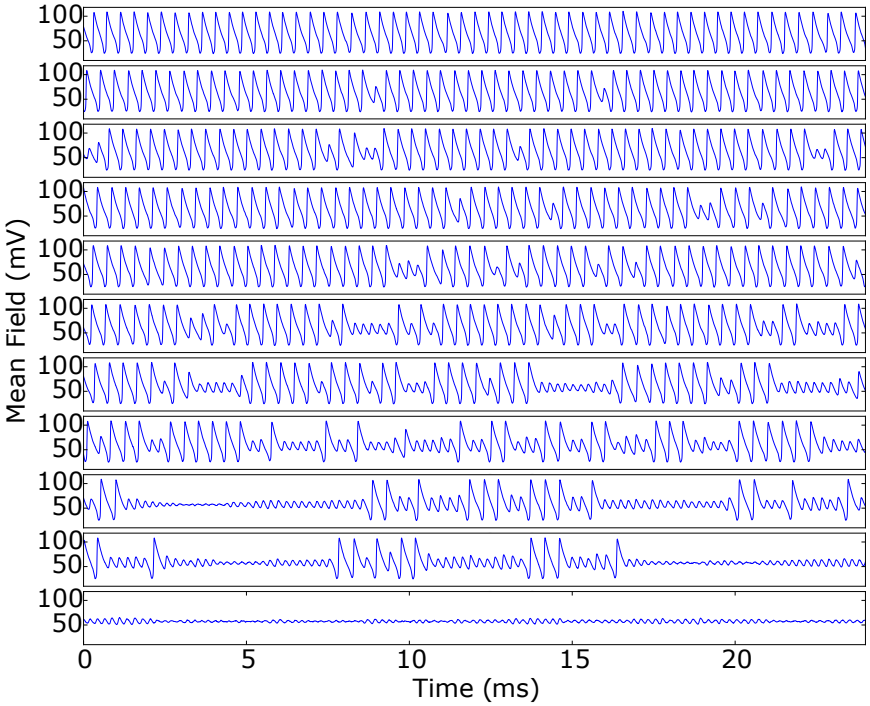

Figure 3.33: Example of chaotic traces close to the upper bound bifurcation when only one laser is selected. Selected data from dataset m03. The DC-pumping current MX ranges from 196.36 mA to 196.52 mA, equally spaced, top to bottom.

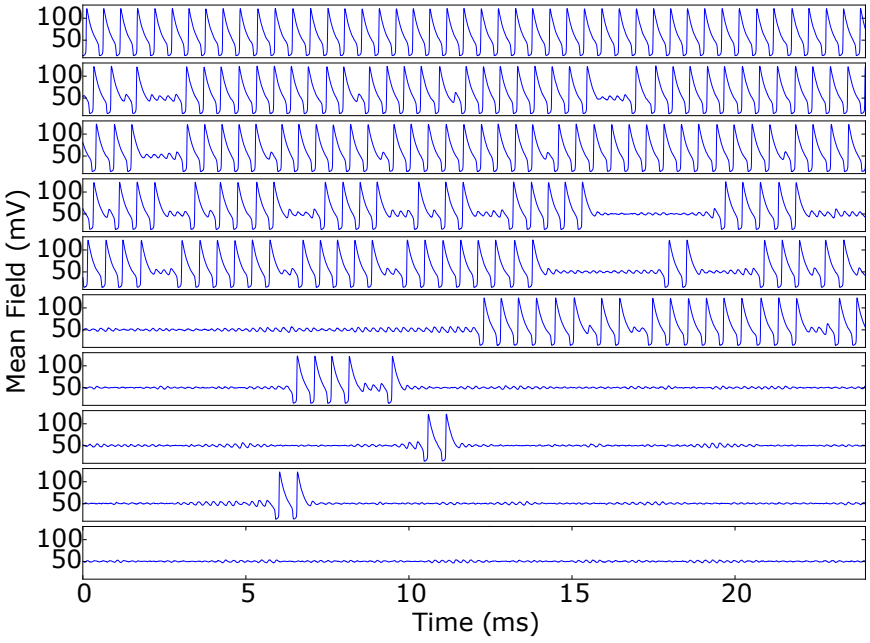

Figure 3.34: Example of chaotic traces close to the upper bound bifurcation when all 451 lasers are selected. Selected data from dataset m04. The DC-pumping current MX ranges from 190.21 mA to 190.38 mA, equally spaced, top to bottom.

Detection of multiple lasers and synchronization In the previous Figures, we have always shown the mean field timetraces as a characterization of the dynamics of the whole system, as we have already stated in observation 2. that the dynamics of any laser under consideration follows the same slow dynamics as the mean field.

This was observed in all of the experimental realizations, where, most of the times, the full detection system on the oscilloscope included the mean field traces, the traces of two chosen single lasers and the output monitoring signal that comes from the power supply, which is proportional to its pumping current value. An example of such a complete detection can be seen in Figure 3.35. Here we show the same data already displayed in Figure 3.27 but with the addition of an intensity trace for the laser $J16$ and the output monitoring signal from the power supply.

Comparing the mean field with the intensities of $M02$ and $J16$, we notice that the timetraces are fully synchronized, both in the small oscillations and in the big spikes. However, looking at the shape of the traces, one can observe that, while in the case of a single-laser population (i) the shape is almost identical to the mean field, in the case of an all-laser population (ii), the intensities of the single detections are slightly different. Notice how the proportion of the downwards "foot" which precedes each maximum of the spikes and the amplitude of the maximum of the spike with respect to the base DC value is different between the single detection traces and the mean field trace.

This was observed in many different realizations, and it stems from the fact that, even though the dynamics of each laser is driven by the same signal, namely the feedback current (which is proportional to the output monitoring signal), each laser will translate these oscillations into a different laser output due to their slight differences in the $L-I$ curves. This means that a laser with an higher threshold will experience a lower amplitude of intensity oscillations than a laser with a lower threshold, given the same feedback current signal. These differences are usually not very marked in the realizations described in this section; however, we will show in section 3.4 how they can be become very important for slightly different realizations of the same type of optoelectronic setup.

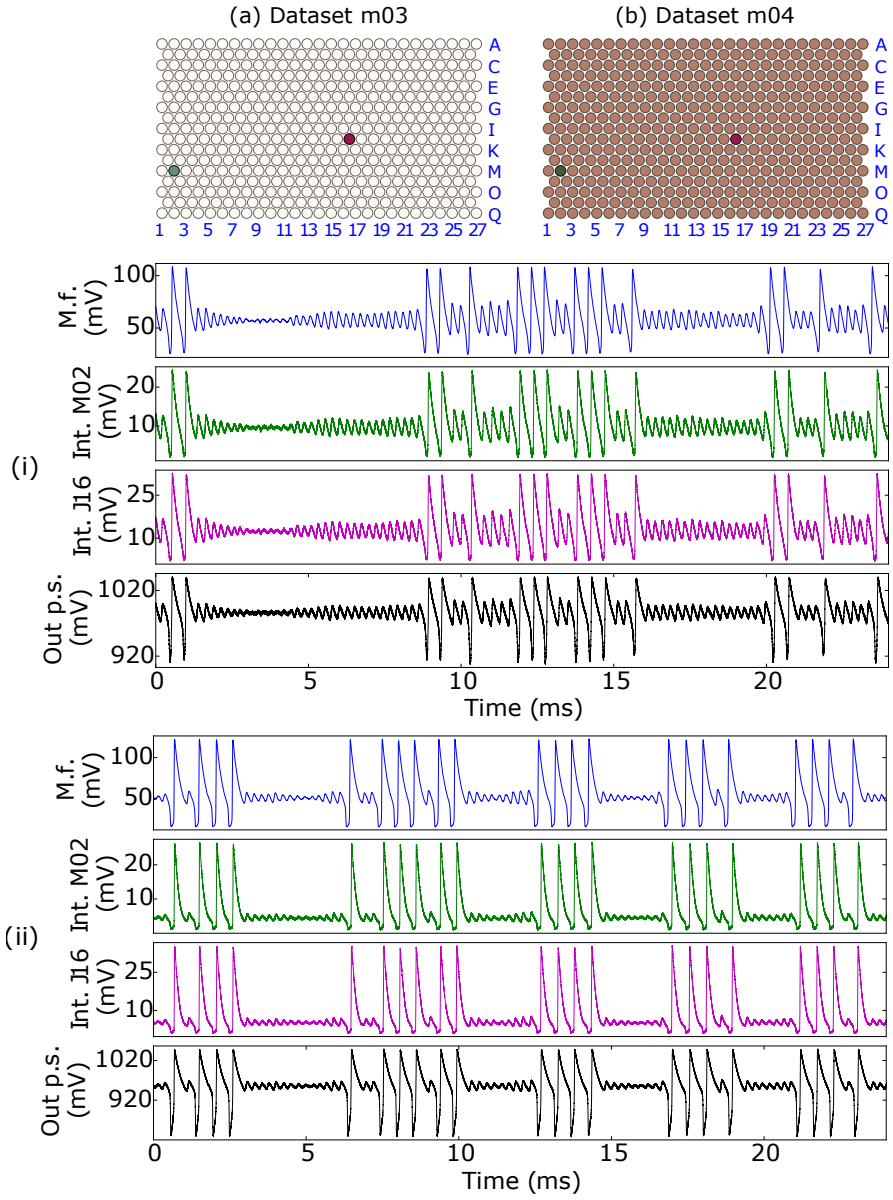

Figure 3.35: Example of detection of multiple lasers at the same time, along with the mean field, in the chaotic regime. Selected data from datasets m03 (a)(i) and m04 (b)(ii). *(Top Images)* Matrix representation of the the selected population, consisting laser $J16$ for (a)(i) and of all 451 lasers for (b)(ii). We detect in both cases the intensities of lasers $M02$ (green dot) and $J16$ (magenta dot). *(i) and (ii)* Dynamics of the selected population, with MX=196.49 mA for (i) and MX=190.30 mA for (ii). The panels represent, from top to bottom: the mean field intensity, the intensity of laser $M02$, the intensity of laser $J16$ and the output monitoring signal from the power supply. All of the timetraces are synchronized and look similar, apart from small amplitude differences.

3.3.5 Dependence of the dynamics on the selected population

In the previous section we remarked how the most visible difference between the type of dynamics of different populations has been found in the shift in the boundaries of the 2D histogram of the mean field extrema. That is, the location of the upper (I^u) and lower (I^l) bound bifurcation currents seem to depend on the selected population, and we also already foreshadowed that their value seems to be proportional to the average threshold value of the selected population.

The fact that the particular shape of the $L-I$ curves must be related to the location of I^u and I^l can be explained by observing that, as far as the current in the electrical feedback loop is concerned, the only difference between one laser and the next is only the amount of light that the particular laser can emit given a certain pumping value. This is due to the nature of the opto-electronic feedback, which realizes an intensity mean field on the feedback photo-detector, therefore ignoring all other coherent properties of the various lasers. When changing a population, we are therefore changing the "effective $L-I$ curve" of the whole system, since the total light output will depend on the $L-I$ curves of only the lasers that have been selected for the feedback. And as it turns out, there is one parameter of the $L-I$ curves of the selected laser that is capable of describing most of their shape, and that is the threshold value. As we are operating close to the global threshold value of the whole population at 183.3 mA, the threshold of each laser will be highly correlated with the amount of light that a laser can produce given a certain oscillation range. As an example, for an oscillation range centered on 183.3 mA, a laser with a lower threshold than the average will contribute much more strongly to the mean field than a laser with a higher threshold than the average, which will still be in the "off" part of its $L-I$ curve. What we will show here, and later in the Analitical and numerical section 3.5, is that the average threshold value is enough to predict the type of dynamics that can be expected from a certain population.

Given that in the following we will refer many times to different types of pumping current values (for the upper and lower bound of the bifurcations and for the thresholds), we introduce the following notation:

$$\begin{aligned} I^u &= \text{Upper bound bifurcation current} \\ I^l &= \text{Lower bound bifurcation current} \\ \mathcal{I}^{th} &= \langle I^{th} \rangle = \text{Average threshold of a certain population} \end{aligned} \tag{3.6}$$

The average threshold of a population will be calculated from the threshold distribution of the single lasers I^{th} acquired during the characterization of the laser matrix, as shown in Figures 3.22 and 3.23. An equivalent notation with

a subscript s will be used when we specify the size s of the population under study:

$$\begin{aligned} I_s^u &= \text{Upper bound current of a population of size s} \\ I_s^l &= \text{Lower bound current of a population of size s} \\ \mathcal{I}_s^{th} &= \langle I_s^{th} \rangle = \text{ Average threshold of a population of size s} \\ \mathcal{I}_{451}^{th} &= \langle I_{451}^{th} \rangle = 183.3 \text{ mA} = \text{ Global average threshold of all 451 lasers} \end{aligned} \tag{3.7}$$

Different groups of the same size but different threshold values A first experimental observation of the relationship between the average threshold of the population and the observed dynamics can be seen in Figure 3.36. Here we fix all of the control parameters, including the DC-pumping current at 193.50 mA, and we record the different types of dynamics that we can observe from different groups of size 7. In the figure, we have selected three of those groups, group A, B and C, which are the ones represented in the panel on the top. Looking at their mean fields, we observe that group A is in the periodic-self oscillation regime; group C is in the stationary state and group B is in the regime in-between the two: the chaotic spiking regime.

Furthermore, looking at the $L - I$ curves of the selected populations (the panels on the right), we note how group A has a higher average threshold of $\mathcal{I}_7^{th} = 185.63$ mA, while group B has a lower value of $\mathcal{I}_7^{th} = 182.88$ mA and group C has an even lower value of $\mathcal{I}_7^{th} = 180.81$ mA. The type of dynamics observed in these groups is then correlated to their average threshold value, so that to higher threshold corresponds an dynamics of higher DC-pumping current in the bifurcation diagram of a single laser.

However these three groups have been arbitrary chosen between the 25 possible measurements of 7 lasers performed for this dataset. In any case, we will show later how this relationships emerges from all of the data taken with the same control parameters, so this figure has to be considered only as a "proof of concept" of our observation.

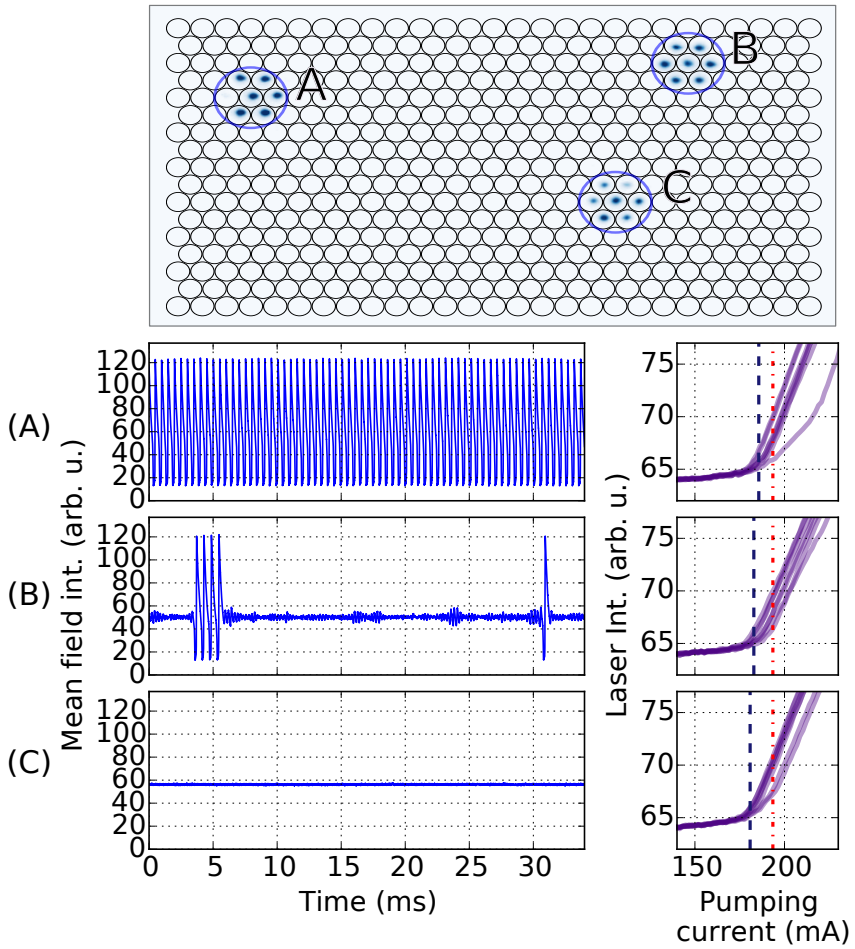

Figure 3.36: Dynamics of small populations of size 7. Selected results from dataset m07, fixing the value of the DC-pumping current. All the other parameters (fixed for all population samplings) are described in Table 3.1. *(Top image)* Imaging of three different populations A, B and C. *(A, B, C)(Left)* Respective dynamics associated with the selected popultaion. *(Right)* Superimposed L-I curves of all the lasers belonging to the population. The black dashed lines show the average threshold for each population (A: 185.63 mA, B: 182.88 mA, C: 180.81 mA) and the dash-dotted lines show the constant current value MX here selected of 193.50 mA.

Dynamics of populations with increasing size at fixed control parameters Let us now consider the dynamics of a population of increasing size, when keeping all the control parameters the same. The figures here reported all come from measurement m06, where we acquired data from 19 groups of different sizes, from 1 to 451 (the whole population). Given what we know about the relationship between the average threshold and the type of dynamics, we expect to see that, as the average threshold of the population gradually reaches its global average value of $\mathcal{I}^{th}_{451} = 183.3$ mA, so does the dynamics of the mean field.

Figure 3.37 shows the result from three different groups from this dataset called D, E and F with populations of increasing sizes of 19, 251 and 451 lasers respectively. The top panel represents an image of the selected populations on the Near field. Note how they are all centred on the same laser, so the population can only add new members when increasing the size but not eliminate old ones. The 2D histogram of the mean field extrema for the three populations show that, even though the general shape of the bifurcation stays the same, the value of the lower (I^l) and upper (I_u) bifurcation bounds are shifted towards lower values when increasing the population size. The corresponding values of the average threshold, visible in the $L - I$ curves in the right panels, also shifts towards lower values, from $\mathcal{I}^{th}_{19} = 185.32$ mA for the D population, to $\mathcal{I}^{th}_{451} = 183.29$ mA for the F population.

This type of measurement between the lower and upper bifurcation bounds and the average threshold of the selected population is better quantified in Figure 3.38. Here we plot the difference in value between the upper (I^u_s) and lower bound currents (I^l_s) at different sizes and their value for the whole population (I^l_{451} and I^u_{451}), as the size of the population increases. The same is done for the difference of the average threshold $\mathcal{I}^{th}_s$ and the global average threshold $\mathcal{I}^{th}_{451}$. What we observe is that the three curves closely follow each other, which means that the average value of the threshold determines what is the corresponding I^l and I^u value of the population. Hence, as the threshold reaches its global average when increasing the size from 1 to 451, I^l and I^u closely follow.

Figure 3.38 also shows that, for this particular realization, the average value of the threshold reaches a maximum at around size 25 and then slowly decreases. This decrease will be the same that we can expect from a deviation to the mean that slowly converges towards the global average, which will go as $\sim s^{-1/2}$, s being the number of lasers. Figure 3.39 shows a fit of such a type of function for the upper bound current data with $s \geq 75$, and we find that the fit closely follows the data. We propose this inverse-square-root function convergence based on how the empirical mean converges to the true statistical mean due to the central limit theorem.

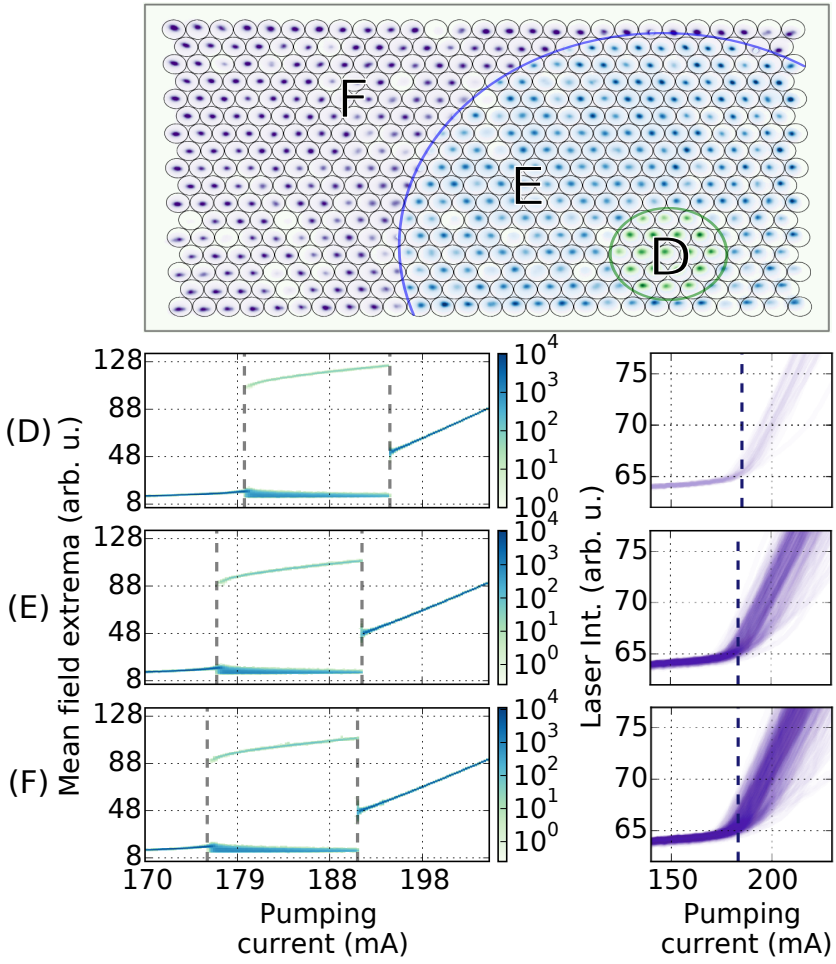

Figure 3.37: Dynamics of populations with increasing size. Selected results from dataset m06. The experimental parameters are described in Table 3.1. *(Top image)* Imaging of three different sample populations D, E, F with populations sizes of 19, 251 and 451 respectively. *(D, E, F)(Left)* Respective 2D histogram of the mean field extrema when varying the DC-pumping current. *(Right)* Superimposed L-I curves of all the lasers belonging to the population. The black dashed lines show the average threshold for each population (D: 185.32 mA, E: 183.70, F: 183.29 mA).

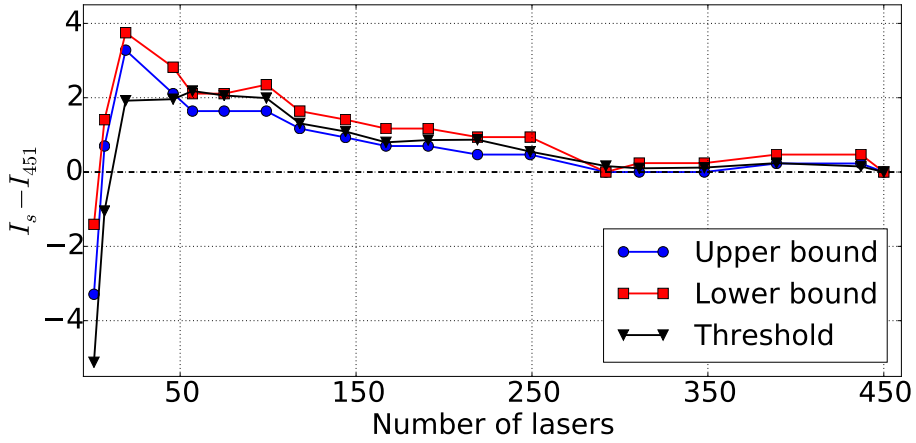

Figure 3.38: Evolution of the current values of the upper bound and lower bound of the bifurcation, along with the average threshold of the population, as the number of selected lasers increases. All data from dataset m06. Note how the trends of all three curves is correlated, and as the threshold naturally reaches its global average value $\mathcal{I}_{451}^{th}$, so do the upper and lower bound current values.

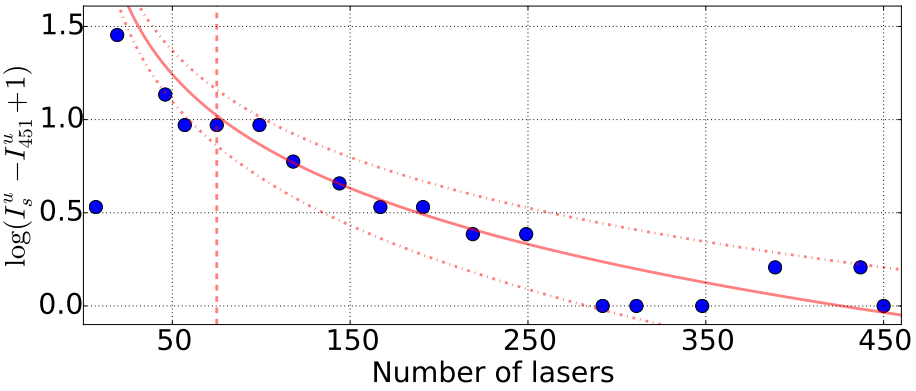

Figure 3.39: Decay of the upper bound current value as the number of selected lasers increases. Same data as in Figure 3.38. The points to the right of the vertical red dashed line (≥ 75) are fitted with a function of the type $I_s^u(s) = a\, s^{-1/2} + b$, which gives as best fit parameters $a = 26.5$ and $b = -0.284$, with $R^2 = 0.924$. The two red point-dashed curves represent the two limits at ± 1 *stddev* from the fit parameters.

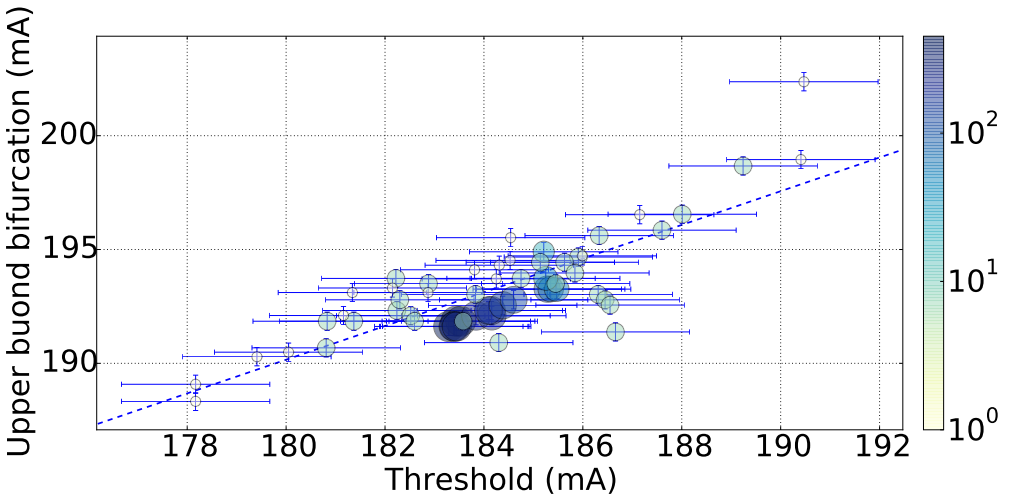

Figure 3.40: Linear fit of the value of the current corresponding to the upper bound of the bifurcation I^u for populations of laser of different sizes, from 1 to 451, as a function of the average threshold of the population $\mathcal{I}^{th}$. The size and color of the scatter points is logarithmically scaled to the group sizes. All data from datasets m05, m06 and m07 (same parameters). The linear fit of the type $I^u(\mathcal{I}^{th}) = a\,\mathcal{I}^{th} + b$ gives as best fit parameters $a = 0.740$ and $b = 56.9$ mA, with $R^2 = 0.673$.

Linear dependence of the upper bound bifurcation current on the average threshold for all populations sizes and mean field convergence In all of the previous figures we remarked how the average threshold was correlated with the observed dynamics in the mean field, when looking at individual cases. Here we present a figure which tests and quantifies this relationship.

Figure 3.40 collects all of the data from datasets m05, m06 and m07 for a total of 60 different groups of variable population size, from 1 to 451. For each group, we plot their upper bound bifurcation value I^u as a function of their average threshold value $\mathcal{I}^{th}$. The size and color of the different scatter points is scaled as the size of each group, so that bigger group sizes will be shown as bigger and darker blue.

We note that, independently on the size of the group, the threshold and upper bound values are linearly dependent, as they are well fitted by a function of the type $I^u(\mathcal{I}^{th}) = a\,\mathcal{I}^{th} + b$. This confirms our observation 3. on the proportionality of the upper bound bifurcation to the average threshold. This experimental finding will be explained in the Analytical and numerical 3.5 section as a consequence of the model.

Furthermore notice how, the bigger the size, the closer the groups get toward the global average value represented by the biggest point. This also means that, as the size of group increases, the type of dynamics converges towards a stable condition which is the one that characterizes the global average. As

another example, looking again at Figure 3.38, we notice that after around 275 lasers, the type of dynamics stays the same and equal to the global average. We therefore observe a convergence of the dynamics towards a simplified case which corresponds to the one having as a bifurcation parameter the global average of the bifurcation parameters of the population. This simplification of the dynamics will be reproduced numerically when studying the physical model.

3.4 Alternative setups, miscellaneous mean field traces and results

In the previous section we described the results obtained when employing the opto-electronic feedback loop composed of a logarithmic amplifier, a fractional-gain amplifier and an high-pass filter as in Figure 3.8. Before turning to the theoretical side of the story on this setup, we present here some additional results that have been acquired using similar but slightly different opto-electronic setups, or in regimes of control parameters that have not been explored in depth. The main difference between these alternative setups and the usual one consists in the fact that in these preliminary versions the electronic feedback loop was not entirely composed of active elements, but also of passive ones. Changing the amplification (or attenuation) also implied a change in the high frequency cut-off. This problem has been later solved by employing all active elements (featuring operation amplifier).

The purpose of this section is to document the work that has been done on these alternative setups, which will also give us some insight on the general properties that one can expect from an opto-electronic type of system. In particular, we will concentrate on possible differences between the dynamics of single elements and that of the main field. We will show that, even if they are always seemingly synchronized, small or even large amplitude differences can be observed in the intensity timetraces of different laser elements.

3.4.1 Setup with variable resistance and high-pass filter

An alternative type of opto-electronic setup that has been employed in the experiment is the one shown in Figure 3.41, which employs a variable resistance (composed of a 100 kΩ fixed resistance in series with a variable [0-100] kΩ resistor) and a high-pass filter.

Dynamics of two lasers: the up-laser and the down-laser When letting all of the lasers participate to the feedback loop and looking at the dynamics of the mean field and of other single lasers at the same time, some differences between different lasers dynamics can be spotted. Figures 3.42 and 3.43 show the simultaneous detection of the mean field and another laser: in the case of Figure 3.42 the "up-laser", and in the case of Figure 3.43 the "down-laser". These two lasers are two out of the 451 lasers of the matrix, and they have only been identified by their relative vertical position, "up" and "down", in the sense that, to go from the "down" laser to the "up" laser experimentally, one has to move up the iris selecting the near field in the vertical position using micrometer screws.

In the case of the up-laser, we notice how the mean field dynamics displays some mixed-mode chaotic spiking, and so does the intensity of the up-laser.

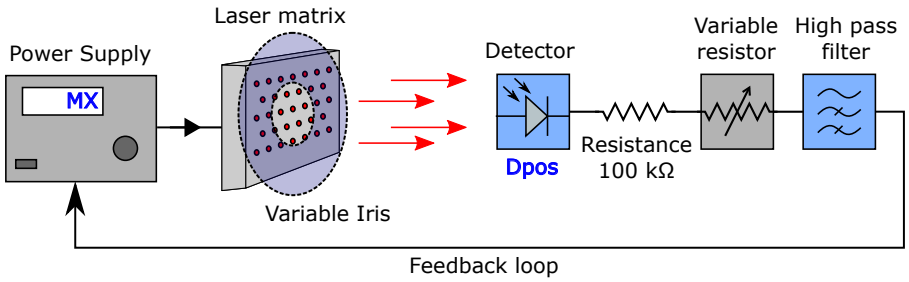

Figure 3.41: Alternative opto-electronic setup, with a variable resistance and a high-pass filter in the feedback loop.

By reconstructing the attractor in 2D with a time delay of $\tau = 40$ μm, we note that, apart from small differences, the two attractors look the same, with a small-oscillations core near the origin, and large excursions that corresponds to the chaotic spikes. The small differences that we can observe are either due to the slightly different response of the photo-detectors, or to small intensity-response differences of the up-laser to the pumping current oscillations.

Instead in the case of the down-laser, given the same experimental condition and the same photo-detectors, we observe that the intensity of the down-laser doesn't display the small amplitude oscillations, or at least not with the same relative amplitude to the peak value of the chaotic spikes, as before. These differences, which can be seen directly from the intensity timetraces, are even more evident if looking at the 2D attractor reconstruction. While the attractor for the mean field looks identical, in the case of the down-laser the core of small amplitude oscillations near the origin has collapsed into a single point.

Another example of the disappearance of the small amplitude oscillations can be visible in Figure 3.44. Here we detect at the same time the down-laser, as before, and another reference-laser which is far from the up and down lasers in the near field. Looking at the timetraces or at the attractors we note that, while the reference laser does show the same small amplitude oscillations as the mean field, the down-laser does not, and the oscillations are reduced to a point in the attractor.

These differences are most certainly due to the threshold value of the down-laser, which must be higher than the up-laser and the reference-laser, as the maximum amplitude of the chaotic spikes is also lower for this laser. Given the same pumping current oscillations from the power supply, its intensity response is lower and, while it stays mostly in the "off" state of the $L - I$ curve for the small oscillations, it spikes along with the mean field for the large current oscillations corresponding to the chaotic spikes.

This type of dynamics suggests that the down-laser only participates to the mean field during the big spikes, and it may even be de-synchronized in the fast variables during the small oscillations.

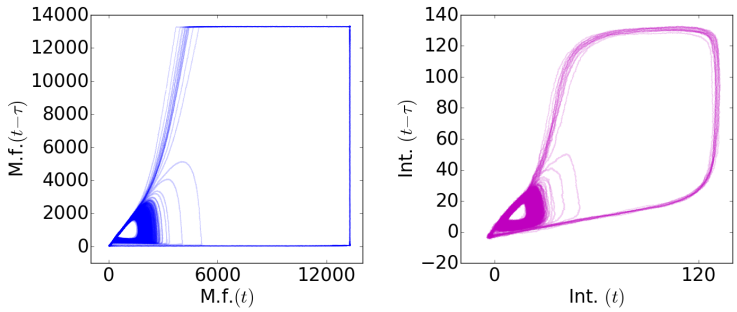

(a) 2D attractor reconstruction with $\tau = 40$ μs.

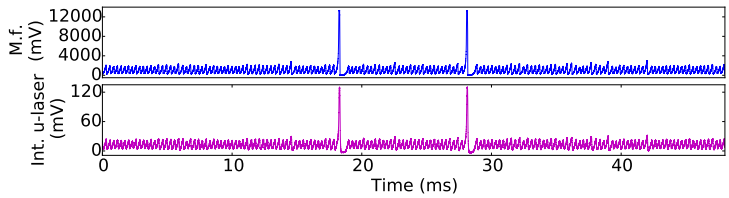

(b) Timetraces of the mean field and the up-laser.

Figure 3.42: Dynamics of the mean field *vs* the up-laser with the alternative setup that includes a variable resistance as in Figure 3.41. Parameters as follows: size=all lasers; $MX = 189.9$ mA; Dpos=3; Variable resistor $\in [0 - 100]$ kΩ and filter cut-off frequency $\in [20 - 5000]$ Hz (data of 11/09/17). In both cases the small amplitude oscillations are visible, both in the timetraces and in the attractors.

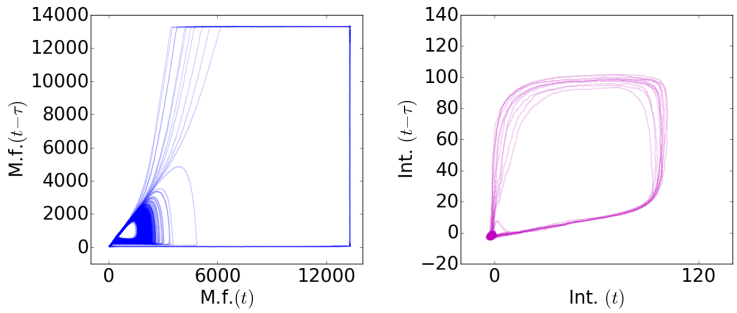

(a) 2D attractor reconstruction with $\tau = 40$ μs.

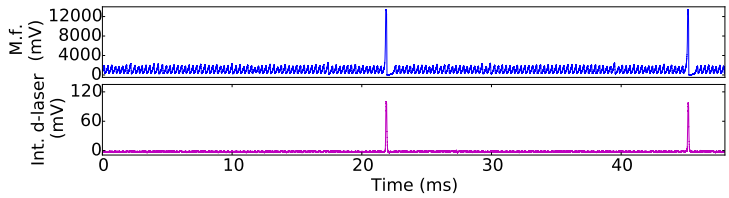

(b) Timetraces of the mean field and the down-laser.

Figure 3.43: Dynamics of the mean field *vs* the down-laser with the alternative setup as in Figure 3.41. Same parameters as in Figure 3.42. In this case only the mean field show the small amplitude oscillations, both in the timetraces and in the attractors.

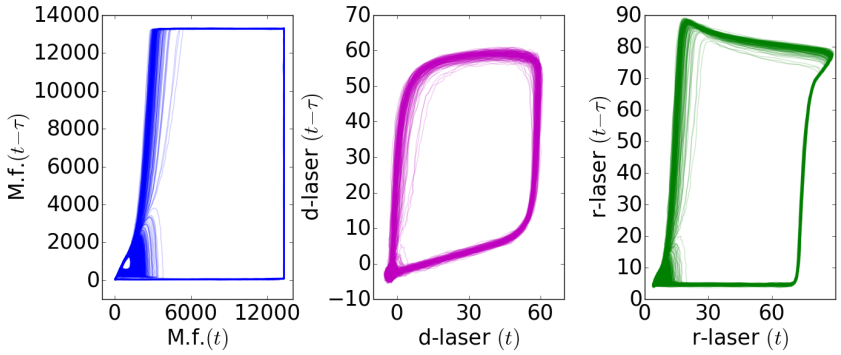

(a) 2D attractor reconstruction with $\tau = 40$ μs for the Mean field (left), the down-laser intensity (middle) and the reference-laser intensity (right).

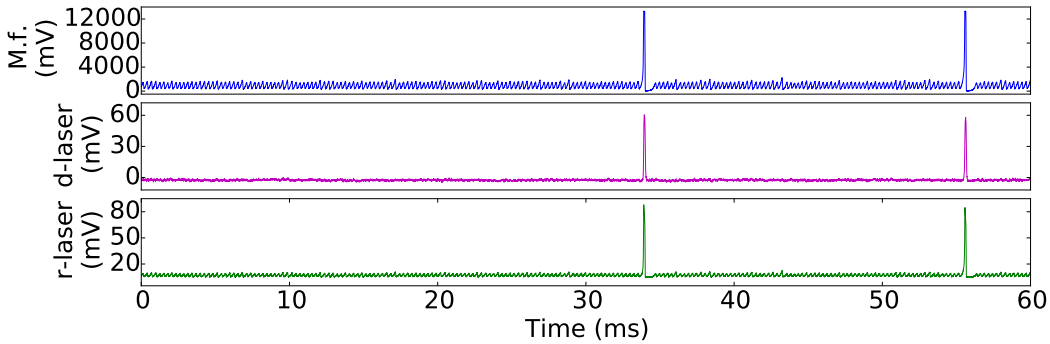

(b) Timetraces of the mean field, the down-laser intensity and the reference-laser intensity.

Figure 3.44: Dynamics of the mean field *vs* the down-laser and a reference-laser with the alternative setup that includes a variable resistance as in Figure 3.41. Similar parameters as in Figure 3.42 (data of 12/09/17). Notice how, apart from differences in the photo-detectors responses, the down-laser doesn't show the small amplitude oscillations, while the reference-laser does.

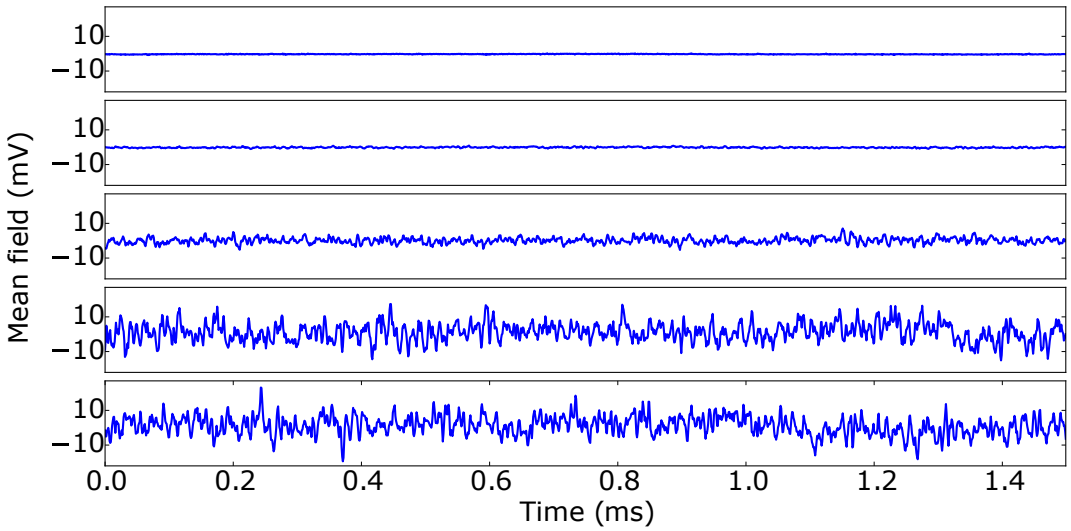

Figure 3.45: Small noisy dynamics as the pumping current is increased. The traces represent the mean field (measured with AC coupling) for a small group of lasers (less than 50), when there is no feedback loop present (we only detect the global intensity at the photo-detector). From top to bottom, the panels represent a pumping current value equal to 0, 170, 180, 210, 220 mA (data of 6/10/17). The small noisy dynamics amplitude increases as the pumping increases, and depends on the threshold value of the selected lasers.

Small noisy dynamics Another type of dynamics that was observed in the mean field does not come from the opto-electronic system, but from the lasers themselves. Even when the opto-electronic feedback is not present (that is, when we only register the global intensity of the lasers onto the photo-detector) there appears to be a small noisy dynamics which gets added to the DC value of the mean field. Figure 3.45 shows some examples of this noisy dynamics at different pumping currents when detecting the light intensity of a small group of lasers (less than 50). This dynamics, which is not present in the system for zero pumping current, gets amplified as soon as we surpass the global threshold value of around 183 mA for the laser matrix. In fact, even though every laser displays the same synchronous noise, the amplitude of the noise depends on the threshold of the particular laser, so the lower the threshold, the higher the amplitude of this noise.

We suspect that this is an electrical noise which comes from the current inside the Circuit Board of the laser matrix. Each laser would then be subjected to the same noise, which is translated into light intensity noise with different amplitudes due to the different $L - I$ response of each laser. Even though this noise is not visible for opto-electronic feedback loops where the amplitude of the current oscillations is large, it will be visible for small current oscillations as we will see later.

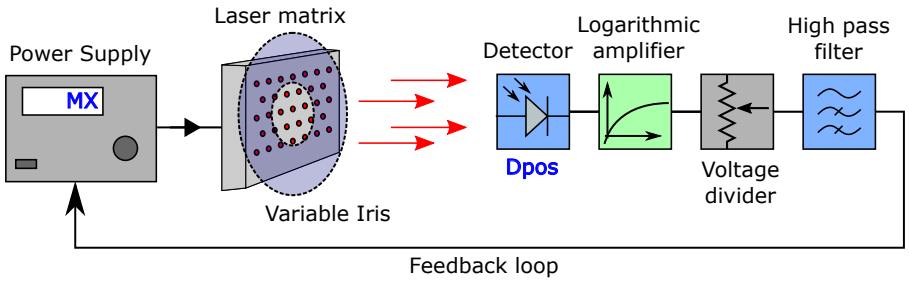

Figure 3.46: Alternative opto-electronic setup, with a logarithmic amplifier, a voltage divider and a high-pass filter in the feedback loop.

3.4.2 Setup with a logarithmic amplifier, a voltage divider and high-pass filter

Here we present another alternative opto-electronic setup composed of a logarithmic amplifier, a voltage divider and a high-pass filter. The logarithmic amplifier is the same as in the usual setup of Figure 3.8, while the voltage divider allows us to transform the output signal with a gain $\in [0, 1]$.

Mean field dynamics and detection of three single lasers: *A*27, *A*26 and *A*25, where only the first two participate to the feedback Figure 3.47 shows the simultaneous detection of the mean field and of three other single lasers: $A27$ (a), $A26$ (b) and $A25$ (c). The control parameters between the three different cases remain the same and the only thing that is changed is the current laser under detection. The only lasers selected by the iris for the feedback are $A27$ and $A26$, while laser $A25$ is outside of the feedback loop but still feels the pumping current oscillations determined by the mean field.

The top panels in each case represent the 2D attractor reconstruction of the mean field, the 2D attractor reconstruction of the current laser under detection and the laser intensity vs mean field plot of the current laser. The last plot can be thought of as a representation of the $L - I$ curve of the current laser that is being explored by the pumping current oscillations. This is because the pumping current of the lasers is just a non-linear transformation of the mean field realized at the feedback photo-detector. The different colors represent different DC-pumping current values, from 168.9 mA (red) to 171.0 mA (blue). The bottom panels represent instead the timetraces of the mean field and of the intensity of the current laser.

Comparing the different detections we note that, even though the mean field is the same, the dynamics of the different lasers is quite different. In particular, laser $A27$ is the only one that participates to the mean field dynamics, while laser $A26$ stays basically at zero intensity the whole time. Looking at the 2D attractor reconstruction of lasers $A27$ we note that it resembles the mean field, while in the case of laser $A26$ the attractor resembles a point at the origin.

Finally when looking at the laser intensity vs mean field plot (the transformed $L - I$ plot), in the case of laser $A27$ we are staying completely on the "on" branch of the $L - I$, while we are completely on the "off" branch for laser $A26$.

If we now compare them to laser $A25$, which is outside of the feedback, we notice that he is in an intermediate condition: its dynamics does resemble the one of the mean field, but with a smaller amplitude and only during the higher part of the oscillation spikes. Looking at the transformed $L - I$ plot, we note how we are on the "on" branch near a second kink point as the one shown for laser $L05$ in Figure 3.20, probably closer to the threshold, which explains the lower intensity. Consequently, the 2D attractor is smaller and contracted into a point for small DC-pumping currents.

This figure shows that, for current oscillations that are in the vicinity of the global threshold of 183 mA, some lasers may not participate to the mean field dynamics, while others may be the principal actors, and others may only participate during the high amplitude spikes.

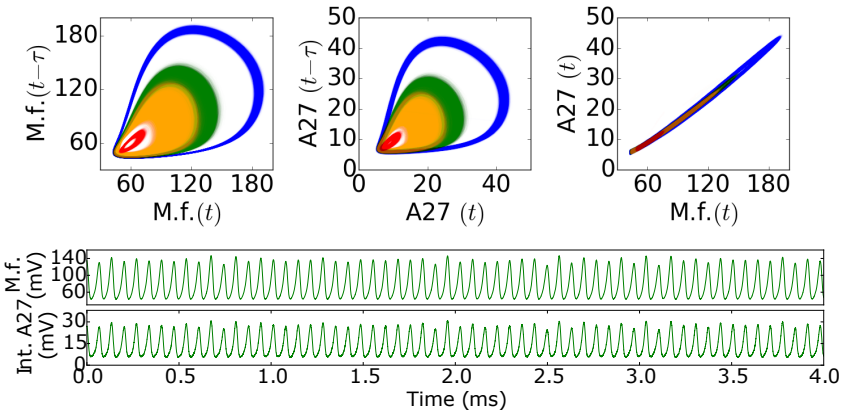

(a) Dynamics of the mean field vs laser $A27$ (inside the feedback).

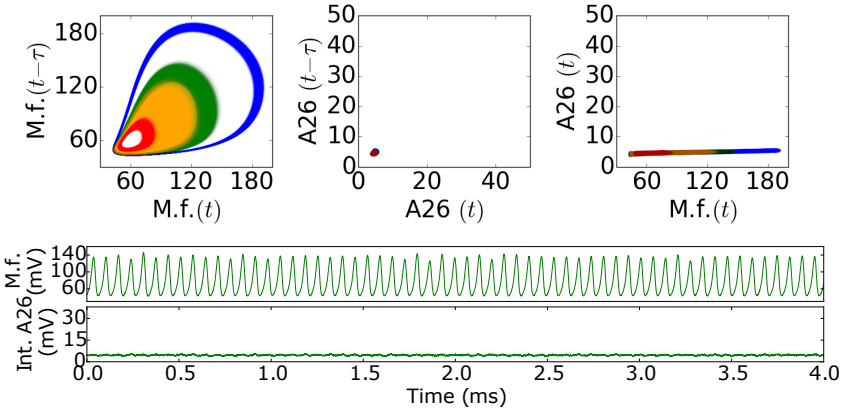

(b) Dynamics of the mean field vs laser $A26$ (inside the feedback).

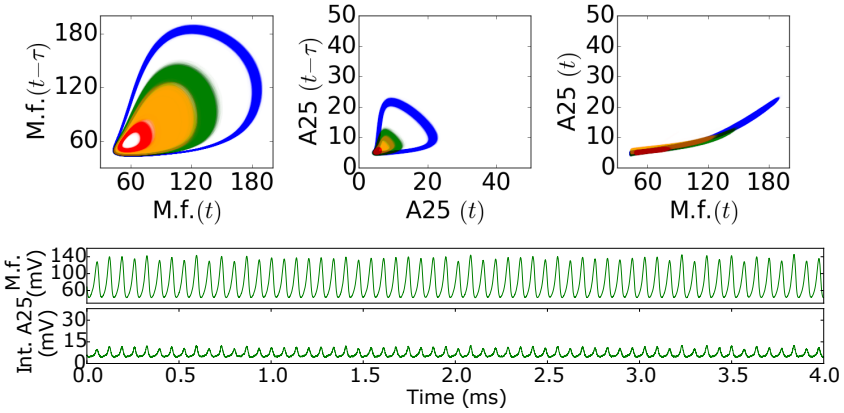

(c) Dynamics of the mean field vs laser $A25$ (outside the feedback).

Figure 3.47: Dynamics of the mean field *vs* the intensities of lasers $A25$, $A26$, $A27$ with the alternative setup that includes a voltage divider as in Figure 3.46. Parameters as follows: size=only lasers $A27$ and $A26$; Dpos=3; $L \in [0, 2]$; filter cut-off frequency $\in [20-5000]$ Hz and variable MX (from red to blue: 168.9, 169.5, 170.0, 171.0 mA) (data of 2/11/17). The main contributor to the mean field dynamics is laser $A27$. *(Top panels)* 2D attractors reconstruction with $\tau = 10$ μs, and Laser intensities - mean field plot for MX=170.0 mA (green plots). *(Bottom panels)* Mean field and lasers intensities timetraces for MX=170.0 mA (green plots).

Dynamics of the mean field and three other lasers: the up-laser, the down-laser and the reference laser In the previous examples we where exploring the cases of large mean field values, which were of the order of hundreds or thousands of mV when measured on the photo-detector. By carefully chosing the control parameters, one can also observe small mean field values, of the order of tens of mV on the photo-detector. For these parameters, the noisy dynamics shown in Figure 3.45 become relevant, and one can see its effects on the single laser intensities.

Figures 3.48 and 3.49 show the simultaneous detection of the mean field and two other lasers, one of which is a fixed reference-laser, and the other is one of the two up- or down-lasers, which are another couple of lasers that are vertically aligned in the near field. The two figures only differ between each for the DCriv and DC-pumping parameters. The feedback selects only one single laser (not one of the detected lasers), so the mean field is just the intensity of this laser.

In both figures, the top panels represent the 2D attractor reconstruction of the mean field and two other lasers, while the top panels shows their traces. Both figures show some type of chaotic spiking regime for the mean field with the same type of noisy dynamics of Figure 3.45 added to the DC value. However, even though the up-laser does show prominently the noisy dynamics, the reference-laser and down-laser do not for the same experimental realization. In particular, one can clearly see a difference in the attractor of the up-laser and the down-laser: while the up-laser displays a noisy dynamics near the origin, the down-laser does not (or at least is not as relevant).

These figures show that the noisy dynamics can be present in the mean field so that it can be felt by all of the lasers, but with an amplitude that depends on the threshold value of each lasers: while for some lasers this can be of small amplitude, for others it can be of higher amplitude.

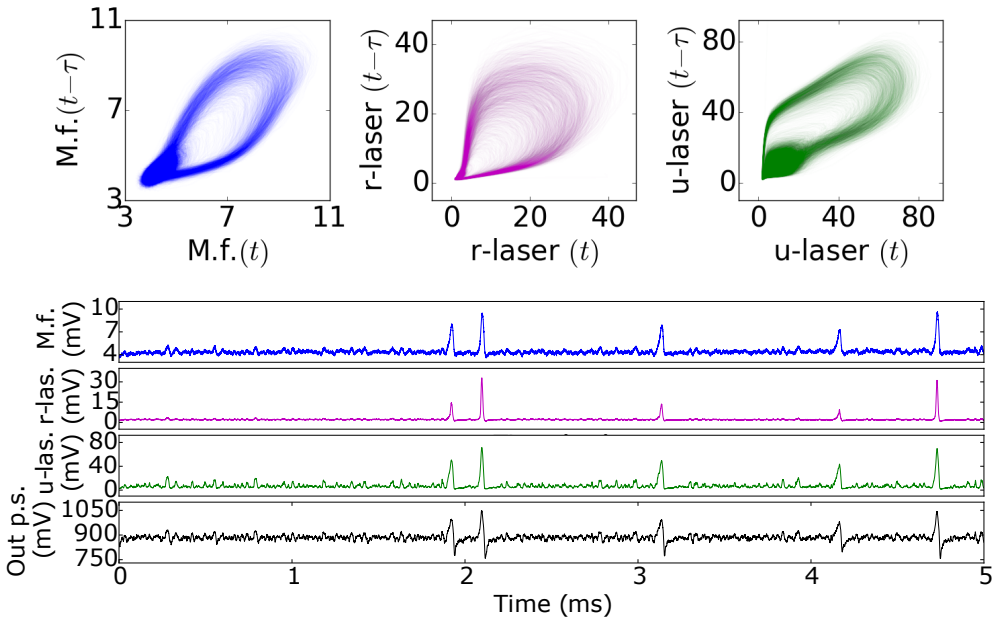

(a) Dynamics of the mean field vs reference-laser and up-laser.

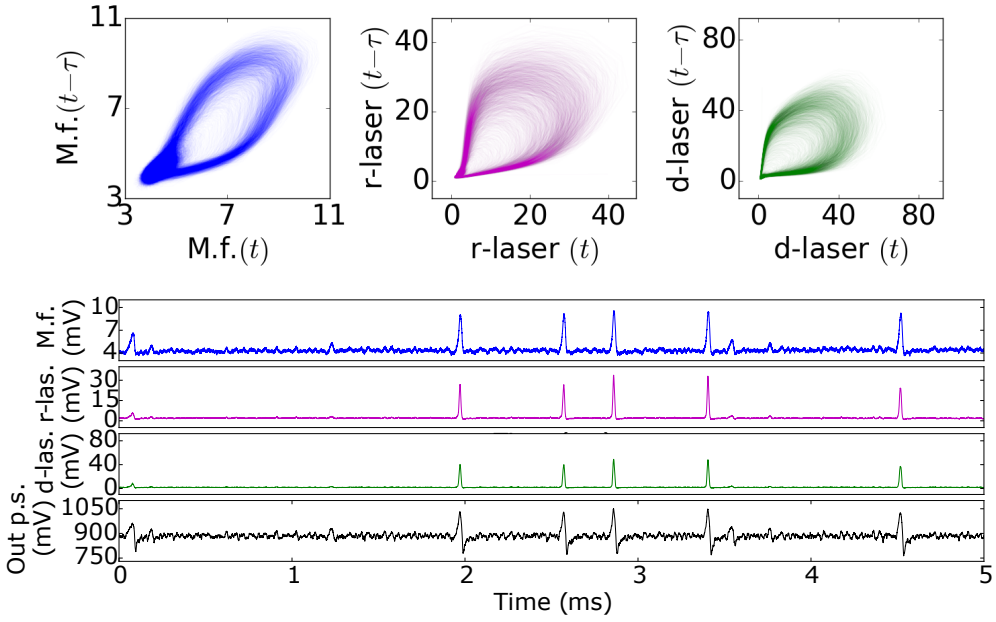

(b) Dynamics of the mean field vs reference-laser and down-laser

Figure 3.48: Dynamics of the mean field *vs* the intensities of lasers reference-laser, up-laser and down-laser with the alternative setup that includes a voltage divider as in Figure 3.46. Parameters as follows: size=only one laser; Dpos=3; DCriv@182.4 mA= 6.6 mV; $L \in [0, 2]$; filter cut-off frequency $\in [20 - 5000]$ Hz and MX=176.2 mA (data of 23/11/17). There is a clear difference in the dynamics of the up-laser and the down-laser for the same control parameters. *(Top panels)* 2D attractors reconstruction with $\tau = 5$ μs. *(Bottom panels)* Timetraces of the mean field, the lasers intensities and the output monitoring signal of the power supply.

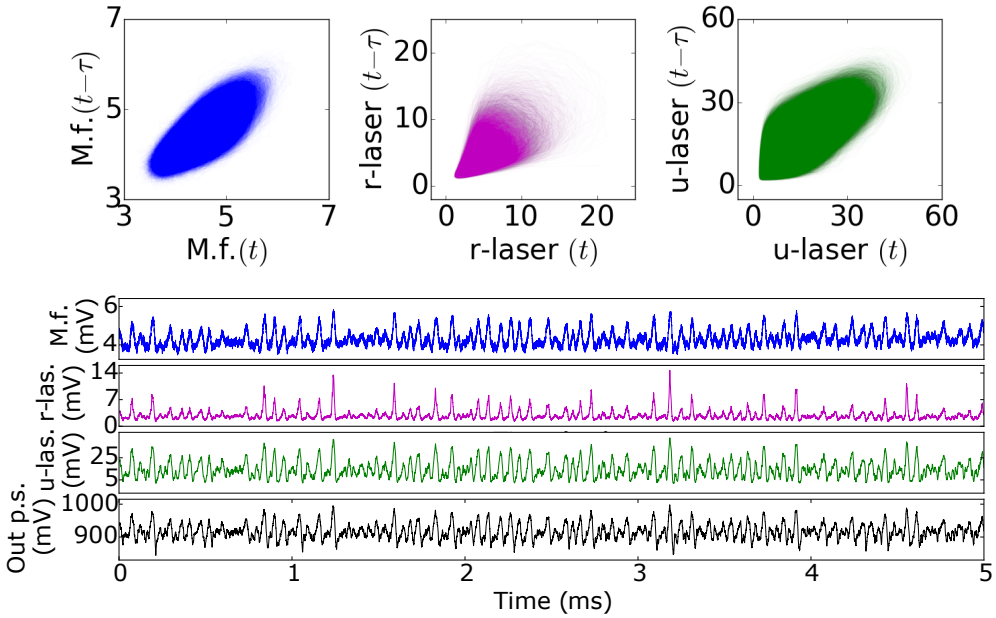

(a) Dynamics of the mean field vs reference-laser and up-laser.

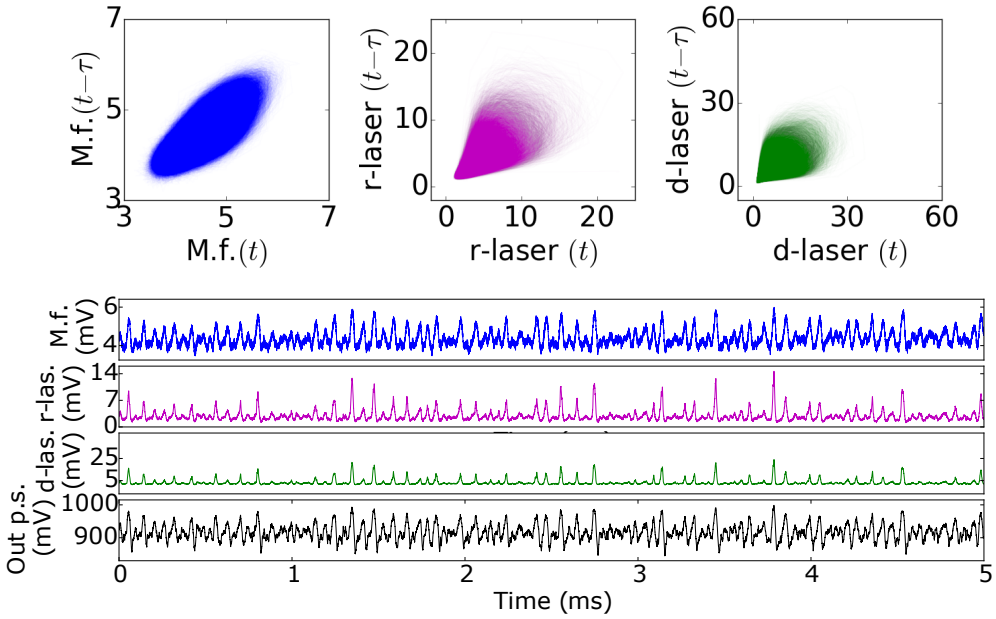

(b) Dynamics of the mean field vs reference-laser and down-laser

Figure 3.49: Dynamics of the mean field *vs* the intensities of lasers reference-laser, up-laser and down-laser with the alternative setup that includes a voltage divider as in Figure 3.46. Same parameters as in Figure 3.48, apart from DCriv@182.4 mA= 8.0 mV and MX=182.4 mA. There is a clear difference in the dynamics of the up-laser and the down-laser for the same control parameters. *(Top panels)* 2D attractors reconstruction with $\tau = 5$ μs. *(Bottom panels)* Timetraces of the mean field, the lasers intensities and the output monitoring signal of the power supply.

3.4.3 Miscellaneous traces of the usual opto-electronic feedback with logarithmic amplifier, fractional-gain amplifier and high-pass filter.

In the previous subsections 3.3.4 and 3.3.5 we reported the results that were obtained by employing the usual opto-electronic feedback loop with a logarithmic amplifier, fractional-gain amplifier and high-pass filter as in Figure 3.8. For the range of selected control parameters, we described a type of dynamics that ranged from stationary steady state, to periodic self-oscillations, to another stationary steady state, with the possibility of observing mixed-mode chaotic-spiking regimes or 2D FitzHugh-Nagumo-like system with noise at the bifurcation boundaries, as shown in Figure 3.24.

However, other types of dynamics were observed for different ranges of parameters, namely: *mixed-mode oscillations* with different winding number (very similar to the ones observed in [Marino 2011]), a *beating-dynamics* with variable amplitude (similar to the one that origins from interacting oscillators with close natural frequencies, as studied in [Pilipchuk 2008], found in vibro-impact processes [Manevitch 2009] or in an elastic system with a strong local stiffness nonlinearity [Kurt 2014]), and a *noisy dynamics* probably caused by electrical noise, as already reported in Figure 3.45.

Figures 3.50, 3.51, 3.52, 3.53 and 3.54 display some examples of the different types of observed dynamics for the mean field and their transition as the DC-pumping current is increased for different experimental parameters.

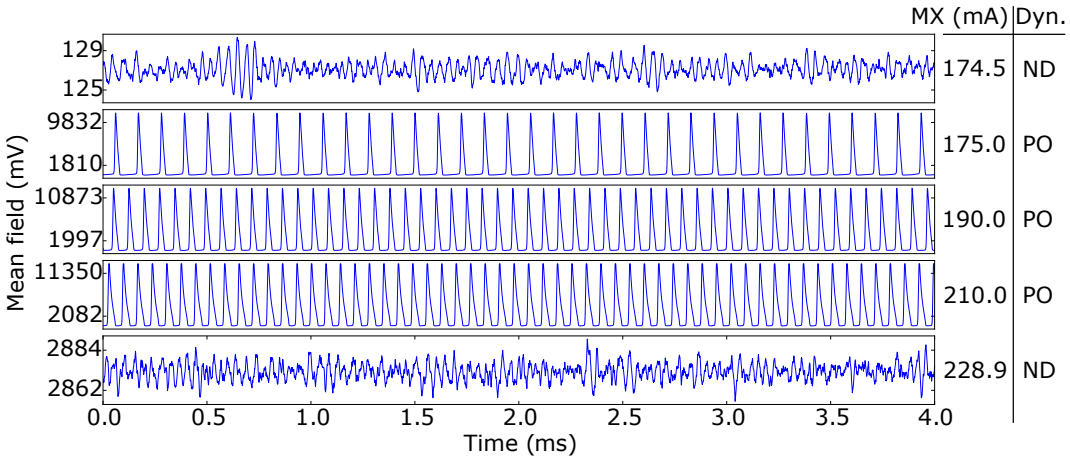

Figure 3.50: Mean field timetraces with the usual opto-electronic feedback as in Figure 3.8, increasing the DC-pumping current. Parameters as follows: size=all lasers; Dpos=2; DCriv@180.0 mA=200 mV; A=2; $L \in [0, 1]$; filter cut-off frequency $\in [20 - 200]$ Hz. From top to bottom, the DC-pumping current is reported on the table on the right (data of 20/12/17). There is a first sudden transition from a noisy dynamics (ND) to periodic self-oscillations (PO), and then again to noisy dynamics.

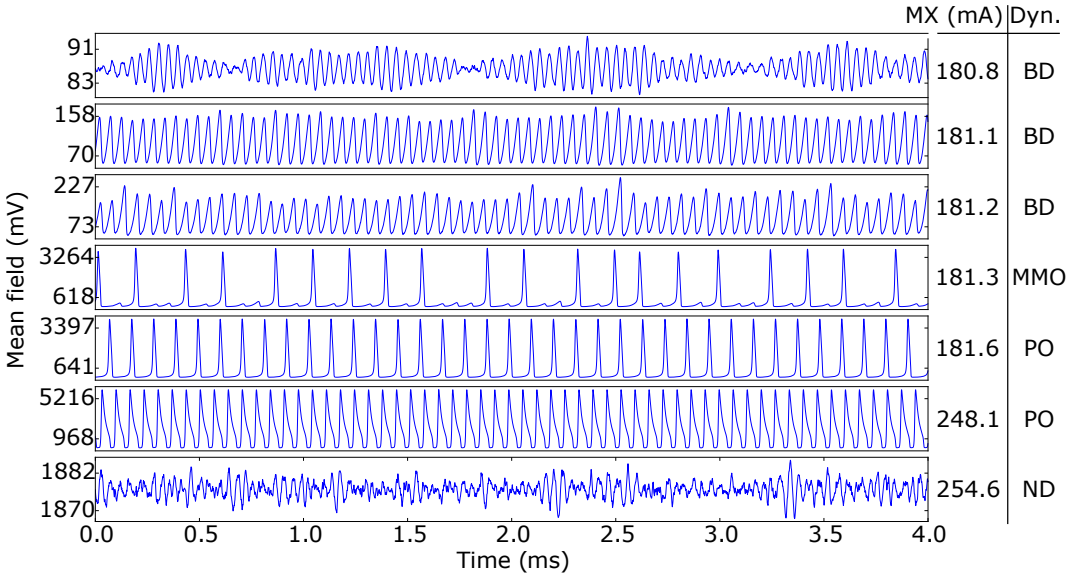

Figure 3.51: Mean field timetraces with the usual opto-electronic feedback as in Figure 3.8, increasing the DC-pumping current. Same parameters as Figure 3.50, apart from DCriv@180.0 mA=80 mV. From top to bottom, the DC-pumping current is reported on the table on the right. One can observe: beating dynamics (BD), mixed-mode oscillations (MMOs), periodic self-oscillations (PO) and noisy dynamics (ND).

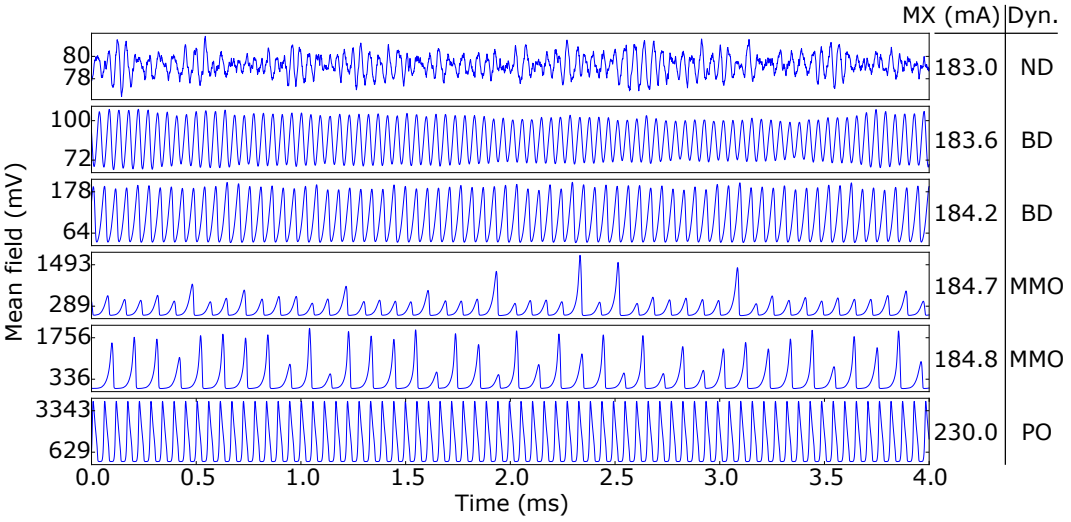

Figure 3.52: Mean field timetraces with the usual opto-electronic feedback as in Figure 3.8, increasing the DC-pumping current. Same parameters as Figure 3.50, apart from DCriv@180.0 mA=60 mV. From top to bottom, the DC-pumping current is reported on the table on the right. One can observe: noisy dynamics (ND), beating dynamics (BD), mixed-mode oscillations (MMOs) and periodic self-oscillations (PO).

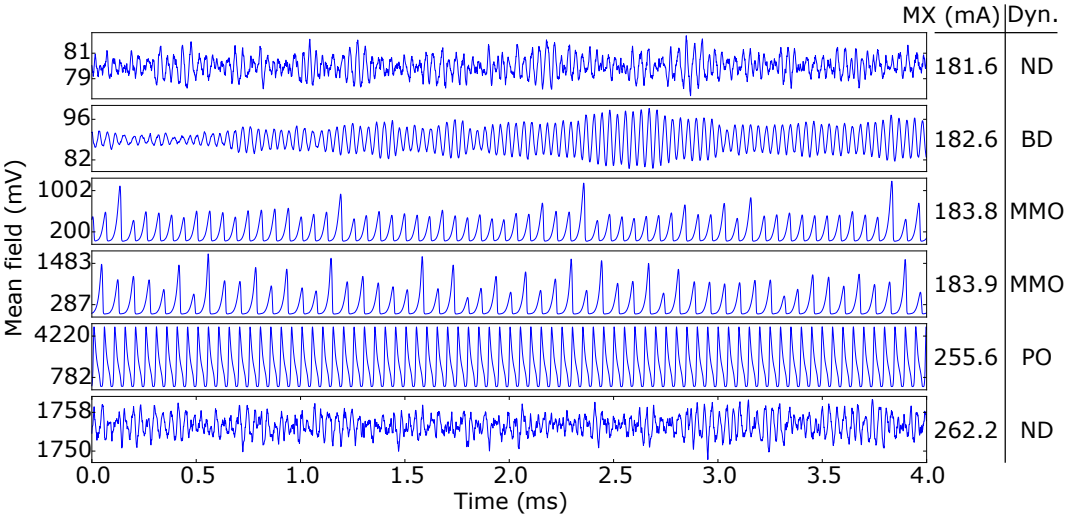

Figure 3.53: Mean field timetraces with the usual opto-electronic feedback as in Figure 3.8, increasing the DC-pumping current. Same parameters as Figure 3.50, apart from DCriv@180.0 mA=70 mV and the cutoff frequency $\sim$ 5 kHz. From top to bottom, the DC-pumping current is reported on the table on the right. One can observe: noisy dynamics (ND), beating dynamics (BD), mixed-mode oscillations (MMOs) and periodic self-oscillations (PO).

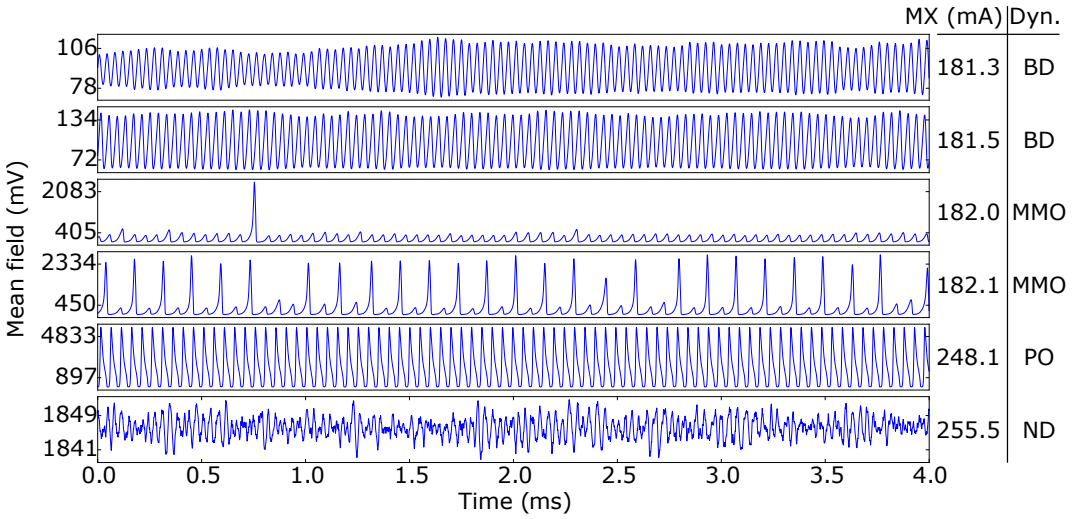

Figure 3.54: Mean field timetraces with the usual opto-electronic feedback as in Figure 3.8, increasing the DC-pumping current. Same parameters as Figure 3.50, apart from DCriv@180.0 mA=80 mV and the cutoff frequency $\sim$ 5 kHz. From top to bottom, the DC-pumping current is reported on the table on the right. One can observe: beating dynamics (BD), mixed-mode oscillations (MMOs), periodic self-oscillations (PO) and noisy dynamics (ND).

3.5 Analytical and numerical study

We will now introduce the 3D theoretical model of a single laser with opto-electronic feedback, and later its $(2N+1)$-dimensional counterpart in the case of N coupled lasers with the same feedback. Both will be studied analytically and through numerical simulations.

3.5.1 Dynamical model for a single laser with opto-electronic feedback

Let us now introduce the dynamical model for the case of a single laser with the type of opto-electronic feedback that comprises a logarithmic amplifier, a fractional gain amplifier and a high-pass filter as shown in Figures 3.4 and 3.8.

It consists of a 3D model that takes into account the dynamics of the photon density S, the carrier density N and the high-pass filtered current I that is reinjected into the laser though the pump current. It is very similar to the one described in [Al-Naimee 2009], and it differs from it in of the shape of the non-linearity transfer function (which is a logarithmic function in this case) and in the order of application of the non-linearity and high-pass filter (first high-pass filter, then non-linearity), which is switched in our case (first the non-linearity, then the high-pass filter). Remarkably, one can obtain very similar results with this model to the one used in [Al-Naimee 2009] despite of these discrepancies, as we will see later.

The evolution of the dynamical variables S, N and I can be described by the usual single-mode semiconductor laser rate equations [Chow 1994], appropriately modified in order to include the AC-coupled feedback loop:

$$\begin{cases} \dot{S} = & [g(N-N_t)-\gamma_0]\,S \\ \dot{N} = & \dfrac{I_0+kI}{e\,V} - \gamma_c N - g(N-N_t)S \\ \dot{I} = & -\gamma_f I + f_F\dot{(}S) \end{cases} \tag{3.8}$$

where:

- I is the high-pass filtered feedback current;
- $f_F \equiv A\ln(1+\alpha' S)$ is the nonlinear transfer function that transforms the intensity power S seen from the photo-detector into the current before the high-pass filter;
- I_0 is the bias current;
- e the electron charge;
- V is the active layer volume;

- g is the differential gain;
- N_t is the carrier density at transparency;
- γ_0 and γ_c are the photon damping ($\simeq 10^{12}$ Hz) and population relaxation rates ($\simeq 10^9$ Hz), respectively;
- γ_f is the cutoff frequency of the high-pass filer;
- k is a coupling coefficient proportional to the photo-detector responsitivity.

Note that in the third equation of system 3.8 the transfer function appears as a derivative due to the fact that the high-pass filter is applied after the nonlinear amplification.

Slow-fast three-time-scale system It is useful both for numerical and analytical purposes to rewrite system 3.8 in the form of a 3D slow-fast system (that is, in the form of three equations with very different characteristic timescales). By introducing the new variables:

$$\begin{cases} x \equiv & \dfrac{g}{\gamma_c} S \\ y \equiv & \dfrac{g}{\gamma_0}(N - N_t) \\ w \equiv & I - f_F\left(\dfrac{\gamma_c}{g} x\right) \end{cases} \tag{3.9}$$

and rescaling the time to the new time scale $t' = \gamma_0\, t$, we can rewrite the system 3.8 as:

$$\begin{cases} \dot{x} = & x(y-1) & \text{(fast)} \\ \dot{y} = & \gamma\left[\delta_0 - y + k_1 w + k_2 \ln(1+\alpha x) - xy\right] & \text{(intermediate)} \\ \dot{w} = & -\epsilon\left[w + A\ln(1+\alpha x)\right] & \text{(slow)} \end{cases} \tag{3.10}$$

where:

- $\delta_0 \equiv \dfrac{I_0 - I_t}{I_{th} - I_t}$ is the normalized pump current, I_t being the transparency current;
- $I_{th} = e\,V\gamma_c\left(\dfrac{\gamma_0}{g} + N_t\right)$ is the definition of the solitary laser threshold current;
- $k_1 \equiv \dfrac{kg}{e\,V\gamma_0\gamma_c}$, $k_2 \equiv Ak_1$, $\alpha \equiv \dfrac{\gamma_c \alpha'}{g}$ are redefined parameters;
- $\gamma \equiv \dfrac{\gamma_c}{\gamma_0} \sim 10^{-3}$ determines the intermediate timescale;

- $\epsilon \equiv \dfrac{\gamma_f}{\gamma_0} \sim 10^{-4} \sim 10^{-4}$ determines the slow timescale;

Note how there are three different timescales in the system 3.10 which are defined by the timescale parameters γ and ϵ. Physically plausible values of these parameters are $\gamma = 4.0 \times 10^{-3}$ and $\epsilon = 10^{-4}$ [Barland 2005].

Slow-manifold Given that the system 3.10 is a slow-fast system, the dynamics will converge towards the slow manifold in the regions where it is stable. Let us now find first the expression of the slow manifold. We will suppose that, as ϵ is small, the zero-th order approximation of the slow manifold in ϵ can be simply obtained from the critical manifold. In the following we will therefore consider the expression for the critical manifold as the slow manifold of the system. We define for convenience the functions f, g and h as:

$$\begin{aligned} f(x,y) &\equiv x(y-1) \\ g(x,y,w,\gamma) &\equiv \gamma\left[\delta_0 - y + k_1 w + k_2 \ln(1+\alpha x) - xy\right] \\ h(x,w) &\equiv -\left[w + A\ln(1+\alpha x)\right] \end{aligned} \tag{3.11}$$

so that the system 3.10 can be written as:

$$\begin{cases} \dot{x} = f(x,y) & \text{(fast)} \\ \dot{y} = g(x,y,w,\gamma) & \text{(intermediate)} \\ \dot{w} = \epsilon\, h(x,w) & \text{(slow)} \end{cases} \tag{3.12}$$

The slow manifold is then defined by the condition $f(x,y) = 0$, $g(x,y,w,\gamma) = 0$. This is satisfied for two cases:

(i) $x = 0$, $g(x,y,w,\gamma) = 0$, which gives:

$$y_w = \delta_0 + k_1 w \tag{3.13}$$

(ii) $y = 1$, $g(x,y,w,\gamma) = 0$, which gives:

$$w_x = \frac{x - k_2\ln(1+\alpha x) + 1 - \delta_0}{k_1} \tag{3.14}$$

The slow manifold is then given by $\Sigma \equiv \Sigma_x \cup \Sigma_y$, where Σ_x and Σ_y are defined as:

$$\begin{aligned} \Sigma_x &\equiv \{(x=0,\, y_w,\, w)\} \\ \Sigma_y &\equiv \{(x,\, y=1,\, w_x)\} \end{aligned} \tag{3.15}$$

While the Σ_x branch belongs to the $x = 0$ plane and is simply a line in the $w - y$ plane, the Σ_y branch belongs to the $y = 1$ plane and has a parabola-like shape in the $w - x$ plane. The two branches intersect exactly on the point with coordinates $\{x = 0,\, y = 1,\, w = (1-\delta_0)/k_1\}$, which we will call point I.

Stability of the slow-manifold Now let's evaluate the stability of the slow-manifold. For small ϵ, the slow manifold will be stable provided that the critical manifold is stable. The slow-manifold will then be stable where the Jacobian calculated on the critical manifold has all negative eigenvalues. The Jacobian of system 3.10 can be written as:

$$\mathbf{J} = \begin{pmatrix} y-1 & x & 0 \\ \gamma\left(\dfrac{\alpha k_2}{\alpha x+1} - y\right) & -\gamma(x+1) & \gamma k_1 \\ -\dfrac{\alpha A \epsilon}{\alpha x+1} & 0 & -\epsilon \end{pmatrix} \tag{3.16}$$

We can evaluate it on the two branches of the critical-manifold Σ_x and Σ_y (setting $\epsilon = 0$).

(i) Stability of Σ_x: The Jacobian on Σ_x can be written as:

$$\mathbf{J}^x = \begin{pmatrix} \delta_0 + k_1 w - 1 & 0 & 0 \\ \gamma(\alpha k_2 - \delta_0 - k_1 w) & -\gamma & \gamma k_1 \\ 0 & 0 & 0 \end{pmatrix} \tag{3.17}$$

The eigenvalues of the top left 2x2 matrix are:

$$\begin{aligned} \lambda_1^x &= -\gamma \\ \lambda_2^x &= \delta_0 + k_1 w - 1 \end{aligned} \tag{3.18}$$

and they govern the stability of the critical manifold. Given that $\gamma > 0$, this branch of the slow-manifold is stable for:

$$w < \frac{1-\delta_0}{k_1} \tag{3.19}$$

Note that this corresponds to the intersection point I between the two branches Σ_x and Σ_y. The Σ_x manifold is then stable for all the values with w value lower than the intersection point.

(ii) Stability of Σ_y: The Jacobian on the critical-manifold branch Σ_y can be written as:

$$\mathbf{J}^y = \begin{pmatrix} 0 & x & 0 \\ \gamma B & -\gamma(x+1) & \gamma k_1 \\ 0 & 0 & 0 \end{pmatrix} \tag{3.20}$$

where $B \equiv \alpha k_2/(\alpha x+1) - 1$. The eigenvalues are then:

$$\lambda_{1,2}^y = \frac{1}{2}\left(-\gamma(x+1) \pm \sqrt{\gamma}\sqrt{4Bx + \gamma(x+1)^2}\right) \simeq \pm\sqrt{\gamma}\sqrt{Bx} \tag{3.21}$$

where we discard the 0 eigenvalue, and we suppose that γ is small. Given that x is limited to $x > 0$ for physical reasons (it comes from a photon density), the eigenvalues have then real part ≤ 0 when $B < 0.$, i.e.:

$$B < 0 \quad \longrightarrow \quad \frac{\alpha k_2 - \alpha x - 1}{\alpha x + 1} < 0 \quad \longrightarrow \quad x > \frac{k_2 \alpha - 1}{\alpha} \tag{3.22}$$

where we also suppose $\alpha > 0$. Note also that, if we calculate the derivative of the parametric function w_x that describes the Σ_y branch in the $w - x$ plane, we obtain:

$$\frac{dw_x}{dx} = \frac{-\alpha k_2 + \alpha x + 1}{\alpha k_1 x + k_1} = -B \cdot \left(\frac{\alpha x + 1}{\alpha k_1 x + k_1} \right) \tag{3.23}$$

which means that the derivative of the w_x has the same sign as $-B$ (supposing that $k_1 > 0$). Given that we just found that Σ_y is stable for $B < 0$, this means that Σ_y is stable when the derivative dw_x/dx is positive, and unstable otherwise.

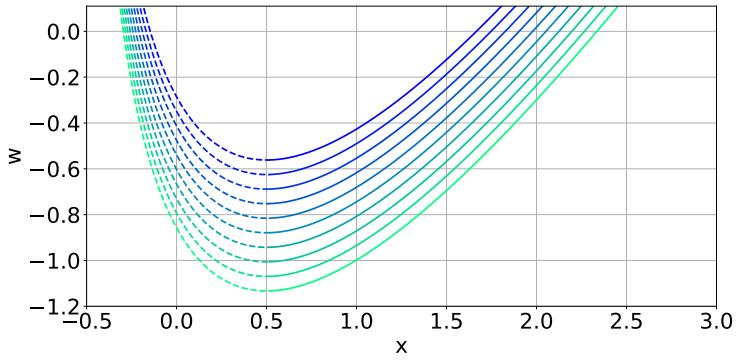

(a) Plot of Σ_y for δ_0 equally spaced from 1.2 to 1.6 (blue corresponds to 1.2, green to 1.6). The curve is dashed when unstable.

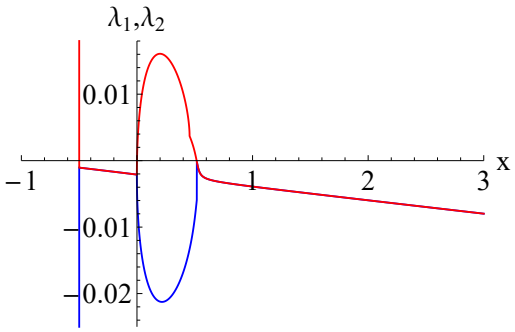

(b) Plot of two of the eigenvalues of the Jacobian along Σ_y. The two curves cross the x-axis at -0.5, 0 and 0.516.

Figure 3.55: Stability of the Σ_y branch of the slow-manifold. Σ_y is plotted in the $w - x$ plane for parameters $\alpha = 2$, $k_1 = 0.7$, $k_2 = 1$, $\gamma = 4.0 \times 10^{-3}$, $\epsilon = 10^{-4}$ (with $A = k_2/k_1$) and variable δ_0. Panel (b) represent the numerical eigenvalues for the full Jacobian, while an approximation for when the curve is unstable is given by $x < (k_2\alpha - 1)/\alpha = 0.5$, which is quite close to the value of 0.516 calculated for the full system.

Motion on the slow-manifold Let' now calculate what is the reduced motion of the system on the two branches of the slow manifold. We have already established that Σ_x is unstable for values of w that are lower than the intersection point with Σ_y, while Σ_y is unstable when the derivative dw_x/dx is negative. The system will not follow the slow-manifold in these regions. On the stable parts, the evolution will go as follows:

(i) Motion on Σ_x: The motion will be governed by the third equation of the system 3.10, that is:

$$\dot{w} = \epsilon\, h(x = 0, w) \quad \longrightarrow \quad \dot{w} = -\epsilon w \tag{3.24}$$

which means that the system will always try to converge towards the point with coordinates $\{x = 0,\ y = \delta_0,\ w = 0\}$, which we will call S_x.

(ii) Motion on Σ_y: The motion will again be governed by the third equation of the system 3.10, that is:

$$\dot{w} = \epsilon\, h(x, w_x) \quad \longrightarrow \quad \dot{w} = -\epsilon\,[w_x + A\ln(1+\alpha x)] \tag{3.25}$$

By substituting the expression for w_x and remembering that $A = k_2/k_1$, one can simplify this equation as:

$$\dot{w} = -\epsilon\left[\frac{x+1-\delta_0}{k_1}\right] \tag{3.26}$$

which means that, supposing that $k_1 > 0$, the system will always try to converge towards the point with coordinates $\{x = \delta_0 - 1,\, y = 1,$ $w = -A\ln(1+\alpha(\delta_0-1))\}$, which we will call S_y.

Summary of the 3D-dynamics In summary, supposing that the parameters are physically plausible (i.e., $k_1, K_2, A, \alpha, \gamma, \epsilon, \delta_0 > 0$), and also supposing that $k_2 > 1/\alpha$ (as is the case of our numerical simulations, a similar analysis can be done otherwise), the dynamics will be as follows:

(i) For $\delta_0 < 1$: The point S_x will be stable, while the point S_y will be unstable. After a first transient, the dynamics will converge towards S_x on the Σ_x branch of the manifold.

(ii) For $1 < \delta_0 < \delta_0^V$: Both S_x and S_y will be unstable. The dynamics will either settle into periodic self-oscillations or chaotic spiking (when close to δ_0^V).

(iii) For $\delta_0 > \delta_0^V$: The point S_x will be unstable, while the point S_y will be stable. After a first transient, the dynamics will converge towards S_y on the Σ_y branch of the manifold.

The value of δ_0^V is:

$$\delta_0^V \equiv \frac{k_2\alpha - 1}{\alpha} + 1 \tag{3.27}$$

and corresponds to the condition where the V point (the minimum of the w_x function) coincides with the S_y point. The relevant points have coordinates:

$$I = \left\{x = 0,\, y = 1,\, w = \frac{1-\delta_0}{k_1}\right\} \qquad \text{(Intersection point between } \Sigma_x \text{ and } \Sigma_y)$$

$$V = \left\{x = \frac{k_2\alpha - 1}{\alpha},\, y = 1,\, w = \frac{1}{k_1}\left(\frac{k_2\alpha - 1}{\alpha} - k_2\ln(k_2\alpha) + 1 - \delta_0\right)\right\}$$

(Minimum of w_x. Determines the boundary of stability for Σ_y)

$$S_x = \{x = 0,\, y = \delta_0,\, w = 0\} \qquad \text{(Attractor on } \Sigma_x \text{)}$$

$$S_y = \{x = \delta_0 - 1,\, y = 1,\, w = -A\ln(1+\alpha(\delta_0-1))\} \qquad \text{(Attractor on } \Sigma_y \text{)} \tag{3.28}$$

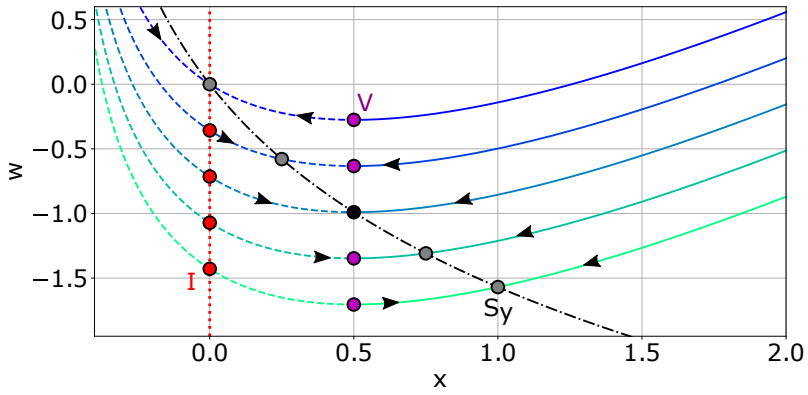

(a) Motion on Σ_y for δ_0 equal to 1, 1.25, 1.5, 1.75 and 2 (blue to green). The system is attracted towards S_y, which is stable for $\delta_0 > (k_2\alpha - 1)/\alpha + 1 = 1.5$ and unstable otherwise. V represents the minimum of w_x as in Eq. 3.38, while I is the intersection point between Σ_x and Σ_y.

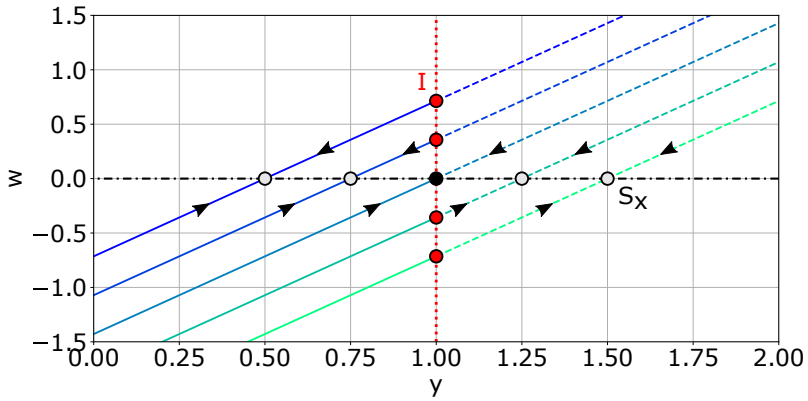

(b) Motion on Σ_x for δ_0 equal to 0.5, 0.75, 1, 1.25 and 1.5 (blue to green). The system is attracted towards S_x, which is stable for $\delta_0 < 1$ and unstable otherwise. I is the intersection point between Σ_x and Σ_y.

Figure 3.56: Motion of the system on the two branches of the slow-manifold Σ_x and Σ_y. Σ_y is plotted in the $w - x$ plane for parameters $\alpha = 2$, $k_1 = 0.7$, $k_2 = 1$, $\gamma = 4.0 \times 10^{-3}$, $\epsilon = 10^{-4}$ (with $A = k_2/k_1$) and variable δ_0, while Σ_x is plotted in the $w - y$ plane for the same parameters and variable δ_0.

Figure 3.56 shows a summary of the motion on the two branches of the slow-manifold for the same parameter range used in the numerical simulations, when changing the δ_0 parameter.

3.5.2 Numerical simulations of a single laser with opto-electronic feedback

Here we will show that the analytical predictions obtained in the previous subsection 3.5.1 about the dynamics of a single laser with opto-electronic feedback, as described by the 3D slow-fast system 3.10, are confirmed by the numerical simulations.

The numerical simulations in this subsection have been performed using the Euler integration method, with an integration step of $\Delta t = 0.1$ (units of γ_0^{-1}).

Some of the Figures here reported come from a study by Alexandre Miazek[7] during his Master 1 stage at the Inphyni lab, under the supervision of Stéphane Barland.

3D dynamics as the bifurcation parameter δ_0 increases. The dynamics basically follows the observations reported in the summary of the 3D dynamics described in the last subsection. Figure 3.57 shows three different simulations for the same parameters but different δ_0. For all simulations, we plot the two branches of the slow-manifold, i.e. Σ_x (green, the line in the $x = 0$ plane, unstable when dashed) and Σ_y (black, the parabola-like function in the $y = 1$ plane, unstable when dashed), along with the relevant points for the dynamics, i.e. I (red, the intersection point between Σ_x and Σ_y), V (magenta, the minimum of Σ_y), S_x (green, the attractor on Σ_x) and S_y (black, the attractor on Σ_y. The blue triangle represents the initial start of the numerical simulation (placed on the Σ_y branch at $x = 1$). The dynamics is as follows:

- *First row ($\delta_0 = 0.75$, $\delta_0 < 1$):* Starting from the initial condition, the system is attracted towards the unstable S_y on the parabola-like Σ_y branch. However, after passing the vertices V of the branch, this branch becomes unstable. The system then crosses over to the line Σ_x, and from here it is attracted towards the stable S_x, where it rests.
- *Second row ($\delta_0 = 1.25$, $1 < \delta_0 < \delta_0^V = 1.5$):* Starting from the initial condition, the system is attracted towards the unstable S_y on the parabola-like Σ_y branch. However, after passing the vertices V of the branch, this branch becomes unstable. The system then crosses over to the line Σ_x, and from here it is attracted towards the unstable S_x. Once it surpasses the intersection point I, Σ_x becomes unstable too. The system continues to follow it a little while longer, before it is expelled from it towards the Σ_y branch again, where it settles following some spiral relaxation oscillations. Once on this branch, the system is back where it started, and the loop starts over again. This motion generates periodic self-oscillations. Figure 3.58 shows again this dynamics in phase space in a more visible plot.

[7] From Université de Lille, alexandre.miazek@gmail.com

- *Third row ($\delta_0 = 1.75$, $\delta_0 > \delta_0^V = 1.5$):* Starting from the initial condition, the system is attracted towards the stable S_y on the parabola-like Σ_y branch. After a first transient, it will just settle on this stable point.

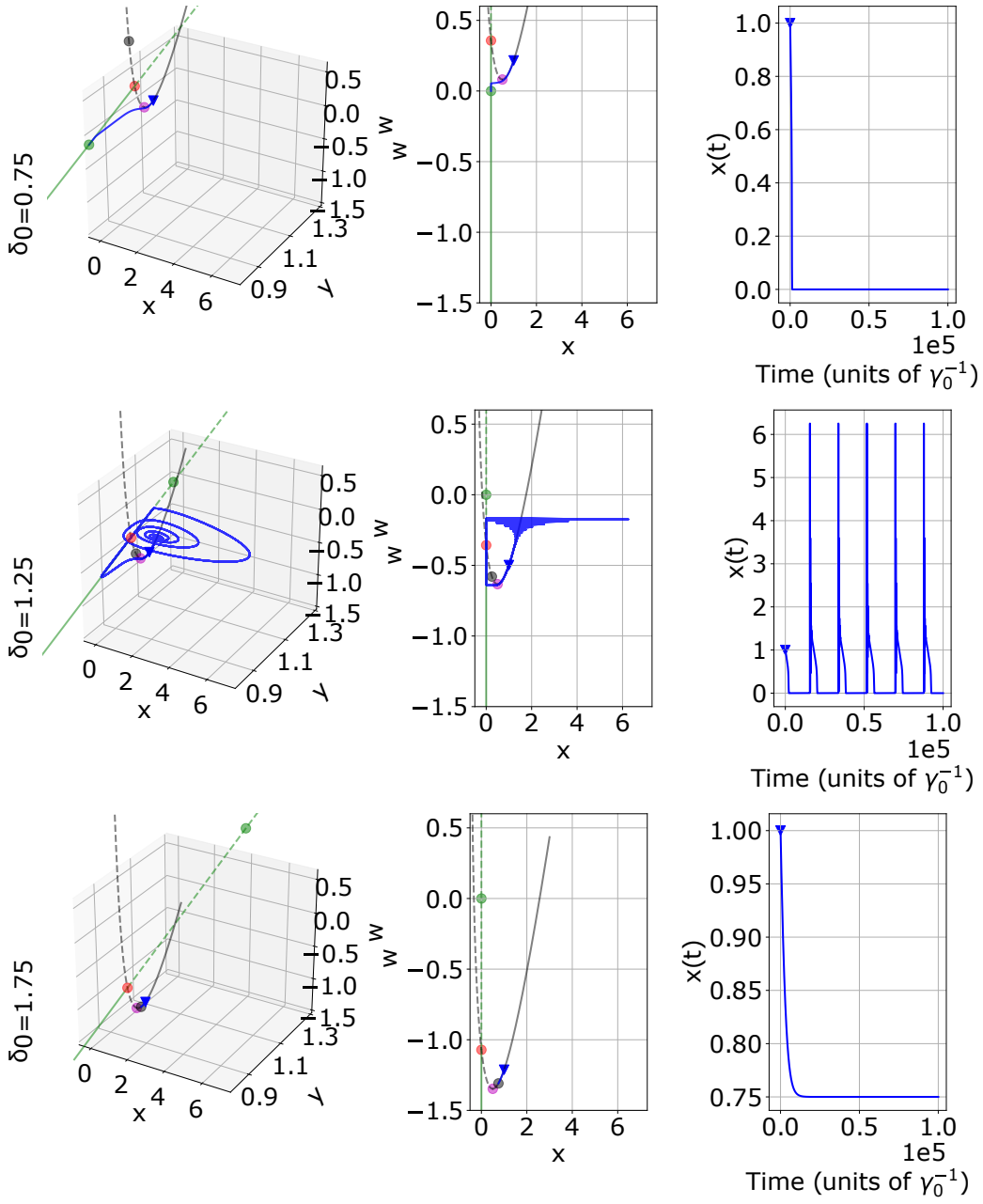

Figure 3.57: Numerical simulations of a single laser with optoelectronic feedback, same parameters as Figure 3.58 with variable δ_0 (without noise). The black curve is the branch Σ_y and the green curve is the branch Σ_x of the slow manifold (unstable when dashed). The plotted points are I (red, intersection point between Σ_x and Σ_y), V (magenta, the minimum of Σ_y), S_x (green, the attractor on Σ_x) and S_y (black, the attractor on Σ_y). The blue point is the initial start of the simulation. $\delta_0 = 0.75$: S_y is unstable while S_x is stable. After a first transient, the system relaxes on S_x. $\delta_0 = 1.25$: both S_x and S_y are unstable. The system performs periodic self-oscillations going from one brach to the other of the slow-manifold. $\delta_0 = 1.75$: S_x is unstable while S_y is stable. After a first transient, the system relaxes on S_y.

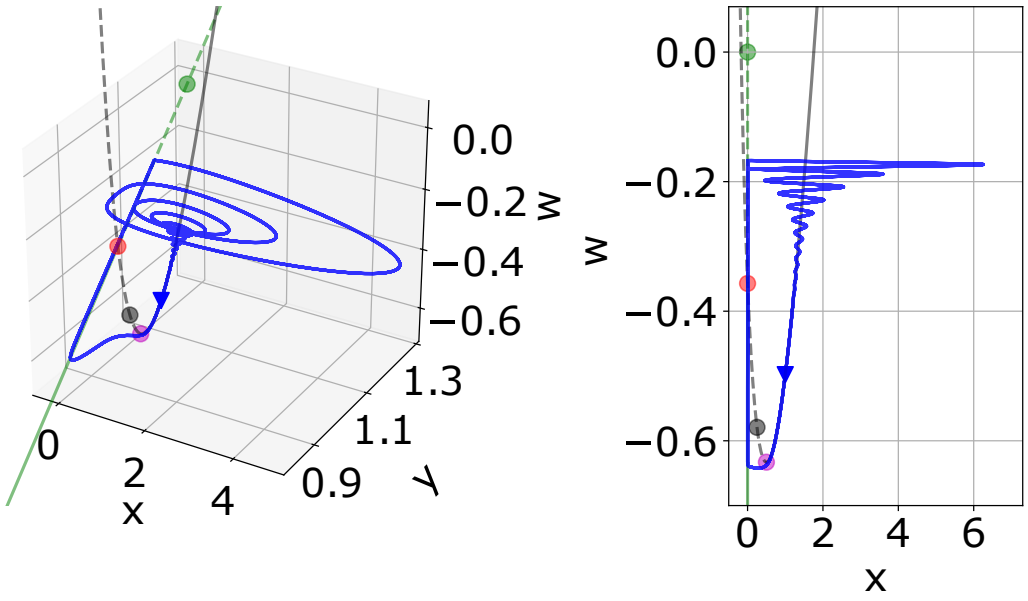

Figure 3.58: Numerical simulation of a single laser with optoelectronic feedback as in system 3.10. The parameters are $\alpha = 2$, $k_1 = 0.7$, $k_2 = 1$, $\gamma = 4.0 \times 10^{-3}$, $\epsilon = 10^{-4}$ (with $A = k_2/k_1$) and $\delta_0 = 1.25$ (without noise). The black curve is the branch Σ_y and the green curve is the branch Σ_x of the slow manifold (unstable when dashed). The plotted points are I (red, intersection point between Σ_x and Σ_y), V (magenta, the minimum of Σ_y), S_x (green, the attractor on Σ_x) and S_y (black, the attractor on Σ_y). The blue point is the initial start of the simulation. The two attractors are unstable, so the system performs periodic self-oscillations going from one branch to the other of the slow-manifold.

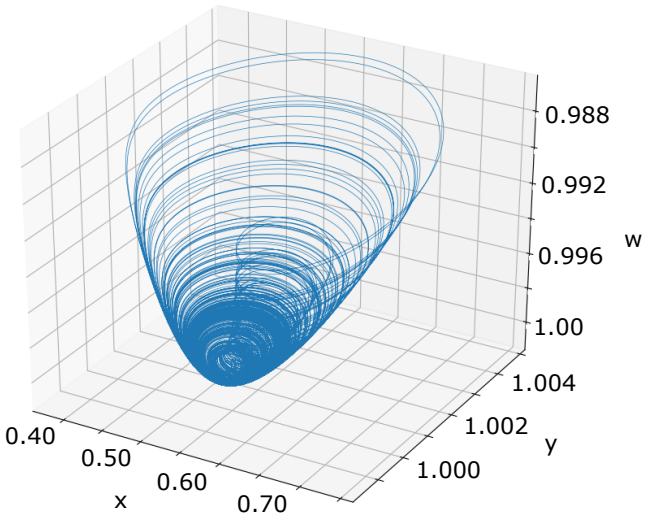

Figure 3.59: Shape of the chaotic attractor near the V point on the Σ_y branch of the slow-manifold. Same parameters as Figure 3.58, with $\delta_0 = 1.5074$. Modified from [Miazek 2018].

Chaotic spiking dynamics When varying the bifurcation parameter δ_0 from the periodic self-oscillation regime to the stable stationary state on S_y (around the value of $\delta_0^V = (k_2\alpha - 1)/\alpha + 1$), the system passes through a cascade of period doubling and chaotic attractors of small amplitude. This is very similar to what was observed in [Al-Naimee 2009].

Figure 3.61 shows a numerical example of suck transition when close to δ_0^V. As displayed in Figure 3.56(a), when close to δ_0^V the position of S_y almost coincides with that of V, the minimum of Σ_y. Near V, the dynamics follows that of a chaotic attractor (visible in Figure 3.59), which makes the system oscillates around this point. If this erratic but deterministic motion pushes the system over a certain threshold, then it will be attracted towards the branch Σ_x where it will perform a loop similar to the one of the periodic self-oscillations, before going back towards the V point. This dynamics will result in chaotic spikes, as the ones in row (b) of the figure.

Numerical bifurcation diagram Figure 3.60 shows a numerical bifurcation diagram when changing δ_0, constructed by plotting the superposition of the extrema of the timetraces for the x variable (the emitted power). The (a) panel of this figure looks very similar to the experimental bifurcation diagrams for a single laser as shown for instance in Figure 3.25. In both cases, we can observe that the system goes through a stationary state, then a periodic self-oscillations state and then another stationary state, with two bifurcation points in between the two transitions. Note that the multiple lines visible during the periodic self-oscillations regime comes from the detection of the local minima of the timetraces during the relaxation oscillations. This fast dynamics (of the order of GHz) is not accessible to us experimentally due to band limitation of

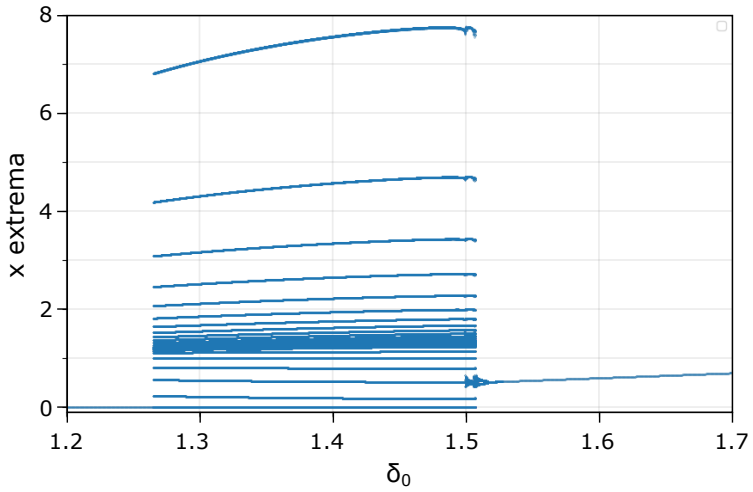

(a) Numerical bifurcation diagram

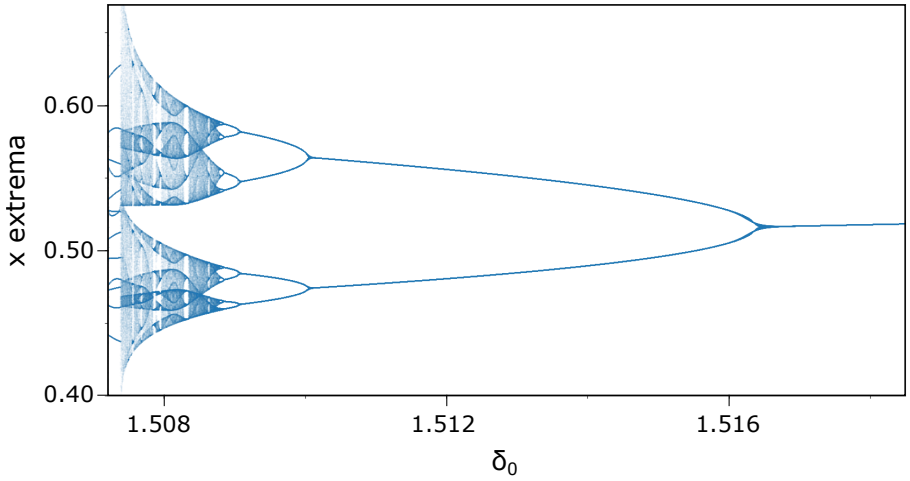

(b) Zoom of the numerical bifurcation diagram around $\delta_0 \simeq 1.5$

Figure 3.60: Numerical bifurcation diagram contructed when changing the δ_0 parameter, same parameters as Figure 3.58. The (a) panel shows double transition from a stationary state to periodic self-oscillations to another stationary state, which is very similar to the experimental bifurcation diagrams of Figure 3.25. The (b) panel shows a zoom of the bifurcation diagram at the second bifurcation point (the analogous of I^u experimentally) where one can observe a transition towards chaos by period doublings. Modified from [Miazek 2018].

our detection system (of the order of MHz), and is therefore not visible in the experimental traces.

The fact that the δ_0 parameters plays the same role as the DC-pumping current MX comes from the definition of δ_0 from the model, which is:

$$\delta_0 \equiv \frac{I_0 - I_t}{I_{th} - I_t} \tag{3.29}$$

where I_0 is the bias current (same as MX), I_{th} is the solitary laser threshold

current and I_t is the transparency current. This means that δ_0 is basically the pumping current MX normalized to the threshold value, and is such that $\delta_0 = 1$ at threshold while $\delta_0 > 1$ above threshold.

Panel (b) of Figure 3.60 shows a zoom of the same bifurcation diagram in panel (a) when close to the second bifurcation point, which we called I^u in the experimental section. Notice the series of period doublings that lead to chaotic windows, in a diagram that resembles an inverted version of the bifurcation diagram of the logistic map.

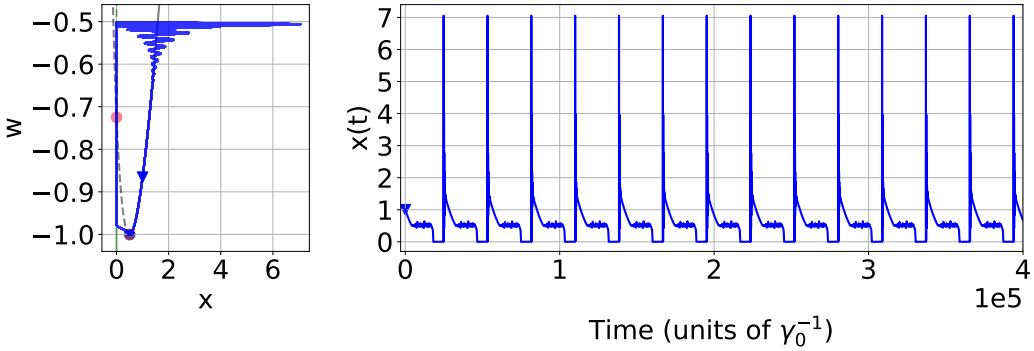

(a) $\delta_0 = 1.507246$

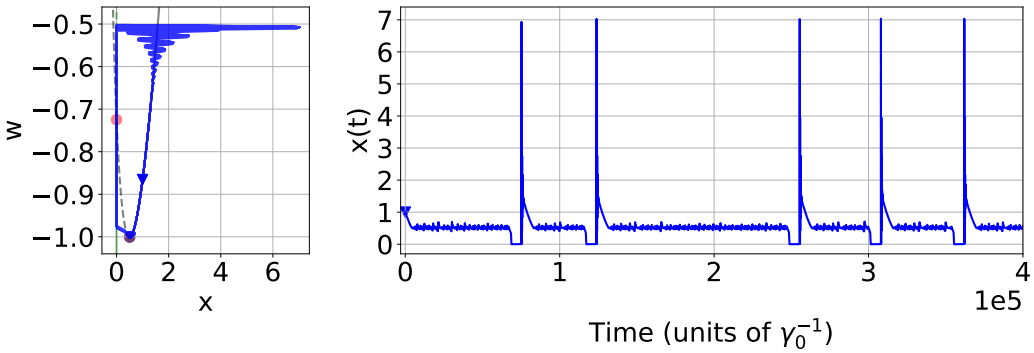

(b) $\delta_0 = 1.507266$

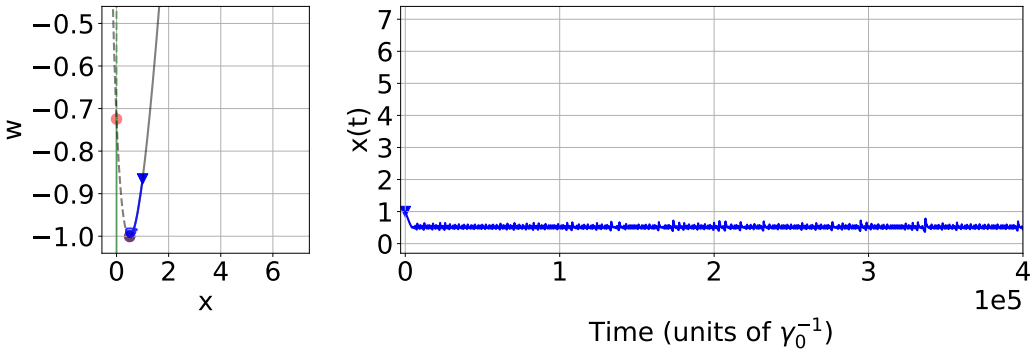

(c) $\delta_0 = 1.507285$

Figure 3.61: Single laser simulations for parameters close to the chaotic spiking regime. Same parameters as Figure 3.58 with variable δ_0 close to $\delta_0^V = (k_2\alpha - 1)/\alpha + 1 = 1.5$ (without noise). The system experiences, from top to bottom: periodic self-oscillations, chaotic spiking and small chaotic oscillations around the stable point.

3.5.3 Dynamical model for N coupled lasers with opto-electronic feedback

We now extend the 3D slow-fast model in order to consider a population of N lasers, which are globally coupled through their common opto-electronic feedback loop, as it is realized in the experiment. Each laser is then governed by the following rate equations:

$$\begin{cases} \dot{x_i} = & x_i(y_i - 1) \\ \dot{y_i} = & \gamma \left[\delta_i - y_i + k_1 w + k_2 \ln\left(1 + \frac{\alpha}{N} \sum_{i=1}^{N} x_i\right) - x_i y_i \right] \\ \dot{w} = & -\epsilon \left[w + A \ln\left(1 + \frac{\alpha}{N} \sum_{i=1}^{N} x_i\right) \right] \end{cases} \tag{3.30}$$

Note that the argument of the logarithmic function now takes into account the normalized sum of all of the x_i, as the nonlinear transfer function that transforms the power seen from the photo-detector into the current before the high-pass filter is modified as:

$$f_F = A \ln\left(1 + \frac{\alpha'}{N} \sum_{i=1}^{N} x_i\right) \tag{3.31}$$

since the photo-detector collects the power from all of the lasers. The pumping parameter for each laser δ_i for a fixed pumping current I_0 now follows a certain peaked distribution (whose exact shape will be discussed later), which comes from the fact that the thresholds of the different lasers follow a Gaussian distribution centered on 183.3 mA with standard deviation of 5.8 mA, as shown in the measurements in Figure 3.23. We can then define the mean field variables X and Y, and the average control parameter Δ as:

$$\begin{aligned} X &\equiv \frac{1}{N} \sum_{i=1}^{N} x_i \\ Y &\equiv \frac{1}{N} \sum_{i=1}^{N} y_i \\ \Delta &\equiv \frac{1}{N} \sum_{i=1}^{N} \delta_i \end{aligned} \tag{3.32}$$

so that the dynamical evolution for these mean field variables can be written as:

$$\begin{cases} \dot{X} = & -X + \dfrac{1}{N}\displaystyle\sum_{i=1}^{N} x_i y_i \\ \dot{Y} = & \gamma\left[\Delta - Y + k_1 w + k_2 \ln\left(1+\alpha X\right) - \dfrac{1}{N}\displaystyle\sum_{i=1}^{N} x_i y_i\right] \\ \dot{w} = & -\epsilon\left[w + A\ln\left(1+\alpha X\right)\right] \end{cases} \tag{3.33}$$

The variable X represents the mean field variable for the intensity output of all the selected lasers (as detected by the photo-detector of the feedback loop), while the variable Y represents the mean field variable for the carrier density.

Slow-manifold for N coupled lasers Before showing some results from numerical simulations for many coupled lasers, let's try to understand how the slow-manifold is modified in the case of N coupled lasers with respect of a single element. Following the same steps as before, we define the functions $\tilde{f}$, $\tilde{g}$ and $\tilde{h}$ as:

$$\begin{aligned} \tilde{f}(X, x_i, y_i) \equiv & -X + \frac{1}{N}\sum_{i=1}^{N} x_i y_i \\ \tilde{g}(X, Y, x_i, y_i, w, \gamma) \equiv & \gamma\left[\Delta - Y + k_1 w + k_2 \ln\left(1+\alpha X\right) - \frac{1}{N}\sum_{i=1}^{N} x_i y_i\right] \\ \tilde{h}(X, w) \equiv & -\left[w + A\ln\left(1+\alpha X\right)\right] \end{aligned} \tag{3.34}$$

The critical manifold is then defined by the condition $\tilde{f}(X, x_i, y_i) = 0$, $\tilde{g}(X, Y, x_i, y_i, w, \gamma) = 0$, and we will consider these expressions as a zero-th order approximation in ϵ of the slow manifold. This is satisfied for the following cases (supposing that $x_i, y_i \geq 0$):

(i) $x_i = 0\ \forall i$, so that $X = 0$, and $\tilde{g}(X, Y, x_i, y_i, w, \gamma) = 0$, which gives:

$$Y_w = \Delta + k_1 w \tag{3.35}$$

Which is the same type of equation that defined Σ_x in the case of a single laser. In this case, the slow-manifold of a single laser of the population will be:

$$y_i(w) = \delta_i + k_1 w \tag{3.36}$$

(ii) $y_i = 1\ \forall i$, so that $Y = 1$, and $\tilde{g}(X, Y, x_i, y_i, w, \gamma) = 0$, which gives:

$$w_X = \frac{X - k_2 \ln(1+\alpha X) + 1 - \Delta}{k_1} \tag{3.37}$$

Which is the same type of equation that defined Σ_y in the case of a single laser. In this case, the slow-manifold of a single laser of the population will be:

$$w(x_i, X) = \frac{x_i - k_2 \ln(1 + \alpha X) + 1 - \delta_i}{k_1} \tag{3.38}$$

(iii) Note that there are other cases for which $\tilde{f}(X, x_i, y_i) = 0$, that are defined by:

$$\sum_{i=1}^{N} x_i(y_i - 1) = 0 \tag{3.39}$$

In particular it could be possible that only N^+ lasers are on, while the rest $(N - N^+)$ are off (so that $x_i = 0$ for those laser). However since this condition has not been observed in the experiment, we will not consider it here.

Discussion on the 3D dynamics of N coupled lasers Given what we already know for the stability and motion of a single laser, we can now extend our observations to the case of N couples lasers. In the previous paragraph, we noted that the two principal branches for the slow-manifold of the mean field were given by:

$$\begin{aligned} &\Sigma_X^{\Delta} \equiv \{(X = 0,\, Y_w,\, w)\} \qquad \text{(line in the } w - Y \text{ plane)} \\ &\Sigma_Y^{\Delta} \equiv \{(X,\, Y = 1,\, w_X)\} \qquad \text{(parabola-like in the } w - X \text{ plane)} \end{aligned} \tag{3.40}$$

which are exactly the same type of structures already described in the case of a single laser. In the $X - Y - w$ space, they correspond to a line in the $w - Y$ plane that belongs to the $X = 0$ plane, and to a parabola-like curve in the $w - Y$ plane that belong to the $Y = 1$ plane. The superscript Δ is introduced to remind ourselves that the bifurcation parameter that governs these curves is now the mean control parameter Δ. If we now look at the motion of the single lasers, their "personal" slow-manifold curves will be given by:

$$\begin{aligned} &\Sigma_{x_i}^{\delta_i} \equiv \{(x_i = 0,\, y_i(w),\, w)\} \qquad \text{(line in the } w - y_i \text{ plane)} \\ &\Sigma_{y_i}^{\delta_i} \equiv \{(x_i,\, y_i = 1,\, w(x_i, X))\} \qquad \text{(parabola-like in the } w - x_i \text{ plane)} \end{aligned} \tag{3.41}$$

Here $y_i(w)$ is the same line structure as in the case of a single laser, governed by the parameter δ_i, while $w(x_i, X)$ is similar to the parabola-like structure of the single laser case, but with the difference that now the logarithmic function is written as $\ln(1 + \alpha X)$, so it is now a function of X. Note also that, since the δ_i belong to a peaked distribution, the position of the $\Sigma_{x_i}^{\delta_i}$ and of the $\Sigma_{y_i}^{\delta_i}$ manifolds in a common $x - y - w$ space of reference will be slightly shifted between each other due to the δ_i distribution.

In summary, the slow-manifold for the N coupled laser is composed of the two branches Σ_X^{Δ} and Σ_Y^{Δ}, which represent a line and a parabola-like structure

in the $x - y - w$ space defined by the same expression for the single laser, but with control bifurcation parameters given by Δ (i.e. the average of the bifurcation parameters δ_i for the single lasers). Furthermore, supposing that the δ_i are distributed according to a sufficiently peaked distribution, the slow-manifolds for the single lasers $\Sigma_{x_i}^{\delta_i}$ and $\Sigma_{y_i}^{\delta_i}$ can be thought of as two "bundles" of lines and parabola-like structures that are distributed around the Σ_X^Δ and Σ_Y^Δ structures, so that the slow-manifold for the mean field represent the average of these structures.

So even though the motion of the mean field will follow the slow-manifolds Σ_X^Δ and Σ_Y^Δ where stable, the single lasers may follow slightly different trajectories due to their peculiar δ_i value. We will see in the following simulations the type of dynamics that this system will follow. In any case, the system mostly follows the slow-manifolds Σ_X^Δ and Σ_Y^Δ, apart during the fast relaxation oscillations, where the lasers can get desynchronized (as we will observe in the numerical simulations). This means that the $(2N+1)$-dimensional system will spend most of its time onto the 1D branches of the slow manifold, thus greatly simplifying its dynamics.

Sketch of a *mean field* description In the previous chapter we identified the slow manifold as a structure that the system will converge to, reducing its dynamical complexity. However a proper mean field description of the coupled system of N lasers could results in a reduced-manifold mean-field description, attracting as $N \to \infty$, in an analogous way to the OA ansatz. In this paragraph we will sketch some steps towards a possible mean field description of the system, which could be a task to be undertaken in the future.

Let us first define our starting point. Here we are dealing with a random $(2N + 1)$-dimensional variable that evolves with time, e.g. a random process:

$$\begin{pmatrix} x_i^N(\delta_i) \\ y_i^N(\delta_i) \\ w^N(\delta_i) \end{pmatrix} \tag{3.42}$$

which is quenched, in the sense that, once we set the δ_i taken randomly from a Gaussian distribution and the initial condition, the evolution will be devoid of noise. We now introduce the empirical mean field variables simply defined as:

$$\begin{aligned} S_x^N &= \frac{1}{N} \textstyle\sum_i^N x_i^N \\ S_y^N &= \frac{1}{N} \textstyle\sum_i^N y_i^N \end{aligned} \tag{3.43}$$

What we would like to affirm is that, supposing that one laser inside of the population (they are exchangeable), for example the first one, converges towards

its limit value as $N \to \infty$, i.e.:

$$x_1^N(t) \to x_\infty(t), \qquad \text{as } N \to \infty \tag{3.44}$$

this would imply that the dynamics of the empirical mean field also converges towards its limit:

$$S_x^N(t) \to \mathbb{E}\left(x_\infty(t)\right), \qquad \text{as } N \to \infty \tag{3.45}$$

where $\mathbb{E}\left(x_\infty(t)\right)$ is the expected value of the empirical mean field according to a known distribution $p\left(x_\infty(t)\right)$, that is:

$$\mathbb{E}\left(x_\infty(t)\right) = \int p\left(x_\infty(t)\right)\, x_\infty(t)\, dx_\infty \tag{3.46}$$

However, knowing or the $p\left(x_\infty(t)\right)$, or affirming that the convergence of one laser implies the convergence of the empirical mean field would require the knowledge of the evolution of the whole $(2N+1)$-dimensional variable a priori, and this is a knowledge that we do not have.

We can then employ two strategies in an attempt to compute the mean field dynamics:

- **Mean field PDE:** We can consider a PDE description of the coupled system as follows. Let us examine the coupled system of the form:

$$\begin{aligned} \dot{x}_i &= x_i(y_i - 1) \\ \dot{y}_i &= \gamma(\delta_0^i - y_i + k_1 w + k_2 \log(1+S) - x_i y_i) \\ \dot{w} &= -\epsilon(w + A\log(1+S)) \end{aligned} \tag{3.47}$$

  where $S = \frac{1}{N}\sum_{i=1}^{N} x_i$. The parameters δ_0^i follow some distribution p_Δ. They are independent realisations of the random variable δ. As a guess, the system should converge to the limit system:

$$\begin{aligned} dx &= x(y-1)dt \\ dy &= \gamma(\delta - y + k_1 w + k_2 \log(1+\mathbb{E}(x)) - xy)dt \\ dw &= -\epsilon(w + A\log(1+\mathbb{E}(x)) \end{aligned} \tag{3.48}$$

  where δ is a random variable describing the disorder. This limit system can be put in PDE form as:

$$\begin{aligned} \partial_t\, g(t,x,y,w,\delta) = \; & -\partial_x(x(y-1)g) \\ & -\gamma\partial_y[(\delta - y + k_1 w + k_2\log(1+S(t)) - xy)g] \\ & +\epsilon\partial_w((w + A\log(1+S(t)))g) \end{aligned} \tag{3.49}$$

  where $S(t) = \int x \cdot g(t,x,y,w,\delta)\, p_\Delta(\delta)\; dx\, dy\, dw\, d\delta$.

- **Moment expansion:** Another possibility to obtain equations for the mean field that are closed in S_x and S_y would be to approximate the coupling terms using a reduced moment expansion. As an example, let us consider the simplified coupled system of the form:

$$\begin{cases} \dot{x_i^N} = x_i^N(y_i^N - 1) \\ \dot{y_i^N} = \delta_i^N + \log(1 + S_x^N) \end{cases} \tag{3.50}$$

In this case, the coupling between the x and y variables is limited to the empirical mean field S_x^N that appears in the second equation. We now introduce the notation:

$$\langle \text{“ ”} \rangle = \frac{1}{N} \sum_i^N \text{“ ”} \tag{3.51}$$

to indicate the average, so that for the averaged system it holds that:

$$\begin{cases} \langle \dot{x} \rangle = \langle xy \rangle - \langle x \rangle \\ \langle \dot{y} \rangle = \langle \delta \rangle + \log(1 + \langle x \rangle) \end{cases} \tag{3.52}$$

We can also express the evolution of the term $\langle \dot{xy} \rangle$ as:

$$\begin{aligned} \langle \dot{xy} \rangle &= \frac{1}{N} \textstyle\sum_i^N (x_i \dot{y_i} + \dot{x_i} y_i) \\ &= \frac{1}{N} \textstyle\sum_i^N [x_i \delta_i + x_i \log(1 + \langle x \rangle) + x_i y_i^2 - x_i y_i] \\ &= \langle \delta \rangle \langle x \rangle + \langle x \rangle \log(1 + \langle x \rangle) + \langle xy^2 \rangle - \langle xy \rangle \end{aligned} \tag{3.53}$$

Now supposing that the term in $\langle xy^2 \rangle$ is approximate $\langle x \rangle$ (as $y \simeq 1$), and introducing the notation:

$$m_x = \langle x \rangle, \qquad m_y = \langle y \rangle, \qquad m_{xy} = \langle xy \rangle \tag{3.54}$$

we can write a closed system for m_x, m_y and m_{xy} as:

$$\begin{cases} \dot{m_x} = m_{xy} - m_x \\ \dot{m_y} = \langle \delta \rangle + \log(1 + m_x) \\ \dot{m_{xy}} = \langle \delta \rangle m_x + m_x \log(1 + m_x) + m_x - m_{xy} \end{cases} \tag{3.55}$$

This procedure can be repeated with an increasing number of moments variables in order to obtain a better approximation of the full system. In this way we can obtain a system for the mean field which has a greatly reduced dimensionality. Also in this case, presently we cannot guarantee that the full system will converge towards this reduced system as $N \to \infty$.

3.5.4 Numerical simulations of N coupled lasers

Let us not turn again to numerical simulations for a confirmation of the type of dynamics expected for N coupled lasers. The numerical simulations here shown have been performed by applying the Euler integration method on system 3.30, with an integration step of $\Delta t = 0.1$ (units of γ_0^{-1}). The figures here reported are an updated version of similar figures reported in [Miazek 2018].

2 coupled lasers Figure 3.62 shows two numerical simulations in the case of two coupled lasers. The parameters are the same as all of the previous simulations for the single laser case (as in 3.58), with the value of the $\delta_{1,2}$ parameters given by (a) $\delta_{1,2} = 1.25 \pm 5.0 \times 10^{-3}$ and (b) $\delta_{1,2} = 1.25 \pm 5.0 \times 10^{-5}$. This value of Δ corrisponds to the regime of periodic-self oscillations in the case of a single laser. Note that the two lasers are always synchronized during the lower part of the Σ_Y^Δ manifold going down and when going up the Σ_X^Δ manifold (with respect to w), but they can get de-synchronized during the fast relaxation oscillations around Σ_X^Δ.

100 and 500 coupled lasers Figures 3.63 and 3.64 show numerical simulations in the case of 100 and 500 coupled lasers. Again the parameters are the same as before (as in 3.58), with the value of the δ_i distributed according to a Gaussian distribution centred around 1.25 and variable standard deviation. The lasers are always synchronized during the lower part of the Σ_Y^Δ manifold going down and when going up the Σ_X^Δ manifold (with respect to w), but they can get de-synchronized during the fast relaxation oscillations around Σ_X^Δ.

Figure 3.65 shows again the case of 500 coupled lasers where the Gaussian distribution of the δ parameter is now centred around 1.507277, so as to be in the chaotic spiking regime. Notice how all of the laser spike together in an erratic manner. A clearly chaotic background dynamics is also visible before and after the spikes. While the amplitude of all the lasers remain the same when following the slow manifold, they can display different amplitudes in the output power during the fast relaxation oscillations. We believe that this case is closest to the experimental condition. A greater degree of de-synchronization would be possible by increasing the spread of the Gaussian distribution of the δ parameters.

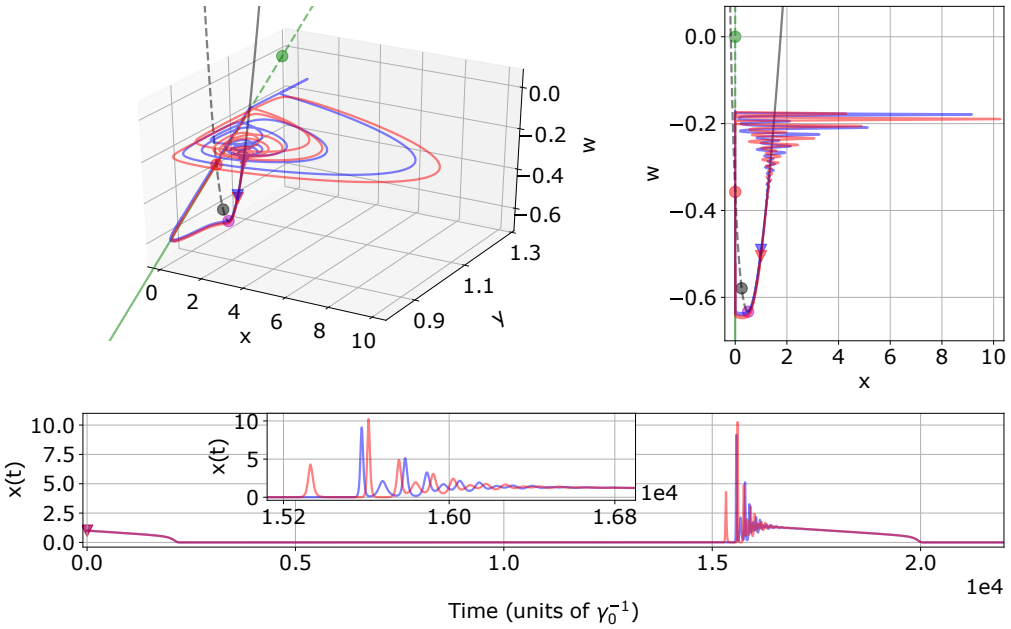

(a) $\delta_{1,2} = 1.25 \pm 5.0 \times 10^{-3}$. The two lasers are mostly de-synchronized during the relaxation oscillations but synchronized elsewhere.

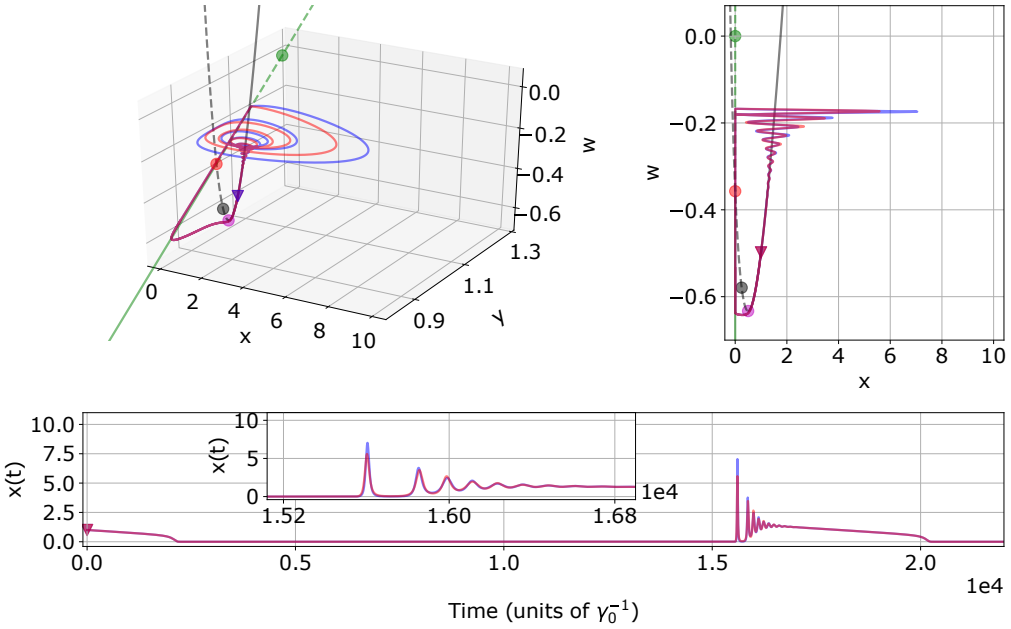

(b) $\delta_{1,2} = 1.25 \pm 5.0 \times 10^{-5}$. The two lasers are mostly synchronized throughout the simulation.

Figure 3.62: Numerical simulations of 2 coupled lasers with optoelectronic feedback as described by system 3.30. The parameters are the same as Figure 3.58, with $\delta_{1,2}$ centred around 1.25. The black curve is the branch Σ_Y^Δ and the green curve is the branch Σ_X^Δ of the mean field slow manifold (unstable when dashed). The plotted points are I (red, intersection point between Σ_X^Δ and Σ_Y^Δ), V (magenta, the minimum of Σ_X^Δ), S_x (green, the attractor on Σ_X^Δ) and S_y (black, the attractor on Σ_Y^Δ). The blue and red triangle points are the initial start of the simulations. The two lasers are always synchronized on the Σ_X^Δ manifold, but they can de-synchronize during the fast relaxation oscillations on the Σ_Y^Δ manifold.

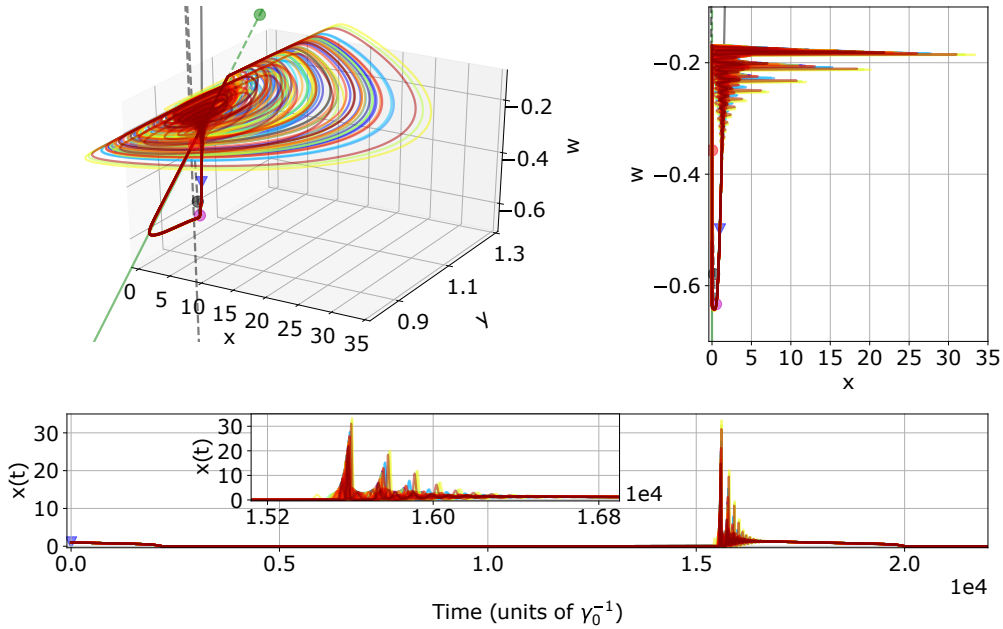

(a) Standard deviation of the Gaussian distribution of δ_i equal to 1.0×10^{-3}

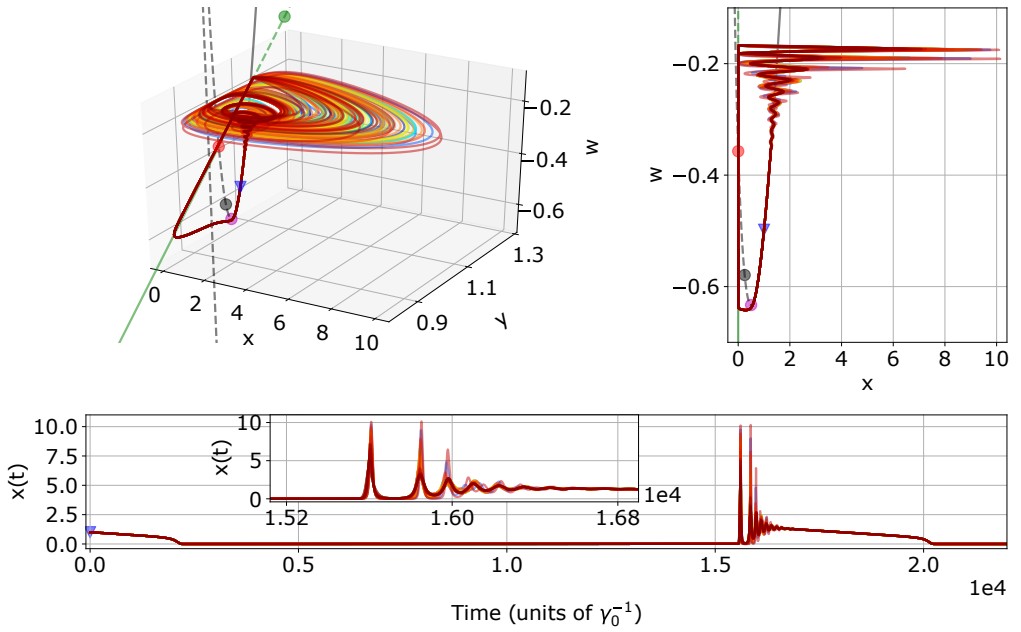

(b) Standard deviation of the Gaussian distribution of δ_i equal to 1.0×10^{-4}

Figure 3.63: Numerical simulations of 100 coupled lasers with optoelectronic feedback as described by system 3.30. The parameters are the same as Figure 3.58, with δ_i distributed according to a Gaussian distribution centred around 1.25 and variable standard deviation. The curves and points here plotted are as in Figure 3.62. The 100 lasers are always synchronized on the Σ_X^Δ manifold, but they can de-synchronize during the fast relaxation oscillations on the Σ_Y^Δ manifold.

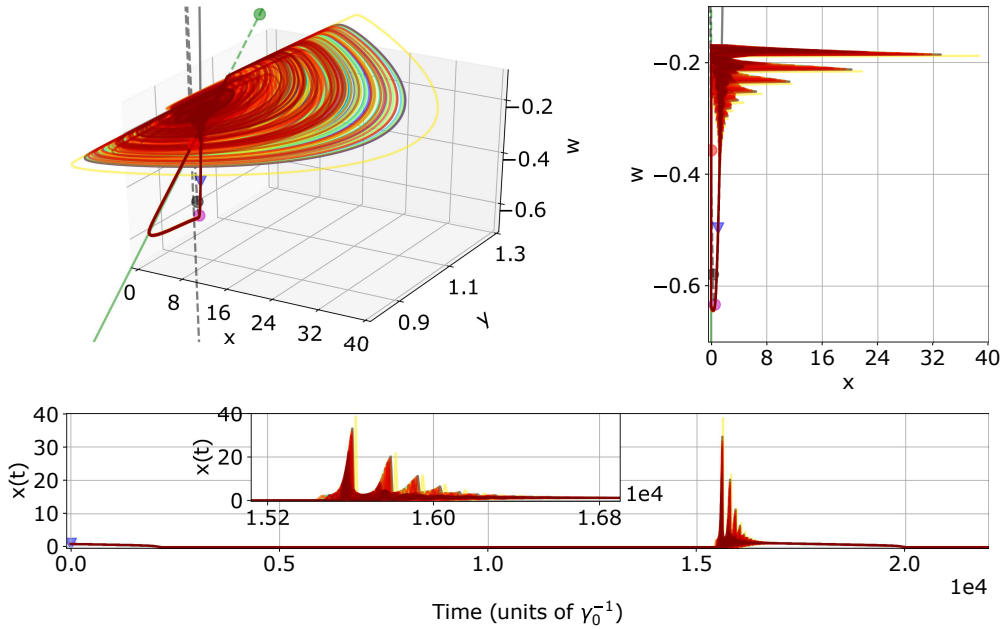

(a) Standard deviation of the Gaussian distribution of δ_i equal to 1.0×10^{-3}

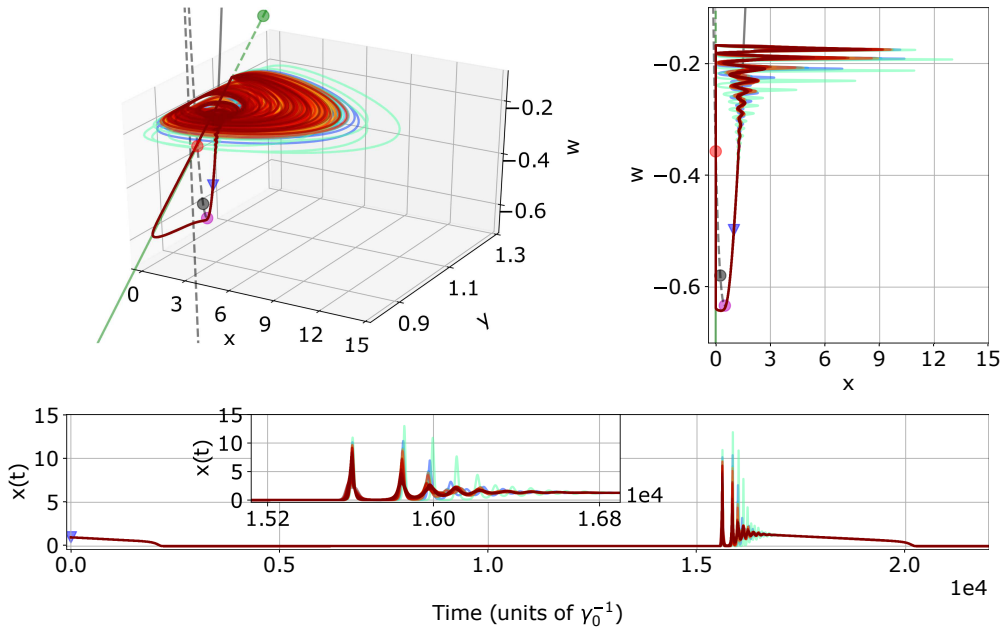

(b) Standard deviation of the Gaussian distribution of δ_i equal to 1.0×10^{-4}

Figure 3.64: Numerical simulations of 500 coupled lasers with optoelectronic feedback as described by system 3.30. The parameters are the same as Figure 3.58, with δ_i distributed according to a Gaussian distribution centred around 1.25 and variable standard deviation. The curves and points here plotted are as in Figure 3.62. The 500 lasers are always synchronized on the Σ_X^Δ manifold, but they can de-synchronize during the fast relaxation oscillations on the Σ_Y^Δ manifold.

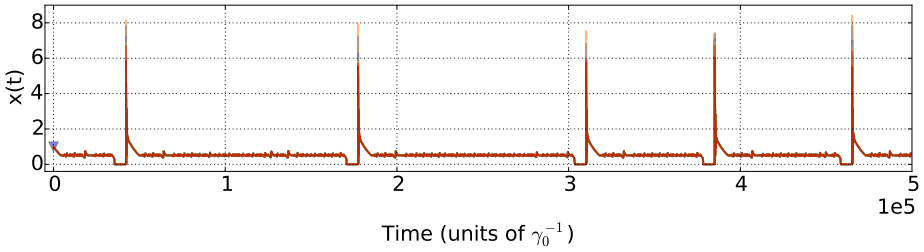

(a) Long timetrace showing chaotic spiking

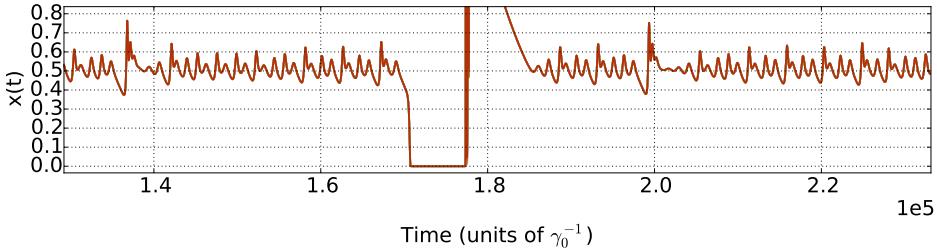

(b) Zoom of the long timetrace around the second spike

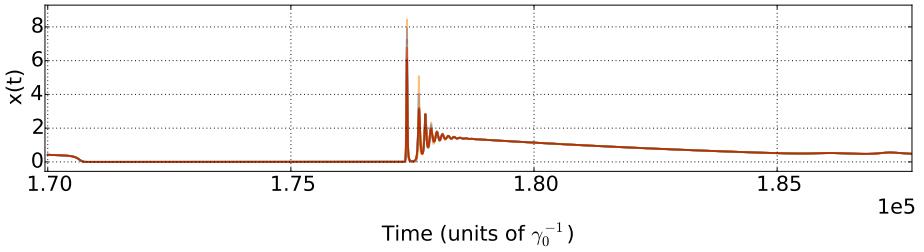

(c) Increased zoom of the second spike

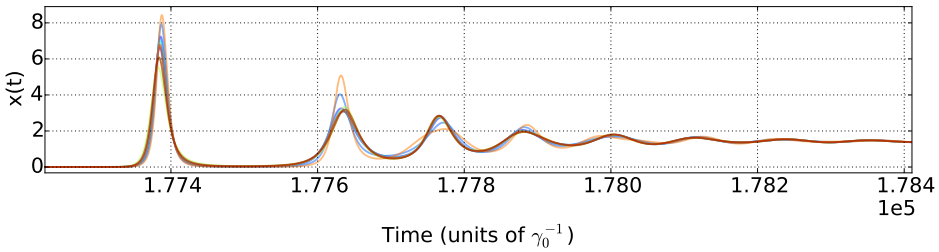

(d) Relaxation oscillations of the second spike

Figure 3.65: Numerical simulations of 500 coupled lasers with optoelectronic feedback as described by system 3.30. The parameters are the same as Figure 3.58, with δ_i distributed according to a Gaussian distribution centred around 1.507277 and standard deviation 1.013462×10^{-4}. Only 10 lasers out of 500 are plotted. The 500 lasers show slightly different amplitudes only during the relaxation oscillations.

Discussion on the distribution of the δ_i In the previous numerical simulations when deciding on the distribution of the δ_i parameter for each laser, we have always chosen a very narrow Gaussian distribution peaked around 1.25. Here we will explain why the distribution must be peaked, and we will give some remarks on its broadness.

If we fix the value of the pumping current I_0, as done in the experiment for each acquisition, the relationship between the δ_i parameter and the threshold I_{th}^i of each laser is given by the definition of δ_i:

$$\delta_i = \frac{I_0 - I_t}{I_{th}^i - I_t} \tag{3.56}$$

From an experimental characterization of the laser population, we know that the laser thresholds are distributed according to an almost Gaussian distribution centered on 183.3 mA and with standard deviation equal to 5.8, as shown in Figure 3.23. We can then assume the Probability Density Function (PDF) of the thresholds to be of the form:

$$\mathrm{PDF}(I_{th}) = \frac{\exp\left(-\dfrac{(I_{th}-\mu)^2}{2\sigma^2}\right)}{\sqrt{2\pi}\sigma} \equiv f(I_{th}) \tag{3.57}$$

with $\mu = 183.3$ mA and $\sigma = 5.8$ mA. We can then calculate the PDF for the δ parameters at fixed I_0 by the following change-of-variable technique:

$$\begin{aligned}\mathrm{PDF}(\delta) &= f(I_{th}(\delta))\left|\frac{dI_{th}(\delta)}{d\delta}\right| \\ &= \frac{1}{\sqrt{2\pi}\sigma}\left|\frac{I_t}{\delta} - \frac{I_0 - I_t + I_t\delta}{\delta^2}\right| \exp\left(-\frac{\left(\dfrac{I_0 + \delta I_t - I_t}{\delta} - \mu\right)^2}{2\sigma^2}\right)\end{aligned} \tag{3.58}$$

where $I_{th}(\delta)$ is just the inverse relation between I_{th} and δ from Equation 3.56. Supposing that $I_0 = 224.125$ mA, $I_t = 20$ mA, $\mu = 183.3$ mA and $\sigma = 5.8$ mA as the physically plausible values which corresponds to a periodic-self oscillating regime for the whole matrix population (so that $\delta = 1.25$ when calculated for global average threshold μ), we obtain the two PDF as in Figure 3.66. Panel (a) shows the probability distribution of the thresholds, centered around 183.3 mA, while panel (b) shows the probability distribution of the δ paramters, centered around 1.25. Note that the standard deviation of the δ distribution is around 4.5×10^{-2}, and is such that most of the distribution stays in the interval $1 < \delta < 1.5$, which is the range of periodic self-oscillations for the range of parameters used in the numerical simulations. However the width of the distribution is around one or two order or magnitude greater than what was used in the numerical simulations. This is because for values much greater

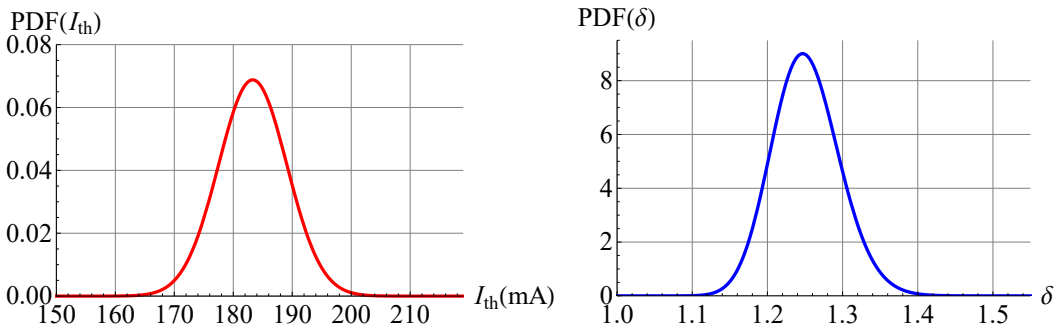

(a) PDF(I_{th}) (b) PDF(δ)

Figure 3.66: Probability Density Distribution function for the laser thresholds (a) and the δ parameters (b), supposing that $I_0 = 224.125$ mA, $I_t = 20$ mA, $\mu = 183.3$ mA and $\sigma = 5.8$ mA. Note that PDF(I_{th}) is centred around 183.3 mA (the global average threshold for the matrix), while PDF(δ) is centred around 1.25 (the middle value of the periodic self-oscillation regime for $\alpha = 2$ and $k_2 = 1$ as in the numerical simulations).

than 10^{-3} we start to see effects that were not observed in the experiment: namely, the possibility of having a very large spread in the different output powers of the various lasers, and the possibility of having some lasers which will stay in the stable stationary regime ($\delta < 1$) while all of the rest are in the periodic self-oscillations regime. We can explain this difference between numerical simulations and experiment by the fact that the α and k_2 parameters in the simulations (which determine the value of $\delta_0^V = (k_2\alpha - 1)/\alpha + 1$) were not optimised to model the experiment, so that we could push the value of δ_0^V farther from 1.5 and a greater spread in the δ distribution could be compensated by a greater range of the periodic self-oscillation dynamics which happen for $1 < \delta < \delta_0^V$.

Comparison with the experimental results We now want to compare our numerical simulations with the experimental results in the case of many coupled lasers. If we look at the case of 500 coupled lasers as in Figure 3.64, we notice how the condition which is closer to the experimental one is case (b), with a smaller Gaussian distribution of the δ_i parameters. This is because all of the lasers are almost always synchronized even during the fast relaxation oscillations, and the only discernible difference between one laser and the next is the amplitude of the emitted power. This is similar to what we remarked in the experimental section as in Figure 3.35, where the only detectable differences between two lasers were very small intensity differences. Note however that in the experiment we are not able to observe the fast relaxation oscillations, which are just averaged by the photo-detectors with MHz band. In any case, a broader distribution as in case (a) would imply a much larger intensity difference between the different lasers, and this was not observed in our range

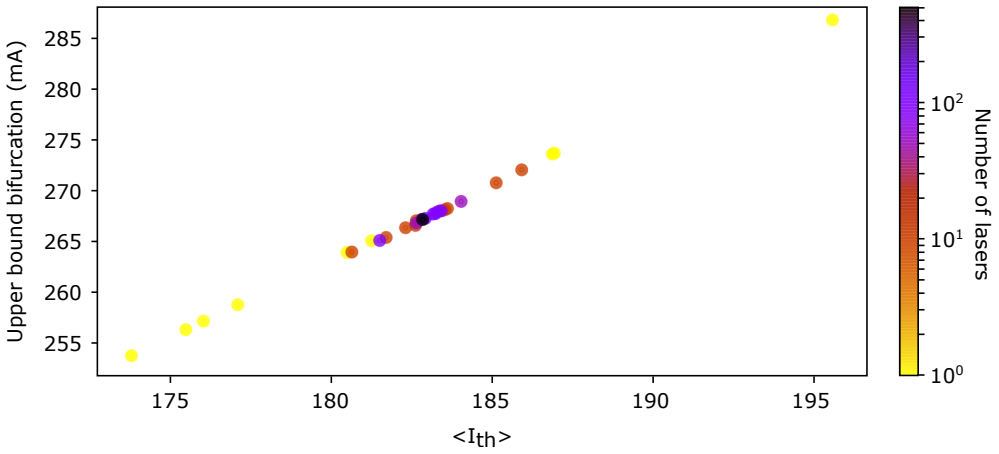

Figure 3.67: Numerical dependence of the upper bound bifurcation current I^u with respect to the average threshold of the population, when considering I_0 as the bifurcation parameter (as in the experiment), for populations of lasers of different size. The thresholds of each population are chosen randomly from a Gaussian distribution with $I_{th} = 183.28$ mA and standard deviation 5.8 mA as in Figure 3.66(a), with $I_t = 20$. There is a clear linear dependence of I^u from the average threshold value, and as the population size increases, the value of the upper bound converges towards a point. The linear fit of the type $I^u(\mathcal{I}^{th}) = a\,\mathcal{I}^{th} + b$ gives as best fit parameters $a = 1.51$ and $b = -10.6$ mA. Modified from [Miazek 2018].

of control parameters.

Linear dependence of the upper bound bifurcation current on the average threshold for all populations sizes and mean field convergence
If we now consider the dynamics of N lasers as the DC-pumping current is increased, in the case of the experiments we observed a linear dependence of the value of the upper bound of the bifurcation I^u with respect to the average threshold for populations of different sized, as summarized in Figure 3.40. A similar figure can be constructed starting from numerical simulations, where one can consider the I_0 DC-pumping current as the bifurcation parameter for a fixed population of size N. Each population is characterized by different thresholds value that are chosen randomly from a Gaussian distribution with $I_{th} = 183.28$ mA and standard deviation 5.8 mA, as was measured in the experiment (see Figure 3.23). By changing the I_0 value, one can observe the 2D histogram of the extrema for the mean field timetrace and determine the upper bound bifurcation value I^u for that population. Plotting these values as a function of the average threshold, we obtain Figure 3.67. This is the numerical analogue of Figure 3.40, and we note that:

- There is again a linear dependence of the upper bound bifurcation value and the average threshold of the population;
- As the population size increases, the upper bound converges towards a

point at $I_{th} = 183.28$ mA (the global average threshold).

This means that, as the number of coupled lasers increases, the type of dynamics converges towards a simplified case that does not depend any more on the number of lasers that participate to the feedback, but is instead analogous to the dynamics of a single laser having as bifurcation value δ the average bifurcation value Δ of the population.

We can explain the linear dependence of the upper bound bifurcation from the average threshold directly from the model as follows. From the relationship between the δ_i parameter and the threshold I^i_{th} of each laser as in equation 3.56, Δ it follows for the mean variable that:

$$\Delta = \frac{I_0 - I_t}{\langle I^i_{th} \rangle - I_t} = \frac{I_0 - I_t}{\mathcal{I}^{th} - I_t} \tag{3.59}$$

where in the last step we use the same notation as in Equation 3.7. Let us now consider the current corresponding to the upper bound bifurcation and call Δ^u the relative Δ value, so that:

$$\Delta^u = \frac{I^u - I_t}{\mathcal{I}^{th} - I_t} \tag{3.60}$$

Rearranging the terms of this equation, one can write it as:

$$I^u = \Delta^u(\mathcal{I}^{th} - I_t) + I_t \tag{3.61}$$

which is a linear dependence of I^u from the average threshold of the selected populations, as found experimentally in Figure 3.40 and numerically in Figure 3.67.

Comment on the experimental and numerical fit parameters of $I^u(\mathcal{I}^{th})$ Given that the linear dependence of I^u from $\mathcal{I}^{th}$ is as in Equation 3.61, the a and b parameters of the linear fit in Figures 3.40 and 3.67 can be interpreted as:

$$\begin{aligned} a &= \Delta^u \\ b &= I_t(1 - \Delta^u) \end{aligned} \tag{3.62}$$

so that we can estimate Δ^u and I_t from the fit parameters. What we obtain is:

$$\begin{aligned} \Delta^u|_{exp} &= 0.74 & \Delta^u|_{num} &= 1.51 \\ I_t|_{exp} &= 218 \text{ mA} & I_t|_{num} &= 20.7 \text{ mA} \end{aligned} \tag{3.63}$$

where the subscripts *exp* and *num* stand for *experimental* and *numerical* respectively. There seem to be some discrepancies between the two measurements. Between the two sets, the more credible values are the numerical ones: note how the Δ^u value is close to 1.5, which is the second bifurcation point

corresponding to δ_0^V as in Equation 3.27 for a single laser, and confirmed by the numerical bifurcation diagram of Figure 3.60. This means that the value of the average bifurcation parameter Δ that corresponds to the upper bound bifurcations is close to the value expected for a single laser. Moreover we recover the value of the transparency current I_t which is equal to our hypothesised value of 20 mA.

In the case of the experiment, two observations can explain the discrepancy with the numerical values: firstly, as noted before in the discussion on the distribution of the δ_i, the values of the α and k_2 parameters that determine the width of the periodic self-oscillations range through the parameter δ_0^V was not optimised in the numerical simulations. This means that there is not a complete correspondence between the Δ values used in the numerical simulations and the Δ values that we can obtain from the experimental data. Secondly, the detection of the thresholds and their distribution has been obtained through the procedure explained in Figure 3.20. We also observed that the LI curves of different lasers may have different inclinations in the "on" state, and more than one turning point. This is different to what is assumed by the model as in Equations 3.10, where the transition between the "off" state and the "on" state is expected to be sharp and to occur precisely at threshold, as can be verified directly from the model (see Appendix G for a derivation). Furthermore, the distribution of the thresholds could be slightly shifted up or down if we defined the threshold transition in a slightly different way. These variations would change the threshold distribution and therefore the I_t value obtained by the experimental fit.

To summarize, the fit parameters obtained in the experimental fit cannot be interpreted "as is" to find the values of Δ^u and I_t. A thorough investigations on the discrepancies mentioned above would be a good way to find quantitative relevant results, but this goes beyond the scope of this measurement. The relevant point is the linear dependence of the upper bound from the average threshold with a convergence towards a single point in the scatter plot both in the experiment and in the numerical simulations.

3.6 Conclusions and perspectives

In this chapter we have introduced a system composed of a laser matrix of 451 semiconductor VCSEL lasers which is coupled to itself through an opto-electronic nonlinear feedback loop. Such feedback allows to realize the mean field of the output power of all the lasers and feed this information back to the pumping current of the lasers themselves, thus allowing an all-to-all type of coupling. Moreover, an iris in the setup allows to select a population of N lasers belonging to the matrix, so that its dynamics can be analysed and compared with similar populations of different sizes.

Given this configuration, the dynamics of the different populations has been as follows:

- **Dynamics of the mean field:** When observing the mean field realized onto the photodetector that participates to the feedback loop, the dynamics consists mainly in either a *stationary stable point*, a *periodic self-oscillation regime* or a *chaotic spiking regime* displaying MMOs. By increasing the pumping current, two bifurcation currents can be identified: one at lower current between a stable point and the periodic self-oscillations and one at a higher current between the self-oscillations and another stable point. Each population of any size displays the same type of bifurcations, even though the current at which they occur can be shifted at lower or higher currents with respect to the global case of 451 lasers.
- **Global synchronization of the output power:** When detecting the light output of single lasers, either inside or outside the selected populations, all lasers behave *synchronously*, so that only small amplitude variations in the output power can be detected. However it could be possible for the various lasers to be de-synchronized in the fast evolution of the output power (as observed in the numerical simulations) or in the carrier dynamics (to whom we do not have direct access).
- **Average threshold as the defining feature of a selected population:** Comparing the dynamics of populations of different sizes, a single characteristic of the laser population is the defining factor in deciding the type of dynamics that can be expected from the population, and that is the *average threshold current* of the population. We have observed that both the upper and lower bound of the bifurcation currents are proportional to the average threshold value, and this proportionality has been measured quantitatively in the case of the upper bound bifurcation.
- **Bifurcation-diagram convergence** Increasing the population size, as the average threshold converges towards its global average value for the whole population of 451 laser, so the type of dynamics converges towards a stable condition regarding the bifurcation diagram. As far as the bi-

furcation is concerned, the dynamics of the full model is then similar to that of a single laser element with a bifurcation parameter δ which is the global average of the δ parameters for the whole population.

To conclude, we have managed to observe a complex dynamics in a network of up to 451 coupled laser in an all-to-all coupling configuration. This type of work belongs to the study of networks of coupled elements, being them phase oscillators (as in the Kuramoto model) or more biologically oriented pulse-coupled oscillators (as with theta-neurons [Luke 2013, Montbrió 2015, Pietras 2016]). As in the case of many of these models, we have observed a synchronized state, where all of the laser elements spike together, being that periodically or chaotically. This last *chaotic spiking regime* is particularly interesting as the lasers synchronously and collectively spike in an erratic manner. This can be seen as a case of *chaos synchronization*, where many chaotic oscillators are made to become synchronized through a common signal, as in the seminal study of two coupled chaotic oscillators in [Pecora 1990]. Furthermore, the coupled system can be made to be *excitable* if perturbed by a pulse in the pumping current, as already verified experimentally in the case of a single element [Al-Naimee 2010]. This last point has not been described nor reported in this thesis, as it was observed in late measurements in collaboration with Erwan Gaymard[8]. We hope that the reader will trust us on this for the moment, as a report on the excitability of the system will hopefully be published soon.

Finally, the dynamics of the $(2N+1)$-dimensional system is mostly reduced to the slow-manifold 1D branches. A future further investigation of the mean field model through a PDE approach or moment expansion could possibly allow us to find an OA-inspired reduced-manifold mean-field convergence of the full model.

[8]Student at the Ecole Universitaire Polytech Nice-Sophia, stagiaire at the INPHYNI lab, erwan.gaymard@etu.unice.fr

Chapter 4

Optical photoswitch of TREK1 channels in HEK293 cells through fibered laser light

4.1 Introduction

In this chapter we will describe the results of a study on the control of actual biological cells using pulses of laser light. This work has been carried out in collaboration with Pierre Walczak[1] and the biology research group in Nice composed by Olena Butenko[2] and Guillaume Sandoz[2] at the *iBV* (**i**nstitut de **B**iologie **V**alrose).

The goal of this study is to control the behaviour of a two-pore domain potassium channel called *TREK1* channel. The well known role of this channel is to allow the flow of leak currents (also called background currents) that are able to stabilize the negative resting membrane potential and counterbalance depolarizations. They are not very active under basal conditions but can be dynamically stimulated by a wide range of stimuli, including mechanical stretch, heat, phospholipids, and polyunsaturated fatty acids. Human TREK-1 is highly expressed in the brain, TREK-1 is also expressed in the prefrontal cortex, hippocampus, hypothalamus, midbrain serotonergic neurons of the dorsal raphé nucleus and sensory neurons of the dorsal root ganglia. They are also expressed in astroglial cells in normal condition as well as in pathological states such as cerebral Hypoxia ischemia [Enyedi 2010].

[1]Université Côte d'Azur, CNRS UMR 7335, Institut de Physique de Nice, 1361 Route des Lucioles, F-06560 Valbonne, France

[2]Centre National de la Recherche Scientifique (CNRS), Institut National de la Santé et de la Recherche Medicale, iBV, Université Côte d'Azur, Valbonne, France Laboratory of Excellence, Ion Channel Science and Therapeutics, Nice, France

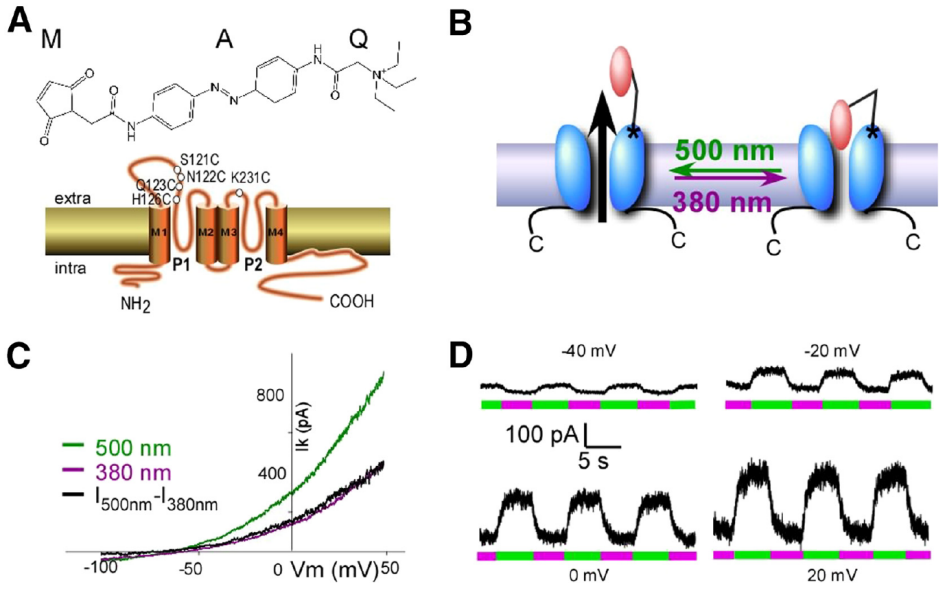

Figure 4.1: *(A)* Structure of the MAQ molecule (**M**aleimide, photoisomerizable **A**zobenzene linker, **Q**uaternary ammonium group) which acts as a photoswitchable tethered ligands on the TREK1 channel. *(B)* Schematic representation of light-gated TREK1 channel. MAQ blocks the pore in the *cis* configuration (when exposed to UV 380 nm light), and it un-blocks it in the *trans* state (when exposed to green 500 nm light). *(C and D)* Whole-cell recording from HEK293T cell expressing TREK1(S121C) and labeled with MAQ. Current was elicited by voltage-ramps (from -100 mV to 50 mV, 1 s in duration). *(D)* The alternating illumination at 500 nm (green) and 380 nm (magenta) reversibly blocks and unblocks the constant outward current, as seen at different holding potentials. Reprinted with permission from [Sandoz 2012].

It has been demonstrated in a recent article [Sandoz 2012] that this channel can be modified in order to render it photoswitchable, that is, able to react with light. Photoswitchable tethered ligands (PTLs) are very sought after in biological engineering as they allow for a fast and reversible control of specific proteins though light manipulation, which is a first step toward *optogenetics*: the ability to regulate electrical activity in living cells through optical control.

The control on this channel has been achieved through the MAQ molecule, whose structure and behaviour are shown in Figure 4.1. It consists of a maleimide (M) that tethers the molecule on the channel via an engineered cysteine, a photoisomerizable azobenzene (A) linker and a pore-blocking quaternary ammonium group (Q). This molecule can exist in two states: a *cis* state which blocks the TREK1 channel and a *trans* state which relieves pore blockage and allows ion conduction. Exposure of this molecule to visible greenish light (500 nm) favours the *trans* state, while exposure to UV light (380 nm) favours the *cis* state. In the [Sandoz 2012] article, it was demonstrated how a

periodic switch between open and closed configuration induced by green and UV light can be measured as a current flowing though the cell, so that one can observe the typical photoswitch traces shown in panel (D) of the figure.

The purpose of this work is to reproduce similar photoswitch traces using a laser UV light coming from a single mode optical fiber instead of the usual LED illumination. The reason for using laser fibered light is that it can be made to be highly localised, instead of being diffused onto the whole sample uniformly. In particular, we aim at operating only onto a part of a cell, or a group of cells, so that we could possibly observe a partial blocking of potassium channels. This mode of operation is innovative and rarely used in biological settings, and it could open the possibility of local optical manipulations of excitable cells based on simple off-the-shelf components.

4.2 Setup

The setup used during this experiment integrates biological voltage-clamping technique equipment with laser and optical elements.

As usual in patch-clamping, a sample containing a culture of cells is placed onto the support and imaging platform, which is visible in picture 4.4. The cells used in this experiment are HEK293 cells (Human embryonic kidney 293 cells) which are transfected with TREKLight plasmid and incubated with MAQ. An apparatus consisting of a patch-clamping probe connected to a data acquisition system allows to perform the whole-cell patch-clamp of a selected cell in the sample, while a microscope overhead allows for imaging of the sample. During voltage-clamping, the voltage difference between the inside and the outside of a cell is kept constant, while the current is recorded by the apparatus. An output monitoring signal proportional to this current is sent to the oscilloscope.

On the optical side, a 70 mW diode laser (Thorlabs L375P70MLD) mounted on a laser diode mounts is pumped though a Thorlabs laser diode controller (here, the "power supply"). This diode can emit UV light at around 375 nm, with a typical LI curve as shown in the right panel of Figure 4.3. The UV laser light is guided through a collimator inside a single mode fiber (P1-305A-FC), with a coating diameter of around 245 μm, a cladding diameter of 125 μm and a core 4 μm. The end of this fiber has been stripped from its coating, so that only the cladding and the core remain, and it has been mounted onto a support which is fixed on a micrometer translation stage, which allows us to move the fiber end and bring it close to the sample. A signal generator with two synchronized channels (Keysight 33600A) is in charge of modulating the pumping current of both a green LED (shining at 500 nm uniformly onto the sample from below) and the laser diode, thus controlling their output power. Both of these two control signals, along with the current response from the patch-clamped cell are acquired with a 200 MHz band-width oscilloscope (Teledyne Lecroy

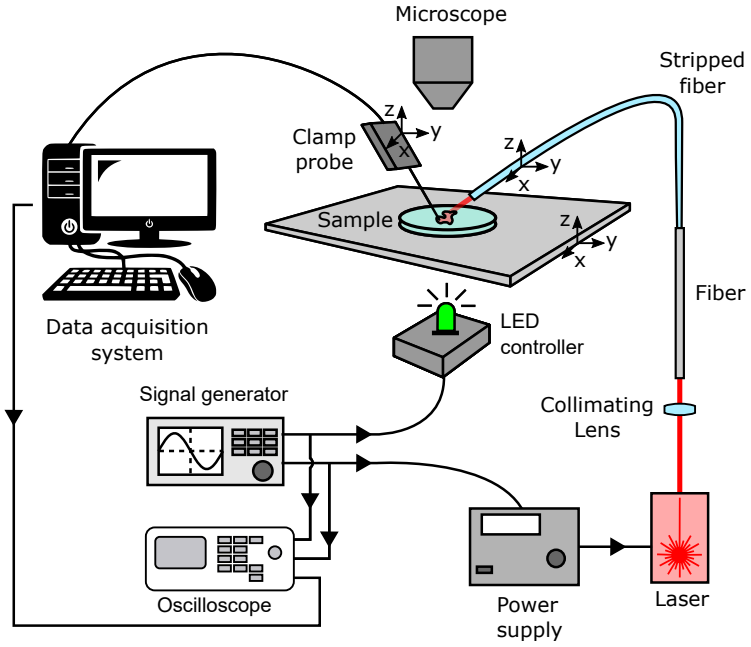

Figure 4.2: Schematic setup for the acquisition of photoswitch traces. While a cell is voltage-clamped through a clamp probe, a stripped fiber is brought close to the sample using a micrometer translation stage so that the laser light is guided onto the clamped cell. A signal generator controls both the LED and the laser intensity. Both traces, along with the current signal of the clamped cell, are acquired on the oscilloscope.

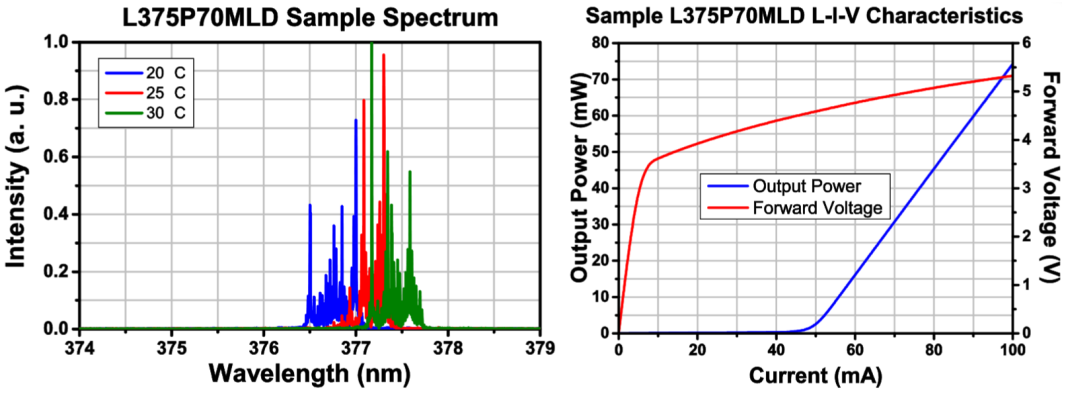

Figure 4.3: Wavelength and LI specification of the Thorlabs L375P70MLD 70 mW diode laser. Taken from the manufacturer specification sheet.

HDO4024).

A microscope apparatus allows us to image the sample in real time at different magnifications. Figure 4.5 shows two of such imaging after a successful clamping of a HEK cell. The picture on the right shows the clamped cell that is being illuminated with the laser light exiting from the fiber core.

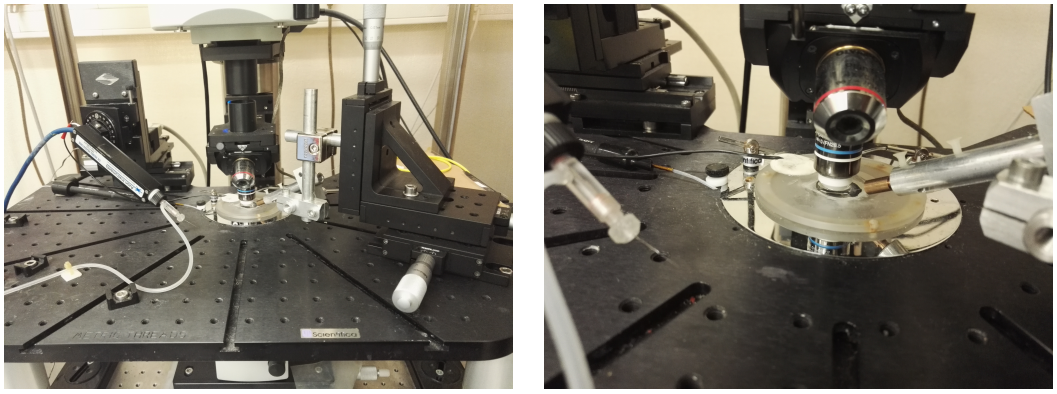

(a) Microscope and support platform for the sample.

(b) Close-up of the sample and the fiber end.

Figure 4.4: Pictures of the setup, close to the cell sample. On the support platform for the sample one can see the clamping probe to the left, and the stripped fiber and its micrometer translation stage on the right.

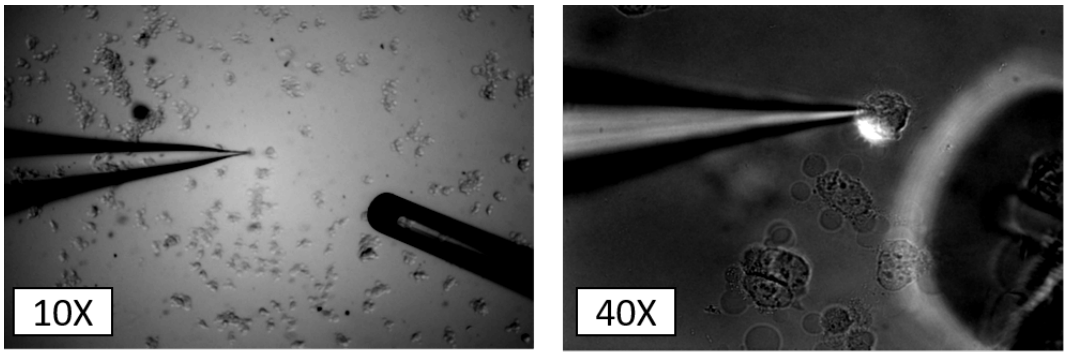

Figure 4.5: Microscope imaging of the sample after a successful clamping of a HEK cell, at two magnifications. The clamping probe in on the left, while the stripped fiber is on the right. In the picture on the right, the cell is being illuminated with the laser light.

4.3 Experimental results

The first stage of the experiment consisted in reproducing a similar photoswitch trace when employing the laser than when employing the LED light. To this end, after their preparation we used both techniques on the same cells, we will describe in the next subsection.

4.3.1 Sample preparation procedure and LED and laser protocol

Sample preparation procedure Firstly, HEK293 cells are transfected with TREKLight plasmid. Then the sample is incubated with MAQ. At this point it

is ready for the manipulation. We then place the cell into the recording chamber, and we patch-clamp in whole-cell configuration. Once the cell is patch-clamped, we apply either the LED or the laser protocol.

LED protocol Here the sample is illuminated with alternated light at 500 nm and 380 nm coming from the LED system underneath the support platform. The full period is of around 10 seconds, with 5 seconds for each of the two wavelength. The photoswitch current is measured from the clamp probe and sent to the data acquisition system.

Laser protocol In this case, the sample is illuminated from below by a 500 nm LED, and from above by 375 nm laser flashes coming from the fiber. In order to illuminate the clamped cell, an additional step is needed which consists in moving the translation stage support of the fiber end and positioning carefully onto the cell. A few flashes of laser light are usually performed to check that the laser light hits the cell, and to image what part of the cell is illuminated. After this, we send two anti-phase square waves at the LED controller and the power supply of the laser so that the LED and laser light are alternated. The periods of illuminations have been chosen to be shorter than the LED protocol, usually of around 2 seconds. A signal proportional to the photoswitch current and the two pumping signals (of the LED and of the laser) are recorded onto the oscilloscope.

In both cases, the clamping has the effect of destroying a part of the cell membrane, so that it will not be possible to observe the photoswitch effect if not for 5 to 10 minutes at maximum. After this, the cell will die and the channels will become inactive. Furthermore, the sample population on the glass cover slip can stay alive for around 1 or 2 hours, after which the cells will die and a new sample has to be prepared.

4.3.2 Comparison between the LED protocol and the laser protocol

Both protocols have been tested, and as a general result, we have always found that the LED protocol performed better than the laser one. Figure 4.6 shows two representative traces of photoswitch using the two protocols. While with the LED protocol the photoswitch current is of the order of 100 pA, with the laser protocol the photoswitch current was always 2 to 10 times smaller. It is hard to explain this difference in amplitude, especially because from a "back of the envelope" calculation, the light intensity reaching the cell should be of the order of 1-2 μW at 100 mA pumping current, concentrated on a region of around 100 μm^2, and at higher pumping currents the laser light has been definitely been observed to be high enough to kill the cells in the sample.

In any case, not all cells are similar, so to eliminate the cell variability and

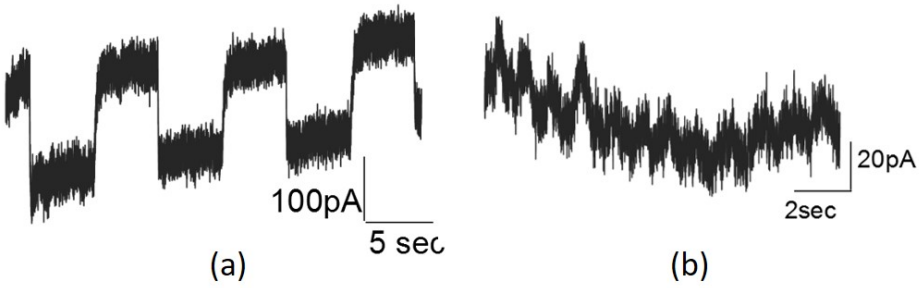

Figure 4.6: Representative traces of photoswitch when using the diode protocol and the laser protocol. *(A)* Recorded photoswitch during the LED protocol with a 10 seconds period. The TREK1 specific current is blocked during UV light (lasting 5 seconds). *(B)* Recorded photoswitch during the laser protocol with a 2 seconds period. The TREK1 specific current is blocked during the laser pulses (lasting 1 second). In this case the photoswitch is 5 to 10 times less visible than in the LED protocol.

only check the efficiency of the LED and laser protocols, we have tested both on the same clamped cell, one shortly after another. This is shown in Figure 4.8. The clamping on this cell was successful, with measured resting membrane potential V_m equal to -30 mV, membrane capacitance C_m equal to 35 pF and input resistance IR equal to 100 MΩ. Panel (a) shows a microscope imaging of the sample, with and without laser light. After a successful clamping, we have first recorded the photoswitch current using the LED protocol, as shown in panel (b). The photoswitch trace has been cutted into 10 seconds periods which have been averaged (normalizing the offset to zero) to produce the averaged response visible in the right figure. The response resembles a square wave, with around 40 pA amplitude.

After this, the laser protocol has been applied. Panel (c) shows the laser signal sent to the power supply (calibrated so that -10 V corresponds to 0 mA and 2 V corresponds to 70 mA pumping current) and a signal proportional to the photoswitch current. Also in this case we have cutted the photoswitch trace in equal segments of 2 seconds to produce the averaged response visible in panel (d). Notice the the step-up of the laser signal corresponds to the down-switch of the current, as the laser has the effect of blocking the TREK1 channels. While the cell signal is not calibrated in this case, as it comes from an output monitoring signal (not calibrated) of the data acquisition system, later measurements with already calibrated traces allows us to estimate its amplitude to around 20 pA, so at least half the amplitude of the response in the LED case.

Given the two averaged responses for the two protocols, we have measured the decay times of the photoswitch when either the 380 nm LED light or the 375 nm laser light are switched on. The two decays are visible in Figure 4.7, and both are congruent with an exponential decay, as compatible with ion channel

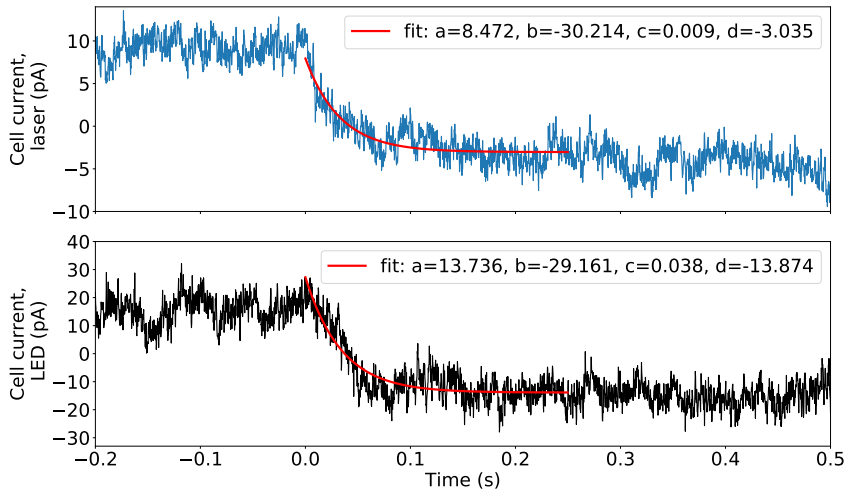

Figure 4.7: Photoswitch decay, comparison between the LED protocol and the laser protocol. The decay is fitted with the function $f(x) = a\exp(b(x-c)) + d$. The exponential decay times $\tau_{exp} = -1/b \simeq 33$ ms are comparable between the two protocols.

dynamics [Sigg 2014]. The exponential decay time is similar for both cases at around 33 ms.

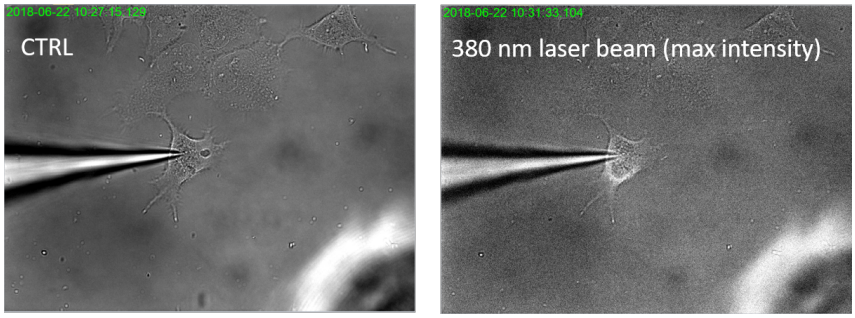

(a) Microscope 40X imaging of the sample. Left is control picture, right is during laser illumination.

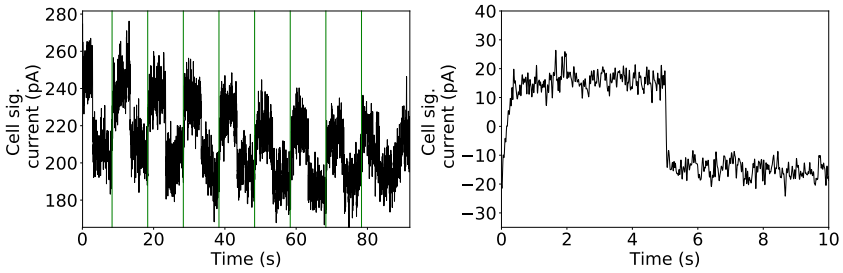

(b) Photoswitch current during LED protocol, 10 seconds period. The averaged response is shown on the right.

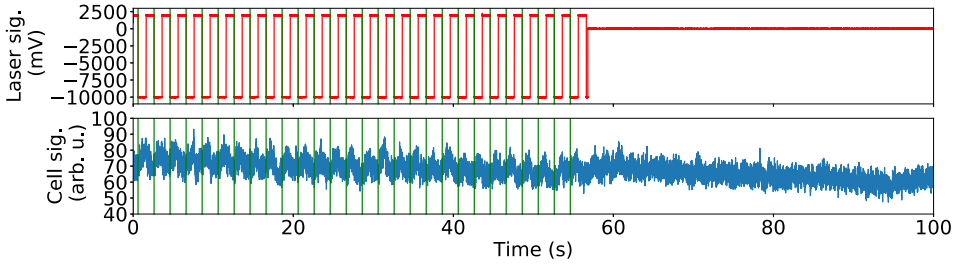

(c) Photoswitch current during laser protocol, 2 seconds period. The top trace represents the laser intensity (min. is 0 mA and max. is 70 mA pumping current), while the bottom trace represents the photoswitch current. The cuts used to calculate the averaged response (d) are shown as green vertical lines.

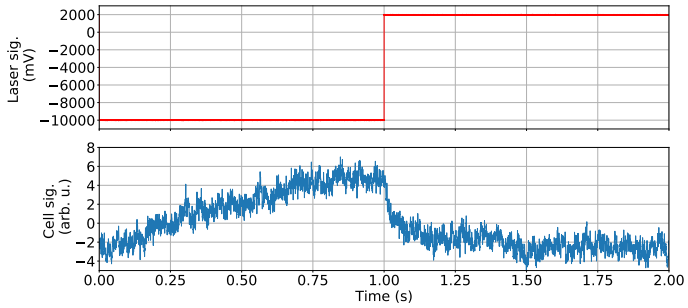

(d) Averaged response for the laser protocol.

Figure 4.8: Photoswitch efficiency comparison between the LED and laser protocol when applied to the same cell in short succession. Data from Cell n. 1 of 22/06/2018, with $V_m = -30$ mV, $C_m = 35$ pF and $IR = 100$ MΩ.

4.3.3 Part vs whole cell illumination

In the second stage of the experiment, we tested if we could observe some amplitude or decay-time changes in the photoswitch current when illuminating the cell either partially or totally. The reasoning behind this is that only the channels that are illuminated will be blocked by the laser light, while the others will not, thus changing the photoswitch response. In order to perform more than one trial on the came cell, after a successful clamping, we tested different laser light intensities at different illuminating positions in the same run.

Figure 4.13 shows the case of Cell n.2 of 10/07/2018. In this case we performed 8 trials, each one consisting in a periodic illumination of the cell with LED and laser light (they can be identified by the periodic square trains in the laser signal), 2 of which where performed while illuminating the cell totally, and 6 of which while illuminating the cell partially, as shown in Figure 4.13. The laser light intensity of each trial can be reconstructed from the laser signal: 1 V corresponds to 75 mA and 2V corresponds to 95 mA pumping current. Each trial has been analysed separately in order to reconstruct the averaged response, which was then fitted with an exponential function. Figure 4.11 shows an example of this analysis in the case of the second trial, which corresponds to whole cell illumination and high laser intensity. Panel (a) shows the timetraces corresponding to this trial, while panel (b) shown the corresponding averaged response.

The averaged response has been constructed in two ways: firstly by following the usual technique of cutting the trace, offsetting each frame by their average value and then averaging the result and secondly by applying an additional normalization which consists in dividing each off-setted frame by its offset value as a way to normalize it in order to keep the frames consistent. The reasoning behind this is that, as time passes, the cell signal slowly decreases, which is a sign that the cell membrane is losing stability so that less current will flow through the channels. This effect is called *rundown* (see [Horn 1992]) and as the cell signal will decrease, so will the amplitude of the photoswitch, hence the renormalization. Note that, due to a calibrating error of the signal generator, the LED and laser signals are not exactly in anti-phase. This does not affect the decay times as the fit has been limited to the interval between the laser switch-on time and the LED switch-on time.

From the plot of the averaged response, for each trial we define three indicators:

- The amplitude ΔV, which is the vertical distance between the two horizontal yellow lines as in Figure 4.11. The top line is defined as the average of the cell signal during the last 0.5 seconds before the laser switch-on time, while the bottom line is defined as the offset of the exponential fit.
- The amplitude ΔV_{norm}, which is the amplitude of the normalized re-

sponse defined as before;

- The exponential decay time τ_{exp}, which is calculated from the exponential fit as $\tau = -1/b$.

These three parameters are plotted for each trial in the laser three panels of Figure 4.13.

The same type of measurement and analysis has been performed again for Cell n.3 of 10/07/2018, as shown in Figure 4.14. The only difference with the previous case is that here we started with partial illumination and then moved to total illumination, as shown in Figure 4.10; and in this case the LED and laser signal are in anti-phase as shown in Figure 4.12.

Comment on the averaged responses analysis Looking at the amplitude and decay times of Figures 4.13 and 4.14, we observe the following:

- It does not seem evident that whole-cell illumination produces higher responses that part-cell illumination. Instead in both cases, the rundown effect seems to dictate the amplitude, so that higher responses are observed in the trial at the beginning of the run with respect to the one at the end of the run, even in the case of normalized responses.
- In the case of the decay times, for both cases they seem to be shorter in the whole-cell illumination than in the part-cell illumination. This could be a first recorded effect of the different illumination conditions.
- The laser power does not seem to be correlated with either amplitude nor decay times, even though a somewhat oscillatory up-and-down pattern is visible in the indicators of Figure 4.13.

In both cases, cell variability is large enough so that it is not possible to compare the indicators of different cells with each other. As an example, while for Cell n.2 the response is of the order of 30 mV and the decay times of the order of 0.4 s, in the case of Cell n.3 the response is of order 8 mV and the decay times are of order 0.12 s.

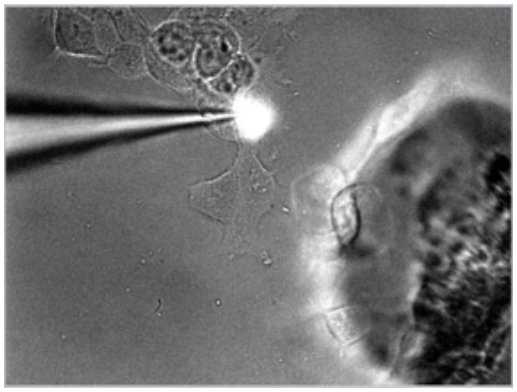

(a) Whole-cell illumination

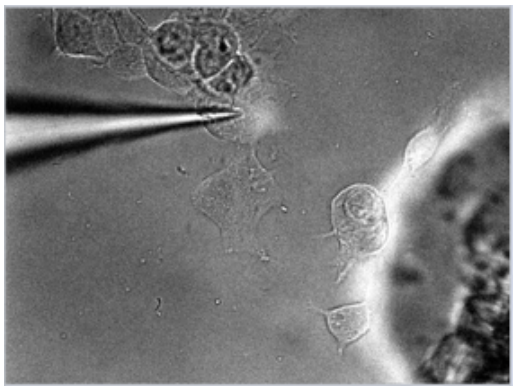

(b) Part-cell illumination

Figure 4.9: Microscope imaging of Cell n.2 of 10/07/2018 at 40X magnification. The photoswitch trials on this cell are divided in two sets: two with *whole-cell illumination* (a) and six with *part-cell illumination* (b). All the trials are visible in Figure 4.13.

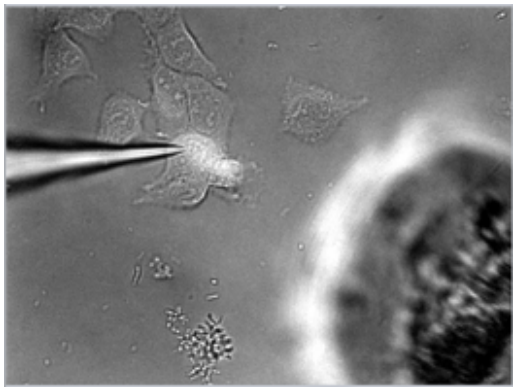

(a) Part-cell illumination

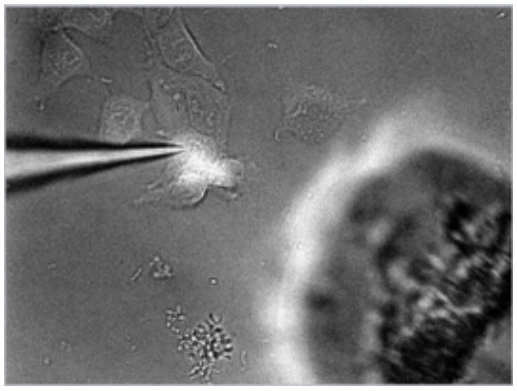

(b) Whole-cell illumination

Figure 4.10: Microscope imaging of Cell n.3 of 10/07/2018 at 40X magnification. The photoswitch trials on this cell are divided in two sets: two with *part-cell illumination* (a) and two with *whole-cell illumination* (b). All the trials are visible in Figure 4.14.

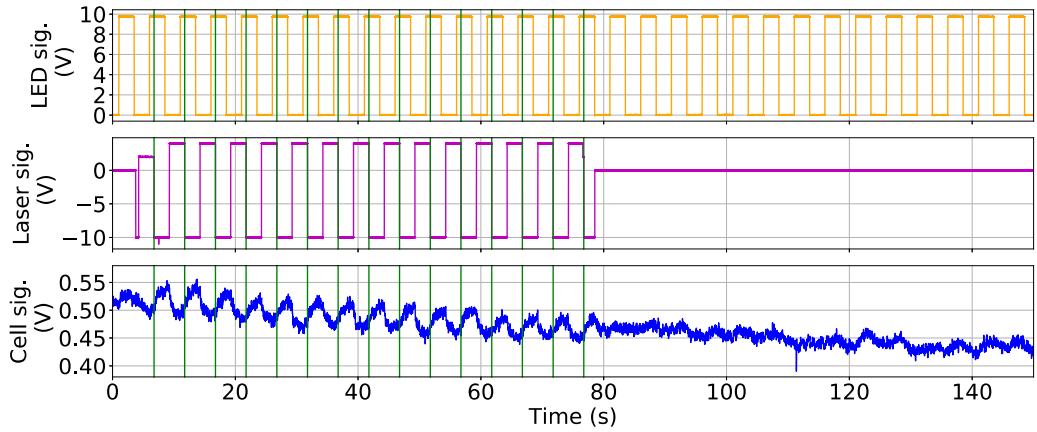

(a) Part of the photoswitch trace corresponding to the second trial in Figure 4.13 (whole cell illuminated - high laser intensity)

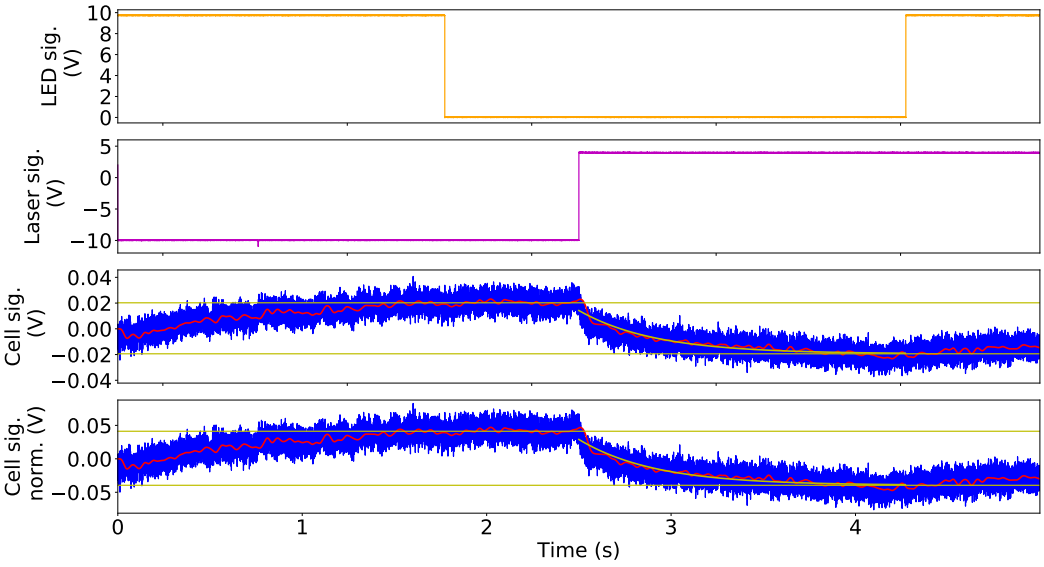

(b) Averaged response, along with LED and laser signals

Figure 4.11: Analysis of the photoswitch trace shown in Figure 4.13 for the second trial (whole cell illuminated - high laser intensity). The averaged response and normalized averaged response are fitted with an exponential function of the type: $f(x) = a\exp(b(x-c)) + d$, with best b fit parameters equal to $b = -2.715\ \mathrm{s}^{-1}$ and $b_{norm} = -2.719\ \mathrm{s}^{-1}$. The two horizontal yellow lines determine the amplitude of the response. The red trace is the Butterworth-filtered version of the response, with cutoff 20 Hz. Note that, due to a calibrating error, the LED and laser signals are not in anti-phase. However this does not affect the decay times here measured.

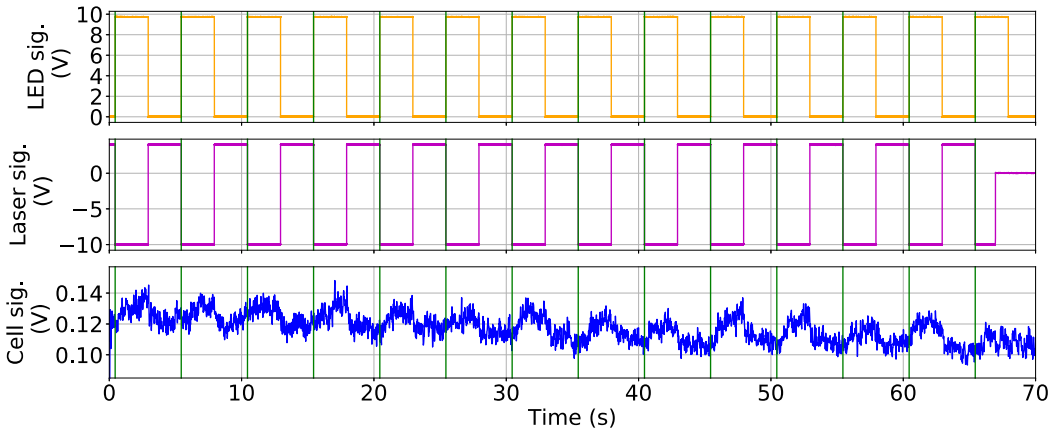

(a) Part of the photoswitch trace corresponding to the first trial in Figure 4.14 (part cell illuminated - high laser intensity)

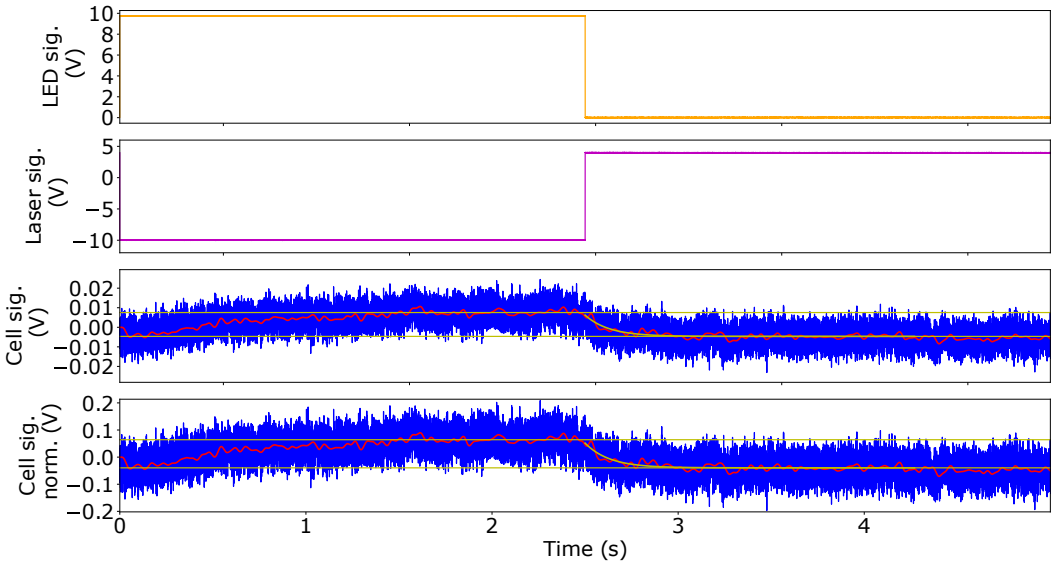

(b) Averaged response, along with LED and laser signals

Figure 4.12: Analysis of the photoswitch trace shown in Figure 4.14 for the first trial (part cell illuminated - high laser intensity). The averaged response and normalized averaged response are fitted with an exponential function of the type: $f(x) = a\exp(b(x-c)) + d$, with best b fit parameters equal to $b = -7.813\ \mathrm{s}^{-1}$ and $b_{norm} = -7.675\ \mathrm{s}^{-1}$. The two horizontal yellow lines determine the amplitude of the response. The red trace is the Butterworth-filtered version of the response, with cutoff 20 Hz.

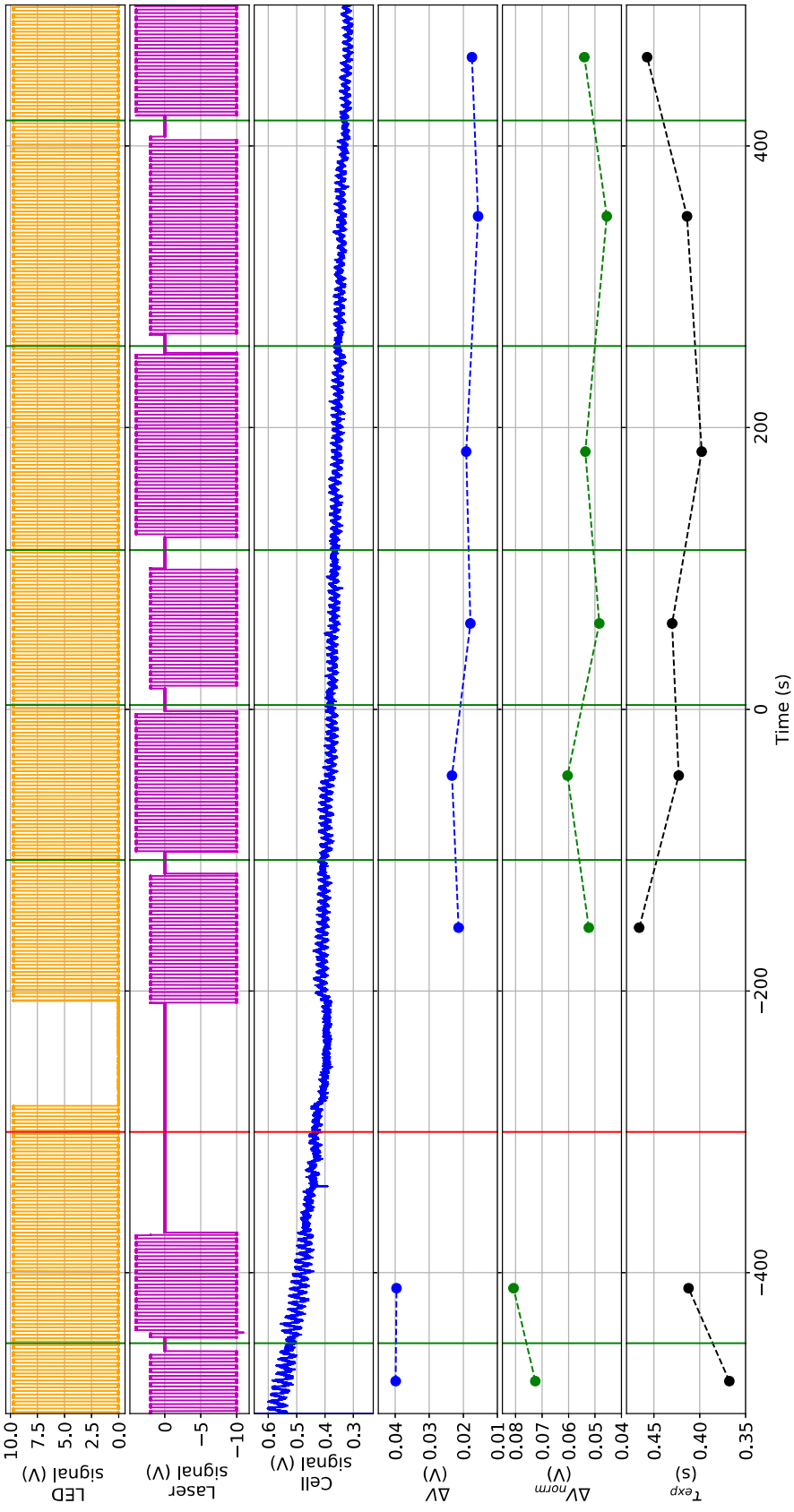

Figure 4.13: Long photoswitch trace acquired using the laser protocol, data from Cell n.2 of 10/07/2018. To the left of the red vertical line the whole cell is illuminated, while to the right only a part is illuminated (case WHOLE-PART, as in Figure 4.9). From top to bottom, the panels represent: the LED signal ("off" at min., "on" at max.); the laser signal (pumping current equal to 0 mA at min., 75 mA at 1V and 95 mA at 2V); the photoswitch current from the cell; the amplitude of the averaged response (for each trial); the amplitude of the normalized averaged response; the exponential decay times of the normalized average response.

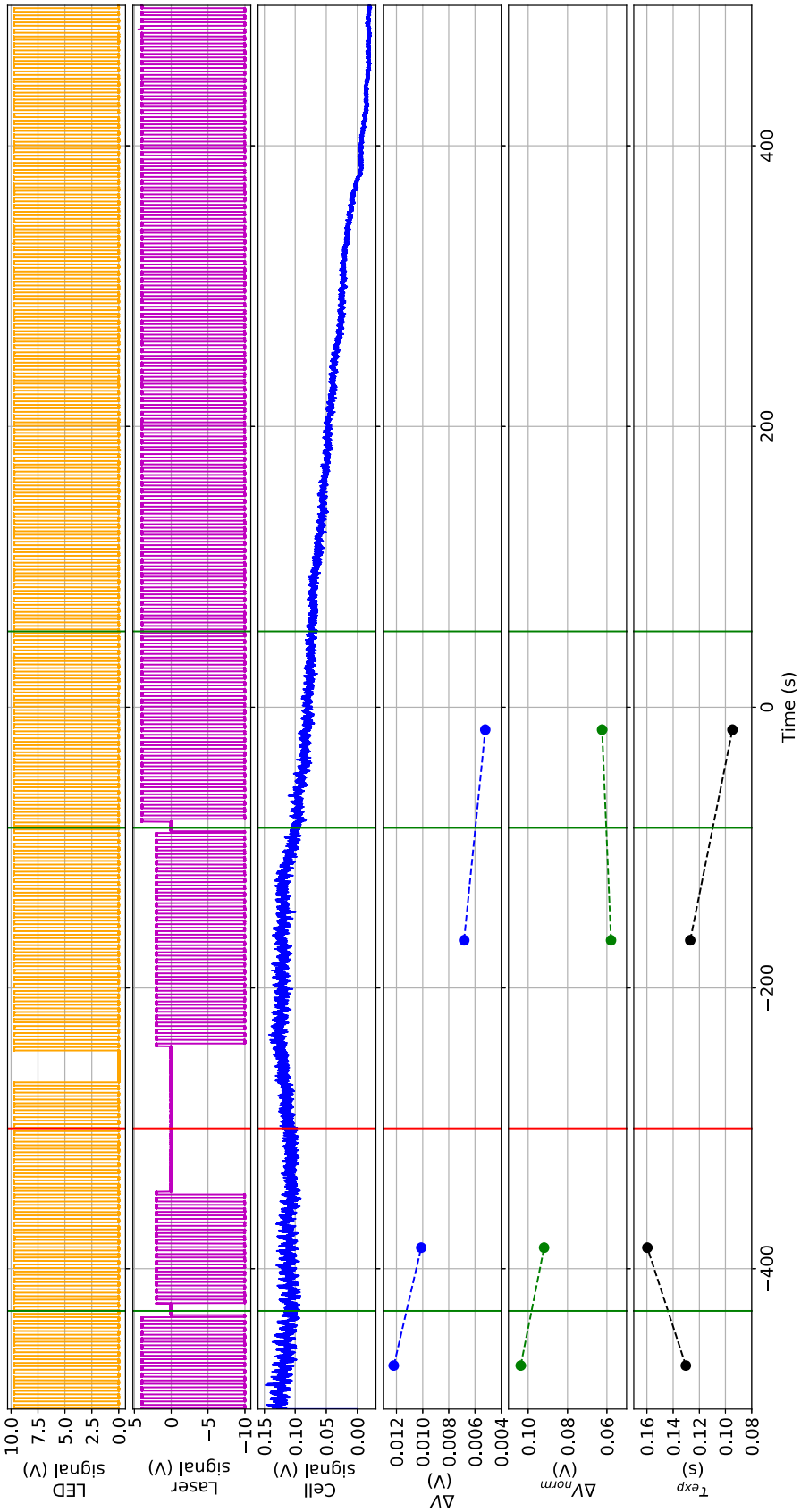

Figure 4.14: Long photoswitch trace acquired using the laser protocol, data from Cell n.3 of 10/07/2018. To the left of the red vertical line only a part of the cell is illuminated, while to the right the whole cell is illuminated (case PART-WHOLE, as in Figure 4.10). From top to bottom, the panels represent: the LED signal ("off" at min., "on" at max.); the laser signal (pumping current equal to 0 mA at min., 75 mA at 1V and 95 mA at 2V); the photoswitch current from the cell; the amplitude of the averaged response (for each trial); the amplitude of the normalized averaged response; the exponential decay times of the normalized average response.

4.4 Conclusion

In this experiment we tested the efficiency of using the light coming from a laser source through an optical fiber as a substitute for LED illumination in generating photoswitch currents. These currents are the result of periodic activation and deactivation of potassium TREK1 channels through periodic illumination at 500 nm and 380 nm. We found that, even though the efficiency of this technique was 2 to 10 times less than in the LED case, we were still able to observe a photoswitch with an exponential time decay which is consistent with the LED protocol. Furthermore, there seemed to be a slight change in amplitude and decay times when employing an whole-cell illumination with respect to part-cell illumination.

The type of manipulation technique here presented based on optical control of ion channel activity could provide additional information about functional localization of single active channel in cell membrane and may have important functional implications in the field of *optogenetics*. Furthermore this novel technique is extendible to hippocampal neurons generated from knock-in mouse where the WT TREK1 channel gene is replaced by TREKLight in the same place in the genome. In this case it could be possible to excite these neurons at different localised positions, and thus opening the possibility of local excitability through light manipulation based on off-the-shelf components. Following the validation of the basic operating principle here described, the next step is to use microlensed fibers which will allow for an even smaller spot size of 2 μm.

Chapter 5

Final conclusion

The work here presented lies at the interface between neuro-inspired biological models and optical laser systems. In the first chapter we have presented how a single laser with injection shares many of the properties that characterize the behaviour of a single neuron: namely, its excitable behaviour, the existence of a refractory period and a resonator property and controllable multipulse excitability. Furthermore, at their most basic levels, both systems can be described by an Adler-like model, which can be further modified in order to display an increasing dynamical complexity.

The strong connection between neuronal systems and optical ones is apparent both in their underlying dynamics and their mathematical modelling. However the rate equations of photonics devises operates at approximately eight orders of magnitude faster than biological time scales. Furthermore photonic neurons could operate in a low-power, spike-encoding hybrid scheme which can open a new way of processing information. For this reason, many studies have attempted to recreate a photonic excitable model as close as possible to neuronal dynamics (as in [Shastri 2015]), which could be very soon implemented in elementary spike computing logical gates, as in the case of ultrafast spatiotemporal pattern recognition circuits [Motoike 2003, Nahmias 2013].

However the real future challenge in the construction of neuro-inspired computing architectures lies in the possibility of parallel photonic information processing that can be implemented through systems of many coupled neuron-like elements. To this end, here we have presented the study of a network of globally coupled lasers, and we have investigated the resulting dynamics with respect to the modification of bifurcation parameters and the selected population of coupled lasers. While for this system we still lack the proper control for performing computational tasks on the network, this work is a first stage exploration of a fully-connected chaotic-spiking opto-electronical network.

This and other types of *optical neural networks* are currently undergoing a

computational revolution which is parallel to the one that is revolutionizing the field of machine learning and artificial intelligence [LeCun 2015]. The potential in parallel computation with similar networks is already showing some very promising results as in the case of spoken digit, speaker recognition and chaotic time-series prediction [Brunner 2013], or the prediction of a Mackey-Glass equation [Dong 2016], only to name two examples. Future research in this topic will surely bring many surprises in the years to come.

Appendices

Appendix A

Derivation of the Adler model from the θ-model

Here we show how it is possible to derive the Adler model:

$$\frac{d\phi}{dt} = \omega - \sin\phi \tag{A.1}$$

starting from the θ-model:

$$\frac{d\theta}{dt} = (1 - \cos\theta) + (1 + \cos\theta)\, I(t) \tag{A.2}$$

assuming that $I(t) = I_0$ is a constant.

Derivation Starting from the θ-model, we make the substitution:

$$I_0 = \frac{\omega + 1}{\omega - 1} = \frac{2}{\omega - 1} + 1 \tag{A.3}$$

so that:

$$\begin{aligned} \frac{d\theta}{dt} &= (1 - \cos\theta) + (1 + \cos\theta) I_0 \\ &= 2 + \frac{2}{\omega - 1} + \frac{2}{\omega - 1}\cos\theta \\ &= \frac{2}{\omega - 1}\,(\omega + \cos\theta) \end{aligned} \tag{A.4}$$

We now introduce the scaled time:

$$\tau = \left(\frac{2}{\omega - 1}\right) t \tag{A.5}$$

so that the evolution according to the new timescale become:

$$\frac{d\theta}{d\tau} = \frac{d\theta}{dt}\frac{dt}{d\tau} = \omega + \cos\theta \tag{A.6}$$

And finally introducing the new variable $\phi = \pi/2 + \theta$ we get:

$$\frac{d\phi}{d\tau} = \frac{d\theta}{d\tau} = \omega + \cos\left(\frac{\pi}{2} + \theta\right) = \omega - \sin\phi \tag{A.7}$$

which is just the Adler model in the new timescale.

Appendix B

A note on relaxation oscillations

In most dynamical settings, as in electronic oscillators or slow-fast systems, "relaxation oscillations" refers to the non-sinusoidal repetitive output signal typically observed in the Van Der Pol oscillator (see [Ginoux 2012] for an interesting historical perspective on the subject). An example of such type of oscillations can also be found in laser systems, as with the thermo-optical pulsing of a semiconductor amplifier [Barland 2003, Marino 2004].

However, in laser physics the term "relaxation oscillations" has come to describe the relaxation process of an unperturbed semiconductor laser towards its stable lasing solution. This relaxation is generally associated with damped oscillations due to the very different time scales of the electric field and carriers (see e.g. [Lugiato 2015] and [Lippi 2000]). Thus this term is widely used in the laser physics community even when the dynamics takes place very close to the stable fixed point, where the oscillations typically do not display prominently the distinctive features of slow-fast systems. The type of oscillations here described have been studied in the case of semiconductor lasers in [Tredicce 1985, Jagher 1996, Erneux 2007, Krauskopf 1997, Kelleher 2012b].

Appendix C

Derivation of the the simplified Class B [Prati 2010] model from the [Tredicce 1985] LIS model

Here we will show how to go from the [Tredicce 1985] model of a Class B laser to the simplified Class B [Prati 2010] model described in Equation 2.40 and what are the necessary parameter identifications.

We start from the [Tredicce 1985] model written using adimensional variables as in equation (10) of the paper:

$$\begin{cases} x' &= (z-1)x + (\theta - \delta z)y + A \\ y' &= -(\theta - \delta z)x + (z-1)y \\ \frac{\kappa}{\gamma_\parallel} z' &= -z\frac{x^2+y^2}{1+\delta^2} - z + z_0 \end{cases} \tag{C.1}$$

where the prime denotes the derivative with respect to the dimensionless time $s = \kappa\, t$. Rewriting the first two equations as:

$$\begin{aligned} x' &= -x + \theta y + (x - \delta y)z + A\cos\phi_I \\ y' &= -y - \theta x + (y + \delta x)z + A\sin\phi_I \end{aligned} \tag{C.2}$$

where we have introduced the phase of the injected field ϕ_I, which in the case of C.1 is set to zero, we recognize that we can rewrite these two equations as:

$$\tilde{\mathbb{E}}' = -(1+i\theta)\tilde{\mathbb{E}} + (1-i\alpha)z\tilde{\mathbb{E}} + \mathbb{A} \tag{C.3}$$

where $\tilde{\mathbb{E}}$ is the complex number with real and imaginary parts given by x and y (i.e. $\tilde{\mathbb{E}} = x + iy$) and we have set $\delta = -\alpha$, $\mathbb{A} = Ae^{i\phi_I}$. The third equation for

z can instead be recast as:

$$\sigma z' = -z\frac{|\tilde{\mathbb{E}}|^2}{1+\alpha^2} - z + z_0 \tag{C.4}$$

where we have introduced the timescale parameter $\sigma = \kappa/\gamma_\parallel$. We now apply the following change of variable:

$$\mathbb{E} \equiv \frac{\tilde{\mathbb{E}}}{\sqrt{1+\alpha^2}} \qquad \longrightarrow \qquad \tilde{\mathbb{E}}' = \mathbb{E}'\sqrt{1+\alpha^2} \tag{C.5}$$

So that, by identifying $z = D$ and $z_0 = \mu$, we can recast the system of equations for $(\mathbb{E}, D)$ as:

$$\begin{cases} \mathbb{E}' = -(1+i\theta)\mathbb{E} + (1-i\alpha)D\mathbb{E} + \mathbb{E}_I \\ \sigma D' = -D|\mathbb{E}|^2 - D + \mu \end{cases} \tag{C.6}$$

where we have introduced $\mathbb{E}_I = \mathbb{A}/\sqrt{1+\alpha^2}$. By employing the timescale change $\tau = (1/\sigma)\, s$ and by denoting with the dot the derivative with respect to τ, this system can be written in the same form as Equation 2.40, i.e.:

$$\begin{cases} \dot{\mathbb{E}} = \sigma\left[-(1+i\theta)\mathbb{E} + (1-i\alpha)D\mathbb{E} + \mathbb{E}_I\right] \\ \dot{D} = \mu - D(1+|\mathbb{E}|^2) \end{cases} \tag{C.7}$$

Summary We can identify the [Tredicce 1985] system with the simplified Class B [Prati 2010] model by the parameter identification:

$$\begin{aligned} &\delta = -\alpha \\ &z_0 = \mu \\ &\frac{A}{\sqrt{1+\alpha^2}} = |\mathbb{E}_I| \quad (\text{with } \phi_I = \arg(\mathbb{E}_I) = 0) \end{aligned} \tag{C.8}$$

and by changing the dynamical variables (x, y, z) to the variables $(\mathbb{E}, D)$ by:

$$\begin{aligned} &\frac{x+iy}{\sqrt{1+\alpha^2}} = \mathbb{E} \\ &z = D \end{aligned} \tag{C.9}$$

and the timescale to the time $\tau = (1/\sigma)\, s = (\gamma_\parallel/\kappa)\, s$.

Appendix D

Derivation of the the simplified Class B [Prati 2010] model from the [Solari 1994] LIS model

Here we will show how to go from the [Solari 1994] model of a Class B laser to the simplified Class B [Prati 2010] model described in Equation 2.40 and what are the necessary parameter identifications.

We start from the system as in equation (2.2) of the paper:

$$\begin{cases} E' = EW + i(\bar{\theta}\, W + \eta)E + \epsilon \\ W' = A^2 - \bar{\mu}\, W(1 + g|E|^2) - |E|^2 \end{cases} \tag{D.1}$$

where the prime denotes the derivative with respect to the dimensionless time s equal to:

$$s = \sqrt{\frac{1+\alpha^2}{\gamma_{\parallel}} \left(\frac{1}{\kappa} + \frac{1}{\gamma_{\perp}} \right)} \tag{D.2}$$

and we introduce the new variables:

$$\begin{aligned} \mathbb{E} &\equiv \sqrt{g} E \\ D &\equiv \bar{\mu} g W + 1 \end{aligned} \tag{D.3}$$

so that we can rewrite this system as:

$$\begin{cases} \mathbb{E}' = \dfrac{1}{\bar{\mu} g} \left[D\mathbb{E}(1 + i\bar{\theta}) - \mathbb{E}(1 + i\bar{\theta} - i\eta\bar{\mu} g) + \epsilon\bar{\mu} g\sqrt{g} \right] \\ D' = \bar{\mu}\left[(1 + gA^2) - D(1 + |\mathbb{E}|^2) \right] \end{cases} \tag{D.4}$$

By setting $\bar{\theta} = -\alpha$, $-\alpha - \eta\bar{\mu}g = \theta$, $\mathbb{E}_I = \epsilon\bar{\mu}g\sqrt{g}$ and $(1 + gA^2) = \mu$, we can further recast it into:

$$\begin{cases} \mathbb{E}' = \dfrac{1}{\bar{\mu}g}\left[D\mathbb{E}(1 - i\alpha) - \mathbb{E}(1 + i\theta) + \mathbb{E}_I\right] \\ D' = \bar{\mu}\left[\mu - D(1 + |\mathbb{E}|^2)\right] \end{cases} \tag{D.5}$$

so that, by employing the timescale change $\tau = \bar{\mu}\, s$, by denoting with the dot the derivative with respect to τ and by introducing the timescale parameter $\sigma = 1/(g\bar{\mu}^2)$, we arrive at the system in the form 2.40:

$$\begin{cases} \dot{\mathbb{E}} = \sigma\left[-(1 + i\theta)\mathbb{E} + (1 - i\alpha)D\mathbb{E} + \mathbb{E}_I\right] \\ \dot{D} = \mu - D(1 + |\mathbb{E}|^2) \end{cases} \tag{D.6}$$

Summary We can identify the [Solari 1994] system with the simplified Class B [Prati 2010] model by the parameter identification:

$$\begin{aligned} A &= \frac{\sqrt{\mu - 1}}{\sqrt{g}} \\ \bar{\theta} &= -\alpha \\ \eta &= -\frac{\sqrt{\sigma}\,(\alpha + \theta)}{\sqrt{g}} \quad \longrightarrow \quad \eta = -\frac{2\pi\Delta'}{\sqrt{g}\sqrt{\sigma}} \\ \bar{\mu} &= \frac{1}{\sqrt{g}\sqrt{\sigma}} \\ \epsilon &= \frac{\sqrt{\sigma}\,\mathbb{E}_I}{g} \end{aligned} \tag{D.7}$$

Note that since the [Solari 1994] system has one parameter more than the [Prati 2010] system, the g parameter is a free parameter that gets simplified in the system 2.40. The dynamical variables (E, W) are changed into the $(\mathbb{E}, D)$ variables by:

$$\begin{aligned} E &= \frac{\mathbb{E}}{\sqrt{g}} \\ W &= \frac{\sqrt{\sigma}(D - 1)}{\sqrt{g}} \end{aligned} \tag{D.8}$$

and the time is changed to the new $\tau = (1/\sqrt{\sigma})\, s$.

Appendix E

Derivation of the the simplified Class B [Prati 2010] model from the [Wieczorek 1999] LIS model

Here we will show how to go from the [Wieczorek 1999] model of a Class B laser, also studied in [Wieczorek 2002] and [Wieczorek 2005a], to the simplified Class B [Prati 2010] model described in Equation 2.40 and what are the necessary parameter identifications.

We start from the system as in equation (1) of [Wieczorek 2002]:

$$\begin{cases} E' = K + \left[\frac{1}{2}(1+i\alpha)n - i\omega\right] E \\ n' = -2\Gamma n - (1+2Bn)(|E|^2 - 1) \end{cases} \tag{E.1}$$

where the prime denotes the derivative with respect of the dimensionless time s scaled in units of the relaxation oscillations. If we introduce the new variables:

$$\begin{aligned} \tilde{\mathbb{E}} &\equiv \frac{E}{\sqrt{\frac{\Gamma}{B} - 1}} \\ D &\equiv 2Bn + 1 \end{aligned} \tag{E.2}$$

after some algebra, we can rewrite the system as:

$$\begin{cases} \tilde{\mathbb{E}}' = \sqrt{\frac{B}{\Gamma - B}} K + \frac{(1+i\alpha)D\tilde{\mathbb{E}} - \tilde{\mathbb{E}}\left[1 + i(\alpha + 4\omega B)\right]}{4B} \\ D' = 2\Gamma - D(2\Gamma - 2B)(1 + |\tilde{\mathbb{E}}|^2) \end{cases} \tag{E.3}$$

We now consider the complex conjugate equation of the field equation for E.3, that we can write as:

$$\mathbb{E}' = \sqrt{\frac{B}{\Gamma - B}} K^\dagger + \frac{(1 - i\alpha)D\mathbb{E} - \mathbb{E}\left[1 - i(\alpha + 4\omega B)\right]}{4B} \tag{E.4}$$

where we suppose that $\Gamma > B$, and we introduced the new variable $\mathbb{E} = \tilde{\mathbb{E}}^\dagger$. If we now set:

$$\begin{aligned} \frac{4B\sqrt{B}}{\sqrt{\Gamma - B}} K^\dagger &= \mathbb{E}_I \\ -\alpha - 4\omega B &= \theta \\ \frac{\Gamma}{\Gamma - B} &= \mu \end{aligned} \tag{E.5}$$

the system can be recast into:

$$\begin{cases} \mathbb{E}' = \dfrac{1}{4B}\left[D\mathbb{E}(1 - i\alpha) - \mathbb{E}(1 + i\theta) + \mathbb{E}_I\right] \\ D' = (2\Gamma - 2B)\left[\mu - D(1 + |\mathbb{E}|^2)\right] \end{cases} \tag{E.6}$$

If we now employ the timescale change $\tau = (2\Gamma - 2B)\, s$, by denoting with the dot the derivative with respect to τ and by introducing the timescale parameter $\sigma = (8B(\Gamma - B))^{-1}$, we arrive at the system in the form 2.40:

$$\begin{cases} \dot{\mathbb{E}} = \sigma\left[-(1 + i\theta)\mathbb{E} + (1 - i\alpha)D\mathbb{E} + \mathbb{E}_I\right] \\ \dot{D} = \mu - D(1 + |\mathbb{E}|^2) \end{cases} \tag{E.7}$$

Summary We can identify the [Wieczorek 1999] system with the simplified Class B [Prati 2010] model by the parameter identification:

$$\begin{aligned} \Gamma &= \frac{\mu}{2\sqrt{2}\sqrt{\sigma}\sqrt{\mu - 1}} \\ K &= \frac{\mathbb{E}_I^\dagger \sqrt{\sigma}}{\sqrt{2}\,(\mu - 1)} \\ \omega &= -\frac{(\alpha + \theta)\sqrt{\sigma}}{\sqrt{2}\sqrt{\mu - 1}} \quad \longrightarrow \quad \omega = -\frac{2\pi\Delta'}{\sqrt{2}\,\sqrt{\sigma}\sqrt{\mu - 1}} \\ B &= \frac{\sqrt{\mu - 1}}{2\sqrt{2}\sqrt{\sigma}} \end{aligned} \tag{E.8}$$

The dynamical variables (E, n) are changed into the $(\mathbb{E}, D)$ variables by:

$$\begin{aligned} E &= \frac{\mathbb{E}^\dagger}{\sqrt{\mu - 1}} \\ n &= \frac{\sqrt{2}\sqrt{\sigma}(D - 1)}{\sqrt{\mu - 1}} \end{aligned} \tag{E.9}$$

and the time is changed to the new $\tau = (2\Gamma - 2B)\, s$.

Appendix F

Approximate formula for the phases of the saddle-node pair (points B, C) of the simplified [Prati 2010] model, in the limit of the Adler model.

In this appendix we will derive an approximate equation to find the phases (the angle with respect to the x-axis in the Argand plane) of the stationary B and C points, as defined in Figure 2.31. To do so, we notice that these two points belong to the intersection between the slow manifold, and the circle centered at zero with radius equal to the value of $|E|$ for the two points, which is approximately $\rho_{B,C} \simeq \sqrt{\mu - 1}$. Note that this is correct only for small injected value, as for higher value the two points will move away from the minimum in Figure 2.31.

From the equation for the slow manfold 2.80, we find that the distance squared ρ^2_{mani} as a function of D of a point on the manifold is given by:

$$\rho^2_{mani}(D) = \frac{E^2_{inj}}{(\alpha^2+1)\,D^2 + 2D(\alpha\theta - 1) + \theta^2 + 1} \tag{F.1}$$

where $E_{inj} = |\mathbb{E}_I|$. If we set this distance equal to the distance squared $\rho^2_{B,C}$, we will find the two values of D which correspond to the B and C points, which are:

$$D_{B,C} = \frac{(\mu-1)(1-\alpha\theta) \pm \sqrt{(\mu-1)\,(\alpha^2+1)\,E^2_{inj} - (\mu-1)^2(\alpha+\theta)^2}}{(\alpha^2+1)\,(\mu-1)} \tag{F.2}$$

where B is the point with higher D value, and C the point with lower D value. By substituting this values back into the equation for the slow manifold 2.80

we get the real and imaginary parts of the two points as:

$$\begin{cases} \Re e(\mathbb{E}_{B,C}) &= \dfrac{\alpha(\mu-1)(\alpha+\theta) \mp \sqrt{(\mu-1)\left(\alpha^2+1\right)E_{inj}^2 - (\mu-1)^2(\alpha+\theta)^2}}{\left(\alpha^2+1\right)E_{inj}} \\ \Im m(\mathbb{E}_{B,C}) &= -\dfrac{(\mu-1)(\alpha+\theta) \pm \alpha\sqrt{(\mu-1)\left(\alpha^2+1\right)E_{inj}^2 - (\mu-1)^2(\alpha+\theta)^2}}{\left(\alpha^2+1\right)E_{inj}} \end{cases} \tag{F.3}$$

Note that we can rewrite these expressions in a more compact form as:

$$\begin{cases} \Re e(\mathbb{E}_{B,C}) &= \dfrac{\sqrt{\mu-1}}{\sqrt{1+\alpha^2}}\left(\alpha z \mp \sqrt{1-z^2}\right) \\ \Im m(\mathbb{E}_{B,C}) &= -\dfrac{\sqrt{\mu-1}}{\sqrt{1+\alpha^2}}\left(z \pm \alpha\sqrt{1-z^2}\right) \end{cases} \tag{F.4}$$

Where we have introduced the new variable:

$$z \equiv \frac{(\alpha+\theta)\sqrt{\mu-1}}{E_{inj}\sqrt{1+\alpha^2}} \tag{F.5}$$

which represents the strength of the detuning, normalized to the injection, so that the Saddle-Node boundary can be written as $z = \pm 1$. In the following derivation we suppose to be inside the locking region, so that $-1 < z < 1$.

We can then find the phase of these points as:

$$\phi_{B,C} = \operatorname{atan2}\left(\Im m(\mathbb{E}_{B,C}), \Re e(\mathbb{E}_{B,C})\right) \tag{F.6}$$

where we can write the arguments of the arctan functions as:

$$\frac{\Im m(\mathbb{E}_{B,C})}{\Re e(\mathbb{E}_{B,C})} = \frac{z \pm \alpha\sqrt{1-z^2}}{-\alpha z \pm \sqrt{1-z^2}} \tag{F.7}$$

We now notice that the arctan of this quotient could be simplified by the following procedure:

$$\begin{aligned} \operatorname{atan2}\left(\Im m(\mathbb{E}_{B,C}), \Re e(\mathbb{E}_{B,C})\right) &\overset{(1)}{\simeq} \arctan\left(\frac{z \pm \alpha\sqrt{1-z^2}}{-z\alpha \pm \sqrt{1-z^2}}\right) \\ &\overset{(2)}{\simeq} \arctan\left(\frac{\pm z}{\sqrt{1-z^2}}\right) + \arctan(\alpha) \\ &= \arcsin(\pm z) + \arctan(\alpha) \end{aligned} \tag{F.8}$$

where we have used the following relationship regarding the sum of arctan functions:

$$\arctan\left(\frac{u+v}{1-uv}\right) \overset{(2)}{\simeq} \arctan(u) + \arctan(v) \tag{F.9}$$

with $u = \pm z/\sqrt{1-z^2}$, $v = \alpha$, and the relationship between arctan and arcsin function written as:

$$\arctan\left(\frac{x}{\sqrt{1-x^2}}\right) = \arcsin(x) \tag{F.10}$$

However, this is now exactly right, as we have been sloppy with the two equal signs $\overset{(1)}{\simeq}$ and $\overset{(2)}{\simeq}$. In the first case, we have not considered the fact that the atan2 function is only equal to the arctan function when $\Re e(\mathbb{E}_{B,C}) > 0$, as seen from the definition of Equation 2.71. For the second equal sign, this equation is only valid when $u \cdot v < 1$, while the complete relationship[1] should read:

$$\arctan\left(\frac{u+v}{1-uv}\right) = \begin{cases} \arctan u + \arctan v & u \cdot v < 1 \\ \arctan u + \arctan v - \pi & u \cdot v > 1;\ u, v > 0 \\ \arctan u + \arctan v + \pi & u \cdot v > 1;\ u, v < 0 \end{cases} \tag{F.11}$$

Dotting all the i's and crossing all the t's and calculating all the angles mod 2π, we can derive the correct value for the two phases $\phi_{B,C}$ to be:

$$\phi_B = \arcsin z + \arctan \alpha - \pi \tag{F.12}$$

and

$$\phi_C = -\arcsin z + \arctan \alpha \tag{F.13}$$

Notice how the half difference between the two points follows an arcsin function with argument z:

$$\frac{\Delta\phi}{2} = \arcsin z - \pi/2 \tag{F.14}$$

which is the same as one would expect from an Adler model, with z as the bifurcation parameter, so that the Saddle-Node bifurcation happens for $z = \pm 1$, as expected from [Solari 1994] in equation 2.64, and from [Zimmermann 2001] in equation 2.82.

[1] Which is extremely difficult to find a reference for online.

Appendix G

Derivation of the LI curve from the model of a single laser with optoelectronic feedback as in Eq. 3.8

Here we will show that the model of a single laser with optoelectronic feedback as in Equations 3.8 in the absence of the feedback loop assumes a sharp transition at threshold between an "off" state and an "on" state in the LI (Light-Intensity) curve of the laser.

Without the AC-coupled feedback loop, these equations reduce to:

$$\begin{cases} \dot{S} = & [g(N - N_t) - \gamma_0]\, S \\ \dot{N} = & \dfrac{I_0}{e\,V} - \gamma_c N - g(N - N_t)S \end{cases} \tag{G.1}$$

The steady states of the system can be found by setting $\dot{S} = \dot{N} = 0$, which gives:

(i) $S = 0$, $N = \dfrac{I_0}{eV\gamma_c}$, which is the "off" state of the laser;

(ii) $S = \dfrac{I_0 - I_{th}}{eV\gamma_0}$, $N = \dfrac{\gamma_0}{g} + N_t$, where:

$$I_{th} \equiv eV\gamma_c \left(\frac{\gamma_0}{g} + N_t \right) \tag{G.2}$$

which is the "on" state of the laser.

Let us now estimate the LI curve in the case of a VCSEL laser. Supposing

that:

$$\begin{aligned}
&\tau_c = 1/\gamma_c = 0.37 \text{ ns} && \text{(carrier lifetime)}\\
&\tau_p = 1/\gamma_0 = 12 \text{ ps} && \text{(photon lifetime)}\\
&v_G = 0.88 \times 10^8 \text{ m/s} && \text{(group velocity)}\\
&D = 9.4\ \mu\text{m} && \text{(output window diameter)}\\
&V = 0.3\ \mu\text{m}^3 && \text{(effective mode volume)}\\
&L_e = 24 \text{ nm} && \text{(active region thickness)}\\
&\eta_i = 1 && \text{(internal quantum efficiency)}\\
&\lambda = 770 \text{ nm} && \text{(emission wavelength)}\\
&T_2 = 1 \times 10^{-3} && \text{(output mirror transmittion coefficient)}\\
&N_{th} = 1.28 \times 10^{18} \text{ cm}^{-3} && \text{(carrier density at threshold)}
\end{aligned} \tag{G.3}$$

as in [Barland 2005], we can calculate the output power from S (the photon density, in units of m^{-3}) as (Equation 7.2.18 [Svelto 2010]):

$$P_{out} = \left(\frac{\gamma_2\, v_G}{2\, L_e}\right)(h\nu)\phi = \left(\frac{\gamma_2\, v_G\, h\, c}{2\, L_e\, \lambda}\right) SV \tag{G.4}$$

where ϕ is the number of cavity photons, c the light speed, h Planck's constant and $\gamma_2 = -\ln(1 - T_2)$. In the "on" state, the output power is then:

$$\begin{aligned}
P_{out} &= \left(\frac{\gamma_2\, v_G\, h\, c}{2\, L_e\, \lambda\, e\, \gamma_0}\right)(I_0 - I_{th})\\
&\simeq 32.42 \text{ mW/mA} \times (I_0 - I_{th})
\end{aligned} \tag{G.5}$$

where the value of the threshold current can be calculated from N_{th} as (Equations 9.4.3 [Svelto 2010] and $I_{th} = (\pi D^2/4)J_{th}$):

$$I_{th} = \left(\frac{\pi D^2}{4}\right)\left(\frac{eL_e}{\eta_i \tau_p}\right) N_{th} \simeq 0.993 \text{ mA} \tag{G.6}$$

Figure G.1 shows a plot of the LI curve and of the carrier density with the parameters here assumed.

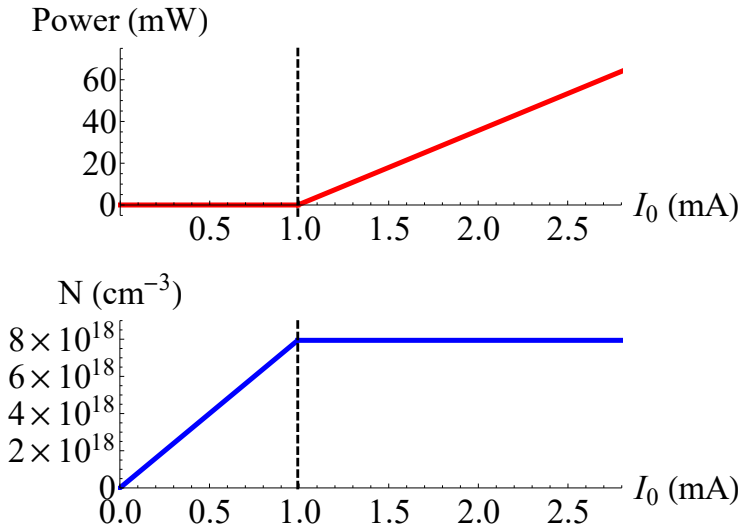

Figure G.1: LI curve calculated from the model of a single laser with optoelectronic feedback 3.8 (without feedback). The parameters of the VCSEL laser are assumed to be as in Equation G.3. The top panel represents the output power, while the bottom panel represents the carrier density, both as function of the pumping current I_0. Note the sharp transition between "off" state and "on" state at $I_0 = I_{th} \simeq 0.993$ mA.

Bibliography

[Abrams 2004] D. M. Abrams and S. H. Strogatz. *Chimera States for Coupled Oscillators*. Physical Review Letters Vol. **93**, No. 17, p. 174102, Oct. 2004.

[Abrams 2008] D. M. Abrams, R. Mirollo, S. H. Strogatz, and D. A. Wiley. *Solvable Model for Chimera States of Coupled Oscillators*. Physical Review Letters Vol. **101**, No. 8, Aug. 2008.

[Acebrón 2005] J. A. Acebrón, L. L. Bonilla, C. J. Pérez Vicente, F. Ritort, and R. Spigler. *The Kuramoto model: A simple paradigm for synchronization phenomena*. Reviews of Modern Physics Vol. **77**, No. 1, p. 137–185, Apr. 2005.

[Adler 1946] R. Adler. *A Study of Locking Phenomena in Oscillators*. Proceedings of the IRE Vol. **34**, No. 6, p. 351–357, Jun. 1946.

[Afraimovich 2014] V. S. Afraimovich, S. V. Gonchenko, L. M. Lerman, A. L. Shilnikov, and D. V. Turaev. *Scientific heritage of L.P. Shilnikov*. Regular and Chaotic Dynamics Vol. **19**, No. 4, p. 435–460, Jul. 2014.

[Al-Naimee 2009] K. Al-Naimee, F. Marino, M. Ciszak, R. Meucci, and F. T. Arecchi. *Chaotic spiking and incomplete homoclinic scenarios in semiconductor lasers with optoelectronic feedback*. New Journal of Physics Vol. **11**, No. 7, p. 073022, 2009.

[Al-Naimee 2010] K. Al-Naimee, F. Marino, M. Ciszak, S. F. Abdalah, R. Meucci, and F. T. Arecchi. *Excitability of periodic and chaotic attractors in semiconductor lasers with optoelectronic feedback*. The European Physical Journal D Vol. **58**, No. 2, p. 187–189, Jun. 2010.

[Alexander 2013] K. Alexander, T. V. Vaerenbergh, M. Fiers, P. Mechet, J. Dambre, and P. Bienstman. *Excitability in optically injected microdisk lasers with phase controlled excitatory and inhibitory response*. Optics Express Vol. **21**, No. 22, p. 26182–26191, Nov. 2013.

[Alpha3031 2018] Alpha3031, *Neuron - Wikipedia*. https://en.wikipedia.org/w/index.php?title=Neuron&oldid=862888039, 2018, page Version ID: 862888039.

[Alsing 1996] P. M. Alsing, V. Kovanis, A. Gavrielides, and T. Erneux. *Lang and Kobayashi phase equation*. Physical Review A Vol. **53**, No. 6, p. 4429–4434, Jun. 1996.

[Amari 1977] S.-i. Amari. *Dynamics of pattern formation in lateral-inhibition type neural fields*. Biological Cybernetics Vol. **27**, No. 2, p. 77–87, Jun. 1977.

[Ananthanarayanan 2009] R. Ananthanarayanan, S. K. Esser, H. D. Simon, and D. S. Modha, *The Cat is out of the Bag: Cortical Simulations with 109 Neurons, 1013 Synapses*. In *Proceedings of the Conference on High Performance Computing Networking, Storage and Analysis*, SC '09, p. 63:1–63:12, (ACM, New York, NY, USA2009), ISBN 978-1-60558-744-8, doi:10.1145/1654059.1654124.

[Antyukhov 1986] V. V. Antyukhov, A. F. Glova, O. R. Kachurin, F. V. Lebedev, V. V. Likhanskii, A. P. Napartovich, and V. D. Pis'mennyi. *Effective phase locking of an array of lasers*. JETP Letters Vol. **44**, No. 2, p. 78–81, 1986.

[Appleton 1922] E. V. Appleton, *Automatic synchronization of triode oscillators*. In *Proc. Cambridge Phil. Soc*, volume 21, p. 231 (1922).

[Aranson 2002] I. S. Aranson and L. Kramer. *The world of the complex Ginzburg-Landau equation*. Reviews of Modern Physics Vol. **74**, No. 1, p. 99–143, Feb. 2002.

[Arecchi 1965] F. Arecchi and R. Bonifacio. *Theory of optical maser amplifiers*. IEEE Journal of Quantum Electronics Vol. **1**, No. 4, p. 169–178, Jul. 1965.

[Arecchi 1984] F. T. Arecchi, G. L. Lippi, G. P. Puccioni, and J. R. Tredicce. *Deterministic chaos in laser with injected signal*. Optics Communications Vol. **51**, No. 5, p. 308–314, Oct. 1984.

[Arenas 2008] A. Arenas, A. Díaz-Guilera, J. Kurths, Y. Moreno, and C. Zhou. *Synchronization in complex networks*. Physics Reports Vol. **469**, No. 3, p. 93–153, Dec. 2008.

[Ashwin 2016] P. Ashwin, S. Coombes, and R. Nicks. *Mathematical Frameworks for Oscillatory Network Dynamics in Neuroscience*. The Journal of Mathematical Neuroscience Vol. **6**, No. 1, Dec. 2016.

[Barland 2003] S. Barland, O. Piro, M. Giudici, J. R. Tredicce, and S. Balle. *Experimental evidence of van der Pol–Fitzhugh–Nagumo dynamics in*

semiconductor optical amplifiers. Physical Review E Vol. **68**, No. 3, p. 036209, Sep. 2003.

[Barland 2005] S. Barland, P. Spinicelli, G. Giacomelli, and F. Marin. *Measurement of the working parameters of an air-post vertical-cavity surface-emitting laser*. IEEE Journal of Quantum Electronics Vol. **41**, No. 10, p. 1235–1243, Oct. 2005.

[Baugher 1989] A. Baugher, P. Hammack, and J. Lin. *Subcritical Hopf bifurcation in a NMR laser with an injected signal*. Physical Review A Vol. **39**, No. 3, p. 1549–1551, Feb. 1989.

[Belousov 1958] B. P. Belousov. *Periodicheski deistvuyushchaya reaktsia i ee mekhanism [Periodically acting reaction and its mechanism]*. Sbornik referatov po radiotsionnoi meditsine [Collection of abstracts on radiation medicine] 1958.

[Benoît 1981] E. Benoît, J. L. Callot, F. Diener, and M. M. Diener. *Chasse au canard (première partie)*. Collectanea Mathematica Vol. **32**, No. 1, p. 37–76, 1981.

[Berglund 2006] N. Berglund and B. Gentz, *Noise-Induced Phenomena in Slow-Fast Dynamical Systems: A Sample-Paths Approach*. Probability and Its Applications. Springer-Verlag, London, 2006, ISBN 978-1-84628-038-2.

[Bick 2011] C. Bick, M. Timme, D. Paulikat, D. Rathlev, and P. Ashwin. *Chaos in Symmetric Phase Oscillator Networks*. Physical Review Letters Vol. **107**, No. 24, p. 244101, Dec. 2011.

[Bland 1988] B. H. Bland, L. V. Colom, J. Konopacki, and S. H. Roth. *Intracellular records of carbachol-induced theta rhythm in hippocampal slices*. Brain Research Vol. **447**, No. 2, p. 364–368, May 1988.

[Boccaletti 2006] S. Boccaletti, V. Latora, Y. Moreno, M. Chavez, and D. U. Hwang. *Complex networks: Structure and dynamics*. Physics Reports Vol. **424**, No. 4, p. 175–308, Feb. 2006.

[Borst 1999] A. Borst and F. E. Theunissen. *Information theory and neural coding*. Nature Neuroscience Vol. **2**, p. 947, Nov. 1999.

[bot 1994] *Diode Laser Arrays*. Cambridge Studies in Modern Optics. Cambridge University Press, 1994, doi:10.1017/CBO9780511524127.

[Bourdet 1987] G. L. Bourdet, R. A. Muller, G. M. Mullot, and J. Y. Vinet. *Active mode locking of a high pressure CW waveguide CO2 laser*. Applied Physics B Vol. **44**, No. 2, p. 107–110, Oct. 1987.

[Braza 1990] P. A. Braza and T. Erneux. *Constant phase, phase drift, and phase entrainment in lasers with an injected signal.* Physical Review A Vol. **41**, No. 11, p. 6470–6479, Jun. 1990.

[Bressloff 2012] P. C. Bressloff. *Spatiotemporal dynamics of continuum neural fields.* Journal of Physics A: Mathematical and Theoretical Vol. **45**, No. 3, p. 033001, 2012.

[Brøns 2008] M. Brøns, T. J. Kaper, and H. G. Rotstein. *Introduction to Focus Issue: Mixed Mode Oscillations: Experiment, Computation, and Analysis.* Chaos: An Interdisciplinary Journal of Nonlinear Science Vol. **18**, No. 1, p. 015101, Mar. 2008.

[Brownlee 2013] C. Brownlee. *Carnivorous Plants: Trapping, Digesting and Absorbing All in One.* Current Biology Vol. **23**, No. 17, p. R714–R716, Sep. 2013.

[Brun 1985] E. Brun, B. Derighetti, D. Meier, R. Holzner, and M. Ravani. *Observation of order and chaos in a nuclear spin–flip laser.* JOSA B Vol. **2**, No. 1, p. 156–167, Jan. 1985.

[Brunel 2000] N. Brunel. *Dynamics of Sparsely Connected Networks of Excitatory and Inhibitory Spiking Neurons.* Journal of Computational Neuroscience Vol. **8**, No. 3, p. 183–208, May 2000.

[Brunner 2013] D. Brunner, M. C. Soriano, C. R. Mirasso, and I. Fischer. *Parallel photonic information processing at gigabyte per second data rates using transient states.* Nature Communications Vol. **4**, No. 1, Dec. 2013.

[Brunner 2015] D. Brunner and I. Fischer. *Reconfigurable semiconductor laser networks based on diffractive coupling.* Optics Letters Vol. **40**, No. 16, p. 3854, Aug. 2015.

[Brunstein 2012] M. Brunstein, A. M. Yacomotti, I. Sagnes, F. Raineri, L. Bigot, and A. Levenson. *Excitability and self-pulsing in a photonic crystal nanocavity.* Physical Review A Vol. **85**, No. 3, p. 031803, Mar. 2012.

[Buck 1988] J. Buck. *Synchronous Rhythmic Flashing of Fireflies. II.* The Quarterly Review of Biology Vol. **63**, No. 3, p. 265–289, Sep. 1988.

[Campenhout 2007] J. V. Campenhout, P. Rojo-Romeo, P. Regreny, C. Seassal, D. V. Thourhout, S. Verstuyft, L. D. Cioccio, J.-M. Fedeli, C. Lagahe, and R. Baets. *Electrically pumped InP-based microdisk lasers integrated with a nanophotonic silicon-on-insulator waveguide circuit.* Optics Express Vol. **15**, No. 11, p. 6744–6749, May 2007.

[Chow 1994] W. W. Chow, S. W. Koch, and M. I. Sargent, *Semiconductor-Laser Physics*. Springer-Verlag, Berlin Heidelberg, 1994, ISBN 978-3-642-64752-9.

[Chow 1998] C. C. Chow. *Phase-locking in weakly heterogeneous neuronal networks*. Physica D: Nonlinear Phenomena Vol. **118**, No. 3, p. 343–370, Jul. 1998.

[Connor 1977] J. A. Connor, D. Walter, and R. McKown. *Neural repetitive firing: modifications of the Hodgkin-Huxley axon suggested by experimental results from crustacean axons*. Biophysical Journal Vol. **18**, No. 1, p. 81–102, Apr. 1977.

[Coombes 2001] S. Coombes. *Phase locking in networks of synaptically coupled McKean relaxation oscillators*. Physica D: Nonlinear Phenomena Vol. **160**, No. 3, p. 173–188, Dec. 2001.

[Corinto 2007] F. Corinto, M. Bonnin, and M. Gilli. *Weakly connected oscillatory network models for associative and dynamic memories*. International Journal of Bifurcation and Chaos Vol. **17**, No. 12, p. 4365–4379, Dec. 2007.

[Coullet 1989] P. Coullet, L. Gil, and F. Rocca. *Optical vortices*. Optics Communications Vol. **73**, No. 5, p. 403–408, Nov. 1989.

[Coullet 1998] P. Coullet, D. Daboussy, and J. R. Tredicce. *Optical excitable waves*. Physical Review E Vol. **58**, No. 5, p. 5347–5350, Nov. 1998.

[Coullet 2005] P. Coullet, J. M. Gilli, M. Monticelli, and N. Vandenberghe. *A damped pendulum forced with a constant torque*. American Journal of Physics Vol. **73**, No. 12, p. 1122–1128, Dec. 2005.

[Crook 1997] S. Crook, G. Ermentrout, M. Vanier, and J. Bower. *The Role of Axonal Delay in the Synchronization of Networks of Coupled Cortical Oscillators*. Journal of Computational Neuroscience Vol. **4**, No. 2, p. 161–172, Apr. 1997.

[De Maesschalck 2015] P. De Maesschalck and M. Wechselberger. *Neural Excitability and Singular Bifurcations*. The Journal of Mathematical Neuroscience (JMN) Vol. **5**, No. 1, Dec. 2015.

[Desroches 2012] M. Desroches, J. Guckenheimer, B. Krauskopf, C. Kuehn, H. Osinga, and M. Wechselberger. *Mixed-Mode Oscillations with Multiple Time Scales*. SIAM Review Vol. **54**, No. 2, p. 211–288, Jan. 2012.

[Diesmann 1999] M. Diesmann, M.-O. Gewaltig, and A. Aertsen. *Stable propagation of synchronous spiking in cortical neural networks*. Nature Vol. **402**, p. 529, Dec. 1999.

[Dolcemascolo 2015] A. Dolcemascolo, *Excitability in a semiconductor laser with optical injection*. Master's thesis, Insubria University, Como, Italy, 2015.

[Dolcemascolo 2018] A. Dolcemascolo, B. Garbin, B. Peyce, R. Veltz, and S. Barland. *Resonator neuron and triggering multipulse excitability in laser with injected signal*. Physical Review E Vol. **98**, p. 062211, Dec 2018.

[Dolcemascolo 2019] A. Dolcemascolo, R. Veltz, F. Marino, , and S. Barland. *Mean field dimensionality reduction of coupled lasers (title subject to change)*. To be submitted 2019.

[Dong 2016] J. Dong, S. Gigan, F. Krzakala, and G. Wainrib. *Scaling up Echo-State Networks with multiple light scattering*. arXiv:1609.05204 [physics] Sep. 2016. arXiv: 1609.05204.

[Dörfler 2013] F. Dörfler, M. Chertkov, and F. Bullo. *Synchronization in complex oscillator networks and smart grids*. Proceedings of the National Academy of Sciences Vol. **110**, No. 6, p. 2005, Feb. 2013.

[Dörfler 2014] F. Dörfler and F. Bullo. *Synchronization in complex networks of phase oscillators: A survey*. Automatica Vol. **50**, No. 6, p. 1539–1564, Jun. 2014.

[Dorogovtsev 2008] S. N. Dorogovtsev, A. V. Goltsev, and J. F. F. Mendes. *Critical phenomena in complex networks*. Reviews of Modern Physics Vol. **80**, No. 4, p. 1275–1335, Oct. 2008.

[Dubbeldam 1999] J. L. A. Dubbeldam and B. Krauskopf. *Self-pulsations of lasers with saturable absorber: dynamics and bifurcations*. Optics Communications Vol. **159**, No. 4, p. 325–338, Jan. 1999.

[Dunn 1983] R. W. Dunn, S. T. Hendow, W. W. Chow, and J. G. Small. *Single-mode operation of Doppler-broadened lasers by injection locking*. Optics Letters Vol. **8**, No. 6, p. 319–321, Jun. 1983.

[Duport 2016] F. Duport, A. Smerieri, A. Akrout, M. Haelterman, and S. Massar. *Fully analogue photonic reservoir computer*. Scientific Reports Vol. **6**, p. 22381, Mar. 2016.

[Eckhaus 1983] W. Eckhaus, *Relaxation oscillations including a standard chase on French ducks*. In F. Verhulst, ed., *Asymptotic Analysis II —*, p. 449–497, (Springer Berlin Heidelberg1983), ISBN 978-3-540-39612-3.

[Eguia 2000] M. C. Eguia and G. B. Mindlin. *Distribution of interspike times in noise-driven excitable systems*. Physical Review E Vol. **61**, No. 6, p. 6490–6499, Jun. 2000.

[Enyedi 2010] P. Enyedi and G. Czirják. *Molecular background of leak K+ currents: two-pore domain potassium channels.* Physiological Reviews Vol. **90**, No. 2, p. 559–605, Apr. 2010.

[Ermentrout 1984] G. Ermentrout and N. Kopell. *Frequency Plateaus in a Chain of Weakly Coupled Oscillators, I.* SIAM Journal on Mathematical Analysis Vol. **15**, No. 2, p. 215–237, Mar. 1984.

[Ermentrout 1986] G. Ermentrout and N. Kopell. *Parabolic Bursting in an Excitable System Coupled with a Slow Oscillation.* SIAM Journal on Applied Mathematics Vol. **46**, No. 2, p. 233–253, Apr. 1986.

[Ermentrout 1991] B. Ermentrout. *An adaptive model for synchrony in the firefly Pteroptyx malaccae.* Journal of Mathematical Biology Vol. **29**, No. 6, p. 571–585, Jun. 1991.

[Ermentrout 1996] B. Ermentrout. *Type I membranes, phase resetting curves, and synchrony.* Neural Computation Vol. **8**, No. 5, p. 979–1001, Jul. 1996.

[Ermentrout 2008] B. Ermentrout, *Ermentrout-Kopell canonical model - Scholarpedia.* `http://dx.doi.org/10.4249/scholarpedia.1398`, 2008.

[Erneux 2007] T. Erneux, E. A. Viktorov, and P. Mandel. *Time scales and relaxation dynamics in quantum-dot lasers.* Physical Review A Vol. **76**, No. 2, p. 023819, Aug. 2007.

[Erneux 2010] T. Erneux, E. A. Viktorov, B. Kelleher, D. Goulding, S. P. Hegarty, and G. Huyet. *Optically injected quantum-dot lasers.* Optics Letters Vol. **35**, No. 7, p. 937, Apr. 2010.

[Farkas 2002] I. Farkas, D. Helbing, and T. Vicsek. *Mexican waves in an excitable medium.* Nature Vol. **419**, No. 6903, p. 131–132, Sep. 2002.

[Faye 2018] G. Faye. *Traveling fronts for lattice neural field equations.* Physica D: Nonlinear Phenomena Vol. **378-379**, p. 20–32, Sep. 2018.

[Fenichel 1979] N. Fenichel. *Geometric singular perturbation theory for ordinary differential equations.* Journal of Differential Equations Vol. **31**, No. 1, p. 53–98, Jan. 1979.

[Fischer 1996] I. Fischer, G. H. M. van Tartwijk, A. M. Levine, W. Elsässer, E. Göbel, and D. Lenstra. *Fast Pulsing and Chaotic Itinerancy with a Drift in the Coherence Collapse of Semiconductor Lasers.* Physical Review Letters Vol. **76**, No. 2, p. 220–223, Jan. 1996.

[FitzHugh 1955] R. FitzHugh. *Mathematical models of threshold phenomena in the nerve membrane.* The bulletin of mathematical biophysics Vol. **17**, No. 4, p. 257–278, Dec. 1955.

[Fournier 2016] N. Fournier and E. Locherbach. *On a toy model of interacting neurons*. Ann. Inst. H. Poincare Probab. Statist. Vol. **52**, No. 4, p. 1844–1876, Nov. 2016.

[Garbin 2014] B. Garbin, D. Goulding, S. P. Hegarty, G. Huyet, B. Kelleher, and S. Barland. *Incoherent optical triggering of excitable pulses in an injection-locked semiconductor laser*. Optics Letters Vol. **39**, No. 5, p. 1254–1257, Mar. 2014.

[Garbin 2015a] B. Garbin, *Excitabilité et solitons temporels de phase dans un système laser neuromorphique*. Ph.D. thesis, Université Nice-Sophia Antipolis, France, 2015.

[Garbin 2015b] B. Garbin, J. Javaloyes, G. Tissoni, and S. Barland. *Topological solitons as addressable phase bits in a driven laser*. Nature Communications Vol. **6**, p. 5915, Jan. 2015.

[Garbin 2017a] B. Garbin, A. Dolcemascolo, F. Prati, J. Javaloyes, G. Tissoni, and S. Barland. *Refractory period of an excitable semiconductor laser with optical injection*. Physical Review E Vol. **95**, No. 1, p. 012214, Jan. 2017.

[Garbin 2017b] B. Garbin, J. Javaloyes, S. Barland, and G. Tissoni. *Interactions and collisions of topological solitons in a semiconductor laser with optical injection and feedback*. Chaos: An Interdisciplinary Journal of Nonlinear Science Vol. **27**, No. 11, p. 114308, Oct. 2017.

[Gavrielides 1997] A. Gavrielides, V. Kovanis, and T. Erneux. *Analytical stability boundaries for a semiconductor laser subject to optical injection*. Optics Communications Vol. **136**, No. 3, p. 253–256, Mar. 1997.

[Ginoux 2012] J.-M. Ginoux and C. Letellier. *Van der Pol and the history of relaxation oscillations: Toward the emergence of a concept*. Chaos: An Interdisciplinary Journal of Nonlinear Science Vol. **22**, No. 2, p. 023120, Apr. 2012.

[Giudici 1997] M. Giudici, C. Green, G. Giacomelli, U. Nespolo, and J. R. Tredicce. *Andronov bifurcation and excitability in semiconductor lasers with optical feedback*. Physical Review E Vol. **55**, No. 6, p. 6414–6418, Jun. 1997.

[Glass 1988] L. Glass and M. Mackey, *From Clocks to Chaos*. Princeton University Press, 1988.

[Golubentsev 1987] A. A. Golubentsev, V. V. Likhanskii, and A. P. Napartovich. *Theory of phase locking of an array of lasers*. Sov. Phys. JETP Vol. **44**, No. 4, p. 676–682, 1987.

[Golubitsky 1988] M. Golubitsky, I. Stewart, and d. schaeffer, *Singularities and Groups in Bifurcation Theory: Volume I*. Applied Mathematical Sci-

ences, Singularities and Groups in Bifurcation Theory. Springer-Verlag, New York, 1988, ISBN 978-0-387-96652-6.

[Golubitsky 2002] M. Golubitsky and I. Stewart, *The Symmetry Perspective: From Equilibrium to Chaos in Phase Space and Physical Space*. Birkhäuser, Basel, 2002nd edn., Mar. 2002, ISBN 978-3-7643-6609-4.

[Gonzalez-Miranda 2002] J. M. Gonzalez-Miranda. *Phase synchronization and chaos suppression in a set of two coupled nonlinear oscillators*. International Journal of Bifurcation and Chaos Vol. **12**, No. 10, p. 2105–2122, Oct. 2002.

[Goulding 2007] D. Goulding, S. P. Hegarty, O. Rasskazov, S. Melnik, M. Hartnett, G. Greene, J. G. McInerney, D. Rachinskii, and G. Huyet. *Excitability in a Quantum Dot Semiconductor Laser with Optical Injection*. Physical Review Letters Vol. **98**, No. 15, p. 153903, Apr. 2007.

[Groos 1985] G. Groos and S. Daan, *The Use of the Biological Clocks in Time Perception*. In J. A. Michon and J. L. Jackson, eds., *Time, Mind, and Behavior*, p. 65–74. Springer Berlin Heidelberg, 1985, ISBN 978-3-642-70491-8, doi:10.1007/978-3-642-70491-8_4.

[Hachair 2006] X. Hachair, F. Pedaci, E. Caboche, S. Barland, M. Giudici, J. Tredicce, F. Prati, G. Tissoni, R. Kheradmand, L. Lugiato, I. Protsenko, and M. Brambilla. *Cavity solitons in a driven VCSEL above threshold*. IEEE Journal of Selected Topics in Quantum Electronics Vol. **12**, No. 3, p. 339–351, May 2006.

[Hagerstrom 2012] A. M. Hagerstrom, T. E. Murphy, R. Roy, P. Hövel, I. Omelchenko, and E. Schöll. *Experimental observation of chimeras in coupled-map lattices*. Nature Physics Vol. **8**, No. 9, p. 658–661, Sep. 2012.

[Hakim 1992] V. Hakim and W.-J. Rappel. *Dynamics of the globally coupled complex Ginzburg-Landau equation*. Physical Review A Vol. **46**, No. 12, p. R7347–R7350, Dec. 1992.

[Hegger 1999] R. Hegger, H. Kantz, and T. Schreiber. *Practical implementation of nonlinear time series methods: The TISEAN package*. Chaos: An Interdisciplinary Journal of Nonlinear Science Vol. **9**, No. 2, p. 413–435, May 1999.

[Henry 1982] C. Henry. *Theory of the linewidth of semiconductor lasers*. IEEE Journal of Quantum Electronics Vol. **18**, No. 2, p. 259–264, Feb. 1982.

[Hodgkin 1948] A. L. Hodgkin. *The local electric changes associated with repetitive action in a non-medullated axon*. The Journal of Physiology Vol. **107**, No. 2, p. 165–181, Mar. 1948.

[Hodgkin 1952a] A. L. Hodgkin and A. F. Huxley. *A quantitative description of membrane current and its application to conduction and excitation in nerve*. The Journal of Physiology Vol. **117**, No. 4, p. 500–544, Aug. 1952.

[Hodgkin 1952b] A. L. Hodgkin, A. F. Huxley, and B. Katz. *Measurement of current-voltage relations in the membrane of the giant axon of Loligo*. The Journal of Physiology Vol. **116**, No. 4, p. 424–448, Apr. 1952.

[Holzner 1987] R. Holzner, B. Derighetti, M. Ravani, and E. Brun. *Observation of a subcritical Hopf bifurcation in a laser with an injected signal*. Physical Review A Vol. **36**, No. 3, p. 1280–1287, Aug. 1987.

[Hoppensteadt 1997] F. C. Hoppensteadt and E. M. Izhikevich, *Weakly Connected Neural Networks*. Applied Mathematical Sciences. Springer-Verlag, New York, 1997, ISBN 978-0-387-94948-2.

[Horn 1992] R. Horn and S. J. Korn, *[8] Prevention of rundown in electrophysiological recording*. In *Methods in Enzymology*, volume 207 of *Ion Channels*, p. 149–155. Academic Press, Jan. 1992, doi:10.1016/0076-6879(92)07010-L.

[Izhikevich 1999] E. M. Izhikevich. *Class 1 neural excitability, conventional synapses, weakly connected networks, and mathematical foundations of pulse-coupled models*. IEEE Transactions on Neural Networks Vol. **10**, No. 3, p. 499–507, May 1999.

[Izhikevich 2000a] E. Izhikevich. *Phase Equations for Relaxation Oscillators*. SIAM Journal on Applied Mathematics Vol. **60**, No. 5, p. 1789–1804, Jan. 2000.

[Izhikevich 2000b] E. M. Izhikevich. *Neural excitability, spiking and bursting*. International Journal of Bifurcation and Chaos Vol. **10**, No. 06, p. 1171–1266, 2000.

[Izhikevich 2007] E. M. Izhikevich, *Dynamical systems in neuroscience: the geometry of excitability and bursting*. Computational neuroscience. MIT Press, Cambridge, Mass, 2007, ISBN 0-262-09043-0 978-0-262-09043-8.

[Jagher 1996] P. C. D. Jagher, W. A. v. d. Graaf, and D. Lenstra. *Relaxation-oscillation phenomena in an injection-locked semiconductor laser*. Quantum and Semiclassical Optics: Journal of the European Optical Society Part B Vol. **8**, No. 4, p. 805, 1996.

[Kelleher 2009] B. Kelleher, D. Goulding, S. P. Hegarty, G. Huyet, D.-Y. Cong, A. Martinez, A. Lemaître, A. Ramdane, M. Fischer, F. Gerschütz, and J. Koeth. *Excitable phase slips in an injection-locked single-mode quantum-dot laser*. Optics Letters Vol. **34**, No. 4, p. 440–442, Feb. 2009.

[Kelleher 2010] B. Kelleher, D. Goulding, B. B. Pascual, S. P. Hegarty, and G. Huyet. *Phasor plots in optical injection experiments.* The European Physical Journal D Vol. **58**, No. 2, p. 175–179, Mar. 2010.

[Kelleher 2011] B. Kelleher, C. Bonatto, G. Huyet, and S. P. Hegarty. *Excitability in optically injected semiconductor lasers: Contrasting quantum- well- and quantum-dot-based devices.* Physical Review E Vol. **83**, No. 2, p. 026207, Feb. 2011.

[Kelleher 2012a] B. Kelleher, D. Goulding, B. Baselga Pascual, S. P. Hegarty, and G. Huyet. *Bounded phase phenomena in the optically injected laser.* Physical Review E Vol. **85**, No. 4, p. 046212, Apr. 2012.

[Kelleher 2012b] B. Kelleher, S. P. Hegarty, and G. Huyet. *Modified relaxation oscillation parameters in optically injected semiconductor lasers.* JOSA B Vol. **29**, No. 8, p. 2249–2254, Aug. 2012.

[Kennel 1992] M. B. Kennel, R. Brown, and H. D. I. Abarbanel. *Determining embedding dimension for phase-space reconstruction using a geometrical construction.* Physical Review A Vol. **45**, No. 6, p. 3403–3411, Mar. 1992.

[Kotani 2014] K. Kotani, I. Yamaguchi, L. Yoshida, Y. Jimbo, and G. B. Ermentrout. *Population dynamics of the modified theta model: macroscopic phase reduction and bifurcation analysis link microscopic neuronal interactions to macroscopic gamma oscillation.* Journal of The Royal Society Interface Vol. **11**, No. 95, p. 20140058, Jun. 2014.

[Kovanis 2010] V. Kovanis, A. Gavrielides, and J. A. C. Gallas. *Labyrinth bifurcations in optically injected diode lasers.* The European Physical Journal D Vol. **58**, No. 2, p. 181–186, Jun. 2010.

[Kozyreff 2000] G. Kozyreff, A. G. Vladimirov, and P. Mandel. *Global Coupling with Time Delay in an Array of Semiconductor Lasers.* Physical Review Letters Vol. **85**, No. 18, p. 3809–3812, Oct. 2000.

[Krauskopf 1997] B. Krauskopf, W. A. Van der Graaf, and D. Lenstra. *Bifurcations of relaxation oscillations in an optically injected diode laser.* Quantum and Semiclassical Optics: Journal of the European Optical Society Part B Vol. **9**, No. 5, p. 797, 1997.

[Krauskopf 2003] B. Krauskopf, K. Schneider, J. Sieber, S. Wieczorek, and M. Wolfrum. *Excitability and self-pulsations near homoclinic bifurcations in semiconductor laser systems.* Optics Communications Vol. **215**, No. 4–6, p. 367–379, Jan. 2003.

[Krupa 2008] M. Krupa, N. Popović, and N. Kopell. *Mixed-Mode Oscillations in Three Time-Scale Systems: A Prototypical Example.* SIAM Journal on Applied Dynamical Systems Vol. **7**, No. 2, p. 361–420, Jan. 2008.

[Kuehn 2015] C. Kuehn, *Multiple Time Scale Dynamics*. Applied Mathematical Sciences. Springer International Publishing, 2015, ISBN 978-3-319-12315-8.

[Kuhnert 1989] L. Kuhnert, K. I. Agladze, and V. I. Krinsky. *Image processing using light-sensitive chemical waves*. Nature Vol. **337**, p. 244, Jan. 1989.

[Kumar 2010] A. Kumar, S. Rotter, and A. Aertsen. *Spiking activity propagation in neuronal networks: reconciling different perspectives on neural coding*. Nature Reviews. Neuroscience Vol. **11**, No. 9, p. 615–627, Sep. 2010.

[Kuramoto 1975] Y. Kuramoto, *Self-entrainment of a population of coupled non-linear oscillators*. In H. Araki, ed., *International Symposium on Mathematical Problems in Theoretical Physics*, p. 420–422, (Springer Berlin Heidelberg1975), ISBN 978-3-540-37509-8.

[Kuramoto 1984] Y. Kuramoto, *Chemical Oscillations, Waves, and Turbulence*. Springer Series in Synergetics. Springer-Verlag, Berlin Heidelberg, 1984, ISBN 978-3-642-69691-6.

[Kuramoto 2002] Y. Kuramoto and D. Battogtokh. *Coexistence of Coherence and Incoherence in Nonlocally Coupled Phase Oscillators*. Vol. **5**, No. 4, p. 6, 2002.

[Kurt 2014] M. Kurt, M. Eriten, D. M. McFarland, L. A. Bergman, and A. F. Vakakis. *Strongly nonlinear beats in the dynamics of an elastic system with a strong local stiffness nonlinearity: Analysis and identification*. Journal of Sound and Vibration Vol. **333**, No. 7, p. 2054–2072, Mar. 2014.

[Laing 2015] C. Laing. *Exact Neural Fields Incorporating Gap Junctions*. SIAM Journal on Applied Dynamical Systems Vol. **14**, No. 4, p. 1899–1929, Jan. 2015.

[Lang 1980] R. Lang and K. Kobayashi. *External optical feedback effects on semiconductor injection laser properties*. IEEE Journal of Quantum Electronics Vol. **16**, No. 3, p. 347–355, Mar. 1980.

[Lang 1982] R. Lang. *Injection locking properties of a semiconductor laser*. IEEE Journal of Quantum Electronics Vol. **18**, No. 6, p. 976–983, Jun. 1982.

[Larger 2015] L. Larger, B. Penkovsky, and Y. Maistrenko. *Laser chimeras as a paradigm for multistable patterns in complex systems*. Nature Communications Vol. **6**, Jul. 2015.

[Larotonda 2002] M. A. Larotonda, A. Hnilo, J. M. Mendez, and A. M. Yacomotti. *Experimental investigation on excitability in a laser with a*

saturable absorber. Physical Review A Vol. **65**, No. 3, p. 033812, Feb. 2002.

[Latimer 1993] P. Latimer. *Use of the Talbot effect to couple the phases of lasers*. Applied Physics Letters Vol. **62**, No. 3, p. 217–218, Jan. 1993.

[LeCun 2015] Y. LeCun, Y. Bengio, and G. Hinton. *Deep learning*. Nature Vol. **521**, No. 7553, p. 436–444, May 2015.

[Lee 2003] T. H. Lee, *The Design of CMOS Radio-Frequency Integrated Circuits, Second Edition*. Cambridge University Press, Cambridge, UK ; New York, 2nd edn., Dec. 2003, ISBN 978-0-521-83539-8.

[Leung 1991] L.-W. S. Leung and C.-Y. C. Yim. *Intrinsic membrane potential oscillations in hippocampal neurons in vitro*. Brain Research Vol. **553**, No. 2, p. 261–274, Jul. 1991.

[Lewis 2003] T. J. Lewis and J. Rinzel. *Dynamics of spiking neurons connected by both inhibitory and electrical coupling*. Journal of Computational Neuroscience Vol. **14**, No. 3, p. 283–309, Jun. 2003.

[Likhanskiĭ 1990] V. V. Likhanskiĭ and A. P. Napartovich. *Radiation emitted by optically coupled lasers*. Soviet Physics Uspekhi Vol. **33**, No. 3, p. 228, 1990.

[Lippi 2000] G. L. Lippi, S. Barland, and F. Monsieur. *Invariant Integral and the Transition to Steady States in Separable Dynamical Systems*. Physical Review Letters Vol. **85**, No. 1, p. 62–65, Jul. 2000.

[Lorensen 1987] W. E. Lorensen and H. E. Cline, *Marching Cubes: A High Resolution 3d Surface Construction Algorithm*. In *Proceedings of the 14th Annual Conference on Computer Graphics and Interactive Techniques*, SIGGRAPH '87, p. 163–169, (ACM, New York, NY, USA1987), ISBN 978-0-89791-227-3, doi:10.1145/37401.37422.

[Lugiato 1984] L. A. Lugiato, P. Mandel, and L. M. Narducci. *Adiabatic elimination in nonlinear dynamical systems*. Physical Review A Vol. **29**, No. 3, p. 1438–1452, Mar. 1984.

[Lugiato 1988a] L. A. Lugiato and C. Oldano. *Stationary spatial patterns in passive optical systems: Two-level atoms*. Physical Review A Vol. **37**, No. 10, p. 3896–3908, May 1988.

[Lugiato 1988b] L. A. Lugiato, C. Oldano, and L. M. Narducci. *Cooperative frequency locking and stationary spatial structures in lasers*. JOSA B Vol. **5**, No. 5, p. 879–888, May 1988.

[Lugiato 2015] L. Lugiato, F. Prati, and M. Brambilla, *Nonlinear Optical Systems*. Cambridge University Press, 2015, doi:10.1017/CBO9781107477254.

[Luke 2013] T. B. Luke, E. Barreto, and P. So. *Complete Classification of the Macroscopic Behavior of a Heterogeneous Network of Theta Neurons.* Neural Computation Vol. **25**, No. 12, p. 3207–3234, Dec. 2013.

[Maass 2002] W. Maass, T. Natschläger, and H. Markram. *Real-time computing without stable states: a new framework for neural computation based on perturbations.* Neural Computation Vol. **14**, No. 11, p. 2531–2560, Nov. 2002.

[Makarov 2001] V. A. Makarov, V. I. Nekorkin, and M. G. Velarde. *Spiking behavior in a noise-driven system combining oscillatory and excitatory properties.* Physical Review Letters Vol. **86**, No. 15, p. 3431–3434, Apr. 2001.

[Manevitch 2009] L. I. Manevitch and A. I. Musienko. *Limiting phase trajectories and energy exchange between anharmonic oscillator and external force.* Nonlinear Dynamics Vol. **58**, No. 4, p. 633–642, Dec. 2009.

[Marino 2004] F. Marino, G. Catalán, P. Sánchez, S. Balle, and O. Piro. *Thermo-Optical "Canard Orbits" and Excitable Limit Cycles.* Physical Review Letters Vol. **92**, No. 7, p. 073901, Feb. 2004.

[Marino 2005] F. Marino and S. Balle. *Excitable Optical Waves in Semiconductor Microcavities.* Physical Review Letters Vol. **94**, No. 9, p. 094101, Mar. 2005.

[Marino 2007] F. Marino, F. Marin, S. Balle, and O. Piro. *Chaotically Spiking Canards in an Excitable System with 2d Inertial Fast Manifolds.* Physical Review Letters Vol. **98**, No. 7, p. 074104, Feb. 2007.

[Marino 2011] F. Marino, M. Ciszak, S. F. Abdalah, K. Al-Naimee, R. Meucci, and F. T. Arecchi. *Mixed-mode oscillations via canard explosions in light-emitting diodes with optoelectronic feedback.* Physical Review E Vol. **84**, No. 4, p. 047201, Oct. 2011.

[Martin-Regalado 1997] J. Martin-Regalado, F. Prati, M. S. Miguel, and N. B. Abraham. *Polarization properties of vertical-cavity surface-emitting lasers.* IEEE Journal of Quantum Electronics Vol. **33**, No. 5, p. 765–783, May 1997.

[Masoller 2005] C. Masoller and A. C. Martí. *Random Delays and the Synchronization of Chaotic Maps.* Physical Review Letters Vol. **94**, No. 13, Apr. 2005.

[Mayol 2001] C. Mayol, M. A. Natiello, and M. G. Zimmermann. *RESONANCE STRUCTURE IN A WEAKLY DETUNED LASER WITH INJECTED SIGNAL.* International Journal of Bifurcation and Chaos Vol. **11**, No. 10, p. 2587–2605, Oct. 2001.

[Mayol 2002] C. Mayol, R. Toral, C. R. Mirasso, and M. A. Natiello. *Class-A lasers with injected signal: Bifurcation set and Lyapunov–potential function.* Physical Review A Vol. **66**, No. 1, p. 013808, Jul. 2002.

[Miazek 2018] A. Miazek, *Synchronisation d'un ensemble de lasers chaotiques, couplés en réseau entièrement connecté.* Rapport de stage master 1 physique, Université de Lille, INPHYNI lab, 2018.

[Michaels 1987] D. C. Michaels, E. P. Matyas, and J. Jalife. *Mechanisms of sinoatrial pacemaker synchronization: a new hypothesis.* Circulation Research Nov. 1987.

[Mirollo 1990] R. E. Mirollo and S. H. Strogatz. *Synchronization of Pulse-Coupled Biological Oscillators.* SIAM Journal on Applied Mathematics Vol. **50**, No. 6, p. 1645–1662, Dec. 1990.

[Modha 2011] D. S. Modha, R. Ananthanarayanan, S. K. Esser, A. Ndirango, A. J. Sherbondy, and R. Singh. *Cognitive Computing.* Commun. ACM Vol. **54**, No. 8, p. 62–71, Aug. 2011.

[Mogensen 1985] F. Mogensen, H. Olesen, and G. Jacobsen. *Locking conditions and stability properties for a semiconductor laser with external light injection.* Quantum Electronics, IEEE Journal of Vol. **21**, p. 784, Aug. 1985.

[Montbrió 2015] E. Montbrió, D. Pazó, and A. Roxin. *Macroscopic Description for Networks of Spiking Neurons.* Physical Review X Vol. **5**, No. 2, p. 021028, Jun. 2015.

[Morris 1981] C. Morris and H. Lecar. *Voltage oscillations in the barnacle giant muscle fiber.* Biophysical Journal Vol. **35**, No. 1, p. 193–213, Jul. 1981.

[Motoike 2003] I. N. Motoike and K. Yoshikawa. *Information operations with multiple pulses on an excitable field.* p. 7, 2003.

[Nahmias 2013] M. A. Nahmias and A. N. Tait. *A Leaky Integrate-and-Fire Laser Neuron for Ultrafast Cognitive Computing.* IEEE JOURNAL OF SELECTED TOPICS IN QUANTUM ELECTRONICS Vol. **19**, No. 5, p. 13, 2013.

[Nakagawa 1994] N. Nakagawa and Y. Kuramoto. *From collective oscillations to collective chaos in a globally coupled oscillator system.* Physica D: Nonlinear Phenomena Vol. **75**, No. 1, p. 74–80, Aug. 1994.

[Nakao 2018] H. Nakao, S. Yasui, M. Ota, K. Arai, and Y. Kawamura. *Phase reduction and synchronization of a network of coupled dynamical elements exhibiting collective oscillations.* Chaos: An Interdisciplinary Journal of Nonlinear Science Vol. **28**, No. 4, p. 045103, Apr. 2018.

[Nekorkin 1999] V. Nekorkin, M. Voronin, and M. Velarde. *Clusters in an assembly of globally coupled bistable oscillators*. The European Physical Journal B - Condensed Matter and Complex Systems Vol. **9**, No. 3, p. 533–543, Jun. 1999.

[Neumann 1977] E. Neumann and J. Bernhardt. *Physical Chemistry of Excitable Biomembranes*. Annual Review of Biochemistry Vol. **46**, No. 1, p. 117–141, Jun. 1977.

[Nixon 2011] M. Nixon, M. Friedman, E. Ronen, A. A. Friesem, N. Davidson, and I. Kanter. *Synchronized Cluster Formation in Coupled Laser Networks*. Physical Review Letters Vol. **106**, No. 22, p. 223901, Jun. 2011.

[Nixon 2012] M. Nixon, M. Fridman, E. Ronen, A. A. Friesem, N. Davidson, and I. Kanter. *Controlling Synchronization in Large Laser Networks*. Physical Review Letters Vol. **108**, No. 21, p. 214101, May 2012.

[Nixon 2013] M. Nixon, E. Ronen, A. A. Friesem, and N. Davidson. *Observing Geometric Frustration with Thousands of Coupled Lasers*. Physical Review Letters Vol. **110**, No. 18, p. 184102, May 2013.

[Nkomo 2013] S. Nkomo, M. R. Tinsley, and K. Showalter. *Chimera States in populations of nonlocally coupled chemical oscillators*. Physical Review Letters Vol. **110**, No. 24, p. 244102, Jun. 2013.

[Noblin 2012] X. Noblin, N. O. Rojas, J. Westbrook, C. Llorens, M. Argentina, and J. Dumais. *The fern sporangium: a unique catapult*. Science (New York, N.Y.) Vol. **335**, No. 6074, p. 1322, Mar. 2012.

[O'Brien 2004] D. O'Brien, S. P. Hegarty, G. Huyet, and A. V. Uskov. *Sensitivity of quantum-dot semiconductor lasers to optical feedback*. Optics Letters Vol. **29**, No. 10, p. 1072–1074, May 2004.

[Olejniczak 2010] L. Olejniczak, K. Panajotov, H. Thienpont, and M. Sciamanna. *Self-pulsations and excitability in optically injected quantum-dot lasers: Impact of the excited states and spontaneous emission noise*. Physical Review A Vol. **82**, No. 2, p. 023807, Aug. 2010.

[Oliva 2001] R. A. Oliva and S. H. Strogatz. *DYNAMICS OF A LARGE ARRAY OF GLOBALLY COUPLED LASERS WITH DISTRIBUTED FREQUENCIES*. International Journal of Bifurcation and Chaos Vol. **11**, No. 09, p. 2359–2374, Sep. 2001.

[Oliveira 2015] H. M. Oliveira and L. V. Melo. *Huygens synchronization of two clocks*. Scientific Reports Vol. **5**, p. 11548, Jul. 2015.

[Olmi 2010] S. Olmi, A. Politi, and A. Torcini. *Collective chaos in pulse-coupled neural networks*. EPL (Europhysics Letters) Vol. **92**, No. 6, p. 60007, Dec. 2010.

[Olmi 2014] S. Olmi, A. Navas, S. Boccaletti, and A. Torcini. *Hysteretic transitions in the Kuramoto model with inertia*. Physical Review E Vol. **90**, No. 4, p. 042905, Oct. 2014.

[Olmi 2015] S. Olmi. *Chimera states in coupled Kuramoto oscillators with inertia*. Chaos: An Interdisciplinary Journal of Nonlinear Science Vol. **25**, No. 12, p. 123125, Dec. 2015.

[Oppo 1985] G. L. Oppo and A. Politi. *Toda potential in laser equations*. Zeitschrift für Physik B Condensed Matter Vol. **59**, No. 1, p. 111–115, Mar. 1985.

[Oppo 1986] G. L. Oppo, A. Politi, G. L. Lippi, and F. T. Arecchi. *Frequency pushing in lasers with injected signal*. Physical Review A Vol. **34**, No. 5, p. 4000–4007, Nov. 1986.

[Ostojic 2014] S. Ostojic. *Two types of asynchronous activity in networks of excitatory and inhibitory spiking neurons*. Nature Neuroscience Vol. **17**, No. 4, p. 594–600, Apr. 2014.

[Ott 2008] E. Ott and T. M. Antonsen. *Low dimensional behavior of large systems of globally coupled oscillators*. Chaos: An Interdisciplinary Journal of Nonlinear Science Vol. **18**, No. 3, p. 037113, Sep. 2008.

[Ott 2009] E. Ott and T. M. Antonsen. *Long time evolution of phase oscillator systems*. Chaos: An Interdisciplinary Journal of Nonlinear Science Vol. **19**, No. 2, p. 023117, Jun. 2009.

[Ott 2011] E. Ott, B. R. Hunt, and T. M. Antonsen. *Comment on "Long time evolution of phase oscillator systems" [Chaos 19, 023117 (2009)]*. Chaos: An Interdisciplinary Journal of Nonlinear Science Vol. **21**, No. 2, p. 025112, Jun. 2011.

[Panaggio 2015] M. J. Panaggio and D. M. Abrams. *Chimera states: coexistence of coherence and incoherence in networks of coupled oscillators*. Nonlinearity Vol. **28**, No. 3, p. R67, 2015.

[Paugam-Moisy 2012] H. Paugam-Moisy and S. Bohte, *Computing with Spiking Neuron Networks*. In G. Rozenberg, T. Bäck, and J. N. Kok, eds., *Handbook of Natural Computing*, p. 335–376. Springer Berlin Heidelberg, 2012, ISBN 978-3-540-92910-9, doi:10.1007/978-3-540-92910-9_10.

[Pazó 2016] D. Pazó and E. Montbrió. *From Quasiperiodic Partial Synchronization to Collective Chaos in Populations of Inhibitory Neurons with Delay*. Physical Review Letters Vol. **116**, No. 23, p. 238101, Jun. 2016.

[Pechenkin 2009] A. Pechenkin. *B P Belousov and his reaction*. Journal of Biosciences Vol. **34**, No. 3, p. 365–371, Sep. 2009.

[Pecora 1990] L. M. Pecora and T. L. Carroll. *Synchronization in chaotic systems*. Physical Review Letters Vol. **64**, No. 8, p. 821–824, Feb. 1990.

[Petitbon 1986] I. Petitbon, P. Gallion, G. Debarge, and C. Chabran. *Locking bandwidth and relaxation oscillations of an injection-locked semiconductor laser*. Electronics Letters Vol. **22**, p. 889–890, Feb. 1986.

[Pietras 2016] B. Pietras and A. Daffertshofer. *Ott-Antonsen attractiveness for parameter-dependent oscillatory systems*. Chaos: An Interdisciplinary Journal of Nonlinear Science Vol. **26**, No. 10, p. 103101, Oct. 2016.

[Pikovsky 2003] A. Pikovsky, M. Rosenblum, and J. Kurths, *Synchronization: A Universal Concept in Nonlinear Sciences*. Cambridge University Press, Cambridge, 1st edn., May 2003, ISBN 978-0-521-53352-2.

[Pilipchuk 2008] V. N. Pilipchuk. *Transitions from strongly to weakly-nonlinear dynamics in a class of exactly solvable oscillators and nonlinear beat phenomena*. Nonlinear Dynamics Vol. **52**, No. 3, p. 263–276, May 2008.

[Politi 1986] A. Politi, G. L. Oppo, and R. Badii. *Coexistence of conservative and dissipative behavior in reversible dynamical systems*. Physical Review A Vol. **33**, No. 6, p. 4055–4060, Jun. 1986.

[Prati 2010] F. Prati, G. Tissoni, C. McIntyre, and G. L. Oppo. *Static and dynamic properties of cavity solitons in VCSELs with optical injection*. The European Physical Journal D Vol. **59**, No. 1, p. 139–147, Jul. 2010.

[Prescott 2008] S. A. Prescott, S. Ratté, Y. De Koninck, and T. J. Sejnowski. *Pyramidal neurons switch from integrators in vitro to resonators under in vivo-like conditions*. Journal of Neurophysiology Vol. **100**, No. 6, p. 3030–3042, Dec. 2008.

[Prucnal 2016] P. R. Prucnal, B. J. Shastri, T. F. d. Lima, M. A. Nahmias, and A. N. Tait. *Recent progress in semiconductor excitable lasers for photonic spike processing*. Advances in Optics and Photonics Vol. **8**, No. 2, p. 228–299, Jun. 2016.

[Pyle 2017] R. Pyle and R. Rosenbaum. *Spatiotemporal Dynamics and Reliable Computations in Recurrent Spiking Neural Networks*. Physical Review Letters Vol. **118**, No. 1, p. 018103, Jan. 2017.

[Rakshit 2017] S. Rakshit, B. K. Bera, M. Perc, and D. Ghosh. *Basin stability for chimera states*. Scientific Reports Vol. **7**, No. 1, p. 2412, May 2017.

[Rayleigh 1894] J. W. S. Rayleigh, *The theory of sound*. University of Michigan Library, Jan. 1894.

[Rimoldi 2017] C. Rimoldi, F. Gustave, L. Columbo, M. Brambilla, S. Barland, F. Prati, and G. Tissoni. *Abnormal chiral events in a semiconductor*

laser with coherent injection. Optics Express Vol. **25**, No. 18, p. 22017–22031, Sep. 2017.

[Rinzel 2013] J. Rinzel and G. Huguet. *Nonlinear Dynamics of Neuronal Excitability, Oscillations, and Coincidence Detection*. Communications on pure and applied mathematics Vol. **66**, No. 9, p. 1464–1494, Sep. 2013.

[Romeira 2013] B. Romeira, J. Javaloyes, C. N. Ironside, J. M. L. Figueiredo, S. Balle, and O. Piro. *Excitability and optical pulse generation in semiconductor lasers driven by resonant tunneling diode photo-detectors*. Optics Express Vol. **21**, No. 18, p. 20931–20940, Sep. 2013.

[Rosenbaum 2017] R. Rosenbaum, M. A. Smith, A. Kohn, J. E. Rubin, and B. Doiron. *The spatial structure of correlated neuronal variability*. Nature Neuroscience Vol. **20**, No. 1, p. 107–114, Jan. 2017.

[Roxin 2005] A. Roxin, N. Brunel, and D. Hansel. *Role of Delays in Shaping Spatiotemporal Dynamics of Neuronal Activity in Large Networks*. Physical Review Letters Vol. **94**, No. 23, p. 238103, Jun. 2005.

[Rzhanov 1993] Y. A. Rzhanov, H. Richardson, A. A. Hagberg, and J. V. Moloney. *Spatiotemporal oscillations in a semiconductor \'etalon*. Physical Review A Vol. **47**, No. 2, p. 1480–1491, Feb. 1993.

[Sandoz 2012] G. Sandoz, J. Levitz, R. H. Kramer, and E. Y. Isacoff. *Optical Control of Endogenous Proteins with a Photoswitchable Conditional Subunit Reveals a Role for TREK1 in GABAB Signaling*. Neuron Vol. **74**, No. 6, p. 1005–1014, Jun. 2012.

[Sarpeshkar 1998] R. Sarpeshkar. *Analog versus digital: extrapolating from electronics to neurobiology*. Neural Computation Vol. **10**, No. 7, p. 1601–1638, Oct. 1998.

[Schmidt 2018] H. Schmidt, D. Avitabile, E. Montbrió, and A. Roxin. *Network mechanisms underlying the role of oscillations in cognitive tasks*. PLOS Computational Biology Vol. **14**, No. 9, p. e1006430, 2018.

[Schwalger 2017] T. Schwalger, M. Deger, and W. Gerstner. *Towards a theory of cortical columns: From spiking neurons to interacting neural populations of finite size*. PLOS Computational Biology Vol. **13**, No. 4, p. e1005507, Apr. 2017.

[Selmi 2014] F. Selmi, R. Braive, G. Beaudoin, I. Sagnes, R. Kuszelewicz, and S. Barbay. *Relative Refractory Period in an Excitable Semiconductor Laser*. Physical Review Letters Vol. **112**, No. 18, p. 183902, May 2014.

[Selmi 2015] F. Selmi, R. Braive, G. Beaudoin, I. Sagnes, R. Kuszelewicz, and S. Barbay. *Temporal summation in a neuromimetic micropillar laser*. Optics Letters Vol. **40**, No. 23, p. 5690, Dec. 2015. arXiv: 1510.07853.

[Shastri 2015] B. J. Shastri, M. A. Nahmias, A. N. Tait, B. Wu, and P. R. Prucnal. *SIMPEL: Circuit model for photonic spike processing laser neurons*. p. 16, 2015.

[Shastri 2016] B. J. Shastri, M. A. Nahmias, A. N. Tait, A. W. Rodriguez, B. Wu, and P. R. Prucnal. *Spike processing with a graphene excitable laser*. Scientific Reports Vol. **6**, p. 19126, Jan. 2016.

[Shil'nikov 1995] A. Shil'nikov, G. Nicolis, and C. Nicolis. *Bifurcation and predictability analysis of a low-order atmospheric circulation model*. International Journal of Bifurcation and Chaos Vol. **05**, No. 06, p. 1701–1711, Dec. 1995.

[Shilnikov 2007] L. P. Shilnikov and A. Shilnikov, *Shilnikov bifurcation - Scholarpedia*. http://dx.doi.org/10.4249/scholarpedia.1891, 2007.

[Sigg 2014] D. Sigg. *Modeling ion channels: Past, present, and future*. The Journal of General Physiology Vol. **144**, No. 1, p. 7–26, Jul. 2014.

[So 2011] P. So and E. Barreto. *Generating macroscopic chaos in a network of globally coupled phase oscillators*. Chaos: An Interdisciplinary Journal of Nonlinear Science Vol. **21**, No. 3, p. 033127, Sep. 2011.

[So 2014] P. So, T. B. Luke, and E. Barreto. *Networks of theta neurons with time-varying excitability: Macroscopic chaos, multistability, and final-state uncertainty*. Physica D: Nonlinear Phenomena Vol. **267**, p. 16–26, Jan. 2014.

[Solari 1994] H. G. Solari and G.-L. Oppo. *Laser with injected signal: perturbation of an invariant circle*. Optics Communications Vol. **111**, No. 1, p. 173–190, Sep. 1994.

[Sorrentino 2007] F. Sorrentino and E. Ott. *Network synchronization of groups*. Physical Review. E, Statistical, Nonlinear, and Soft Matter Physics Vol. **76**, No. 5 Pt 2, p. 056114, Nov. 2007.

[Spiegler 2011] A. Spiegler, T. R. Knösche, K. Schwab, J. Haueisen, and F. M. Atay. *Modeling Brain Resonance Phenomena Using a Neural Mass Model*. PLoS Computational Biology Vol. **7**, No. 12, Dec. 2011.

[Strogatz 2000] S. H. Strogatz. *From Kuramoto to Crawford: exploring the onset of synchronization in populations of coupled oscillators*. Physica D: Nonlinear Phenomena Vol. **143**, No. 1-4, p. 1–20, Sep. 2000.

[Svelto 2010] O. Svelto, *Principles of Lasers*. Springer US, 5th edn., 2010, ISBN 978-1-4419-1301-2.

[Szalai 2013] R. Szalai, *Knut: A continuation and bifurcation software for delay-differential equations*. http://gitorious.org/knut, 2013.

[Tait 2013] A. N. Tait, M. A. Nahmias, Y. Tian, B. J. Shastri, and P. R. Prucnal, *Photonic neuromorphic signal processing and computing* (2013).

[Tartwijk 1995] G. H. M. v. Tartwijk and D. Lenstra. *Semiconductor lasers with optical injection and feedback*. Quantum and Semiclassical Optics: Journal of the European Optical Society Part B Vol. **7**, No. 2, p. 87, 1995.

[Terrien 2018] S. Terrien, B. Krauskopf, N. G. R. Broderick, R. Braive, G. Beaudoin, I. Sagnes, and S. Barbay. *Pulse train interaction and control in a microcavity laser with delayed optical feedback*. Optics Letters Vol. **43**, No. 13, p. 3013–3016, Jul. 2018.

[Thorpe 2001] S. Thorpe, A. Delorme, and R. V. Rullen. *Spike-based strategies for rapid processing*. Neural Networks Vol. **14**, No. 6-7, p. 715–725, 2001.

[Timofeev 2012] I. Timofeev, M. Bazhenov, J. Seigneur, and T. Sejnowski, *Neuronal Synchronization and Thalamocortical Rhythms in Sleep, Wake and Epilepsy*. In J. L. Noebels, M. Avoli, M. A. Rogawski, R. W. Olsen, and A. V. Delgado-Escueta, eds., *Jasper's Basic Mechanisms of the Epilepsies*. National Center for Biotechnology Information (US), 4th edn., 2012.

[Tinsley 2012] M. R. Tinsley, S. Nkomo, and K. Showalter. *Chimera and phase-cluster states in populations of coupled chemical oscillators*. Nature Physics Vol. **8**, No. 9, p. 662–665, Sep. 2012.

[Tononi 2008] G. Tononi. *Consciousness as integrated information: a provisional manifesto*. The Biological Bulletin Vol. **215**, No. 3, p. 216–242, Dec. 2008.

[Touboul 2011] J. Touboul, F. Wendling, P. Chauvel, and O. Faugeras. *Neural mass activity, bifurcations, and epilepsy*. Neural Computation Vol. **23**, No. 12, p. 3232–3286, Dec. 2011.

[Trebacz 2006] K. Trebacz, H. Dziubinska, and E. Krol, *Electrical Signals in Long-Distance Communication in Plants*. In F. Baluška, S. Mancuso, and D. Volkmann, eds., *Communication in Plants: Neuronal Aspects of Plant Life*, p. 277–290. Springer Berlin Heidelberg, 2006, ISBN 978-3-540-28516-8, doi:10.1007/978-3-540-28516-8_19.

[Tredicce 1985] J. R. Tredicce, F. T. Arecchi, G. L. Lippi, and G. P. Puccioni. *Instabilities in lasers with an injected signal*. JOSA B Vol. **2**, No. 1, p. 173–183, Jan. 1985.

[Trela 2013] N. Trela, H. J. Baker, and D. R. Hall. *Locking and wavelength selection of an ultra-collimated single-mode diode laser bar by a volume*

holographic grating. Optics Express Vol. **21**, No. 4, p. 4512–4517, Feb. 2013.

[Turconi 2013] M. Turconi, B. Garbin, M. Feyereisen, M. Giudici, and S. Barland. *Control of excitable pulses in an injection-locked semiconductor laser*. Physical Review E Vol. **88**, No. 2, p. 022923, Aug. 2013.

[Uskov 1998a] A. V. Uskov, Y. Boucher, J. Le Bihan, and J. McInerney. *Theory of a self-assembled quantum-dot semiconductor laser with Auger carrier capture: Quantum efficiency and nonlinear gain*. Applied Physics Letters Vol. **73**, No. 11, p. 1499–1501, Sep. 1998.

[Uskov 1998b] A. V. Uskov, J. McInerney, F. Adler, H. Schweizer, and M. H. Pilkuhn. *Auger carrier capture kinetics in self-assembled quantum dot structures*. Applied Physics Letters Vol. **72**, No. 1, p. 58–60, Jan. 1998.

[van der Pol 1927] B. van der Pol. *VII. Forced oscillations in a circuit with non-linear resistance. (Reception with reactive triode)*. The London, Edinburgh, and Dublin Philosophical Magazine and Journal of Science Vol. **3**, No. 13, p. 65–80, Jan. 1927.

[Van der Sande 2017] G. Van der Sande, D. Brunner, and M. C. Soriano. *Advances in photonic reservoir computing*. Nanophotonics Vol. **6**, No. 3, Jan. 2017.

[Van Vreeswijk 1994] C. Van Vreeswijk, L. F. Abbott, and G. B. Ermentrout. *When inhibition not excitation synchronizes neural firing*. Journal of Computational Neuroscience Vol. **1**, No. 4, p. 313–321, Dec. 1994.

[Vandoorne 2014] K. Vandoorne, P. Mechet, T. V. Vaerenbergh, M. Fiers, G. Morthier, D. Verstraeten, B. Schrauwen, J. Dambre, and P. Bienstman. *Experimental demonstration of reservoir computing on a silicon photonics chip*. Nature Communications Vol. **5**, p. 3541, Mar. 2014.

[Varela 2001] F. Varela, J.-P. Lachaux, E. Rodriguez, and J. Martinerie. *The brainweb: Phase synchronization and large-scale integration*. Nature Reviews Neuroscience Vol. **2**, p. 229, Apr. 2001.

[Veltz 2011] R. Veltz and O. Faugeras. *Stability of the stationary solutions of neural field equations with propagation delays*. The Journal of Mathematical Neuroscience Vol. **1**, No. 1, p. 1, 2011.

[Walker 1969] T. J. Walker. *Acoustic synchrony: two mechanisms in the snowy tree cricket*. Science (New York, N.Y.) Vol. **166**, No. 3907, p. 891–894, Nov. 1969.

[Wang 1978] C. P. Wang. *Master and slave oscillator array system for very large multiline lasers*. Applied Optics Vol. **17**, No. 1, p. 83–86, Jan. 1978.

[Watanabe 1994] S. Watanabe and S. H. Strogatz. *Constants of motion for superconducting Josephson arrays.* Physica D: Nonlinear Phenomena Vol. **74**, No. 3-4, p. 197–253, Jul. 1994.

[Wechselberger 2007] M. Wechselberger, *Canards - Scholarpedia.* `http://dx.doi.org/10.4249/scholarpedia.1356`, 2007.

[Wieczorek 1999] S. Wieczorek, B. Krauskopf, and D. Lenstra. *A unifying view of bifurcations in a semiconductor laser subject to optical injection.* Optics Communications Vol. **172**, No. 1, p. 279 – 295, 1999.

[Wieczorek 2002] S. Wieczorek, B. Krauskopf, and D. Lenstra. *Multipulse Excitability in a Semiconductor Laser with Optical Injection.* Physical Review Letters Vol. **88**, No. 6, p. 063901, Jan. 2002.

[Wieczorek 2005a] S. Wieczorek, B. Krauskopf, T. B. Simpson, and D. Lenstra. *The dynamical complexity of optically injected semiconductor lasers.* Physics Reports Vol. **416**, No. 1–2, p. 1–128, Sep. 2005.

[Wieczorek 2005b] S. Wieczorek and B. Krauskopf. *Bifurcations of n - homoclinic orbits in optically injected lasers.* Nonlinearity Vol. **18**, No. 3, p. 1095–1120, May 2005.

[Wilson 1972] H. R. Wilson and J. D. Cowan. *Excitatory and inhibitory interactions in localized populations of model neurons.* Biophysical Journal Vol. **12**, No. 1, p. 1–24, Jan. 1972.

[Wilson 1973] H. R. Wilson and J. D. Cowan. *A mathematical theory of the functional dynamics of cortical and thalamic nervous tissue.* Kybernetik Vol. **13**, No. 2, p. 55–80, Sep. 1973.

[Winfree 1967] A. T. Winfree. *Biological rhythms and the behavior of populations of coupled oscillators.* Journal of Theoretical Biology Vol. **16**, No. 1, p. 15–42, Jul. 1967.

[Winfree 1984] A. T. Winfree. *The prehistory of the Belousov-Zhabotinsky oscillator.* Journal of Chemical Education Vol. **61**, No. 8, p. 661, Aug. 1984.

[Winfree 2001] A. T. Winfree, *The Geometry of Biological Time.* Interdisciplinary Applied Mathematics. Springer-Verlag, New York, 2nd edn., 2001, ISBN 978-0-387-98992-1.

[Yacomotti 2006] A. M. Yacomotti, P. Monnier, F. Raineri, B. B. Bakir, C. Seassal, R. Raj, and J. A. Levenson. *Fast Thermo-Optical Excitability in a Two-Dimensional Photonic Crystal.* Physical Review Letters Vol. **97**, No. 14, p. 143904, Oct. 2006.

[York 1991] R. York and R. Compton. *Quasi-optical power combining using mutually synchronized oscillator arrays.* IEEE Transactions on Mi-

crowave Theory and Techniques Vol. **39**, No. 6, p. 1000–1009, Jun. 1991.

[Yu 1999] D. Yu, W. Lu, and R. G. Harrison. *Dynamic bistability and spiral waves in a laser.* Journal of Optics B: Quantum and Semiclassical Optics Vol. **1**, No. 1, p. 25, 1999.

[Zeberg 2015] H. Zeberg, H. P. C. Robinson, and P. Århem. *Density of voltage-gated potassium channels is a bifurcation parameter in pyramidal neurons.* Journal of Neurophysiology Vol. **113**, No. 2, p. 537–549, Jan. 2015.

[Zehnlé 1992] V. Zehnlé and H. Zeghlache. *Theoretical study of a laser with injected signal. II. Periodic perturbation.* Physical Review A Vol. **46**, No. 9, p. 6028–6035, Nov. 1992.

[Zhou 2002] C. Zhou and J. Kurths. *Spatiotemporal coherence resonance of phase synchronization in weakly coupled chaotic oscillators.* Physical Review. E, Statistical, Nonlinear, and Soft Matter Physics Vol. **65**, No. 4 Pt 1, p. 040101, Apr. 2002.

[Zhou 2018] Q. Zhou, *Mesh Processing — PyMesh 0.2.0 documentation.* `https://pymesh.readthedocs.io/`, 2018.

[Zimmermann 2001] M. G. Zimmermann, M. A. Natiello, and H. G. Solari. *Global bifurcations in a laser with injected signal: Beyond Adler's approximation.* Chaos: An Interdisciplinary Journal of Nonlinear Science Vol. **11**, No. 3, p. 500–513, Sep. 2001.